ABSTRACT

Title of Dissertation: EXAMINATION OF PHOTOCHEMISTRY AND METEOROLOGY OF ATMOSPHERIC POLLUTANTS FROM THE NORTH CHINA PLAIN

Sarah Benish, Doctor of Philosophy, 2021

Dissertation directed by: Professor Russell R. Dickerson, Department of Atmospheric and Oceanic Science

Increasingly severe air pollution over metropolitan regions in China has raised attention in light of its local and regional impacts on health and climate. Computer models can simulate complex interactions between photochemistry and meteorology to inform policy decisions in reducing ground-level pollution. However, models rely on an accurate portrayal of emissions that often possess large uncertainties over regions with evolving pollution characteristics. This work is comprised of a quantitative analysis of air pollutants in the North China Plain that strives to improve such uncertainties by identification of important sources and meteorological conditions for pollution through the combination of observations and models. Measurements used in this dissertation focus on *in situ* observations from the Spring 2016 Air chemistry Research in Asia (ARIAs) campaign, which sampled atmospheric composition across

the heavily populated and industrialized Hebei Province in the North China Plain. High amounts of ozone (O_3) precursors were found throughout and even above the planetary boundary layer, continuing to generate O_3 at high rates to be potentially transported downwind. Evidence for the importance of anthropogenic VOCs on O_3 production is presented. Concentrations of NO_x and VOCs even in the rural areas of this highly industrialized province promote widespread O_3 production and in order to improve air quality over Hebei, both NO_x and VOCs should be regulated. The ARIAs airborne measurements also provide a critical opportunity to characterize chlorofluorocarbons (CFCs) over a suspected CFC-11 source region in China, finding mixing ratios were well above 2016 global background levels. Based on correlations of CFCs with compounds used in their manufacture, I identify likely source regions of new CFCs production and release, in violation of the Montreal Protocol. Finally, I examine the influence of meteorology on surface and aloft measurements during ARIAs. A multiday persistent high pressure episode is presented as a case study to examine the influence of regional transport on air quality measured during ARIAs. This dissertation provides valuable information for understanding one of the most polluted regions in China. Coordinated field and modeling efforts can together provide scientific guidance to inform pollution control measures to meet air quality targets in China.

EXAMINATION OF PHOTOCHEMISTRY AND METEOROLOGY OF ATMOSPHERIC POLLUTANTS FROM THE NORTH CHINA PLAIN

by

Sarah Elizabeth Benish

Dissertation submitted to the Faculty of the Graduate School of the
University of Maryland, College Park, in partial fulfillment
of the requirements for the degree of
Doctor of Philosophy
2021

Advisory Committee:
Professor Russell R. Dickerson, Chair
Professor Ross J. Salawitch
Assistant Professor Timothy P. Canty
Senior Research Scientist Xinrong Ren
Assistant Research Professor Hao He
Associate Professor Akua Asa-Awuku, Dean's Representative

Dedication

This thesis is dedicated to my family, particularly my parents, Daniel and Barbara Benish, and my grandmother Marilyn Schmitz, who have been my greatest supporters, especially in my academic endeavors. Their ongoing encouragement and words of wisdom throughout my life has been never-ending. Thank you for always believing in me.

Acknowledgements

I would like to acknowledge all the people who made this thesis possible. First, I would like to thank my advisor, Russ Dickerson, for his guidance, support, and dedication to my graduate studies. Throughout the many hurdles I faced with my research, he always made time to meet to discuss the next step. Next, thank you to Ross Salawitch and Tim Canty for constructive criticisms on my writing and research and supporting my involvement in science policy. Your advice, suggestions, and feedback have made me a better scientist. I would also like to thank all the scientists involved in the ARIAs field campaign, particularly Xinrong Ren and Hao He for collecting the airborne observations used in this dissertation and helping me with translation. I would also like to acknowledge Drs. Sihua Lu and Min Shao from Peking University for providing the invaluable VOCs observations, as well as to Dr. Bo Yao from the China Meteorological Administration and Dr. Steve Montzka from NOAA for helping conduct an intercomparison experiment during a global pandemic. Without the input and support from the international scientific community on my research, this work would never have been accomplished. Thank you to the agencies that funded my research, with special thanks to the National Science Foundation and the Maryland Department of the Environment.

Lastly, thank you to the multitudes of people who helped me get to the place I am today. I never would have applied to graduate school without the guidance and support from Tracey Holloway from the University of Wisconsin-Madison and Brad Pierce from NOAA. Thank you for offering me a chance to pursue my research interests and for your continued mentoring throughout my career. To all the graduate students I

have met at UMD, especially in the atmospheric chemistry group, I cannot imagine surviving graduate school without you. A special thanks to everyone in the Department of Atmospheric and Oceanic Science, especially the front office staff, who ensures everything in the department runs smoothly. To my parents, Barb and Dan, siblings, Lucas and Laura, my grandmother, Marilyn, and close friends, Carrie Biesinger, Katie Reed, and Jane Sitter, thank you for your encouragement along the way. To my partner Ryan, thank you for always making me laugh when I needed it the most. Finally, thank you to Darwin, my cat, for eating all the lizards that got into the house while I was writing this dissertation.

Table of Contents

List of Tables

List of Figures

List of Abbreviations

AGAGE	Advanced Global Atmospheric Gases Experiment
AGL	Above Ground Level
AMF	Air Mass Factor
ARIAs	Air chemistry Research in Asia
BC	Black carbon
BEIS	Biogenic Emission Inventory System
CAA	Clean Air Act
CAAQS	Chinese Ambient Air Quality Standards
CB6r2	Carbon Bond mechanism (version 6, revision 2)
CCl_4	Carbon tetrachloride
C_2Cl_4	Tetrachloroethylene/perchloroethylene
CFC	Chlorofluorocarbon
CFSv2	Climate Forecast System version 2 Operational analysis
CH_4	Methane
CMA	China Meteorological Administration
CMAQ	Community Multiscale Air Quality model
CMEE	China Ministry of Ecology and the Environment
CO	Carbon monoxide
CO_2	Carbon dioxide
cP	Continental polar
DISCOVER-AQ	Deriving Information on Surface Conditions from Column and VERtically Resolved Observations Relevant to Air Quality
EDGAR	Emissions Database for Global Atmospheric Research
EPA	Environmental Protection Agency
F0AM	Framework in 0-Dimensional Atmospheric Modeling
FID	Flame Ionization Detection
FT	Free troposphere
GC	Gas chromatography
HCFC-22	Hydrochlorofluorocarbon 22
HCHO	Formaldehyde
HYSPLIT	Hybrid Single-Particle Lagrangian Integrated Trajectory model
IUPAC	International Union of Pure and Applied Chemistry
KORUS-AQ	Korea-United States Air Quality study
LPG	Liquified petroleum gas
LST	Local standard time
MDA8	Maximum Daily Average 8-hour Ozone
MIR	Maximum Incremental Reactivity
MOPITT	Measurements of Pollution in the Troposphere
MP	Montreal Protocol
MS	Mass spectrometry
MSL	Mean Sea Level
mT	Maritime tropical
NAAQS	National Ambient Air Quality Standards
NASA	National Aeronautics and Space Administration

NCEP	National Centers for Environmental Prediction
NCP	North China Plain
NIER	Korean National Institute of Environmental Research
NMHC	Non-methane hydrocarbon
NOAA	National Oceanic and Atmospheric Administration
NO_x	Nitrogen oxides
NSF	National Science Foundation
O_3	Ozone
ODS	Ozone Depleting Substance
OFP	Ozone Formation Potential
OH	Hydroxyl radical
OMI	Ozone Monitoring Instrument
PBL	Planetary boundary layer
PKU	Peking University
PM	Particulate Matter
PRD	Pearl River Delta
PSC	Polar stratospheric cloud
PSCF	Potential Source Contribution Function
RF	Research Flight
SCD	Slant Column Density
SJZ	Shijiazhuang
SMOKE	Sparse Matrix Operator Kernel Emissions
SOA	Secondary Organic Aerosol
SO_2	Sulfur dioxide
SPF	Spray polyurethane foam
SSA	Single scattering albedo
SZA	Solar zenith angle
TO-15	Toxics Organics-15
UV	Ultraviolet
VCD	Vertical Column Density
VOC	Volatile organic compound
WAS	Whole Air Sample
WCB	Warm conveyor belt
WMO	World Meteorological Organization
WRF	Weather Research Forecasting model
XT	Xingtai
YRD	Yangtze River Delta

Chapter 1 Introduction

Industrialization throughout the world sparked increased innovation and rapid urbanization. Historically, by-products from our increasingly technological and inventive society such as coal and fossil fuel combustion products, as well as the development of new synthetic chemicals**,** led to unforeseen consequences when released into the atmosphere. A series of severe pollution events as a result of human activities (anthropogenic emissions) in the 19th and 20th centuries brought international attention to the high concentrations of air pollution, particularly caused by the burning of high-sulfur coal. In the mid-1900s, a realization that motor vehicle emissions could contribute to urban smog in sunny areas (Crutzen, 1971; Haagen-Smit, 1952) led to better emission standards on cars and limits on the amount of sulfur in gasoline. Emissions of chlorofluorocarbons (CFCs) from use as refrigerants, foam blowing aerosol sprays, and propellants were eventually regulated after the discovery that these compounds lead to the depletion of the stratospheric ozone layer (Molina and Rowland, 1974).

Epidemiological studies revealed the unseen health effects of particulate matter (PM) and other air pollutants on the human respiratory and circulatory systems (Nel, 2005; Vodonos et al., 2018), resulting in an increased risk of death, high hospital admission rates, and a rise in infant mortality during air pollution episodes (Gao et al., 2015; Ge et al., 2011; Guttikunda and Goel, 2013; Thach et al., 2010). Carbon dioxide (CO_2) levels have also raised concerns over the greenhouse effect and detrimental impacts to human cognitive functions. Exposure to indoor concentrations of CO_2 (950-

2500 ppmv, well above the Occupational Safety and Health Administration's limit of 500 ppmv) have been associated with worsened decision-making performance (Cao et al., 2019; Satish et al., 2012) and lower math test results (Shaughnessy et al., 2006).

This dissertation aims to better understand the important sources and meteorological conditions of air pollution observed aloft in 2016 over Hebei Province, China, a strong economic power and home to over 75 million people. The observational research presented here lends some insights into air pollution in China and its impact on the composition of the atmosphere on both local and global scales.

1.1. Ozone (O_3) Photochemistry

1.1.1 Tropospheric O_3 Production and Sensitivity

Boundary layer O_3 is a secondary pollutant produced by reactions of nitrogen oxides (NO_x=NO+NO_2) and volatile organic compounds (VOCs) in the presence of UV radiation available in sunlight (Crutzen and Zimmerman, 1991). Ozone is harmful to the human respiratory system (Bell et al., 2006; Jerrett et al., 2009) and to photosynthetic processes by vegetation (Avnery et al., 2011; Reich and Amundson, 1985a), while some VOCs, such as benzene and chloroform, are known to be hemotoxic and carcinogenic (Lan et al., 2004). Many countries, including the United States and China, have implemented policy measures to control O_3 and its precursors. In the United States, the Environmental Protection Agency enforces a surface O_3 standard according to the current National Ambient Air Quality Standards (NAAQS) of 70 parts per billion by volume (ppbv), calculated as the daily maximum of an eight-hour running mean. In China, urban surface O_3 is regulated under the Chinese Ambient

Air Quality Standards (CAAQS) of approximately 75 ppbv, also calculated as the daily eight-hour running mean. Since O_3 is not emitted directly, it is necessary to understand the mechanisms in which tropospheric O_3 precursors, mainly NO_x and VOCs, are produced and destroyed.

The main source of NO_x to the atmosphere is high temperature combustion of fossil fuels (33 Tg N y^{-1}), but soil emissions, lightning, and biomass burning also add considerable amounts to the atmosphere (in total about 18 Tg N y^{-1}) (Seinfeld and Pandis, 2006). The reaction between nitrogen dioxide (NO_2) and the hydroxyl radical (OH) to form nitric acid (HNO_3), ultimately scavenged in the atmosphere, is the major sink of NO_x. At night, the main sink occurs through NO_x oxidation to form nitrate (NO_3) and dinitrogen pentoxide (N_2O_5), followed by N_2O_5 hydrolysis. The lifetime of NO_x ranges from hours to a few days (Seinfeld and Pandis, 2006). Total reactive nitrogen (NO_y) is the sum of NO_x with its atmospheric oxidation products including HNO_3, nitrous acid (HONO), the nitrate radical (NO_3), dinitrogen pentoxide (N_2O_5), peroxynitric acid (HNO_4), peroxyacyl nitrate (PAN), alkyl nitrates ($RONO_2$), and peroxyalkyl nitrates ($ROONO_2$). Interactions between NO_y and VOCs can lead to photochemical O_3 production and, on regional and global scales, have a large impact on OH concentrations (Wallace and Hobbs, 2006).

Carbon monoxide (CO) is another important O_3 precursor regulated by the NAAQS. Sources of CO include the oxidation of anthropogenic and biogenic volatile organic compounds (VOCs) (Cheng et al., 2017), incomplete fossil fuel combustion, and biomass burning. Reaction with OH is the most important sink of CO. The chemical lifetime of tropospheric CO is about 30-90 days (Seinfeld and Pandis, 2006).

The term VOC describes a class of carbon containing compounds in the vapor phase excluding CO, CH_4, and carbon dioxide (CO_2). Sources of VOCs include biogenic emissions from trees and other vegetation that release compounds such as isoprene and monoterpenes, as well as anthropogenic sources from many industrial processes. Biogenic emissions are the largest source of VOCs globally, exceeding anthropogenic emissions by a factor of ~10 (Atkinson and Arey, 2003). However, emissions of VOCs from human activities in urban areas play an important and sometimes critical role in the production of O_3 (Atkinson and Arey, 2003; Helmig and Bottenheim, 2009; Klimont et al., 2002) due to differences in reactivity between biogenic and anthropogenic VOCs.

In order for O_3 to be produced, it is first necessary for OH to be generated:

$O_3 + hv \rightarrow O_2 + O(^1D)$ R1

$O(^1D) + H_2O \rightarrow 2\ OH$ R2

The oxidation of CO by OH then goes on to make O_3 following these reactions (Crutzen, 1971):

$CO + OH \rightarrow CO_2 + H$ R3

$H + O_2 + M \rightarrow HO_2 + M^*$ R4

$HO_2 + NO \rightarrow NO_2 + OH$ R5

$NO_2 + hv \rightarrow NO + O$ R6

$O + O_2 + M \rightarrow O_3 + M^*$ R7

The resulting net reaction is:

$CO + 2O_2 \rightarrow CO_2 + O_3$

The rate limiting step of this sequence is R5 or R6, since NO can also react with O_3 to form NO_2, thus decreasing O_3. If NO reacts with HO_2 to make NO_2, then there is a net production of O_3 during sunlit conditions. Additionally, aerosols with a high single scattering albedo (SSA), such as sea salt, can increase UV flux and accelerate R6, thereby increasing the production of O_3 (Dickerson et al., 1997).

As noted earlier, the formation of O_3 is also influenced by VOC oxidation. In the following series of reactions, the simplified notation R represents a generic organic group, RH is the simplified notation for VOCs, and R' denotes the same generic organic group removing CH_2:

$$RH + OH \rightarrow H_2O + R \qquad R8$$

$$R + O_2 + M \rightarrow RO_2 + M^* \qquad R9$$

$$RO_2 + NO \rightarrow NO_2 + RO \qquad R10$$

At this point, NO_2 photolyzes to produce an O atom, which is rapidly converted to O_3. However, the RO radical continues to react:

$$RO + O_2 \rightarrow R'CHO + HO_2 \qquad R11$$

$$HO_2 + NO \rightarrow NO_2 + OH \qquad R12$$

$$2\ (NO_2 + hv \rightarrow NO + O) \qquad R13$$

$$2\ (O + O_2 + M \rightarrow O_3 + M^*) \qquad R14$$

The resulting net reaction is:

$$RH + 4O_2 \rightarrow R'CHO + H_2O + 2O_3$$

An example of RH and R'CHO is CH_4 and formaldehyde (HCHO). Further oxidation of R'CHO by reaction with OH, $O(^1D)$, or Cl may yield CO and CO_2. The

termination step (the loss of HO_x radicals) is reliant upon the concentration of NO_x. At low levels of NO_x, the HO_2 radical is terminated via reaction with itself:

$$HO_2 + HO_2 \rightarrow H_2O_2 + O_2 \qquad \text{R15}$$

However, in areas with high levels of NO_x, the major sink of HO_x is through NO_2 oxidation by OH:

$$NO_2 + OH + M \rightarrow HNO_3 + M^* \qquad \text{R16}$$

The nonlinear production of O_3 with respect to its precursors, NO_x and VOCs, is best illustrated by the isopleth plot (Figure 1.1). When one of the O_3 precursors is the limiting reactant, the rate of O_3 production is considered VOC- or NO_x-sensitive (Finlayson-Pitts and Pitts, 1999; Sillman et al., 1990). Note as an air parcel moves from a source region such as a city to a more rural area, the limiting reagent can change.

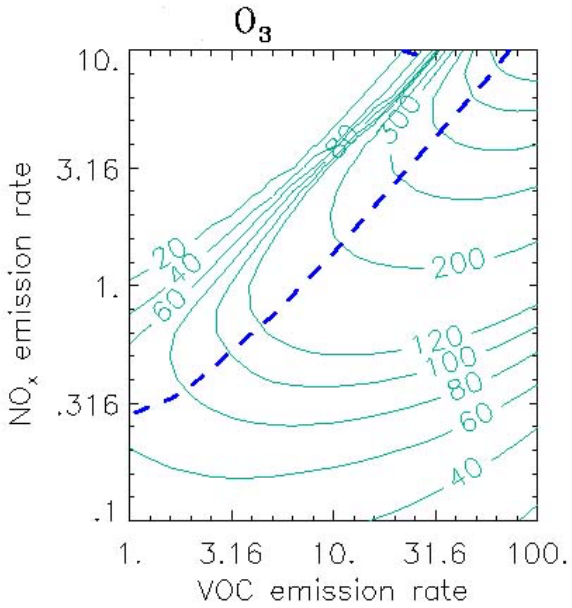

Figure 1.1. Ozone isopleths (Units: ppbv, thin green lines) simulated by a regional photochemical box model as a function of NO_x and hydrocarbon (VOC) emissions. The dashed blue line depicts the transition from VOC-sensitive (above) to NO_x-sensitive (below) conditions. Figure from http://www-personal.umich.edu/~sillman/ozone.htm.

Characterizing this nonlinear chemistry and understanding how it varies in time and space has important implications for surface O_3 control strategies.

In the case of low NO_x concentrations, the production of O_3 varies with the concentration of NO and is relatively independent of VOC levels. In this scenario, the production of O_3 is considered NO_x-sensitive because production is limited by ambient concentrations of NO_x. Alternatively, in the case of high NO_x concentrations, the production rates of O_3 increase with rising VOC concentrations and decrease with increasing NO_x concentrations. In this case, the production of O_3 is considered to be VOC-sensitive since the production is limited by the concentration of VOCs. Development of effective O_3 mitigation policy therefore depends upon accurately characterizing the photochemical NO_x-VOC regime.

1.1.2 Stratospheric O_3 Depletion

Approximately 90% of the atmosphere's O_3 is located in the stratosphere, residing in what is known as the O_3 layer (Seinfeld and Pandis, 2006). Unlike tropospheric O_3, stratospheric O_3 is produced naturally by the photolysis of molecular oxygen. Stratospheric O_3 forms a protective shield from the short wavelength (high energy) portion of UV-B radiation (λ=280-315 nm) as well as, together with molecular oxygen, the UV-C (λ=100-280 nm) part of the spectrum. Exposure to UV-radiation is known to cause DNA, cellular, and structural damage as well as destruction of folic acid, a B vitamin. Exposure to UV-radiation can lead to skin cancer and a suppressed immune system in humans (Marrot and Meunier, 2008; Šitum et al., 2008) as well as impact amphibians and other wildlife by stunting development (Ankley et al., 2002; Häkkinen et al., 2001), reducing hatching success (Blaustein et al., 1997), increasing

susceptibility to infection (Garcia et al., 2006), and limiting survival (Formicki et al., 2008).

The mechanism behind the formation of the protective O_3 layer is termed the Chapman mechanism, which overpredicts O_3 concentrations by a factor of two or more (Jacob, 1999), while still accurately estimating the general shape of the vertical profile. The Chapman mechanism explains that O_3 is formed by the photolysis of atmospheric oxygen (see Jacob, 1999):

$$O_2 + hv \rightarrow O + O$$

$$O + O_2 + M \rightarrow O_3 + M^*$$

$$O_3 + hv \rightarrow O_2 + O$$

$$O + O_3 \rightarrow O_2 + O_2$$

For the first two reactions resulting net is:

$$3O_2 + M \rightarrow 2O_3 + M^*$$

For the second two reactions:

$$2O_3 + hv \rightarrow 3O_2$$

The unexpected discovery of falling springtime stratospheric O_3 levels over Antarctica (Farman et al.,1985) prompted scientific pursuits that eventually led to one of the most successful international environmental policies in the 20th century (Solomon, 2019). It was already known that high altitude supersonic aircraft plans like the Concorde with its large emissions of NO_x could pose a serious threat to the O_3 layer (Fahey et al., 1995; Johnston, 1973). Additionally, research suggested chlorine monoxide (ClO) released by CFCs might destroy O_3 (Molina and Rowland, 1974). After the discovery of the O_3 hole, Farman et al. (1985) boldly suggested that these

declining O_3 levels were due to human use of chlorofluorocarbons (CFCs). While the expected O_3 depletion was relatively small and far in the future, anticipated serious hazards prompted an O_3 protection strategy in 1985 that signaled for more research but contained no legally binding goals for CFCs reduction (Benedick, 1991).

Additional laboratory studies and field experiments revealed the mechanisms and conditions leading to O_3 loss. Catalytic loss of stratospheric O_3 was found to occur by routes with hydrogen oxide radicals (HO_x), NO_x, or chlorine or bromine radicals (ClO_x or BrO_x) (Osterman et al., 1997). Previously unknown chemical mechanisms associated with O_3 depletion were identified to include the ClO+ClO cycle (Molina and Molina, 1987) and the BrO+ClO cycle (McElroy et al., 1986). Aircraft measurements flying from Chile to the Antarctic in 1987 revealed the "smoking gun" for the role of CFCs in depletion of the O_3 layer when elevated measurements of ClO were observed to be co-located with decreases in O_3 (Anderson et al., 1989). In addition to the discovery of O_3 destruction pathways, balloonsonde data over Antarctica showed O_3 perturbations in the region from 10-20 km where polar stratospheric clouds (PSC) could provide a site for heterogeneous reactions (Solomon et al., 1986). These studies led to the ban of production and consumption of CFCs starting in 1996 for developed countries. Rowland and Molina, as well as Paul Crutzen, were awarded the 1995 Nobel Prize in Chemistry for the first papers hypothesizing the connection between human pollution and O_3 depletion.

Since CFCs are inert in the troposphere due to long lifetimes (on the order of decades or more), these compounds only begin to react in the stratosphere when they

photolyze to release Cl atoms (Osterman et al., 1997). For example, in the case of $CFCl_3$ (known as CFC-11 or Freon-11):

$$CFCl_3 + hv \rightarrow CFCl_2 + Cl$$

$$Cl + O_3 \rightarrow ClO + O_2$$

$$ClO + O \rightarrow Cl + O_2$$

The net reaction is:

$$O_3 + O \rightarrow 2O_2$$

This catalytic cycle is terminated once the radical ClO_x is converted to non-radical reservoirs, such as HCl and $ClNO_3$. However, these reservoirs eventually return to ClO_x.

1.2 Air Pollution in China

1.2.1 The Role of Industrialization and Urbanization on Air Pollution

China has spent the last two decades in a "period of strategic opportunity," facilitating domestic development and the expansion of global leadership in industry (Department of Defense, 2018). In 2016, the time of the field study used in this dissertation, both the International Monetary Fund and the World Bank ranked China first in terms of economic size on a purchasing power parity (PPP) basis, a metric that estimates exchange rates to make more accurate comparisons across different countries (Morrison, 2018). The transformation from an agricultural giant to a service and industrial tycoon brought rapid infrastructure development, urbanization, and rising per capita income, resulting in a big shift of the composition of gross domestic product (GDP) (Figure 1.2) that did not come without an environmental cost.

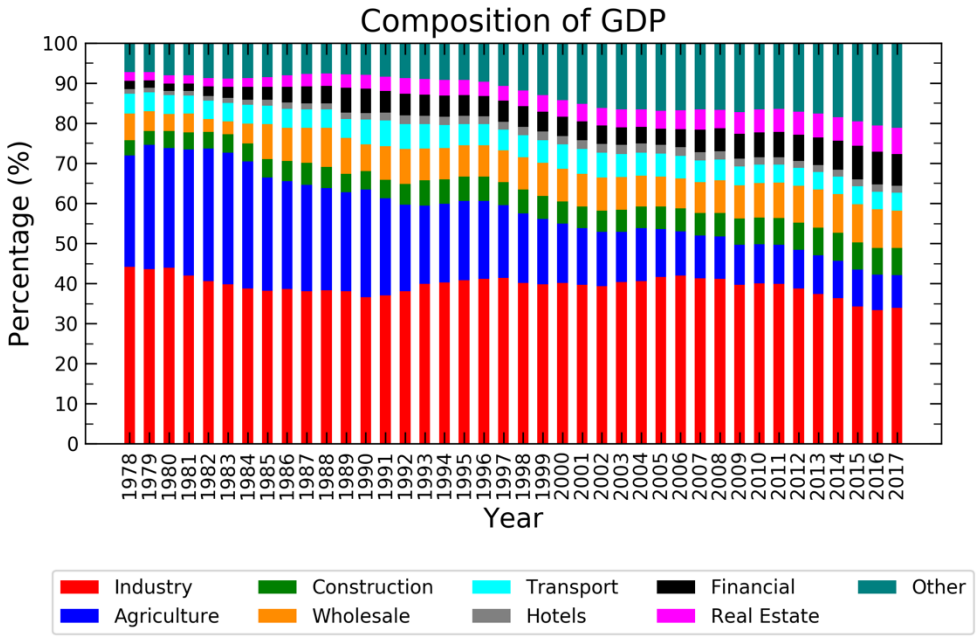

Figure 1.2. Annual composition of Gross Domestic Product (GDP) in China from 1978-2017. Data from Table 3-2 from the National Bureau of Statistics of China, 2018.

Industry was the main driver of economic growth in China, contributing 35-45% of the GDP over the last several decades. From 1978 to 2013, the Chinese GDP increased by a factor of 26, with the industrial sector growing the fastest (Tang and Zhang, 2017). The booming industrial sector allowed China to become a world leader in industrial output, including mining and ore processing, cement, coal, petroleum, chemicals, and fertilizer production, and manufacture of consumer products and telecommunications equipment.

In addition, China is one of the world's largest agricultural economies (Carter, 2011), with farming, forestry, animal husbandry, and fisheries accounting for nearly 10% of GDP (much higher than in developed nations, where agriculture makes up ~1% of GDP). As a global producer of rice, wheat, cotton, corn, barley, and apples, Chinese government support combined with low labor costs helps agricultural products stay

profitable. Multiple components of the service sector (including transport, wholesale/retail trade, hotel/catering, and financial services) have doubled in size over the past two decades, but still behind many other countries.

China is the largest producer and consumer of coal in the world (British Petroleum Company, 2017). However, the share of coal as part of energy consumption has decreased from 75% in the 1990s to 61% in 2016. Sulfur dioxide emissions have continued to decline over the last several years (He et al., 2012; Krotkov et al., 2016; Li et al., 2017a) as a result of desulfurization and increased efficiency of coal-fired power plants, the introduction of scrubbers (Liu et al., 2015), and phasing out the most polluting power plants (Guan et al., 2014). In the NCP, SO_2 emissions mainly from coal-burning decreased by 50% from 2012 to 2015 (Krotkov et al., 2016). Emissions of NO_x in China are more complicated, showing only minor improvements, mostly after 2011 (De Foy et al., 2016; Krotkov et al., 2016; Liu et al., 2017). Regulation of NO_x includes installation of NO_x control systems on power plants, closing heavily polluting factories, and strengthening emission standards for vehicles (Liu et al., 2020; Wu et al., 2017). Renewable energy in China has increased rapidly, making China the world's largest renewable energy producer (solar and wind) in the world (Organization for Economic Cooperation and Development, 2020).

1.2.2 Air Pollution in China: State of the Issue

Air pollution, previously considered a local problem for large and heavily populated cities, has grown into a regional issue in China. In the last three decades, the urban population has risen by over 550 million and now 775 million people—approximately the population of Europe—live in cities (Tang and Zhang, 2017). This

rapid urbanization turned agricultural lands into city clusters and megacities (Shao et al., 2006). In addition to industrialization and urbanization, the dependence on coal for power generation and the increase in motor vehicles from 5.5 million in 1990 to 148 million in 2014 (a 26 fold increase in 25 years) exacerbated poor air quality in China (Wu et al., 2017). Prior to vehicle emission controls in China in 2000, vehicles were estimated to contribute 77% of CO and 68% of NO_x concentrations in Beijing (Hao et al., 2000).

An environmental legal framework to control pollution in China existed as early as the 1980s, but most control measures were not enforced until the 2000s (Beyer, 2006; Feng, J., Liao, H.,Gu, 2016; Florig et al., 2002). The 11th Five Year Plan (2006-2010) introduced policies to reduce emissions and establish concentration targets, but these standards still lag behind other United States and WHO exposure limits to protect human health (Table 1.1). For example, the WHO cautions against daily average exposures of $PM_{2.5}$ at a level higher than 25 $\mu g/m^3$ (World Health Organization, 2018), but by the end of 2010, fewer than 1% of China's 500 largest cities met this concentration limit (Zhang and Crooks, 2012). In 2015, only 22% of the 338 monitored cities met the Class II CAAQS (Ministry of Environmental Protection, 2016). China's 13th Five-Year Plan (2016-2020) pledges to further reduce fine PM by at least 25%, ensure that cities achieve a 25% reduction in the number of days with severe air pollution, and slash nationwide emissions of VOCs from chief regions and industries by at least 10% (Central Committee of the Communist Party of China, 2016).

Table 1.1. Overview of the Class II Chinese Ambient Air Quality Standards (CAAQS, applicable for all areas except special regions like national parks), the National Ambient Air Quality Standards (NAAQS) in the United States, and 2005 World Health Organization (WHO) air quality standards.

Pollutant	**Averaging Time**	**China, Class II CAAQS**	**United States, NAAQS**	**World Health Organization**
Particulate Matter ($PM_{2.5}$), $\mu g/m^3$	1 day	75	35	25
	1 year	35	12	10
Nitrogen dioxide (NO_2), ppbv	1 hour	97	100	97
	1 year	19	53	19
Sulfur dioxide (SO_2), ppbv	1 hour	175	75	—
	24 hour	52	—	7
Ozone (O_3), ppbv	1 hour	93	—	—
	8 hour	75	70	47
Carbon monoxide (CO), ppmv	1 hour	8	35	—
	8 hour	3	9	—

The unique distribution of myriad emission sources combined with seasonal changes in meteorology results in a complex environment for the formation of secondary air pollutants in China. In wintertime, indoor heating, household emissions, and stagnant meteorological conditions help to build up heavy pollution across northern China in the form of haze (Li et al., 2016c; Zhang et al., 2015a). In spring, wind-blown dust originating from the Taklimakan and Gobi deserts is transported by large-scale circulation to China and other North American regions (Ding et al., 2017; Hu et al., 2016). During the Asian Summer Monsoon season, the strength and temporospatial extension of the prevailing southerly winds substantially influence the distribution and trans-boundary transport of aerosols over eastern China (Cao et al., 2015; Cheng et al., 2016; Li et al., 2016e). The western conveyor belt lofting associated with wave cyclones and dry convection can also play an important role in springtime

interhemispheric transport of pollutants over China (Cooper et al., 2004; Dickerson et al., 2007).

Once lofted above the PBL, pollution can travel long distances turning a local pollution problem into a regional issue. While Asian desert dust has long known to be transported into the Pacific by the prevailing westerly winds on the order of weeks (Duce et al., 1980), in some episodic or multiday events, pollution is transported in a matter of days (Jaffe et al., 1999; Oh et al., 2015; Stohl et al., 2003). Pollution from East Asia can affect visibility (Lin et al., 2014; Quan et al., 2011) and increase the production of surface O_3 in regions as far away as North America (Jaffe et al., 2003).

1.2.3 Impacts of Poor Air Quality

High concentrations of air pollutants result in various problems relating to public health, economic loss, and environmental degradation. In a changing climate, these consequences are expected to cause even more damage (Acevedo-Whitehouse and Duffus, 2009; Hong et al., 2019; Xie et al., 2019).

Exposure to ambient levels of air pollution are linked to myriad adverse health outcomes due to physiological changes in pulmonary and cardiovascular functions resulting in increased emergency room visits, hospital admissions, and premature death (Landrigan et al., 2018; Lelieveld et al., 2015). In China, over 1.5-2.2 million people die prematurely each year because of adverse health consequences related to air pollution (Liang et al., 2020). More than 50% of 2015 global deaths attributed to ambient air pollution occur in China and India (Landrigan et al., 2018). While most epidemiological evidence focuses on health effects due to short and long term exposure to air pollution (Chen and Kan, 2008), even low levels of tropospheric O_3 are associated

with an increased risk of premature mortality (Bell et al., 2006), especially among vulnerable populations like the elderly (Di et al., 2017) and people with pre-existing conditions (Abelson and Stieb, 2011).

Ambient concentrations of air pollution are also responsible for large economic health and agricultural losses. L. Li et al. (2016) assessed the health-related economic losses in 74 cities in China in 2015 and found elevated PM_{10} and SO_2 impacted 1.63 and 2.32% of GDP. Even the short-term 2013 extreme haze event in Beijing was estimated to result in 45,350 acute bronchitis and 23,720 asthma cases, resulting in an economic loss of $253.8 million (Gao et al., 2015). Agricultural crops and vegetation exposed to air pollution reduces net photosynthesis (Reich and Amundson, 1985b), which can lower crop yields (Carter et al., 2017) and threaten Chinese food security. In 2008, the economic loss to the agricultural sector due to industrial air pollution in China was estimated to be close to US$1.5 billion (Wei et al., 2014).

High levels of air pollutants can degrade the environment and alter the atmosphere. High O_3 concentrations pose a risk to Chinese forests, which play important roles in climate change mitigation strategies (Li et al., 2017b). High aerosol loading in China can alter rainfall (Li et al., 2016e) and diminish solar radiation reaching the surface, effecting cloud formation and atmospheric stability (Li et al., 2007). Additionally, strongly absorbing aerosols may influence atmospheric heating rates and evolution of the PBL (Li et al., 2017c).

Climate change may alter synoptic conditions as well as the frequency and duration of pollution events. Absorbing aerosols like black carbon (BC) are responsible for increased precipitation and moderate cooling in China (Menon et al., 2002), altering

the regional climate. An enhanced Siberian High due to Arctic warming can help strengthen the northerly winds in the North China Plain, effectively leading to a 100-200 $\mu g/m^3$ reduction in $PM_{2.5}$ (Zhao et al., 2018). Global models predict that the removal of fossil-fuel generated particles, which affects the hydrological cycle and masks the anthropogenic rise in global temperature, may increase rainfall by 10-30% over northern China (Lelieveld et al., 2019). The change in precipitation could affect how long reactive pollutants remain in the atmosphere.

1.3 Overview of the ARIAs Field Campaign

The Air chemistry Research in Asia (ARIAs) campaign, a scientific project jointly conducted by American and Chinese institutions funded by the National Science Foundation (NSF), collected airborne observations of air pollution over Hebei Province, China. The goal of ARIAs was to characterize and quantify the composition of trace gases and aerosols over Hebei to improve modeling tools used to evaluate the effectiveness of air pollution reduction policies. Only limited studies conducted by other groups measure the vertical distribution of pollutants over East Asia and integrate observations from multiple platforms including aircraft, surface stations, satellite retrievals, and model simulations. The ARIAs project aimed to address these gaps, as well as enrich the National Aeronautics and Space Administrations (NASA) Korean-US Air Quality (KORUS-AQ) study, which occurred in South Korea at the same time as ARIAs. Since six of the world's top ten worst air quality cities in 2016 are located in Hebei, including the capital city of Shijiazhuang, this region is of great scientific interest to guide regulation to protect human health.

Throughout May and June 2016, the ARIAs campaign conducted 11 research flights in southern Hebei Province. The aircraft campaign measured CO, O_3, NO_2, NO/NO_y, SO_2, VOCs, and aerosol scattering and absorption near the surface to 3500 m pressure altitude under a variety of synoptic conditions, using the instruments described in Table 1.2. The Y-12 research aircraft was based at Luancheng Airport, located in southeast Shijiazhuang, the capital and largest city in Hebei, and its major economic center. The Y-12 flew vertical spirals over Shijiazhuang as well as three other locations: Julu, Quzhou, and Xingtai. The flight sampling occurred east of the Taihang Mountains, with Xingtai at the foothill of this mountain range.

Table 1.2. Y-12 research aircraft instrumentation during ARIAs.

Variable	**Method**
Aircraft Position	Global Positioning System (GPS)
Meteorology (Temperature, Relative humidity, Pressure, 2-D Wind)	Cloud water inertial probe (CWIP)
Greenhouse Gases ($CO_2/CH_4/CO/H_2O$)	Cavity Ring Down Spectroscopy Picarro Model G2401-m
Ozone (O_3)	UV-absorption, TECO 49C
Sulfur dioxide (SO_2)	Pulsed fluorescence, TECO 43C
Nitrogen dioxide (NO_2)	Cavity enhanced absorption spectroscopy, Los Gatos RMT-200 CRDS
NO/NO_y	Chemiluminescence, modified TECO 42C with an external Molybdenum converter at 375°C
Aerosol Scattering, b_{scat} (450, 500, 700, nm)	Nephelometer, TSI Model 3563
Aerosol Absorption, b_{abs} (565 nm)	Particle Soot Absorption Photometer (PSAP)
Black Carbon (370, 470, 520, 590, 660, 880, 950 nm)	Aethalometer, Magee Model AE31
Black Carbon	Single-Particle Soot Photometer (SP2)
VOCs	Grab Canisters, GC-MSD/FID

Additionally, the coordinated Atmosphere-Aerosol-Boundary Layer-Cloud (A^2BC) Interaction Joint Experiment collected surface measurements of trace gases and aerosols in northwest Xingtai from May to December 2016. An intensive observation period occurred in May and June 2016 to coincide with ARIAs. Nestled in the Taihang Mountains, agricultural crops, consisting heavily of winter wheat planted in October, harvested, and stubble burned in June (Liu and Si, 2011), surround the A^2BC surface site. Populated by approximately 7 million people, the area around Xingtai contains industries like coal mining, coal-burning power plants, cement and steel industries, chemical processing, iron-smelting, and glass manufacturing.

1.4 Research Objectives

The work detailed in this dissertation focuses on characterizing the composition of atmospheric pollutants in one of the most populated and industrialized areas in the world by combining both surface and aloft observations with modeling analyses. While the ARIAs campaign cannot describe air pollution for all of China, aircraft observations are particularly rare in this area and can provide insight into boundary layer photochemistry and transport. This work addresses several research questions, outlined below:

1) How is aloft O_3 photochemistry affected by NO_x and VOCs in Hebei Province and which VOCs are most influential in the production of O_3? What characteristic pollution source signatures are present and how do they compare to previous studies in China and to other areas where pollution control measures have been successfully implemented?

2) Do atmospheric abundances of CFCs observed over a suspected source region agree with global and Northern Hemisphere background levels? How do different meteorological conditions affect the levels and sources of measured CFCs?
3) How do meteorological conditions affect the vertical distribution and transport of trace gases over the NCP? Do atmospheric models agree with observations?

The research addressing Question 1 is illustrated in Chapter 2 of this dissertation. This chapter addresses levels of O_3 and its precursors and uses a box model constrained by aircraft observations to estimate the rate of O_3 production. Several VOC reactivity scales are deployed to identify which compounds are most influential in the production of O_3. Ratios of trace gases and VOCs are compared to published emission factors and peer-reviewed studies to characterize pollution sources present over Hebei. This work was published in *Atmospheric Chemistry and Physics* in November 2020 (Benish et al., 2020a).

Chapter 3 of this dissertation assesses levels of CFCs obtained from whole air sample canisters collected from the Y-12 research aircraft. Correlations among different halocarbons used as feedstock are examined to understand whether CFCs are being newly produced or released from banks. Using ensemble HYSPLIT backward trajectories, I identify possible source regions of CFCs. This chapter is presently under review in the *Journal of Geophysical Research: Atmospheres*.

The next chapter of this dissertation, Chapter 4, examines how meteorology and chemistry interact to influence air pollution in the NCP. Backward trajectories and aloft

weather analyses guide the determination of the origin of sampled airmasses. A case study during a persistent high pressure episode reveals that a maritime tropical (mT) airmass over the Yellow Sea passed over a heavily industrialized coastal region before being sampled by the Y-12 research aircraft.

Lastly, the final chapter of this dissertation provides concluding remarks and directions for future study.

Chapter 2 Aircraft Observations of Ozone, Nitrogen Oxides, and Volatile Organic Compounds over Hebei Province, China

2.1 Introduction

Explosive urbanization and rapid industrialization contributed to high ground-level O_3 and particulate matter (PM) over the past several decades in the North China Plain (NCP) (Johnson et al., 2006; Ran et al., 2011; Shao et al., 2009; Zhang et al., 2014b). Household burning of coal used for cooking and heating, emissions from gasoline, diesel, and liquified petroleum gas (LPG) vehicles, as well as large-scale burning of winter wheat residues in the NCP are some of the many sources responsible for O_3 precursors, such as NO_x and VOCs (Chen et al., 2017; Long et al., 2016; Stavrakou et al., 2016). Ozone is harmful to both the human respiratory system (Bell et al., 2006; Jerrett et al., 2009) and to photosynthetic processes by vegetation (Avnery et al., 2011; Reich and Amundson, 1985a), while some VOCs, such as benzene and chloroform, are known to be hemotoxic and carcinogenic (Environmental Protection Agency - Integrated Risk Information System, 2003; Lan et al., 2004). Several studies using the NASA Ozone Monitoring Instrument (OMI) have found reductions of some pollutants like SO_2 over the NCP (He et al., 2012; Krotkov et al., 2016; Li et al., 2010, 2017a), but NO_2 pollution still remains severe in China (Figure 2.1).

Ozone is created through the oxidation of NO by hydroperoxyl radicals (HO_2) and organic peroxy radicals (RO_2), products of carbon monoxide (CO) and VOC oxidation. When one of these precursors is the limiting reactant, the rate of O_3

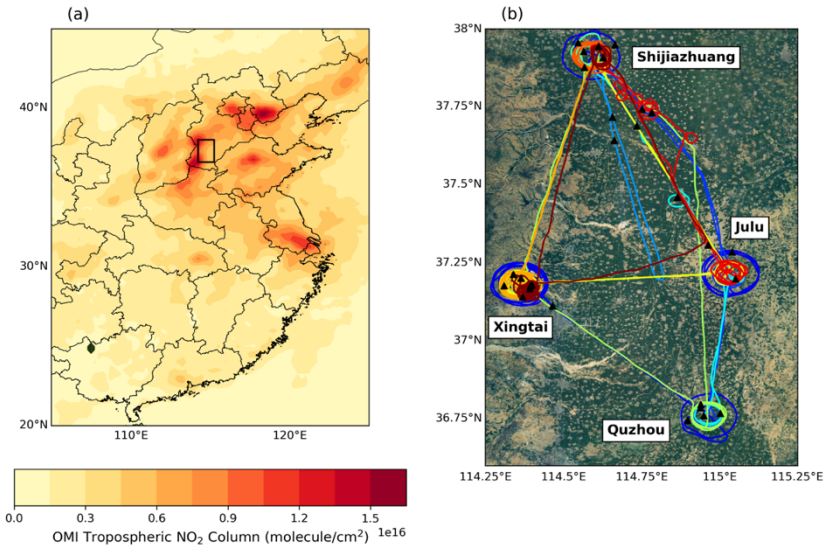

Figure 2.1. (a) May and June 2016 OMI tropospheric column NO_2 from NASA Goddard Earth Sciences Data and Information Services Center. The North China Plain is clearly seen in the center with high column NO_2 concentrations; the black rectangle indicates the ARIAs campaign domain and corresponds to the region shown in panel b. (b) Map of 11 ARIAs flight tracks (colored by flight number) and location of VOC samples (black triangles). The background map is provided by Esri, Copyright: © 2009.

production is considered VOC- or NO_x-sensitive (Finlayson-Pitts and Pitts, 1999; Sillman et al., 1990). The role of VOCs on the formation of O_3 depends on the characteristics of the environment, including the main emission sources of primary pollutants and ambient temperature (Pusede et al., 2014), and the interaction of aerosols within the PBL to reduce photolysis (An et al., 2019). High aerosol concentrations have been shown to decrease photolysis and hinder summer surface O_3 formation by 25 ppbv on average in Xi'an, China (Feng et al., 2016), which pose a challenge for pollution control strategies.

Natural emissions are the largest source of VOCs globally and react more efficiently with OH than most anthropogenic compounds (Di Carlo et al., 2004), but exhibit a strong seasonal, diurnal, and spatial dependence (Li et al., 2013). Biogenic VOCs have been found to play a significant role in the formation of O_3 at the surface

(Ma et al., 2019; Zong et al., 2018) and throughout the boundary layer in the NCP (Wang et al., 2008a), as well as influence production of $PM_{2.5}$ (Guo et al., 2014) and secondary organic aerosols (SOA) (Wu et al., 2020b). In particular, isoprene has been estimated to account for 27% of the total O_3 production in June 2010 in Beijing (Mo et al., 2018), suggesting the need to consider biogenic isoprene emissions together with the dominating anthropogenic VOCs in formulating O_3 control strategies. Quantifying the abundance of NO_x and the suite of VOC chemicals throughout the lower troposphere is urgently needed to better understand the photochemistry of O_3 production in the NCP, which in turn will lead to the development of successful mitigation strategies.

In-situ airborne measurements provide valuable information regarding the horizontal and vertical distributions of air pollutants over a large spatial area. Airborne measurements are necessary to characterize air pollution over large cities, as well as surrounding areas. Ozone and PM are produced throughout the planetary boundary layer (PBL), so aircraft observations can lead to a more complete picture of pollution formation and transport than is available only from surface observations. While several airborne campaigns have deployed to investigate the regionally transported pollution problem in East Asia, including the NASA Korea-United States Air Quality Study (KORUS-AQ) (Al-Saadi et al., (2015), see https://www-air.larc.nasa.gov/missions/korus-aq/docs/White_paper_NASA_KORUS-AQ.pdf), that occurred at the same time as our measurements, few airborne studies characterize the source region of severe smog within the Hebei Province region of China.

Through Chinese/American partnerships with Peking University, Beijing Normal University, and the University of Maryland, we conducted a field campaign in Hebei Province, China called ARIAs. The ARIAs campaign was designed to characterize and quantify the composition of trace gases and aerosol optical properties over Hebei to improve tools used to evaluate the effectiveness of air pollution reduction policies. Since air pollution transport from Asia typically peaks in early to mid-spring (Liu et al., 2003), we hoped to provide detailed altitude profiles over the Asian source region to enable Lagrangian experiments with KORUS-AQ, but only two sustained transport events occurred (Peterson et al., 2019). Despite the infrequent transboundary pollution events, ARIAs observations generated valuable characteristic pollution signatures that helped describe combustion efficiency and its impact downwind (Halliday et al., 2019) to correct model biases of CO in global chemistry-climate models (Gaubert et al., 2020), and to show that MOPITT bias increases at high CO concentrations (Tang et al., 2020). Furthermore, ARIAs measurements characterized aerosol optical properties in the PBL and FT during clean and polluted conditions (Wang et al., 2018a), as well as used in the validation of the multiaxis differential optical absorption spectroscopy (MAX-DOAS) profiles of NO_2, SO_2, HONO, HCHO, CHOCHO, and aerosols (Wang et al., 2019b).

The Ministry of Environmental Protection of the People's Republic of China reported six of the top ten cities with the worst air quality in 2016 were located in Hebei (including the capital city of Shijiazhuang). The North China Plain is one of the most polluted regions in the world, but implementation of pollution reduction measures through the Five-Year Plans has allowed for decreasing trends of many pollutants. In

particular, Zhang et al. (2020) found an increased number of days of clean/light haze and a decreased number of days with heavy haze, along with a significant decline of SO_2 concentrations. Similarly, using observations from MODIS and OMI, Si et al. (2019) found AOD and SO_2 to decrease from 2006 to 2015, while NO_2 rose by 4.79% in the NCP during this period. While surface NO_2 decreased 20% from May 2014 to December 2018 throughout China, there are still a large number of measurement stations with increasing trends of NO_2 due to changes in meteorological conditions and aerosol emissions (Fan et al., 2020), illustrating the need for more research characterizing air pollution in this region. In this study, we analyze concentrations of O_3, NO_x, NO_y, CO, and VOCs obtained during 11 research flights between May and June 2016. The VOC chemical reactivity and impact on O_3 production is assessed and we utilize an observation-constrained box model to evaluate photochemical properties of the production of O_3 that occurs throughout the lower free troposphere.

2.2 Materials and Methods

2.2.1 Air sampling and Analysis

The ARIAs campaign included 11 research flights from May-June 2016 in Hebei Province (Figure 2.1). Flight days were chosen based on meteorological conditions associated with smog events, such as higher temperatures, little cloud cover, low relative humidity, weak winds, and shallow PBL height (Tang et al., 2012). The Y-12 aircraft was based at Luancheng Airport (114.59°E, 37.91°N, 58 m above sea level (ASL)), located in southeast Shijiazhuang (population around 10 million), a major economic center in Hebei, including pharmaceutical and textile industries, machinery

and chemical manufacturing, construction, and electronics production. Flight sampling occurred east of the Taihang Mountains and the Y-12 flew vertical spirals from ~300 m to ~3500 m over Shijiazhuang as well as three other locations: Julu (115.02°E, 37.22 °N, 30 m ASL), Quzhou (114.96°E, 36.76°N, 40 m ASL), and Xingtai (114.36°E, 37.18°N, 182 m ASL). A full description of pollutant summary statistics and flight path for each flight is provided in Table 2.1.

Various instruments aboard the Y-12 aircraft collected trace gas, aerosol, and meteorological data. The aircraft instrumentation (Table 1.2) included different gas and particle sample inlets on the top of the fuselage and pressure/temperature/humidity sensors (Cloud Water Inertial Probe (CWIP), Rain Dynamics) installed under one wing of the aircraft (Figure 2.2). Flight position data were recorded using a portable global positioning system (GPS) and the CWIP. The aircraft was equipped with the following trace gas analyzers: (1) a Picarro cavity ring down spectrometer (CRDS) for measurements of CH_4, CO_2, CO, and H_2O; (2) a Thermal Electron Corporation (TECO) Model 49C UV absorption O_3 analyzer; (3) a TECO Model 43C pulsed fluorescence SO_2 analyzer; (4) a Los Gatos Research Model RMT-200 CRDS NO_2 analyzer; and (5) a TECO Model 42C NO-NO_y analyzer. Power constraints and a converter issue led to limited NO_y, NO_x, and CO measurements during the campaign, particularly in the lower free troposphere (LFT). We remove observations of NO/NO_y over three spiral locations due to limited measurements. Negative values indicate readings around the detection limit, usually at high altitudes. The aircraft was also equipped with an inlet to measure aerosols up to ~5.0 μm diameter and aerosol optical properties, including a

Table 2.1. Summary statistics of the 1-second measured concentrations for O_3, NO_2, NO_y, and CO (units=ppbv) and flight path descriptions (JU=Julu, SJZ=Shijiazhuang, XT=Xingtai, QZ=Quzhou) for each flight during ARIAs. Negative values of NO_2 indicate when the instrument was measuring around the detection limit.

Date (DOY)	Start/ End (LST)	Mean O_3 (Range)	Mean NO_2 (Range)	Mean NO_y (Range)	Mean CO (Range)	Flight Description
May 8 (129)	10:30/ 14:32	76.6 (62.7-83.9)	No data	15.6 (9.0-29.4)	No data	Spirals over JU (400-3500 m) at 10:58, QZ (350-3500 m) at 12:00, XT (400-3000 m) at 12:23, and SJZ (100-3500 m) at 14:05.
May 15 (136)	12:17/ 15:04	64.6 (54.4-85.8)	No data	No data	No data	Spirals over JU (400-3500 m) at 12:43 and QZ at 13:41.
May 16 (137)	15:03/ 15:54	85.3 (70.5-96.0)	No data	22.8 (6.1-29.6)	No data	Flight to the southeast to the W of JU. Flight altitude about 400 m.
May 17 (138)	8:21/11:13	80.1 (45.0-99.1)	8.8 (–0.1-38.4)	30.2 (0.2-89.7)	590.5 (114.3-6053.6)	Low altitude transect to JU, with spirals at JU (650-2800 m) at 9:47 and QZ (400-3000 m) at 10:19.
May 19 (140)	15:42/ 17:09	97.1 (75.4-130.2)	1.4 (–0.1-6.8)	11.3 (3.6-29.1)	131.4 (90.8-540.0)	Spirals over the airport.
May 21 (142)	11:57/ 13:41	99.5 (67.1-145.6)	1.9 (–0.1-16.4)	No data	238.5 (80.5-564.5)	Flew to southeast at low altitude (1000 m) to a point (114.9 °E, 37.6 °N). Spirals over QZ (300-3000 m) at 12:40 and XT (300-2400 m) at 13:34.
May 28 (149)	10:16/ 13:26	86.3 (63.5-100.3);	3.2 (–0.1-27.0);	No data	332.2 (97.1-1264.9);	Morning flight flew spirals over XT (350-3000

	16:29/ 18:24	88.9 (72.9-112.3)	2.6 (0.01-10.4)		215.2 (88.1-963.3)	m) at 11:02 and JU (450-2500 m) at 12:29. During the afternoon flight, spirals over XT (350-3000 m) at 16:57.
June 2 (154)	13:47/ 14:53	94.9 (79.6-106.3)	1.5 (–0.1-5.4)	24.3 (14.9-70.7)	256.7 (95.1-487.5)	Spirals over the airport.
June 6 (158)	10:08/ 12:01	99.9 (67.5-134.7)	0.7 (–0.1-4.9)	No data	296.2 (105.1-573.2)	Low altitude (< 2000 m) spirals to the SE of SJZ. Spirals over JU at 10:44.
June 11 (163)	11:02/ 13:45	76.7 (57.2-90.8)	2.3 (–0.1-6.7)	16.9 (11.1-23.8)	187.4 (88.2-412.9)	Low altitude transect (2000 m) to NE JU. Spirals over XT (600-3000 m) at 11:54 and SJZ (600-3000 m) at 13:12.

nephelometer (TSI Model 3563) to measure aerosol scattering, a particle soot absorption photometer (PSAP) to measure aerosol absorption, and an aethalometer (Magee Model AE31) and a Single-Particle Soot Photometer (SP2, Droplet Measurement Technologies) to measure black carbon. Observed aerosol optical properties have been summarized by F. Wang et al. (2018); further details on aircraft instrumentation are given by Ren et al. (2018).

Figure 2.2. Left: Picture of the gas (alt-facing) and aerosol inlet (forward facing) on top of the Y-12 aircraft; arrow indicates air flow. Right: Picture of the Cloud Water Inertial Probe (CWIP) on the Y-12 aircraft installed under the port wing.

Twenty-six whole air samples (WAS) were collected directly into 3.2 L fused silica lined electropolished stainless steel canisters (Entech Instrument Inc., Simi Valley, CA) at a variety of pressure altitudes from 400 m to 3500 m between 1:30 and 9:00 UTC (9:30 and 17:00 local time). The sampling period for the WAS canisters was approximately 1-2 minutes during the spirals. Samples were analyzed for 54 VOCs and 16 halocarbons. Since the halogenated species have negligible effects on O_3 production, we exclude these species from the analysis presented here (see Chapter 3 for halocarbon analysis). We also exclude 2 WAS canisters from this analysis due to evidence of contamination after sampling. The first sample was collected on May 21 at 399 m pressure altitude. This sample was heavily polluted with i-butane (25.8 ppbv), i-pentane (57.7 ppbv), as well as longer chain alkanes like 2,3-dimethylbutane (4.2 ppbv), 2-methylpentane (5.9 ppbv), cyclopentane (2.7 ppbv), 2-methylheptane (16.1 ppbv), and 3-methylpentane (3.5 ppbv) in addition to aromatics like toluene (41.3 ppbv) and benzene (20.8 ppbv). Many of these compounds are typical of fuel evaporation or from petrochemical industries, indicating this canister may have directly sampled the plume

of one of these sources. Since this study is primarily focused with evaluating aloft VOCs away from their direct emission sources, the data from this canister were removed from this analysis. The second contaminated sample was collected on May 28 at 3:36 UTC. This sample was filled to ambient pressure at 3000 m in relatively clean air, based on in situ observations at the time the canister was collected (CO=111 ppbv, CH_4=1890 ppbv, CO_2=406 ppmv, O_3=84 ppbv). The concentrations of VOCs for this sample are outliers relative the associated abundances of the trace gases. This anomaly is indicative of valve leakage during transit or ambient air entering the WAS canister after the flight. The observed CO to acetylene ratio (ppbv/ppbv), often used as a tracer for the age of an air mass, was much smaller in this sample (70 ppbv/ppbv) compared to other samples collected at a similar altitude (~400 ppbv/ppbv).

Limited samples collected over one province in one season may not be able to represent O_3 chemistry for all of China, but the scarcity of airborne VOC measurements in this region makes these data valuable for characterizing the composition of air throughout and above the PBL, demonstrating how the production of O_3 aloft differs from that at the surface.

The VOC analytical techniques used by the College of Environmental Sciences and Engineering at Peking University (PKU) in Beijing have been summarized in the past (Mo et al., 2015; Wang et al., 2010a), and we briefly describe the method here. The WAS canisters were cleaned following a standard sampling procedure, pressured with nitrogen and vacuumed three times to 2.6 Pa. The hydrocarbons were quantified using a gas chromatograph equipped with a mass selective detector (GC-MSD, Hewlett Packard 5975/7890, USA) and a flame ionization detector (FID) coupled with a

cryofocusing pre-concentration system (Entech Instrument 7100A, Simi Valley, CA). This system used a Dean Switch™ (Agilent Technologies, Santa Clara, CA, USA) to introduce the effluent into a DB-624 column (60 m × 0.25 mm × 1.8 μm; J&W Scientific, Folsom, CA, USA) with an MSD to separate and analyze C4–C12 hydrocarbons and halocarbons. A PLOT (Al/KCl) column (30 m × 0.25 mm × 3.0 μm; J&W Scientific) with an FID was used to measure the C2–C4 hydrocarbons.

The Photochemical Assessment Monitoring Stations (PAMS) (55 NMHCs) and Toxic Organic-15 (TO-15) standard mixtures were used to calibrate the GC-MSD/FID system that measured the C2–C12 VOCs. Samples with known concentrations of four VOCs (bromochloromethane, 1,4-difluorobenzene, chlorobenzene-d5 and 1-bromo-3-fluorobenzene) were used as internal standards for each sample to calibrate the system. The GC-MSD/FID system was calibrated at five concentrations, ranging from 0.5 to 8 ppbv, for each of these four compounds before sample analysis. Correlation coefficients, ranging from 0.987 to 0.999 showed that the integral areas of peaks were proportional to the concentrations of the target compounds. A gas standard (diluting from 1 ppmv to 2 ppbv) was measured each day to check the stability of the system. Summary statistics of the VOCs along with the method detection limit (MDL) (ranging from 0.002 to 0.027 ppbv) are reported in Table 2.2. Total uncertainty for VOC measurements reflects instrument noise, plus uncertainty in calibration standards, contamination, and pressurization. Best estimate of the total uncertainty is ±20% with 95% confidence due to uncertainties associated with airborne sampling platforms. Intercomparison experiments of VOC measurements between PKU and other laboratories showed good agreement (Liu et al., 2008b).

Table 2.2. Summary statistics of alkanes, alkenes/alkynes, and aromatics quantified for all WAS canisters (pptv), as well as the method detection limit (MDL, in pptv), rate constants with OH (kOH), maximum incremental reactivity (MIR) value, and ratio to CO (pptv/ppbv) for compounds with R>0.50. Values less than 1 pptv are not shown.
* TO-15 method, where the standard deviation of seven replicates near the detection limit are multiplied by 3.14 (Student's t value with 99% confidence).
‡ Reaction rate coefficient with OH.
† Maximum Incremental Reactivity (MIR, units=g O_3/g VOC), from Carter, (2010).

	Mean (STD)	**Min**	**50th**	**Max**	**MDL** *	**kOH‡**	**MIR†**	**Ratio to CO**
Alkanes								
Ethane	2648 (710)	1804	2525	4154	50	$6.90 \times 10^{-12} \times e^{-1000/T}$	0.28	2.5
Propane	1391 (231)	978	1356	1887	21	$7.60 \times 10^{-12} \times e^{-585/T}$	0.49	-
n-Butane	363 (278)	83	259	1210	30	$9.80 \times 10^{-12} \times e^{-425/T}$	1.15	-
2,2-Dimethylbutane	13 (14)	2	9	64	7	$3.22 \times 10^{-11} \times e^{-781/T}$	1.17	-
2,3-Dimethylbutane	44 (93)	2	11	400	5	$1.24 \times 10^{-17} \times T^2 \times e^{-585/T}$	0.97	-
i-Butane	624 (997)	56	246	3963	29	$1.16 \times 10^{-17} \times \times T^2 \times e^{225/T}$	1.23	-
n-Pentane	119 (113)	19	71	479	5	$2.44 \times 10^{-17} \times \times T^2 \times e^{183/T}$	1.31	-
i-Pentane	674 (1255)	32	168	5444	12	3.70×10^{-12}	1.45	-
Cyclopentane	34 (64)	2	12	296	26	$2.67 \times 10^{-11} \times e^{-590/T}$	2.39	-
Methyl-cyclopentane	26 (29)	2	15	115	8	7.66×10^{-12}	2.19	-
2-Methylpentane	111 (144)	8	61	667	5	5.30×10^{-12}	1.5	-
3-Methylpentane	53 (88)	3	26	395	7	5.40×10^{-12}	1.8	-
2,3-Dimethylpentane	27 (33)	4	19	152	4	$1.95 \times 10^{-11} \times e^{-330/T}$	1.34	-
2,4-Dimethylpentane	31 (53)	3	11	228	5	$2.49 \times 10^{-11} \times e^{-443/T}$	1.55	-
2,2,4-Trimethylpentane	433 (1117)	9	57	5422	3	$2.09 \times 10^{-12} \times (\frac{T}{298})^{2.00} \times e^{140/T}$	1.26	-

2,3,4-Trimethylpentane	232 (652)	9	33	3253	8	$9.85 \times 10^{-12} \times e^{-124/T}$	1.03	-
n-Hexane	123 (180)	6	46	699	16	$1.53 \times 10^{-17} \times T^2 \times e^{414/T}$	1.24	-
Cyclohexane	15 (13)	1	9	44	16	$2.88 \times 10^{-17} \times T^2 \times e^{-309/T}$	1.25	-
Methyl-cyclohexane	17 (23)	3	10	114	8	1.18×10^{-11}	1.70	-
2-Methylhexane	39 (72)	6	18	362	8	6.86×10^{-12}	1.19	-
3-Methylhexane	44 (88)	7	16	438	6	7.15×10^{-12}	1.61	-
n-Heptane	41 (52)	9	22	255	7	$1.59 \times 10^{-17} \times T^2 \times e^{478/T}$	1.07	-
2-Methylheptane	399 (1106)	11	63	5515	8	$2.51 \times 10^{-17} \times T^2 \times e^{447/T}$	1.07	-
3-Methylheptane	15 (13)	7	11	59	9	$2.51 \times 10^{-17} \times T^2 \times e^{447/T}$	1.24	-
Octane	26 (19)	10	23	102	12	$2.76 \times 10^{-17} \times T^2 \times e^{378/T}$	0.90	-
n-Nonane	22 (12)	13	17	72	21	$2.51 \times 10^{-17} \times T^2 \times e^{447/T}$	0.78	-
n-Decane	58 (57)	14	38	288	10	$3.13 \times 10^{-17} \times T^2 \times e^{416/T}$	0.68	
Alkenes/Alkynes								
Acetylene	803 (465)	234	578	1934	48	$1.69 \times 10^{-12} \times e^{-233/T}$	0.95	1.4
Ethylene	884 (923)	185	405	3536	30	$2.14 \times 10^{-12} \times e^{411/T}$	9.00	2.9
Propylene	168 (44)	102	164	308	25	$3.0 \times 10^{-11} \times e^{300/T}$	11.66	-
1-Butene	23 (10)	10	19	46	30	$6.60 \times 10^{-12} \times e^{465/T}$	9.73	-
cis-2-Butene	3 (6)	-	1	31	23	$1.10 \times 10^{-11} \times e^{487/T}$	14.24	-
trans-2-Butene	3 (3)	-	2	16	31	$1.01 \times 10^{-11} \times e^{550/T}$	15.16	-
Isoprene	35 (39)	2	20	138	15	$2.70 \times 10^{-11} \times e^{390/T}$	10.61	-
1-Pentene	8 (3)	4	7	18	9	$5.86 \times 10^{-12} \times e^{500/T}$	7.21	-
cis-2-Pentene	2 (3)	-	1	16	8	6.54×10^{-11}	10.38	-
trans-2-Pentene	2 (3)	-	1	14	8	6.69×10^{-11}	10.56	-
1-Hexene	6 (5)	3	5	27	11	3.70×10^{-11}	5.49	-
Aromatics								
Benzene	510 (521)	63	330	2183	7	$2.30 \times 10^{-12} \times e^{-190/T}$	0.72	1.8
Toluene	757 (1188)	31	300	4402	5	$1.80 \times 10^{-12} \times e^{340/T}$	4.00	-

Styrene	14 (12)	4	8	45	13	5.80×10^{-11}	1.73	-
m/p-Xylene	108 (155)	16	62	789	2	1.87×10^{-11}	7.80	-
o-Xylene	43 (51)	8	28	263	3	1.36×10^{-11}	7.64	-
Ethylbenzene	73 (85)	12	45	423	3	7.00×10^{-12}	3.04	-
Isopropylbenzene	15 (8)	7	13	48	20	6.61×10^{-12}	2.52	0.02
n-Propylbenzene	15 (20)	4	10	104	16	5.80×10^{-12}	2.03	0.06
2-Ethyltoluene	14 (17)	5	9	89	10	1.86×10^{-11}	5.59	0.05
3-Ethyltoluene	19 (18)	4	13	88	20	1.18×10^{-11}	7.39	0.05
4-Ethyltoluene	19 (26)	4	11	132	20	1.19×10^{-11}	4.44	0.07
1,3-Diethylbenzene	20 (28)	4	8	248	10	1.86×10^{-11}	7.10	0.15
1,4-Diethylbenzene	27 (40)	8	18	218	10	1.18×10^{-11}	4.43	0.12
1,2,3-Trimethylbenzene	18 (24)	7	13	130	2	3.27×10^{-11}	11.97	0.07
1,2,4-Trimethylbenzene	30 (30)	8	23	160	3	3.25×10^{-11}	8.87	0.08
1,3,5-Trimethylbenzene	10 (11)	3	6	54	4	5.67×10^{-11}	11.76	-

The Atmosphere-Aerosol-Boundary Layer-Cloud (A^2BC) Interaction Joint Experiment campaign collected meteorological, aerosol, and trace gas information from a ground-based site in Xingtai (114.36°E, 37.18°N, 182 m ASL) from May to December 2016 (Wang et al., 2018b, 2019b). An intensive observation period in May and June 2016 was conducted to coincide with ARIAs. Data from A^2BC instruments used in our analysis include: (1) a NO_x analyzer with a molybdenum converter (Ecotech model 9841A); (2) an infrared absorption CO analyzer (Ecotech model 9830A); and

(3) a UV absorption O_3 analyzer (Ecotech model 9810A). Results of NO_2, SO_2, HONO, HCHO, CHOCHO, and aerosols derived from the Differential Optical Absorption Spectrometer (DOAS) are summarized by Yang Wang et al., (2019). The A^2BC site is located in northwest Xingtai, nestled in the east foothill of the Taihang Mountains. Agricultural crops surround the site, consisting heavily of winter wheat, that is harvested, with the stubble burned in June (Liu and Si, 2011). Xingtai is a city with approximately 7 million people and is surrounded by industry including coal mining and coal-burning power plants, cement and steel industries, chemical processing, iron-smelting, and glass manufacturing.

2.2.2 Box Model Simulations

A box model called Framework in 0-Dimensional Atmospheric Modelling (F0AMv3.1) (Wolfe et al., 2016) is used to evaluate oxidation processes to understand O_3 photochemical production both at the surface and aloft. The box model simulations cover the Y-12 flight tracks during seven flights and daytime hours at the A^2BC supersite in Xingtai (where the Y-12 conducted spirals) using the Carbon Bond Mechanism, version 6, revision 2 (CB6r2). Both the Y-12 flights and surface simulations define a physical loss lifetime of 24 hours to mitigate build-up of long-lived oxidation products over multiple days of integration.

For the ARIAs flight data, the model is constrained by 1-minute average observed concentrations of NO_2, CO, and O_3. Due to the limited number of grab canisters per flight, VOCs are constrained based on the altitude of the sampling relative to the height of the PBL, which is determined using potential temperature and water vapor vertical profiles for each flight. All WAS canister data collected below the top

of the PBL during a flight are averaged. Data from all of the WAS canisters for the entire campaign collected above the research flight's PBL are averaged for that flight. Periodic missing Y-12 NO_2 data due to internal auto-zeroing are linearly interpolated since gaps were short (~2 minutes). The chemical system defined by each set of observations is integrated 5 days forward in time, in 1-hour time steps with diurnal variation of solar zenith angle (SZA), in order for calculated reactive intermediates to achieve diel steady state. Reaction rate constants are calculated using aircraft measurements of pressure, temperature, and relative humidity. The SZA is determined based on the time and location of the aircraft, and used to calculate photolysis rates as described below.

For the A^2BC surface data, the model is constrained by 5-minute average concentrations of VOCs, NO_2, CO, and O_3 on days that a flight occurred. For May 17, surface data for NO_2 is filled with 1-hour average data collected for other days of the month, due to missing surface measurements on this day. The average concentrations from the WAS canisters below 500 m are used as ground concentrations since A^2BC did not measure VOCs at the surface. Similar to the flight data, the chemical system for the surface observations is integrated for 3 days forward in time, in 1-hour time steps with time-varying SZA, to reach diel steady state. Reaction rate constants are calculated from ground measurements of pressure, temperature, and relative humidity. Time and ground elevation are used to calculate the SZA, which controls photolysis frequencies as described below.

Photolysis frequencies, not measured during ARIAs or at the A^2BC supersite, evolve over the course of a model step and are calculated by combining cross sections

and quantum yields with solar spectra derived from the NCAR Tropospheric Ultraviolet and Visible (TUV) version 5.2 radiation model. At the start of the model run, input solar zenith angle, altitude or elevation, O_3 column, and surface albedo are used for linear interpolation across TUV lookup tables (F0AM's "hybrid" method). We use SZA and altitude/elevation from ARIAs/A^{2}BC measurements and constant values for ozone column (325 DU) and surface albedo (0.17), which we estimate based on concurrent data from the OMI Level 3 OMDOAO3e data product (https://disc.gsfc.nasa.gov/datasets/OMDOAO3e_003/summary?keywords=OMDOAO3e_003). A correction factor of 0.8, determined by trial and error, is used to scale *j*-values to better agree with the observed NO/NO_2 ratio.

The impact of aerosols on O_3 production depends on the optical properties as well as the vertical distribution (Dickerson et al., 1997; Kelley et al., 1995). In the presence of scattering and absorbing aerosols, photolysis frequencies will be altered, thus changing the O_3 formation and atmospheric oxidizing capability (Wu et al., 2020a). Previous research over China has shown that as AOD increases, the extinction effect of aerosols on photolysis frequencies decreases due to a higher proportion of scattering aerosols under high AOD conditions (Wang et al., 2019a). Optical depth, single scattering albedo, and angstrom exponent during ARIAs (see Wang et al., 2018a) are used in the TUV online calculator (https://www2.acom.ucar.edu/modeling/tropospheric-ultraviolet-and-visible-tuv-radiation-model) to assess the impact of aerosols on photolysis frequencies. Most of the aerosol particles during ARIAs were concentrated in the lowest 2 km of the atmosphere with a single scattering albedo at 550 nm of 0.85 and an average AOD

~0.2. The impact of aerosol optical properties measured during ARIAs on photolysis frequencies is small compared to the default setting, so no additional adjustments are made to the model values.

The method described here to constrain VOCs introduces large uncertainty due to the sparsity of measurements obtained over a large area that potentially consists of a wide variety of chemical compositions. However, the production of O_3 aloft is not well characterized over Hebei, so our observations may help improve the understanding of air pollution in this region, despite this limitation. Additionally, unlike a 3-dimensional chemical transport model, the box model simulations do not include advection or emissions. These processes, while important, are not included in the box model since O_3 precursors were measured and used to constrain the box model calculations. Box modelling is used to gain an understanding of O_3 production and its sensitivity to ambient levels of NO_x and VOCs based upon measured meteorological parameters and the concentration of a wide variety of chemical species.

2.2.3 Ozone Production and Sensitivity Calculations

The photochemical production of O_3 during the daytime is determined by the production rate of NO_2 molecules from the HO_2+NO and RO_2+NO reactions minus the loss mechanisms (Finlayson-Pitts and Pitts, 1999). Thus, the net O_3 production rate, net(PO_3) can be estimated following Equation 1:

$$net(PO_3) = k_{HO_2+NO}[HO_2][NO] + \sum_{i=1}^{n} k_{RO_{2i}+NO}[RO_{2i}][NO] - P(RONO_2)$$
$$-k_{OH+NO_2+M}[OH][NO_2][M] - k_{HO_2+O_3}[HO_2][O_3] - k_{OH+O_3}[OH][O_3]$$
$$-k_{O(^1D)+H_2O}[O(^1D)][H_2O] - L(O_3 + alkenes) \quad (1)$$

where k denotes the different reaction rate constants and RO_{2i} is the concentration of individual organic peroxy radicals. The terms subtracted from the production of O_3 are the loss mechanisms: the formation of nitrates, $P(RONO_2)$, the reaction of OH and NO_2 to form nitric acid, the reactions of OH and HO_2 with O_3, the reaction of $O(^1D)$ with H_2O, and the reactions of O_3 with alkenes. Additional terms not included here are the rate of O_3 loss by dry deposition and direct loss on aerosol surfaces (dilution is the only physical loss in the current F0AM setup).

We evaluate the sensitivity of O_3 production to NO_x and VOCs using the ratio of L_N/Q, where L_N is the radical loss through reactions with NO and Q is the primary radical production (Kleinman, 2005a). When L_N/Q is much less than 0.5, the O_3 production regime is NO_x-limited; when L_N/Q ratio is much higher than 0.5, the regime is VOC-limited. Different environments can have varying amounts of organic nitrates that impact the cut-off value of L_N/Q, so this value could vary around 0.5 (Kleinman, 2005b).

2.3 Observations of Nitrogen Oxides, Carbon Monoxide, and Ozone

Our observations confirm heavy loadings of air pollution over Hebei. Vertical profiles show peak median concentrations of NO (1.6 ppbv), NO_2 (4.4 ppbv) and NO_y (25.7 ppbv) below 500 m with large variability (Figure 2.3). Median concentrations of NO and NO_2 drop off gradually with altitude, while median NO_y remains close to ~15 ppbv throughout most of the profile. Between 500 and 1000 m, sufficient levels of NO_x are observed (median=3.8 ppbv), indicating continued production of O_3 in the PBL. Above 3000 m, median concentrations of NO and NO_2 fall to 350 pptv and 106 pptv, respectively (not measured simultaneously), still sufficient to produce O_3 as air parcels

travels downwind. Median mixing ratios of O_3 and CO remain high (~80 ppbv and ~120 ppbv, respectively) throughout the altitudes sampled by the Y-12.

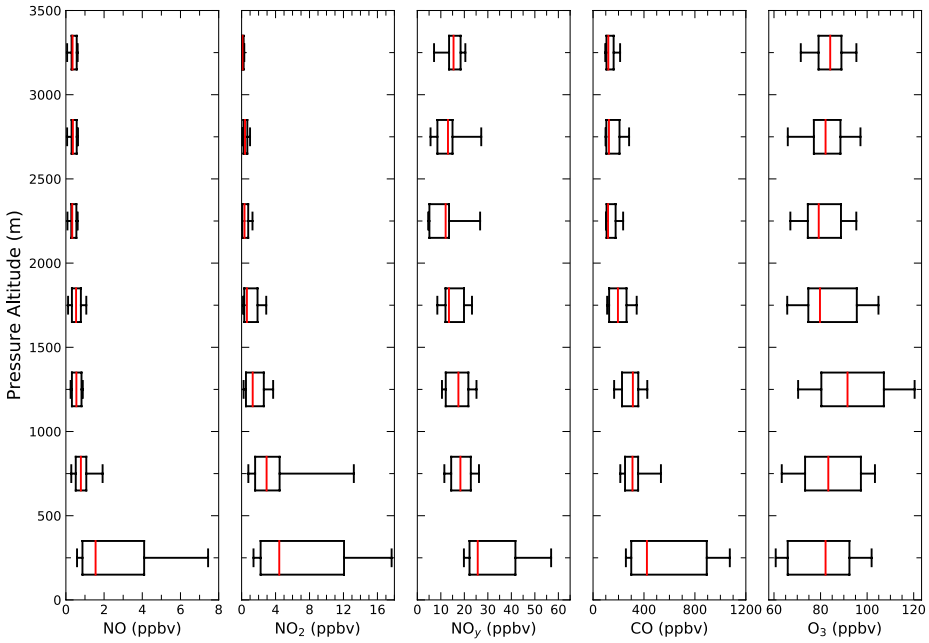

Figure 2.3. Box and whisker plots of 1-second profiles of NO, NO_2, NO_y, CO, and O_3 for data collected in 500 m bins. The whiskers show the 10th and 90th percentiles, the box denotes the 25th and 75th percentiles, and the central red line indicates the median value within each bin. Average PBL height for all ARIAs flight is ~1500 m. The total number of observations at altitudes above 2500 m of NO and NO_y is small (~2,200 or about ~30 minutes of measurements) since the NO/NO_y instrument cannot measure both species simultaneously.

Unlike previous airborne studies over Beijing from 1994-2005 that found increased O_3 concentrations below 1 km with constant levels (~52 ppbv) between 1 and 2 km (Ding et al., 2008), our O_3 concentrations peaked between 1000 and 1500 m (median = 91.6 ppbv). Low ratios of NO_x/NO_y (<0.30) indicate significant O_3 production had already occurred, but the strong correlation (R=0.71, Figure 2.4)

between 1-minute NO_z (NO_y-NO_x) and O_x (O_3+NO_2), an empirical estimate of the O_3 production efficiency (OPE), below 1500 m demonstrates moderate production of O_3 continued during sampling. The OPE of ~3.5 during ARIAs is smaller than the average

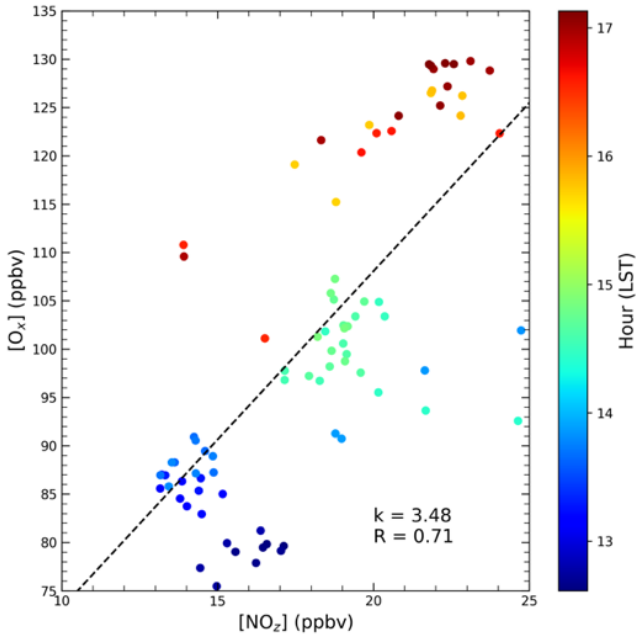

Figure 2.4. Scatter plot of 1-minute average O_x (O_3+NO_2) as a function of NO_z (NO_y-NO_x) less than 30 ppbv below 1500 m. The color shows the local hour of collection. The line is the linear regression with the slope (k) and Pearson R correlation coefficient.

OPE value of ~8 obtained during 2013 DISCOVER-AQ flights in Houston (Mazzuca et al., 2016) and ~7.5 procured during 2011 DISCOVER-AQ flights in Baltimore-Washington, D.C. region (Hembeck et al., 2019). The higher OPE values obtained from these airborne U.S. studies are likely due to the lower NO_x concentrations observed in the U.S. relative to Hebei.

Maps of O_3 and NO_2 on the Y-12 flight tracks (Figure 2.5) show the largest concentrations around the spiral locations as well as between the three most northern cities, Shijiazhuang, Julu, and Xingtai. Regions of elevated NO_2 do not always correspond with high O_3 concentrations. The flight with the maximum observed NO_2

mixing ratio (35.3 ppbv) during ARIAs occurred on May 17 around 8:30 am LST. The aircraft was flying a flat transect at 500 m from Shijiazhuang to Julu when a large peak of NO_2, CO_2 (500 ppmv), and NO (15 ppbv) was sampled. Concentrations of O_3 were low during the time of the peak (~60 ppbv), indicating NO-O_3 titration, but O_3 levels were quite high (>90 ppbv) throughout the remainder of the flight. The maximum O_3 concentration (142.5 ppbv) was measured on May 21 during descent into Luancheng

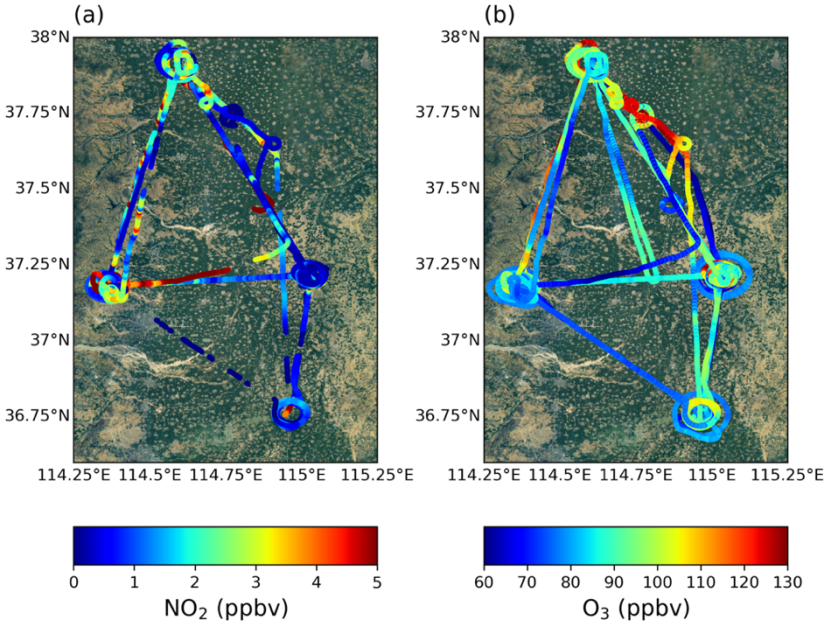

Figure 2.5. Maps of the ARIAs flight track colored by the 1-second measured mixing ratio (ppbv) of NO_2 (a) and O_3 (b). The background map is provided by Esri, Copyright: ©2009.

Airport in Shijiazhuang. Measurements of NO_x were not available for this flight, but elevated CO concentrations (565 ppbv) were observed. High concentrations of O_3 were also observed away from the large megacities. For instance, an O_3 plume (~125 ppbv) was sampled on June 6 at 1500 m over a more suburban area between Shijiazhuang and Julu with NO_2 levels ~500 pptv.

Vertical profiles of trace gases over the four spiral locations (Figure 2.6) generally show the highest concentrations over the two largest cities, Shijiazhuang and Xingtai. These two megacities exhibit the greatest variability below 500 m altitude of all trace gases discussed here. At 3000 m, Xingtai demonstrates the most NO_2 (~800 pptv), while the other spiral locations show ~300 pptv. Median profiles of NO_y below 500 m are highest over Julu (27.6 ppbv). Median vertical profiles of CO are relatively consistent (~300 ppbv) below 2000 m over the spiral locations, while Julu shows the highest median concentration between 2500 and 3000 m (209.1 ppbv). Measurements of CO above Xingtai indicate a large spread in observations at all altitudes from the lowest 500 m (10^{th} percentile= 258 ppbv, 90^{th} percentile=1049 ppbv) up to 2000 m (10^{th} percentile=97.7 ppbv, 90^{th} percentile = 135 ppbv). This variability may be partially

explained by the possible burning of wheat straw during early summer 2016. Strong correlations between ethane and acetylene, two biomass burning markers (see Sect. 3.2), further suggest wheat residue burning over Xingtai. Median vertical profiles of O_3 below 500 m were 10-25 ppbv higher in Shijiazhuang (median=96.2 ppbv) than the other spiral locations. Concentrations of O_3 are generally stable or slightly increasing in the lowest 2000 m, and median O_3 is 75-80 ppbv even at altitudes as high as 2500-

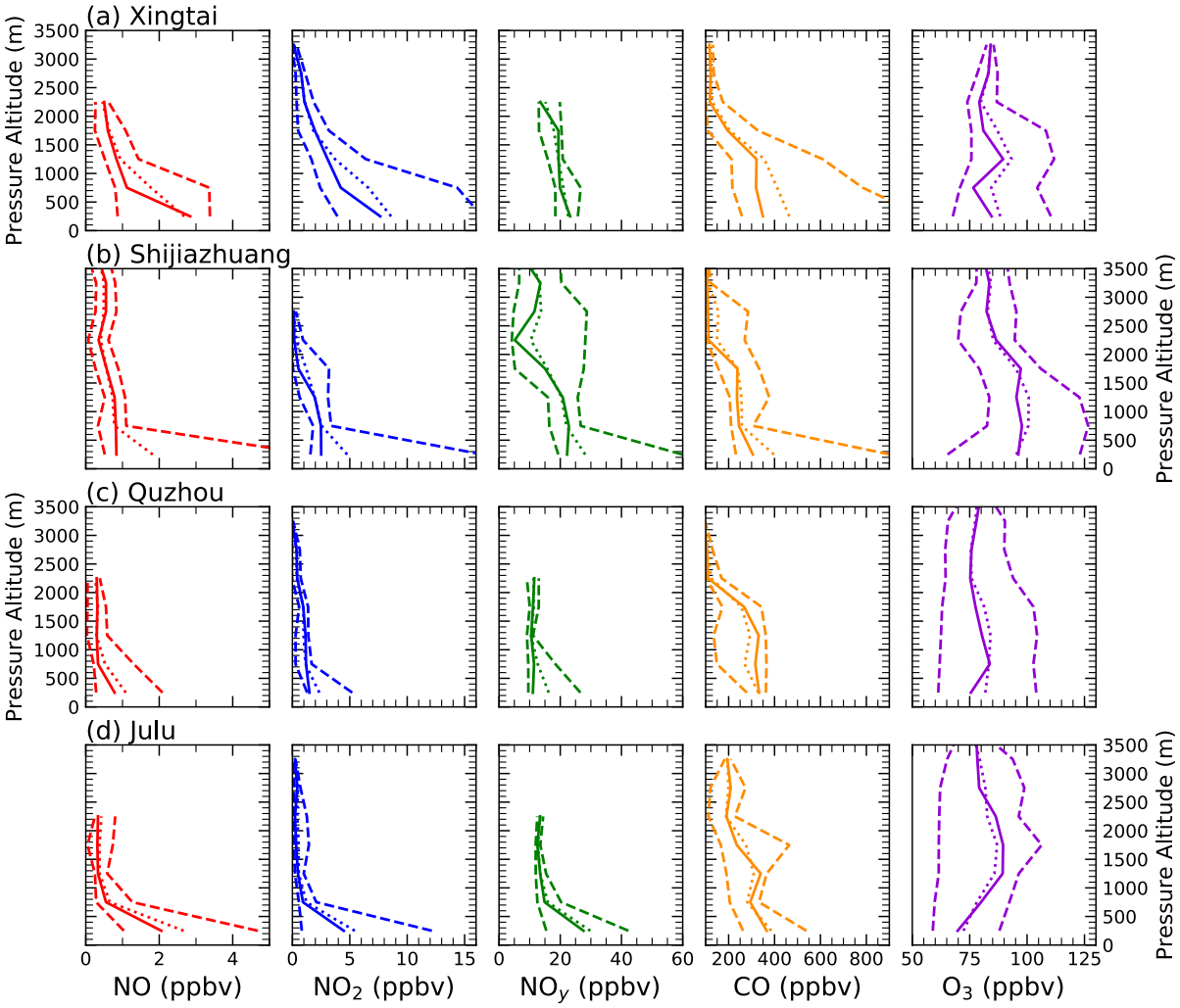

Figure 2.6. Vertical profiles of 1-second NO (red), NO_2 (blue), NO_y (green), CO (orange), and O_3 (purple) in 500 m bins over the 4 spiral locations: Xingtai (a), Shijiazhuang (b), Quzhou (c), and Julu (d). The dashed lines indicate the 10th and 90th percentiles, the solid line is the median and the dotted line is the mean. We remove observations of NO/NO_y above 2500 m over three spiral locations due to limited measurements.

3000 m. Xingtai shows the smallest variability of aloft O_3 levels above 2000 m, likely due to the position of this city on the leeward side of the Taihang Mountains.

The vertical profiles of O_3 compared to concurrent surface measurements in Xingtai indicates the A^2BC site usually observed larger average concentrations than observed aloft, but this difference was highly dependent upon time of day (Figure 2.7). The early afternoon profiles on May 8 showed average surface concentrations only slightly higher than the Y-12 measurements at ~400 m, while the mid-afternoon profiles on May 21 showed ~25 ppbv higher surface O_3 concentrations than Y-12 observations. At low altitudes (~700 m), the late morning flight (around 11:00 LST) on May 28 observed levels of O_3 ranging from 72-80 ppbv, comparable to average surface concentrations of 78 ppbv at the same time due to the development of the PBL which mixes the residual O_3 aloft. By contrast, the afternoon flight (approximately 17:00 LST)

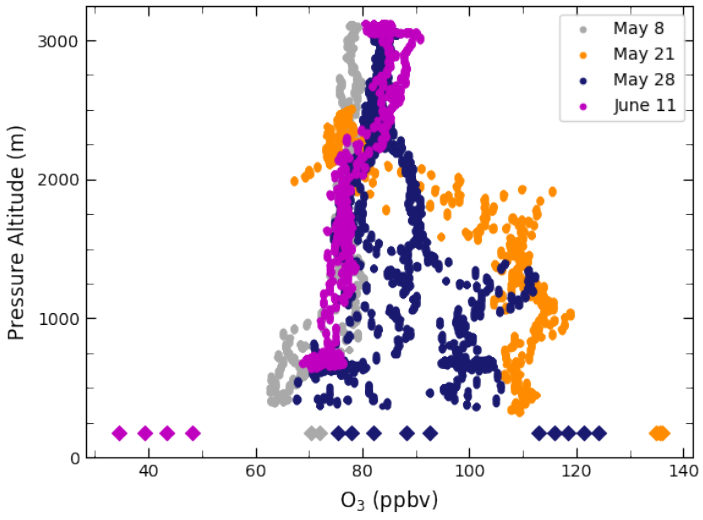

Figure 2.7. Vertical profiles (N=19) of 1-second O_3 concentrations (ppbv) from the Y-12 (circles) compared to concurrent average concentrations measured at the A^2BC site in Xingtai (diamonds). The average surface O_3 concentration was computed by averaging the 5-minute data interval starting 30 minutes before the spiral until 30 minutes after the spiral was completed.

at the same altitude later that day observed ~25 ppbv lower levels of O_3 compared to the surface (average=121 ppbv). All profiles on June 11 showed 10-30 ppbv lower average surface concentrations than measured during the Y-12 spirals.

The overall measured concentrations (1-second data, standard deviation, minimum, and maximum values) of NO_x, CO, and O_3 in this study are compared with other airborne studies in China including KORUS-AQ flights when outflow was directly from China (Table 2.3). Comparable to our range of NO_x levels from concentrations near the detection limit to 53.2 ppbv, autumn flights in the Yangtze River Delta in 2007 documented large variability in NO_x concentrations, ranging from 3 to 40 ppbv (Geng et al., 2009), while April 2006 observations in northern China similarly find a mean concentration ~5 ppbv (Wang et al., 2008b). The minimum CO concentration during ARIAs (80.5 ppbv) was measured in the lower free troposphere, which is a much smaller minimum concentration than reported by earlier studies. The warm-sector PBL air ahead of a cold front in April 2005 in Shenyang Province in northeast China found ~300 ppbv CO between 1000 and 4000 m (Dickerson et al., 2007), generally larger than most ARIAs profiles (except for Julu). The maximum value of CO during ARIAs (over 6 ppmv) agrees better with the literature, although there are few reported aircraft measurements of CO in Northeast Asia. Average and maximum O_3 concentrations during ARIAs were much higher than in other studies, but comparable to KORUS-AQ measurements from May 24-29 when the flow of air was direct from China. Since the majority of past airborne studies occurred over the sea areas during other seasons, it is not surprising that a polluted or industrialized

environment like Hebei experienced much larger amounts of O_3 than previously reported.

Table 2.3. Aircraft monitoring results (all altitudes mostly in the PBL, 1-second data) in comparison with other airborne studies in the region. All units are ppbv.

		NO_x		**CO**		**O_3**	
Location	Time Period	Ave (STD)	Min/Max	Ave (STD)	Min/Max	Ave (STD)	Min/Max
This Study, ARIAs	May-June 2016	5.1 (7.9)	–1.3/53.2	290.7 (309.6)	80.5/6054	85.0 (15.6)	45.0/145.6
KORUS-AQ[*]	May 24-29	1.3 (4.9)	—	258.2 (144.5)	—	89.8 (17.5)	—
Yellow Sea, coastal and offshore[a]	April 2011	2.45	0.49/9.58	980	630/1950	76.3	43.0/126.5
YRD[b]	October 2017	—	3/40	—	3000/7000	—	20/60
Northeast China[c]	April 5, 2007	—	—	~300	—	~70	—
Northern China[d]	April 2006	5.01	—	—	—	43.8	—
Bohai Sea[e]	March 2002	—	–/18	—	–/18	—	35/65
Japan Sea[f]	April 1996	—	–/–	—	–/–	—	70/90

[*] Statistics calculated for 1-second data during three flights at all altitudes during the "extreme pollution period" (Choi et al., 2019) where the KORUS-AQ DC-8 flew over the Yellow Sea to measure outflow from China.
[a] Yang et al., (2016).
[b] Geng et al., (2009).
[c] Dickerson et al., (2007)
[d] Wang et al., (2008).
[e] Hatakeyama et al., (2005).
[f] Inomata et al., (2006).

The ratios between combustion tracers can be used to understand the source and efficiency. During high-efficiency combustion in modern power plants, fuel carbon is converted to CO_2 with near unit efficiency, resulting in low CO/CO_2 (<0.10%), while low-efficiency combustion (cold or smoldering processes or low-technology

combustion) yields larger ratios. The regression of 1-second CO against CO_2 (Figure 2.8) shows high linear correlation (R=0.90) and high ratios of CO/CO_2 (3.1%) together with large amounts of SO_2. These measurements are illustrative of low-efficiency fossil fuel combustion, likely from residential coal burning as these observations were all collected at ~500 m, and are compared to other studies in Table 2.4. Our results indicating the prevalence of low-efficiency combustion agree with KORUS-AQ airborne data over the Yellow Sea during Chinese-sourced inflow (1-4% CO/CO_2) (Halliday et al., 2019), as well as with December 2017 surface measurements at Jingdezhen station in central China of 2.6% when air mass transport was from northern China (Xia et al., 2020). Compared to earlier studies in rural and urban areas of Beijing in the mid-2000s (Han et al., 2009; Wang et al., 2010b) and to 2011 measurements in Nanjing (Huang et al., 2015), the ARIAs CO/CO_2 ratio is 0.1-2.7% lower, evident of some success of regional pollution control strategies. By contrast, our CO/CO_2 ratio is

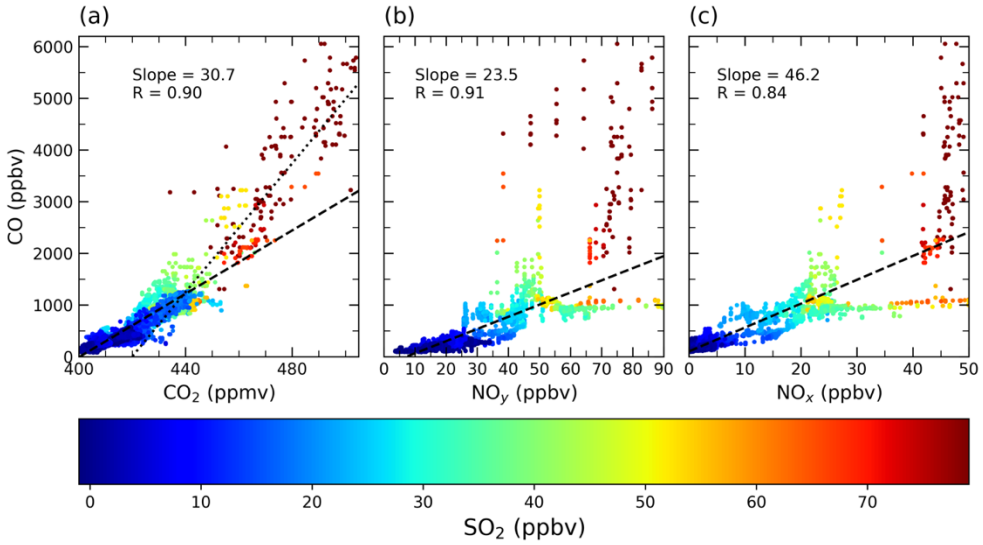

Figure 2.8. Scatter plots of 1-second (a) CO and CO_2, (b) CO and NO_y, and (c) CO and NO_x colored by the SO_2 mixing ratio for all ARIAs flights. The dashed line shows the linear regression for each plot. The dotted line in panel a indicates the higher ratio commonly associated with biomass and biofuel burning.

higher than satellite-derived ratios over megacities that have implemented extensive pollution control measures (Silva et al., 2013). Similarly, compared to airborne measurements from the 2015 Wintertime INvestigation of Transport, Emissions, and Reactivity (WINTER) campaign in the Baltimore/Washington, D.C. region (Ren et al., 2018), our CO/CO_2 ratio is about a factor of 6 larger. Higher CO/CO_2 ratios (~6%) with less than 0.1 ppm SO_2, as seen briefly during three ARIAs flights, are more in line with emissions from burning of wheat straw in Hebei of ~6% (Cao et al., 2008), and other inefficient, biofuel combustion.

Table 2.4. Comparison of CO/CO_2 ratios during ARIAs to other ground-based and aloft measurements in China and developed regions of the world. Stars (*) indicate aircraft studies.

Study	**Location**	**Year**	**CO/CO_2 (%)**
This Study*	North China Plain	May-June 2016	3.1
Wang et al. (2010)	Miyun, rural Beijing	Winter 2004	5.8
		Winter 2008	3.8
Huang et al. (2015)	Nanjing, China	2011	3.4-4.2
Silva et al. (2013)	Beijing/Tianjin	June 2009-May 2010	4.3
	London		0.6
	Mumbai		1.4
	New York		1.3
Han et al. (2009)	Beijing, China	2005-2006	Fall: 3.0 Winter: 4.4
Tang et al. (2018)*	West Sea	May-June 2016	2.18
	Seoul		1.18
Xia et al. (2020)	Jingdezhen station, central China	December 2017	2.6
	Jingdezhen station, polluted event	18-21 January 2017	1.4
Ren et al. (2018)	Baltimore/Washington, D.C.	Winter 2016	0.53

The $\Delta CO/\Delta NO_y$ ratio (equivalent to the slope in a CO vs. NO_y plot) (Figure 2.8) is an indicator for distinguishing plumes with efficient O_3 formation, Typical values of this ratio are ~40 in background air and between ~4-7 in fresh emissions plumes in Houston (Neuman et al., 2009). The $\Delta CO/\Delta NO_y$ ratio of 23.5 measured during ARIAs

indicates some photochemical aging and contributions from fossil fuel or biomass burning, but high values of CO, NO_y, and SO_2 suggests sampling of air parcels heavily influenced by power plants. The CO/NO_x emission ratio (Figure 2.8) from ARIAs agrees with higher emission ratios of gasoline vehicles, while higher amounts of CO, NO_x, and SO_2 indicate coal burning from the residential sector or inefficient electric generating units. While most of these observations are reflective of the prevalence of low efficiency fossil fuel combustion, the aircraft sampled a plume on June 6 while flying spirals over Julu containing 0.9% CO/CO_2 and 0.4% SO_2/CO_2 (Figure 2.9), likely due to a coal-burning power plant operating at high combustion efficiency, either using a sulfur scrubber or burning low sulfur fuel.

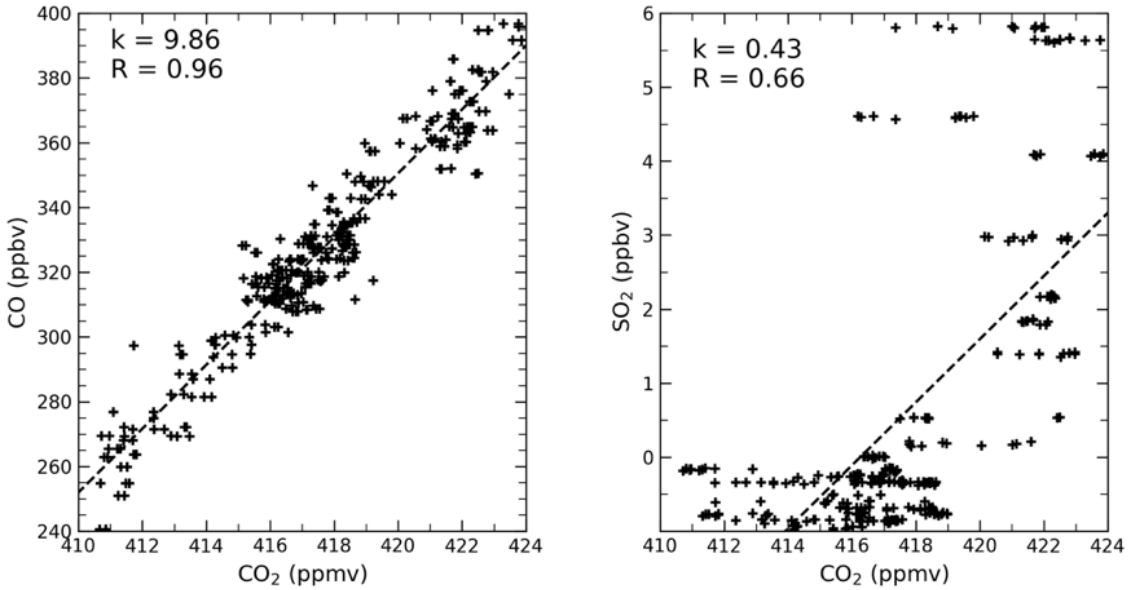

Figure 2.9. Scatter plot of 1-second CO (ppbv) and CO_2 (ppmv) (left) and SO_2 (ppbv) and CO_2 (right) sampled during a plume over Julu on June 6.

2.4 Observations and Sources of VOC

The total measured VOC mixing ratios ranged from 4 to 23 ppbv, largely dependent upon the altitude of collection, and was mostly dominated by alkanes (Figure 2.10). The samples associated with the largest concentrations of O_3 were all collected at altitudes ~500 m during a period with stagnant high pressure. Generally, the samples collected below 500 m showed larger amounts of alkenes/alkynes and aromatics than canisters collected elsewhere in the PBL.

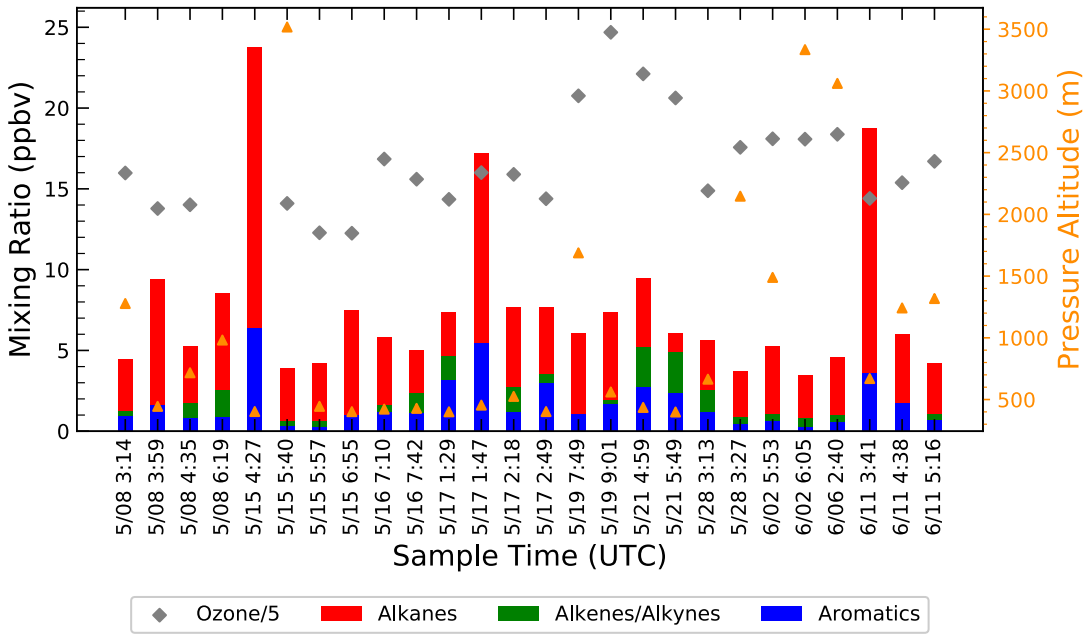

Figure 2.10. Total VOC mixing ratio for each WAS canister during ARIAs colored by alkanes (red), alkenes/alkynes (green), and aromatics (blue). The concurrent O_3 mixing ratio, divided by 5, is shown in grey diamonds (using left y-axis) and the pressure altitude of the sample is denoted by orange triangles (using right y-axis).

The top VOCs ranked by mean volume mixing ratio (Table 2.5) shows that alkanes dominate the total measured VOC mixing ratio during ARIAs (68%), followed by alkenes/alkynes (17%), and aromatics (15%). The top 10 VOC species are C2-C5 alkanes, C2-C3 alkenes/alkynes, benzene, and toluene. The observed mixing ratios of

ethane and propane are 2.65 ppbv and 1.39 ppbv, respectively, which together accounts for ~52% of the total alkane mixing ratio.

Table 2.5. Comparison of the top 10 most abundant species measured in this study with other ground observations in China (Units: ppbv).

	43 Cities[a]		**QZ**[b]	**GZ**[d]	**FS**[e]	**LZ**[f]	**BJ**[b]	**NJ**[c]	
	January-February 2001		July 2014	June 2011-May 2012	December 2008	2013	May 2014	June-August 2014	
	Ave	Range	Range	Ave	Ave	Ave	Ave	Ave	Range
Ethane	2.65	1.80-4.15	3.7-17.0	3.53	3.66	16.91	-	4.37	0.04-19.35
Propane	1.39	0.98-1.89	1.5-20.8	1.31	4.34	16.26	3.40	2.44	0.20-6.74
Ethylene	0.88	0.18-3.54	2.1-34.8	1.92	2.99	28.46	-	2.33	0.27-23.68
Acetylene	0.80	0.23-1.93	2.9-58.3	1.94	-	32.82	-	2.17	0.02-7.96
Toluene	0.76	0.03-4.40	0.4-11.2	0.48	4.59	18.87	1.01	1.33	0.01-5.40
i-Pentane	0.67	0.03-5.44	0.3-18.8	0.60	1.72	1.84	2.43	0.99	0.01-4.32
i-Butane	0.62	0.06-3.96	0.4-4.6	-	2.67	4.66	2.43	1.03	0.01-3.48
Benzene	0.51	0.06-2.18	0.7-10.4	0.81	0.62	6.00	1.94	0.82	0.02-11.79
2,2,4-Trimethylpentane	0.43	0.01-5.42	-	-	0.22	-	0.10	-	0.01-0.63
2-Methylheptane	0.40	0.01-5.52	-	-	0.08	0	1.49	-	0.01-0.46

[a]43 Cities, China (Barletta et al., 2005).
[b]QZ, Quzhou, BJ, Beijing (Li et al., 2015b).
[c]NJ, Nanjing, Yangtze River Delta (An et al., 2017).
[d]GZ, Guangzhou, Pearl River Delta (Zou et al., 2015).
[e]FS, Foshan, Pearl River Delta, haze days (Guo et al., 2011).
[f]LZ, Lanzhou (Jia et al., 2016).

The levels of ambient VOCs during ARIAs are generally lower than prior surface observations since measurements were taken in the PBL away from primary sources. Prior ground-based studies have similarly found alkanes to contribute the

majority (>50%) of the total VOC concentration in late spring in the Beijing-Tianjin-Hebei region (Li et al., 2015b; Tang et al., 2009; Yuan et al., 2013). The most abundant species during ARIAs are comparable to previous studies finding ethane, propane, and acetylene among the most prevalent, but likely have different sources based on the study location (Jia et al., 2016; Li et al., 2015b; Mo et al., 2015; Tang et al., 2009). In the Beijing-Tianjin-Hebei region, ambient acetylene, ethylene, and other light alkanes have been attributed to emissions from gasoline vehicles (Li et al., 2015b), while in Guangzhou, the widespread use of LPG has resulted in high levels of propane (Guo et al., 2011). Additionally, our observations have higher amounts of branched alkanes, such as 2,2,4-trimethylpentane and 2-methylheptane (both components of gasoline), but lower amounts of isoprene due to collection over mostly urban regions with lower ambient temperatures than the summer months. Since isoprene with a lifetime of hours (Seinfeld and Pandis, 2006) in the summer typically exhibits a strong vertical gradient in the PBL (Huang et al., 2017), we find the mean amount of isoprene measured during ARIAs is about 7 times lower than average May 2014 surface measurements in Beijing (Li et al., 2015b), as well as ~200 pptv lower than June-July 2007 airborne measurements in the PBL in NE China (Xue et al., 2011). Next, we examine the potential sources contributing to observations of VOCs by comparing with ratios and correlations from known sources.

Since CO can be a marker for anthropogenically emitted hydrocarbons, particularly combustion products, we first use the ratios of various VOCs to CO to reveal insight into changes in emissions in the region. Ratios of VOCs to CO can vary substantially among cities (Baker et al., 2008; Warneke et al., 2007), but in general can

provide details about fuel types and combustion efficiency between metropolitan regions. Despite ARIAs measurements sampling in close proximity to local VOCs sources, most VOCs do not correlate strongly with CO, reflective of the lack of common source signatures and some photochemical aging of the sampled airmasses. We report slopes of VOCs/CO in Table 2.2 when R>0.50. Ethane has the strongest correlation with CO (R=0.72) and the slope (2.5 pptv/ppbv) agrees well with ratios from urban areas of the United States in 1999-2005 (2.4 pptv/ppbv) (Baker et al., 2008) as well as with charcoal burning emission ratios (Andreae and Merlet, 2001). The ARIAs emission ratio of benzene/CO (1.8 pptv/ppbv) is slightly higher than found in urban regions of the United States (0.7, Baker et al., 2008) and Mexico City (0.93-1.20, Apel et al., 2010), likely due to higher emissions by widespread combustion of coal and agricultural residues (Zhang et al., 2015b). By contrast, the ARIAs emission ratios of ethylene and acetylene to CO (2.9. and 1.4 pptv/ppbv, respectively) are lower than observed in urban areas in the United States (4.1 and 3.4 pptv/ppbv, respectively) and Mexico City (7.90-8.40 and 8.20-9.60 pptv/ppbv, respectively), where the dominant source was reported to be transportation-related (Baker et al., 2008). The lower ratio of ethylene/CO is comparable to emission ratios reported from charcoal burning (2.3 pptv/ppbv) (Andreae and Merlet, 2001).

Ethane is the most abundant VOC in this study and correlates well with indicators for biomass and coal burning (R>0.81), such as acetylene, ethylene, benzene, and SO_2. The ratio of acetylene to ethane (Figure 2.11) during ARIAs is 0.59, comparable to the ratio found in a plume of fresh biomass burning in Canada (Blake et al., 1994) and within the range of crop residue burning (~0.2-0.6) found in other studies in China (Chen et al., 2017). High ratios of benzene/propane (1.12) are comparable to dry grass combustion samples collected in the central Pearl River Delta (PRD) (1.6) (Wang et al., 2005) and further confirm the presence of VOCs due to biomass burning.

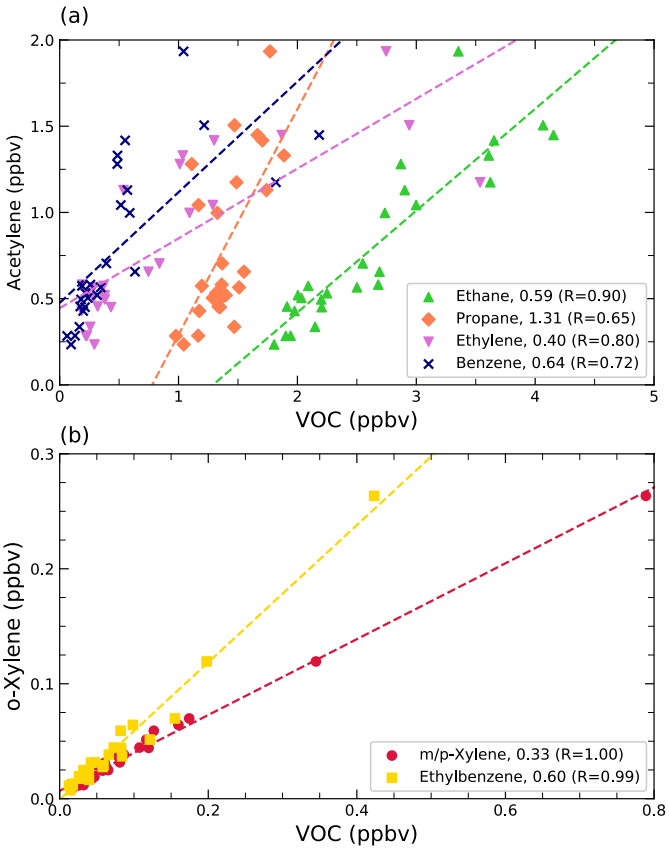

Figure 2.11. (a) Scatterplot of acetylene with ethane (green upward triangles), propane (orange diamonds), ethylene (purple downward triangles), and benzene (navy ×'s) for all WAS canisters during ARIAs. (b) Regression plots of o-xylene with m/p-xylene (red circles) and ethylbenzene (yellow squares). The dashed lines show the results of a linear least squares regression line for all data points.

The C3 and C4 alkanes, including propane and the butanes, are the three main components of LPG and their correlation acts as an indicator for LPG leakage. In this study, a moderate correlation (R~0.50) is found between n-butane and propane and i-butane with n-butane. The ratio of n-butane/propane during ARIAs is 0.60, which agrees well with ratios from vehicle emissions (Liu et al., 2008a), but is lower than slopes measured in the PRD (2.1) (Lai et al., 2009), where VOCs originated from LPG leakage. Additionally, propane correlates well with acetylene and ethylene (Figure 2.11), two well-known vehicular emission tracers.

Since acetylene and propane have comparable photochemical lifetimes with respect to OH attack, the ratio can be used to assess the relative importance of fossil fuel combustion and LPG leakage (Goldan et al., 2000). LPG contains propane but not acetylene (acetylene/propane<1) while combustion of fossil fuels commonly produces small amounts of propane relative to acetylene (acetylene/propane>1) (Conner et al., 1995; Gilman et al., 2013; Russo et al., 2010; Watson et al., 2001). In this study, the acetylene/propane ratio (Figure 2.11) is greater than 1, indicating emissions from vehicles (Fraser et al., 1998). These results suggest vehicles are largely responsible for the C3 and C4 alkanes as well as the C2 alkenes/alkynes observations.

The C5 alkanes and some C6 alkanes like 2,3-dimethylbutane and 2-methylpentane are found in vehicular exhaust and in gasoline vapor (Tsai et al., 2006). The i-pentane to n-pentane ratio is commonly used to identify the contributions of natural gas, vehicular emissions, and fuel evaporation since these alkanes have similar boiling points, vapor pressures, and reaction rate coefficients with OH. In areas heavily dominated by natural gas drilling, ratios lie between 0.82-0.89 (Gilman et al., 2013),

while higher ratios are associated with vehicle emissions (2.2-3.8) and fuel evaporation (1.8-4.6) (Jobson et al., 2004; McGaughey et al., 2004; Russo et al., 2010; Wang et al., 2013). In this study, i-pentane and n-pentane are highly correlated (R=0.93), indicating a common source of these compounds. The slope is 10.3, higher than reported in previous studies in China (Li et al., 2019), and the large i-pentane concentrations are likely reflective of gasoline evaporation due to the extremely volatile nature of i-pentane. The influence of fuel evaporative emissions is further identified by strong correlations between C4-C7 alkanes and alkenes typical of fuel evaporative emissions. Strong correlations of many long-chain alkanes (C6-C7 and octane) with i-pentane (R>0.73 except for cyclohexane) but absence of correlations with acetylene indicates solvent evaporation may be another source of long-chain alkanes.

Typically, the ratio of cis-2-butene/trans-2-butene is used to determine the source of C4 alkenes (Li et al., 2015b; Velasco et al., 2007). However, in this study, all measurements of cis-2-butene and trans-2-butene are below the detection limit, so assessing the ratio and correlation is not possible. Previous studies in this region in China have attributed C4 alkenes to vehicular emissions (Li et al., 2015b).

The correlation between the C7-C8 aromatics is strong (R>0.76) and revealing of typical signatures from incomplete combustion. The toluene/ethylbenzene ratio (10.7) is higher than traffic and urban emission ratios (~5-8), but closer to ratios associated with biomass burning (9.41) (Monod et al., 2001; Parrish et al., 1998a). Toluene also correlates with all C7-C9 alkanes (R>0.64) and with i-pentane (R=0.85), compounds from diesel and gasoline evaporation. High levels of toluene reported in Hong Kong by Ho et al., (2004) were suggested to be emitted from gasoline

evaporation, while Chan et al., (2006b) attributed the high toluene levels in different PRD cities to industrial solvent usage.

There is an excellent correlation (R>0.99) between o-xylene and m/p-xylene (Figure 2.11) and the slope (0.33) is comparable to the emission ratio found in a tunnel study (0.35) (Liu et al., 2008a). The o-xylene/ethylbenzene (0.60, Figure 2.11) slope is lower than vehicle exhaust emission ratios (1.2-1.8) (Conner et al., 1995; Jobson et al., 2004; Kirchstetter et al., 1996; Rogak et al., 1998; Sagebiel et al., 1996), but the correlation is extremely strong, suggesting the preferential loss of xylenes during transport due to their higher reactivity. These correlations and ratios suggest incomplete combustion from vehicular emissions and biomass burning are an important source of C7 and C8 aromatics.

The ratio between benzene/toluene (B/T) is a useful indicator to distinguish between vehicular emissions and other combustion sources. A ratio ~0.5 is often attributed to vehicular sources (Brocco et al., 1997; Perry and Gee, 1995), while ratios larger than 1 have been reported for coal or charcoal burning (Andreae and Merlet, 2001; Moreira Dos Santos et al., 2004). Benzene was observed at high mean ratios over Hebei (0.51 ppbv) and the average B/T ratio is 1.8±1.6 ppbv/ppbv. The correlation of some hydrocarbons can highlight the differences between B/T>1 (N=17) and B/T<1 (N=9). The correlation found between benzene and acetylene when all samples are grouped together (Figure 2.11) substantially improves just considering "traffic-related" samples (B/T<1) (R=0.93), suggesting a contribution of vehicular sources to benzene and acetylene measurements.

2.5 The effect of VOCs on Ozone Formation

In order to effectively reduce O_3 concentrations, it is crucial to understand the relative importance of individual VOCs in terms of the production of O_3 because each VOC exhibits different chemical reactivities. In this section, we present results using the loss rate of each VOC species with OH and ozone formation potential (OFP) assuming no influence of aerosols. Since the aerosol effect on O_3 formation is dependent upon time of day (solar zenith angle), meteorology, levels of local and neighboring aerosols, and the VOC/NO_x ratio, the calculations presented here are simplified compared to the more complicated chemical composition of the atmosphere, but are still useful to help inform control strategies.

2.5.1 OH loss rate of VOC species

The calculation of the first-order loss rate of OH with different VOCs, termed OH reactivity, provides a measure of the potential to produce HO_2 and RO_2, key intermediate species in the production of O_3 (Stroud et al., 2008). Since the reaction with OH accounts for the majority of loss of most VOCs, the rate constant (obtained from the Master Chemical Mechanism version 3.3.1 (MCM3.3.1) and the National Institute of Standards and Technology (NIST) Chemical Kinetics database (www.kinetics.nist.gov/)) for the reaction between OH and various hydrocarbons reflects the overall reactivity of that hydrocarbon (Finlayson-Pitts and Pitts, 1999). OH reactivity for each VOC species (VOC_i) is defined by Equation 2:

$$OHR(VOC_i) = k_{OH+VOC_i} * [VOC_i] \quad (2)$$

Where k_{OH+VOC_i} is the reaction rate constant between OH and VOC_i. Among the VOC groups, alkanes and alkenes/alkynes both contribute the most to the total VOC

reactivity, accounting for 37% each. Aromatics accounted for 26% of the total VOC reactivity. The relative contribution of the top 10 VOCs ranked by mean OH reactivity (Table 2.6) shows ethylene, propylene, and isoprene among the top measured alkene species, together contributing ~33% to total OH reactivity. Among the alkanes, 2-methylpentane and i-pentane contribute the most (13%) to total OH reactivity, followed by the branched pentanes and propane. Aromatic compounds such as toluene and m/p-xylene constitute 13% to total OH reactivity. Previous ground-based summer studies in China have found larger contributions of isoprene to OH reactivity, ranging from ~10-30% (Li et al., 2015b; Xue et al., 2017), than ARIAs (7.2%).

Table 2.6. Top 10 VOC species (mean and percentage breakdown) which contribute to O_3 formation based on OH reactivity and O_3 formation potential during ARIAs.

OH Reactivity			**Ozone Formation Potential**		
Species	Mean (s^{-1})	%	Species	Mean (ppbv O_3)	%
Ethylene	0.18	15.7	Toluene	5.81	19.6
Propylene	0.11	9.6	Ethylene	4.65	15.7
Toluene	0.10	8.9	m/p-Xylene	1.87	6.3
2-Methylheptane	0.09	7.9	Propylene	1.72	5.8
Isoprene	0.08	7.2	i-Pentane	1.47	5.0
i-Pentane	0.06	5.1	2,2,4-Trimethylpentane	1.30	4.4
m/p-Xylene	0.05	4.1	2-Methylheptane	1.02	3.4
2,3,4-Trimethylpentane	0.03	3.0	i-Butane	0.93	3.1
2,2,4-Trimethylpentane	0.03	2.8	o-Xylene	0.72	2.4
Propane	0.03	2.7	1,2,4-Trimethylbenzene	0.67	2.3

2.5.2 Ozone formation potential of VOCs

Since OH reactivity only provides a qualitative identification of the most reactive species and does not reflect products and their production of further free radicals, we next consider the contribution to the formation of O_3 using ozone formation potential (OFP). The OFP of a VOC relies on the quantity maximum incremental reactivity (MIR), which represents the amount of O_3 formed from the addition of a small amount of the VOC species in interest under high NO_x conditions. Values of MIR (unit: g O_3/ g VOC) have been calculated based on model simulations evaluated with smog chamber measurements (Carter, 2010, 1994). The OFP is calculated according to Equation 3:

$$OFP\ (VOC_i) = MIR_{VOC_i} * [VOC_i] \quad (3)$$

This method gives an estimate of only the first 24 hours after initial release. The median measured VOC/NO_x ratio for all WAS canisters was 4.9 ppbv/ppbv. In comparison, the ratio of reactive organic gas to NO_x (ROG/NO_x) in Los Angeles is 7.6 ppbv/ppbv (Carter, 1994). VOCs experience photochemical loss from emission sources near the surface to measured aloft concentrations. Estimation of OFP from aircraft observations throughout the PBL indicates how formation of O_3 may be different from previous surface studies.

To identify the major contributors to O_3 formation in this region, the 10 species with the highest mean OFP are listed in Table 2.6. Aromatic compounds are the largest contributor to total OFP (43%), followed by alkanes (30%) and alkenes/alkynes (27%). Toluene and ethylene make the largest contributions (19.6% and 15.7%, respectively) to total OFP. The high MIR of these compounds (MIR=4.0 g O_3/g VOC and 9.00 g

O_3/g VOC, respectively) and large mixing ratios (4.9% and 5.7% of the total measured VOC volume mixing ratio) drives their important contribution to O_3 formation. The relatively short lifetime of ethylene (~1.4 days) combined with the large range of measured mixing ratios (0.18 to 3.54 ppbv) suggests sampling of air masses with little to moderate photochemical processing, indicating the large range of influence on OFP. The most reactive compound in terms of OFP is trans-2-butene (MIR=15.16 g O_3/g VOC), but its low concentration results in only 0.2% to total OFP. At the other extreme, ethane accounts for a relatively high percentage of total measured VOC volume mixing ratio (17.0%) yet only contributes 2.1% to OFP due to its low reactivity (MIR=0.49 g O_3/g VOC).

Previous studies in China report aromatics and alkenes account for the most OFP (Cai et al., 2010; Cheng et al., 2010; Jia et al., 2016; Liang et al., 2017; Wang et al., 2010a, 2016; Xie et al., 2008; Zheng et al., 2009). At a surface site in Beijing (May 2014), Li et al. (2015) found m/p-xylene, ethylene, toluene, propylene, and o-xylene are most influential to OFP, while at a ground station in Tianjin (August 2018), Han et al. (2020) found that ethylene, isoprene, toluene, m/p-xylene, and propylene were important contributors to OFP. Our study supports a larger contribution of anthropogenic VOCs than biogenic VOCs in spring, although summer studies indicate a major role for isoprene to the formation of O_3 in the NCP (Han et al., 2020; Zong et al., 2018). Since isoprene is mostly emitted by biogenic sources during the warmer summer months with strong solar radiation and when soil moisture is sufficient for plant growth, we expect isoprene to have a larger impact on O_3 production in the summer than during spring, the time of our study. J. H. Tang et al. (2007) concluded

ethylene, toluene, and m/p-xylene are the main contributors to OFP during spring 2005 at the surface in the PRD, citing emissions from industry and vehicular exhaust. Our study agrees with past research in urban areas in China identifying the most reactive VOCs in terms of OFP; O_3 appears to be formed more slowly above the surface and in nonurban areas, but production is still substantial.

National measures for Chinese VOCs abatement were released in 2015, mainly focused on the reduction of anthropogenic VOCs from sources in the petrochemical industry, organic chemical industry, packaging printing, and industrial coating, not considering reactivity or chemical speciation (Li et al., 2018a). A 2010 VOC emission inventory study concluded the top 15 OFP species (including m/p-xylene, toluene, propylene, o-xylene, and ethylbenzene) contributed 69% of total OFP, but only accounted for 30% of the total emission of VOCs by mass (Liang et al., 2017). Our analysis of the top 10 species ranked by mean OFP shows these compounds contribute 68% to total OFP but only represent 37% of the total volume mixing ratio. Li et al., (2018) classifies industrial coal burning, biomass burning, and motorcycles to the top three VOC emission sources in Shijiazhuang, but OFP is highest for furniture coating, automobile coating, diesel vehicles, fuel evaporation, and gasoline vehicles. These results confirm that reactivity scales and emissions rates should be considered together when formulating control strategies for O_3.

2.6 Photochemical Ozone Production and Sensitivity

In this section, we describe calculated net photochemical production rates of O_3 using the box model constrained by aircraft observations. Ozone production rates calculated from the box model are high in major urban center, particularly Shijiazhuang and Xingtai, but also between these cities (Figure 2.12). The highest rates (>10 ppbv/hour) are generally found closer to the surface, but in some instances upwards of 2000 m. The largest net production rate of O_3 (over 16 ppbv/hour) was located along the Taihang Mountains between Shijiazhuang and Xingtai. This large net production

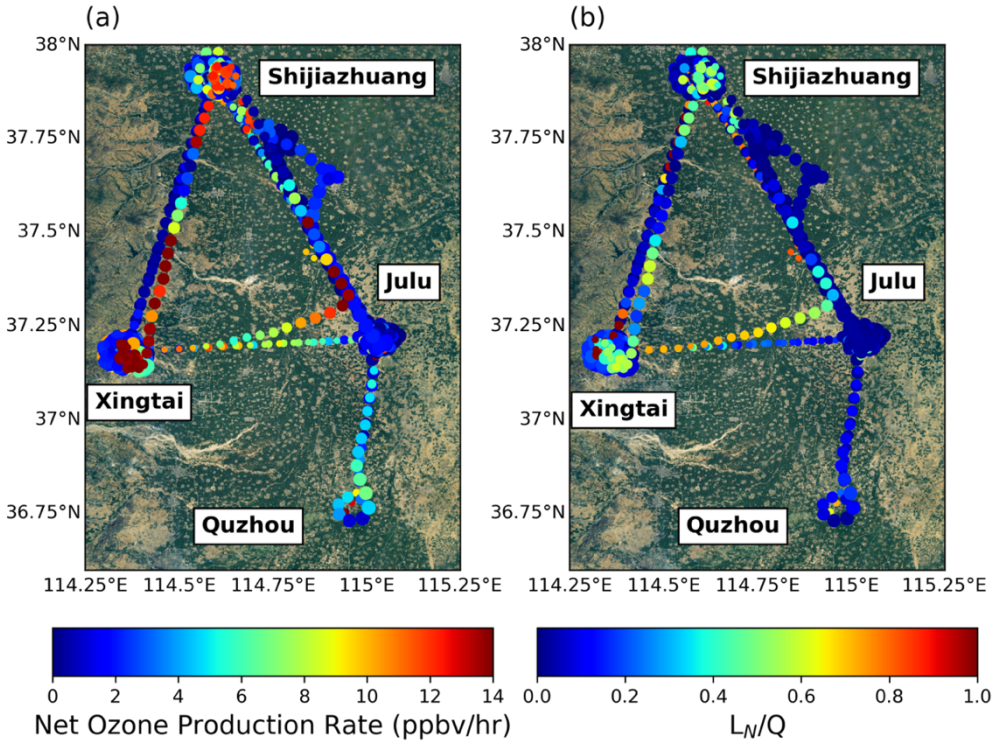

Figure 2.12. (a) Map of the net production rates of O_3 calculated using F0AM box model results along the Y-12 flight track during ARIAs. (b) Map of L_N/Q, an O_3 sensitivity indicator, along the Y-12 flight path. Ozone production is VOC-sensitive when $L_N/Q > 0.5$ and NO_x-sensitive when $L_N/Q < 0.5$ (Kleinman, 2005a). The size of the dots in both plots is proportional to the production rate of O_3. The background map is provided by Esri, Copyright: ©2009.

rate occurred ~2000 m on June 11, 2016 when NO, NO_y, NO_2, and O_3 were ~2 ppbv, ~18 ppbv, ~3 ppbv, and ~75 ppbv, respectively.

Vertical profiles of production, loss, and net rates of O_3 (Figure 2.13) show that HO_2+NO made more O_3 than RO_2+NO during the campaign. The major loss of O_3 was due to the termination of NO_2 through its reaction with OH below 2500 m. Reaction with $O(^1D)$ is the main loss of O_3 above 2500 m. A maximum of net O_3 production for the mean profile was observed in the lowest 500 m of ~7 ppbv/hour. In the PBL between 1500-2000 m, where median NO and NO_2 were 534 and 625 pptv, respectively, O_3 production rates were ~4 ppbv/hour. In the lower FT from 2500 to

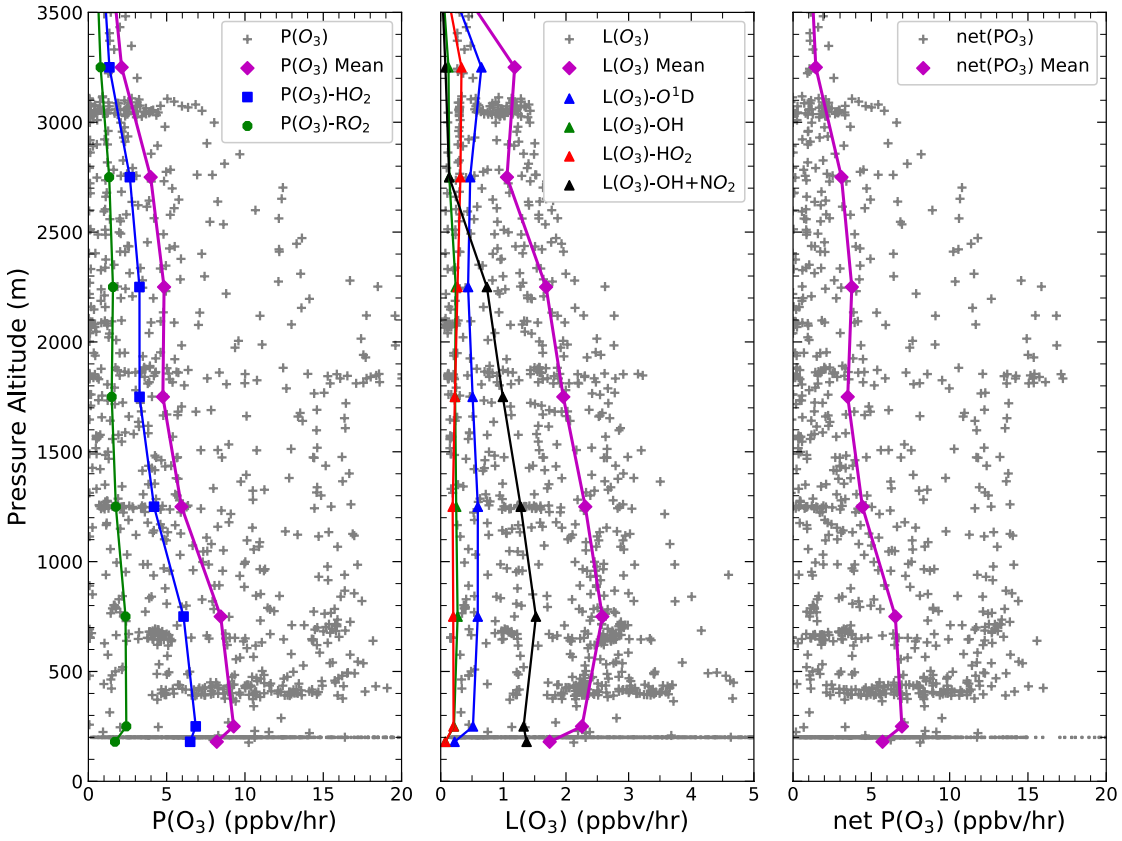

Figure 2.13. Vertical profiles of the rate of production of O_3 (left), O_3 loss rate (middle), and net O_3 production rate (right) during ARIAs.

3000 m, peak net O_3 production rates still reached ~3ppbv/hour and were conducive to long-range transport.

Values of L_N/Q (Figure 2.12) indicate production rates of O_3 are mostly NO_x-sensitive (i.e., $L_N/Q < 0.5$) in the PBL over Hebei and some of the largest net production rates of O_3 are associated with NO_x-sensitivity. In order to control aloft O_3 production that has the potential to be transported downwind, NO_x is the most important precursor to control. However, at low altitudes near urban centers, the production rate of O_3 tends to be more VOC-sensitive (i.e., $L_N/Q > 0.5$), particularly during morning flights. In urban regions of China, an O_3 formation transition from VOC-limited at the surface to NO_x-limited at ~1 km has been documented (Chen et al., 2013; Han et al., 2020). Additionally, many studies conclude O_3 production in urban areas of China is VOC-sensitive in spring, while likely more NO_x-sensitive in more rural areas (Ran et al., 2011; Xue et al., 2013). Using updated emissions from a nonlinear joint analytical inversion of VOCs and NO_x from the Ozone Mapping and Profile Suite Nadir Mapper (OMPS-NM) formaldehyde and OMI NO_2 columns during KORUS-AQ in WRF-CMAQ, Souri et al. (2020) found the maximum daily 8 hour average surface O_3 over the NCP to increase by 4.56 ppbv, suggesting that emission control strategies on VOCs should be prioritized. Pusede et al., (2014) assessed the temperature dependence of emission control scenarios to lower O_3 in San Joaquin Valley, California and concluded reducing organic emissions at moderate and high temperatures with co-occurring NO_x decreases will further diminish the number of O_3 violations. Thus, the control of NO_x as well as VOCs may be necessary to control both aloft and near-ground O_3 production in the NCP.

2.7 Summary

High concentrations of O_3 and its precursors were pervasive over Hebei Province, China in Spring 2016. In this study, we quantify the composition and photochemical nature of the lower troposphere associated with smog events. Measurements of trace gases including O_3, CO, NO_x, NO_y, and of aerosol optical properties were acquired in May and June 2016. Twenty-six samples analyzed for 54 VOCs were taken aboard a Y-12 research aircraft mostly in the PBL. Our observations confirm heavy loadings of pollution over Hebei.

The major conclusions of our study are:

1. We observed high amounts O_3, ranging from 45 ppbv to 145 ppbv, with the highest values found over Shijiazhuang. The highest NO_x concentrations were observed over Xingtai below 500 m. The highest NO_x and CO concentrations were 53.2 ppbv and 6054 ppbv, respectively. Ratios of CO/CO_2 indicate inefficient combustion from residential coal and biomass burning throughout the region but have decreased in China since the early 2000s suggesting the implementation of successful pollution control strategies.
2. Concentrations of total measured VOCs reveals alkanes contribute the most by volume mixing ratio (68%), while alkenes/alkynes and aromatics together supply the most (74%) to the calculated OH loss rate. Aromatics constitute most (43%) to the total calculated OFP and toluene, ethylene, m/p-xylene, propylene, and i-pentane play significant roles in the aloft formation of O_3 in this region. In contrast to other surface studies in summer, we find a lower contribution of biogenic sources (e.g. isoprene) to the formation of O_3 in the PBL. Sources of

VOCs include vehicular emissions, biomass burning, and fuel and solvent evaporation.

3. High amounts of NO_x and VOCs throughout the PBL over nonurban parts of Hebei Province are found to generate O_3 at a peak mean rate of ~7 ppbv/hour below 500 m. The lower free troposphere (from ~2500 to ~3000 m) was also frequently polluted with CO and NO_2 averaging ~125 ppbv and ~140 pptv with peak net production rates of O_3 ~3 ppbv/hour, allowing for continued formation of O_3 as the air mass travels downwind. The O_3 production regime is found to be NO_x-limited throughout the PBL over Hebei, while more VOC-limited at low altitudes near urban centers.

Our measurements in spring 2016 over Hebei cannot represent all of China or the seasonal variation of O_3 photochemistry, but measurements from an airborne platform make a valuable addition to the understanding of one of the most polluted regions in China, and indeed the world. The photochemistry of O_3 production is highly dependent upon the interaction of radiation and aerosols within the PBL and future work is needed to assess optical properties of aerosols at wavelengths relevant to photolysis of O_3 to $O(^1D)$ and thus OH. We show that to improve air quality in Hebei Province, both NO_x and VOCs from vehicles and fuel evaporation should be targeted. While VOCs are already targeted for emission reduction in China, the substantial concentrations of O_3 observed in this study further confirm the formation of a reactivity-oriented control strategy is urgent.

Chapter 3 Airborne Observations over Hebei Province, China Confirm Production and Use of CFCs

3.1 Introduction

The discovery of the Antarctic ozone hole prompted international action to reduce production, trade, and emissions of chlorofluorocarbons (CFCs) and other ozone depleting substances (ODSs). The resulting effort, the Montreal Protocol on Substances That Deplete the Ozone Layer (hereafter, the Montreal Protocol), is responsible for decreases in atmospheric abundances of ODSs and the start of the recovery of the ozone layer (World Meteorological Organization, 2018). First introduced as nontoxic and nonflammable refrigerants in the 1930s (Midgley, 1937), CFCs emissions have decreased since the 1990s (Cunnold et al., 1997) as replacements became dominant (Elkins et al., 1993) and the banks of unreleased material from refrigeration and rigid foams (Vollmer et al., 2009) and fugitive emissions from industry both diminished (Sherry et al., 2018). In addition to contributing to stratospheric O_3 depletion, ODSs are potent greenhouse gases, thus the phase out of these compounds has enormous benefits for both the stratospheric ozone layer and the climate system (Velders et al., 2013).

The recently observed slowdown in the decline of CFC-11 (trichlorofluoromethane, CCl_3F) concentrations suggests unreported new production despite declared near-zero production since 2010 (Montzka et al., 2018). Regional chemical transport model simulations merged with CFC-11 observations from Gosan, South Korea and Hateruma, Japan identified Shandong and Hebei provinces as responsible for 40-60% of the global rise in CFC-11 emissions, but was not sensitive

to regions north and west of Hebei (Rigby et al., 2019). Undercover operations by the Environmental Investigation Agency (EIA) and the New York Times reported new production of CFC-11 to supply the spray polyurethane foam (SPF) industry (Buckley and Fountain, 2018; Environmental Investigation Agency, 2018). During the foaming process, 86-100% of the blowing agent may be emitted for flexible foams, while 4-25% is emitted during the manufacture of rigid foams (UNEP, 2018). Lickley et al. (2020) estimated the size of CFCs stored in banks, concluding this pathway accounts for much of the current estimated CFC-11 and CFC-12 (dichlorodifluoromethane, CCl_2F_2) emissions, apart from the recent increase in CFC-11 after 2012, and suggests further analysis of CFC-113 (trichlorotrifluoroethane, $C_2Cl_3F_3$) feedstock leakage and the potential for unreported production and use. Lastly, emissions of CFC-114 (dichlorotetrafluoroethane, $C_2Cl_2F_4$) appear to be increasing slightly at a rate of 1.9 ± 0.84 kt yr^{-1} (2007-2016), with a large fraction originating in northeastern Asia and the Chinese mainland, despite the ban on production of this compounds under the Montreal Protocol (Vollmer et al., 2018).

The historical production pathway for CFC-11 and CFC-12 occurs by fluorinating CCl_4 (carbon tetrachloride) in the presence of an antimony catalyst. By varying industrial operating conditions, production ratios of CFC-11/CFC-12 range from 30:70 to 70:30 (Technology and Economic Assessment Panel, 2006), with CFC-11 usually the desired historical product due to low cost and ease of use as a blowing agent for SPF. While consumption and production of CCl_4 for dispersive purposes (i.e. as a solvent or cleaning agent) was banned by the Montreal Protocol since 2010, continued use for feedstock applications are allowed and unregulated. Despite bans on

CCl_4 new production, Lunt et al. (2018) found emissions in eastern China did not decline between 2009 and 2016, indicating a new source or sources of emissions in Shandong province after 2012. Under normal operating conditions, production of CFC-11 as a by-product in other chemical manufacturing pathways, such as the production of HCFC-22, is not technically feasible and small (0.1%) (Technology and Economic Assessment Panel, 2018). Surface studies in the Pearl River Delta (PRD) before the 2010 global phase-out found strong correlations between CFC-11 and CFC-12 (r^2~0.30-0.80), suggesting similar sources or use patterns (Guo et al., 2009; Zhang et al., 2010b). Production of CFC-113/CFC-114 and HCFC-22 typically occurs by fluorinating C_2Cl_4 (tetrachloroethylene) and $CHCl_3$ (chloroform), respectively.

Through Chinese/American partnerships with Peking University, Beijing Normal University, and the University of Maryland, an airborne field campaign called Air chemistry Research in Asia (ARIAs) was conducted over one of the suspected source regions of CFC-11 within China during 2016. Airborne observations in the planetary boundary layer (PBL) provide a rare opportunity to characterize aloft concentrations of ODSs to help understand the origin of CFCs emissions. We report observations of 27 whole air sample (WAS) canisters taken throughout the PBL onboard a Y-12 research aircraft in Hebei Province during May and June 2016. We find many of the 16 halocarbons quantified in this study, including CFC-11, CFC-12, CFC-113, and CFC-114, were often observed to be well above global background concentrations. Furthermore, our analysis suggests new production of some CFCs through correlations of CFCs and feedstocks, CCl_4 and C_2Cl_4, used in their production. By combining correlations with CFCs and feedstock with backward trajectories, we

find evidence for new production of CFC-12 only when flow is from Inner Mongolia/Shanxi, and of CFC-114 only from Shandong, but widespread new production of CFC-11 from all source regions. These could have adverse consequences for ozone and climate.

3.2 Experiment

3.2.1 Y-12 Aircraft Measurements

A comprehensive description of sample collection, flight path information, and VOC analytical details is provided in Chapter 2, so an abbreviated summary follows. The ARIAs campaign included 11 research flights conducted in May and June 2016 over the highly industrialized and heavily populated Hebei Province in northern China (Figure 2.1). The Y-12 collected trace gas, meteorological, and aerosol optical property data, as well as 27 whole air samples (WAS) throughout the PBL from 500 m to 3500 m pressure altitude (Table 1.2). Previous work has summarized this campaign, including (Benish et al., 2020a), F. Wang et al. (2018), and Y. Wang et al. (2019). Further details on aircraft instrumentation are given by Ren et al. (2018).

In collaboration with the College of Environmental Science and Engineering at Peking University, 27 WAS canisters were collected directly into evacuated 3.2 L fused silica lined, electropolished stainless steel canisters (Entech Instrument Inc., Simi Valley, CA). We remove fourteen halocarbons from the analysis presented here due to measurements below the detection limit for over half the samples. Additional details on the analytical technique of VOCs are summarized elsewhere (Mo et al., 2015; Wang et al., 2010a).

3.2.2 Intercomparison Experiment and Uncertainty Analysis

While sampling and analytical methods and techniques may cause differences in abundances reported by different laboratories, the most influential factors are usually the calibration standards and scales used to determine the concentrations (Rhoderick et al., 2015). Previous VOCs intercomparison experiments between Peking University (PKU) and other laboratories have shown good agreement (Liu et al., 2008b), but did not include CFCs. In order to tie directly to AGAGE and remote atmospheric levels, we performed an intercomparison experiment with the China Meteorological Administration (CMA). Results of an intercomparison experiment conducted in May 2020 follow below to enable a better understanding how elevated concentrations measured during ARIAs were above background atmospheric levels.

The PKU group prepared a total of four samples on May 11, 2020: two each for a pair of halocarbon concentrations obtained by diluting a 1 ppmv TO-15 standard gas manufactured by Linde (65 compounds, from Spectra Gases Inc., Stewartsville, NJ, USA). All samples were prepared into 3.2 L fused silica lined electropolished stainless steel canisters (Entech Instrument Inc.) that were cleaned by a Canister Cleaning System (3100 Entech Instrument Inc.) following a standard sampling procedure pressured with nitrogen and evacuated three times to 2.6 Pa. The two prepared concentrations were approximately 820 pptv (sample numbers 1848 and 1864) and 2.3 ppbv (sample numbers 0272 and 0113) for the 27 reported halocarbons with a final pressure of ~1723 hPa (25 psi). After sample preparation, PKU quantified 27 halocarbons from May 12 to 14, 2020 in these prepared standard samples using the GC-MSD/FID system detailed in Section 3.2.2.

Flasks containing the four samples were received by CMA on May 18 and analyzed for 12 halocarbons on May 21 using a custom-built "Medusa" gas chromatographic system with mass spectrometric detection (Agilent 6890/5975B, USA) (Zhang et al., 2017), adhering to the measurement and calibration techniques and procedures developed by AGAGE (Miller et al. 2008). One sample with the lower concentration (sample number 1864) was not quantified due to inadequate pressure in the canister (i.e., leakage may have occurred during transfer). All measurement data collected at PKU and CMA were reported to a third party, who conducted an initial analysis. Figure 3.1 shows the concentration ratios between CMA and PKU for each sample, along with the average ratio. The error bar on the average ratio for each species is the standard deviation about the mean of the three individual comparison ratios. The PKU group measured higher halocarbon concentrations than CMA for all gases except CCl_4. Only the two higher concentration prepared samples resulted in larger values of CCl_4 at CMA than PKU. For many compounds including the CFCs, there is noticeable variation of the ratio among samples, yielding a precision is generally about 2%. By contrast, the ratios for $CHCl_3$ and CH_3Br did not vary much between samples and result in a precision of 0.2 to 0.7%. The compound with the greatest imprecision is CH_3CCl_3, with a standard deviation of 13.2%.

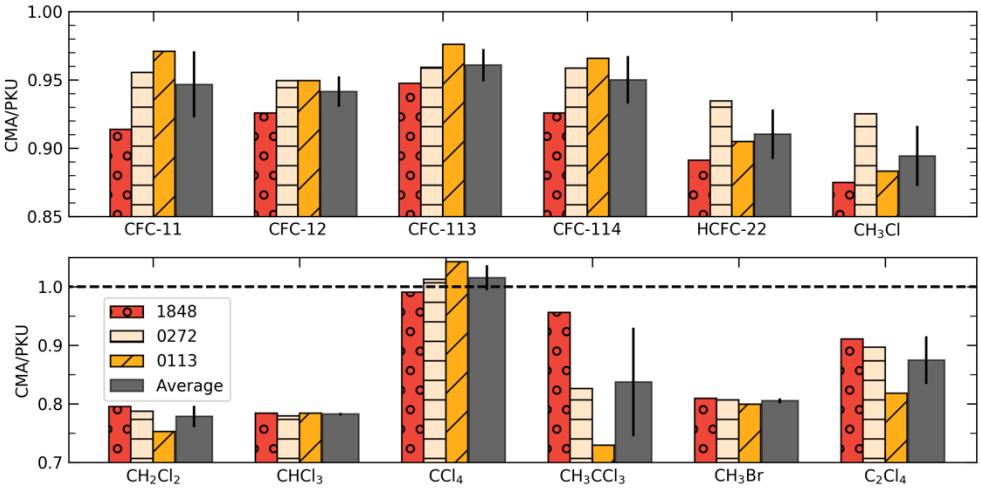

Figure 3.1. Ratios of the CMA to PKU measured concentrations for 12 halocarbons analyzed during a March 2020 intercomparison experiment. Sample 1848, the red bar with circles, was prepared with a concentration ~820 pptv and the bars with lines were prepared with concentrations ~ 2ppbv. The thick grey bar denotes the average value of all the bars for each compound. The error bar shows the standard deviation of the three prepared samples for each compound.

Previous scientific literature on CFCs is largely from groups with long-established histories of precise and accurate measurements of CFCs based on independently-prepared and maintained standard scales, such as NOAA and AGAGE (Montzka et al., 2011). In order to enable an accurate understanding of ARIAs measurements in China relative to background atmospheric levels, we use the average CMA/PKU ratio to adjust the ARIAs observations, such that our reported abundances of CFCs and related compounds are on the same calibration scale used in prior AGAGE studies. Table 3.1 reports summary statistics of the uncorrected and corrected ARIAs data. We acknowledge several limitations associated with this correction. First, three samples constitute a small sample number for determining a correction. Since no repeated measurements of the same canisters were conducted, we have a limited understanding of the stability or precision of each canister. Second, the three canisters were prepared at concentrations generally larger than the ambient atmospheric

abundance of most compounds measured during ARIAs. Lastly, a different TO-15 Linde cylinder was used in the 2020 intercomparison experiment than in our 2016 airborne measurements. Both cylinders have ± 5% analytical accuracy. Although this analysis cannot rigorously characterize the CMA/PKU ratio, we do demonstrate below that PKU can accurately quantify the abundance of CFCs to better than 15% total uncertainty. Our scientific conclusions regarding current emissions of CFCs and related species are unaltered upon use of the raw measurements provided by PKU; we adjust to the CMA/AGAGE scale to provide a more meaningful comparison to the literature.

Table 3.1. Summary statistics and average CMA/PKU correction factor for 12 halocarbons (pptv) quantified during ARIAs. The first number denotes the uncorrected value and the second number shows the corrected concentration using the average CMA/PKU ratio obtained from the intercomparison experiment.

	Ave	**STD**	**Min**	**25th**	**50th**	**75th**	**Max**	**CMA/PKU**
CFC-12	587/552	99/93	438/412	504/473	581/546	629/591	797/749	0.94
HCFC-22	426/388	164/149	221/201	339/308	379/345	475/432	1091/992	0.91
CFC-114	43/41	104/98	17/16	20/19	23/22	26/25	571/543	0.95
CH_3Cl	1071/953	301/268	573/510	828/737	1016/904	1272/1132	1970/1753	0.89
CH_3Br	12/9	3/2	8/6	10/8	11/9	13/11	19/16	0.81
CFC-11	370/351	377/358	210/200	268/255	296/281	335/318	2277/2163	0.95
CFC-113	83/79	10/10	62/60	76/73	82/78	89/92	99/95	0.96
CH_2Cl2	1412/1101	1660/1295	82/64	367/286	812/634	1976/1541	8487/6620	0.78
$CHCl_3$	102/79	74/58	15/12	61/48	74/58	150/117	324/253	0.78
$C_2H_3Cl_3$	3/2	1/1	2/1	2/2	2/2	3/3	5/4	0.84
CCl_4	88/89	21/21	53/54	74/75	86/88	102/104	138/140	1.02
C_2Cl_4	13/11	7/6	4/3	7/6	11/9	17/15	37/32	0.87

We estimate the total error associated with this correction approach for each compound. First, we use Equation 4 to quantify the difference between the measured value (CMA concentration, V_A) and observed concentration (PKU measured value, V_O) for each sample:

$$Bias = abs(V_A - V_O)/V_A * 100 \qquad (4)$$

Table 3.2 reports the bias for each compound for every sample and the average used in the error calculation. The standard deviation (± 1σ) of the three values represents how precise the PKU measurements are compared to CMA is also listed in Table 3.2.

Table 3.2. Accuracy for each prepared sample and average accuracy and precision used to calculate the total uncertainty.

Common name	Bias (%)			Average Bias (%)	Precision (%)	Total Uncertainty (%)
	1868	0272	0113			
CFC-11	9.4	4.7	3.0	5.7	2.7	13.8
CFC-12	8.0	5.3	5.3	6.2	1.3	13.1
CFC-113	5.6	4.3	2.4	4.1	1.3	12.3
CFC-114	8.0	4.3	3.6	5.3	2.0	13.1
HCFC-22	12.2	7.0	10.5	9.9	2.2	15.6
Chloromethane	14.3	8.1	13.2	11.9	2.7	17.3
Dichloromethane	25.8	27.0	32.9	28.5	3.1	31.3
Chloroform	27.5	28.3	27.5	27.8	0.4	30.0
Carbon tetrachloride	0.9	1.2	4.1	1.5	1.4	11.8
1,1,1-Trichloroethane	4.6	21.1	37.1	20.9	13.2	35.6
Bromomethane	23.5	24.0	25.1	24.2	0.7	26.7
Tetrachloroethylene	9.8	11.6	22.3	14.6	5.5	21.5

Next, we identify uncertainty associated with the preparation of the CMA/AGAGE primary scale. Since CMA uses the AGAGE quaternary calibration standard, their uncertainties propagate from this scale and their own measurement uncertainties. The AGAGE uncertainty (U_{x1}) is computed using Equation 5:

$$U_{x1} = sqrt(P_{x1}^2 + P'^2_{x1} + Q_{x1}^2) \quad (5)$$

where P_{x1} is the precision of the AGAGE calibration (0.2%), P'_{x1} is the precision of the AGAGE calibration of the quaternary standard used by CMA (0.2%), and Q_{xi} is the CMA measurement precision (0.5%). The total estimated uncertainty with the preparation of the CMA/AGAGE scale used in this analysis is 1.1% (95% confidence interval).

The uncertainty associated with the PKU scale is based upon the preparations originating from the 1 ppmv TO-15 standard. Before dilution, the nitrogen cleaning pipeline on the diluter (4600A Entech Instrument Inc.) was opened for over 30 minutes, followed by opening the standard gas pipeline for more than 10 minutes to stabilize the system. The diluter used mass flow controllers (7300 Series, Unit Instruments, Yorba Linda, CA) and a multi-port mixing chamber to dynamically mix source gases before flow was directed into the evacuated canister. The two mass flow controllers have a reported ± 1% accuracy and ± 0.15% repeatability. Additionally, the TO-15 standard from Linde reports ± 5% analytical accuracy. The measurement precision of the PKU GC-MSD/FID system is estimated to be within 5% (Mo et al., 2015). The PKU uncertainty (U_{x2}) is found by adding these by adding these four errors in quadrature for a total of 11.2% (95% confidence interval). The total uncertainty was assessed by adding the average accuracy, precision, and CMA (U_{x1}) and PKU (U_{x2}) uncertainties discussed above in quadrature.

The total uncertainty for the 12 halocarbons is estimated to range 12-36% (95% confidence interval). We remove bromoform from this analysis due to the large total uncertainty and since over half of the ARIAs samples were below the detection limit.

Four other compounds (chloroethane, 1,2-dichloroethane, 1,2-dichloropropane, and chlorobenzene) are included in this analysis but were not analyzed by CMA so the concentration cannot be adjusted or the uncertainty assessed.

3.2.4 Trajectories, clustering, and potential source contribution function

To explore the influence of air masses on CFCs levels, 24 hour ensemble backward trajectories arriving at the time and location of each WAS canister are calculated using the National Oceanic and Atmospheric Administration (NOAA) Hybrid Single-Particle Lagrangian Integrated Trajectory Version 4 model (HYSPLIT-4, (http://ready.arl.noaa.gov/HYSPLIT.php) (Draxler and Hess, 2014; Stein et al., 2015). The trajectories are initialized from the nearest hour, latitude, longitude, and pressure altitude for 26 of the 27 WAS canisters. We exclude one WAS canister that contained 2163 pptv of CFC-11 from the back trajectory analysis since such a high concentration necessitates close proximity to the source. Twenty-seven ensemble members for each WAS canister are created from 3 planes of 9 trajectories, each plane at +/– 0.1 sigma (about 250 m). The 9 trajectories on each plane are offset in the horizonal by 1 grid point (Air Resources Laboratory, n.d.). A total of 702 backward trajectories are computed for this study.

Trajectories are based on hourly output 36 km meteorological fields over East Asia, simulated using the Weather Research and Forecasting (WRF) model version 3.8.1. Initial and boundary conditions are derived from ECMWF ERA reanalysis data to drive WRF. Observational and analysis nudging are conducted to improve the WRF simulations.

Many studies have used similar clustered backward trajectories to describe meteorological patterns associated with different trace gas and aerosol concentrations (e.g., Moody & Galloway, 1988). After the HYSPLIT trajectories are calculated, trajectories are loaded into a GIS-based software called TrajStat (http://meteothink.org/docs/trajstat/index.html, Y. Q. Wang et al., 2009) and assigned their corresponding measurements of CFCs.

Since the main objective of using back trajectories is to determine the origins of air masses, we select angle distance as the cluster model (Sirois and Bottenheim, 1995). The mean angle between two backward trajectories (d_{12}) is defined using the law of cosines (Equation 6) as:

$$d_{12} = \frac{1}{n}\sum_{i=1}^{n} cos^{-1}\left(0.5\frac{(A_i+B_i+C_i)}{\sqrt{A_iB_i}}\right) \quad (6)$$

where $A_i = (X_1(i) - X_0)^2 + (Y_1(i) - Y_0)^2$, $B_i = (X_2(i) - X_0)^2 + (Y_2(i) - Y_0)^2$, and $C_i = (X_2(i) - X_1)^2 + (Y_2(i) - Y_1)^2$. The variables X_0 and Y_0 define the position of the receptor site (i.e., WAS canister sampling latitude and longitude) and $X_1(Y_1)$ and $X_2(Y_2)$ refer to the two backward trajectories. A three-cluster solution is adopted by assessing changes in total spatial variation with different cluster numbers using TrajStat.

The potential source contribution function (PSCF) can be used to identify the possible areas of origin of observed high concentrations of pollutants at a receptor site (Fedkin et al., 2018; Hui et al., 2019; Wu et al., 2018b), including CFC-11 (Lin et al., 2019). Regions in the grid with higher PSCF values indicate the corresponding location is a potential source region of CFCs release. The PSCF field (Equation 7) is calculated by:

$$PSCF_{ij} = \frac{m_{ij}}{n_{ij}} \qquad (7)$$

Here, n_{ij} is the total number of endpoints that fall in the ijth cell and m_{ij} is the number of endpoints for which measured values exceed a specified criterion value in the ijth cell. The 75th percentile of data for each CFC are selected as the criterion values, meaning the highest 25% of the samples are used for defining the potential source regions. The geographic region covered by the trajectories is divided into an array of 0.5° x 0.5° grid cells.

To reduce the influence of small values of n_{ij}, an arbitrary weighting function W_{ij} is multiplied by the PSCF values. The weighted scheme used here is obtained by trial and error by repeatedly running the TrajStat program, a method widely used in the literature (Fedkin et al., 2018; Hopke et al., 1995; Lin et al., 2019; Polissar and Hopke, 2001). The weighting function used in this study is defined as:

$$W_{ij} = \begin{cases} 1.00, & 80 < n_{ij} \\ 0.70, & 20 \leq n_{ij} < 80 \\ 0.42, & 10 \leq n_{ij} < 20 \\ 0.05, & n_{ij} \leq 10 \end{cases}$$

Previous studies used the mean (Hui et al., 2019; Lin et al., 2019), 50th percentile (Li et al., 2016d; Polissar et al., 1999), 75th percentile (Gao et al., 2012; Zhao et al., 2015), and 90th percentile (Cheng and Lin, 2001; Fang et al., 2018) as criterion values from the measurement data. In this study, we tested the mean, 50th percentile, 75th percentile, and 90th percentile of CFC-11, CFC-12, CFC-113, CFC-114, HCFC-22, and CCl_4 mixing ratios to examine the impact of criterion values on PSCF results. While several studies reported that the 90th percentile is best for estimating long-lived halocarbon sources using PSCF (Cheng and Lin, 2001; Fang et al., 2018), we choose

the 75th percentile since these concentrations were substantially above 2016 global, tropospheric background levels.

3.3 Ambient Levels of Halogenated Compounds

Sixteen halogenated compounds were identified and quantified in this study and summary statistics and global and Northern Hemisphere background levels are reported in Table 3.3 for each species. In a few cases, concentrations below the global and Northern Hemisphere backgrounds are observed. These near background concentrations indicate that some regions of Hebei are not greatly affected by local sources of ODSs.

Table 3.3. Range, average, standard deviation (STD), and quartile mixing ratios (rounded to the nearest pptv) for 27 samples collected during ARIAs. The 2016 global atmospheric abundances (pptv) are from Table A-1 in the 2018 World Meteorological Organization (WMO) Ozone Assessment and the mean May 2016 mixing ratios from Trinidad Head, Ireland are reported by AGAGE. The star (*) denotes compounds that were not adjusted from the May 2020 intercomparison experiment.

Common name	**Formula**	**Range**	**Ave (STD)**	**25th/75th percentiles**	**Global atmospheric abundance (2016)**	**Trinidad Head, Ireland (May 2016)**
CFC-11	CCl_3F	200-2163	351 (358)	256/312	230.2	231.55
CFC-12	CCl_2F_2	412-749	552 (93)	475/584	515.9	515.96
CFC-113	$C_2Cl_3F_3$	60-95	79 (9)	73/85	71.7	71.72
CFC-114	$C_2Cl_2F_4$	16-543	41 (98)	19/24	15	16.32
HCFC-22	CHF_2Cl	201-992	338 (345)	311/432	235.3	250.24
Carbon tetrachloride	CCl_4	54-140	89 (21)	76/100	80.5	80.68
Chloromethane	CH_3Cl	510-1753	953 (268)	740/1084	555	590.16

Bromomethane	CH_3Br	6-16	9 (2)	8/11	6.8	7.54
Chloroethane*	C_2H_5Cl	4-173	43 (36)	22/60	-	-
Dichloromethane	CH_2Cl_2	64-6620	1101 (1295)	353/1495	34	66.49
Chloroform	$CHCl_3$	12-253	79 (58)	48/97	8.9	15.58
1,1,1-Trichloroethane	$C_2H_3Cl_3$	1-4	2 (1)	2/3	2.6	2.87
1,2-Dichloroethane*	$C_2H_4Cl_2$	15-419	123 (87)	74/173	12.8	-
1,2-Dichloropropane*	$C_3H_6Cl_2$	9-774	112 (140)	52/115	-	-
Tetrachloroethylene	C_2Cl_4	3-32	11 (6)	7/14	1.5	2.58
Chlorobenzene*	C_6H_5Cl	1-24	8 (5)	4/12	-	-

A timeseries of ambient CFC-11, CFC-12, HCFC-22, CCl_4, CFC-113, and CFC-114 levels with respect to the 2018 WMO global background concentrations are shown in Figure 3.2. Concentrations with respect to Northern Hemisphere levels measured at Trinidad Head, Ireland change little since these compounds are long-lived. The median enhancement of various ODSs with respect to the global background is 22% (<1-840% range), 6% (<1-45% range), 47% (<1-322% range), 9% (<1-74% range), 10% (<1-33% range), and 47% (9-3520% range) for CFC-11, CFC-12, HCFC-22, CCl_4, CFC-113, and CFC-114, respectively. Most of the halocarbons discussed here are present in amounts higher than reported by the WMO Ozone Assessment in 2016. When one outlier is excluded, the mean ± standard deviation mixing ratio of CFC-11

(281 ± 44 pptv) is approximately ~51 pptv higher than global background levels. Considering all samples, mean CFC-12 (552 ± 93 pptv) is ~36 pptv higher than background concentrations, mean CFC-113 (79 ± 9 pptv) is ~7 ppbv above background, and mean CFC-114 (41 ± 98 pptv) is ~26 pptv above background.

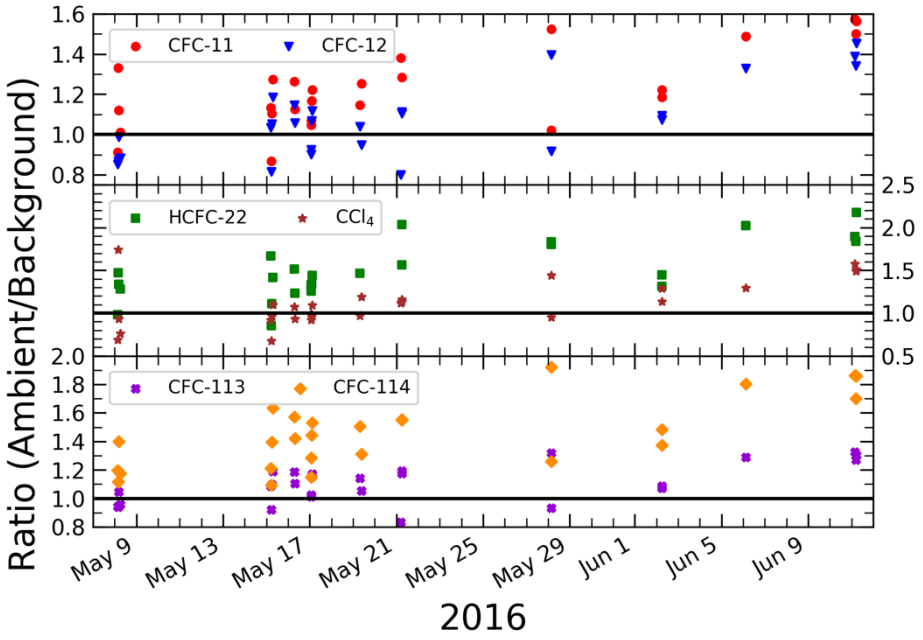

Figure 3.2. Timeseries of the ratios of observed ambient to background tropospheric abundances of CFC-11 (red circles) and CFC-12 (blue triangles) (top panel), HCFC-22 (green squares) and CCl_4 (brown stars) (middle panel), and CFC-113 (purple x's) and CFC-114 (orange diamonds) (bottom panel) collected in WAS canisters during the ARIAs campaign. The thick black line in each panel indicates where the ambient/background ratio is equal to 1 using the 2016 global atmospheric abundance from the 2018 WMO Ozone Assessment (see Table 3.3).

Compared to baseline AGAGE observations which restrict air sampling to times when airmasses approach from the clean air sector, mixing ratios of CFCs during ARIAs are expected to be higher since measurements are taken closer to sources. The concentration variability (assuming it is larger than can be explained by measurement issues of precision and accuracy) of CFCs serves as an indicator of relative emission strength (Wang et al., 1998) and together with the enhancement of ODSs above

background concentrations suggests emissions of these compounds, either from production (illegally, accidental by-product, or non-emissive from allowed purposes) or leakage from banks.

The samples with the lowest concentrations of CFCs were obtained near Quzhou. A sample collected on May 15 at 5:40 UTC at 3518 m pressure altitude recorded the lowest amounts of CFC-11, CFC-114, HCFC-22, and CCl_4 (200, 16, 201, and 54 pptv, respectively). Values of CFC-12 and CFC-113 were also low (420 and 66 pptv, respectively) in this sample, but not the minimum values observed. Back trajectories from HYSPLIT indicate the air mass originated from the eastern portion of Mongolia, bringing cleaner, cooler and drier air to Hebei (Figure 3.3).

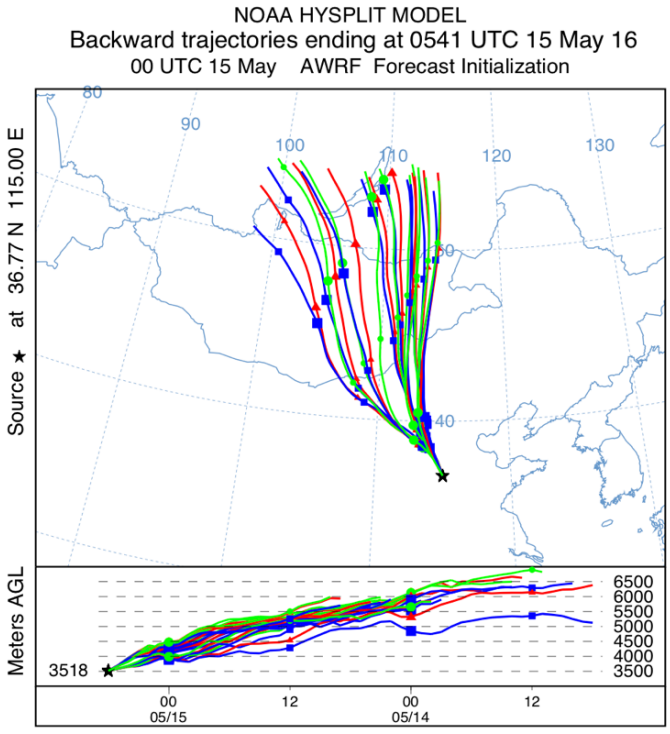

Figure 3.3. 24-hour backward ensemble HYSPLIT trajectories for the WAS canister collected on May 15 at 5:40 UTC which recorded the lowest mixing ratios of CFC-11, CFC-114, HCFC-22, and CCl4 (210, 16, 221, and 53 pptv, respectively). The bottom plot depicts vertical motions and shows substantial subsidence in this air.

The other sample with the lowest amounts of CFC-12 and CFC-113 (412 and 60 pptv, respectively) was obtained on May 21 at 4:59 at 436 m pressure altitude. This sample had the highest amounts of CFC-114 and HCFC-22 (543 and 992 pptv, respectively) and elevated CFC-11 (318 pptv). The backward HYSPLIT trajectories show anticyclonic flow bringing a warm, moist airmass from the Yellow Sea over southern Shandong and northern Jiangsu provinces (Figure 3.4) on May 21. The impact of airmass source regions on concentrations of CFCs will be further explored in Section 3.6.

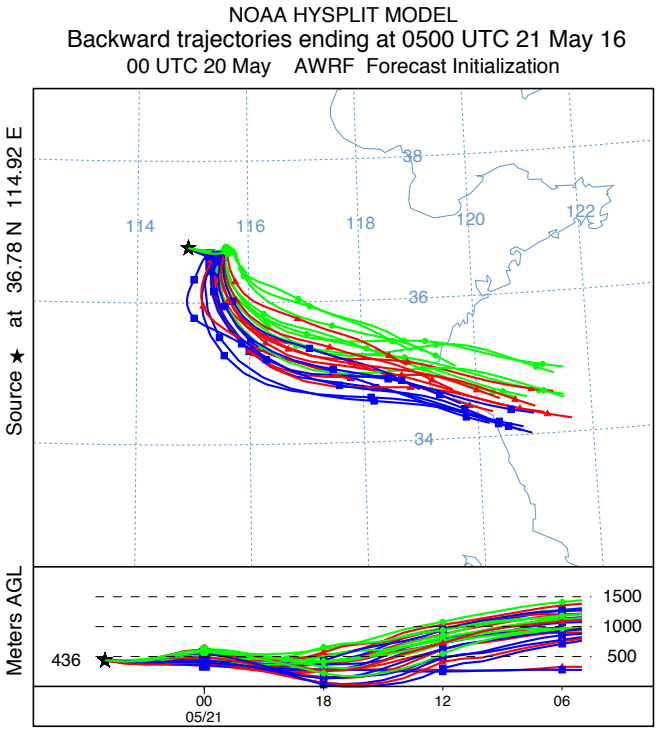

Figure 3.4. 24-hour backward ensemble HYSPLIT trajectories for the WAS canister collected on May 21 at 4:59 UTC which recorded the lowest mixing ratios of CFC-12 and CFC-113 (438 and 62 pptv, respectively), but highest amounts of CFC-114 and HCFC-22 (571 and 1091 pptv, respectively).

A few WAS canisters during stagnant meteorological conditions contained unusually large concentrations of ODSs. On May 21 at a pressure altitude of 1490 m

over Xingtai (37.175°N, 114.394°E), one WAS canister contained 2163 pptv CFC-11. It is plausible this sample collected CFC-11 released nearby from local foam blowing applications or from other industrial operations. Likewise, the maximum value of CFC-114 (528 pptv above background levels) and HCFC-22 (757 pptv above background mixing ratios) measured on May 21 suggests sampling of local operations in Quzhou that did not release CFC-12 and CFC-113. Global mole fractions of low abundance CFCs (<20 pptv) such as CFC-114 declined more slowly between 2012 and 2016 with a substantial fraction originating from China (Vollmer et al., 2018). Previous evidence suggests a small fraction of CFC-114 is due to its presence as an impurity in some HFCs, but the process responsible for this is unknown (World Meteorological Organization, 2018). The large range of mixing ratios of HCFC-22 above background levels is not surprising since this refrigerant is a replacement for CFC-12 and is being phased out. Mixing ratios of HCFC-22 have been increasing in many regions in China (Wu et al., 2018a; Yao et al., 2012), reflecting continued growth in production and consumption. The mean mixing ratio of HCFC-22 in this study is about 168 pptv higher than that measured in China in 2001 (Barletta et al., 2006), some of which is due to increases in the background atmosphere.

3.4 Comparison of CFC-11, CFC-12, and CFC-113 Mixing Ratios with other Studies in China

Mean mixing ratios of CFC-11, CFC-12, and CFC-113 measured during ARIAs are compared to past surface and airborne studies in China as well as the WMO global background in Figure 3.5. Before the global phase-out of CFCs in 2010, large variations of CFC-11, CFC-12, and CFC-113 levels were evident throughout China. The

production of CFCs in China ceased ahead of schedule in mid-2007 (Wan et al., 2009) and studies across China observed decreasing mixing ratios of CFC-11 and CFC-12 during this time. The largest change in concentrations of CFCs occurred in the Pearl

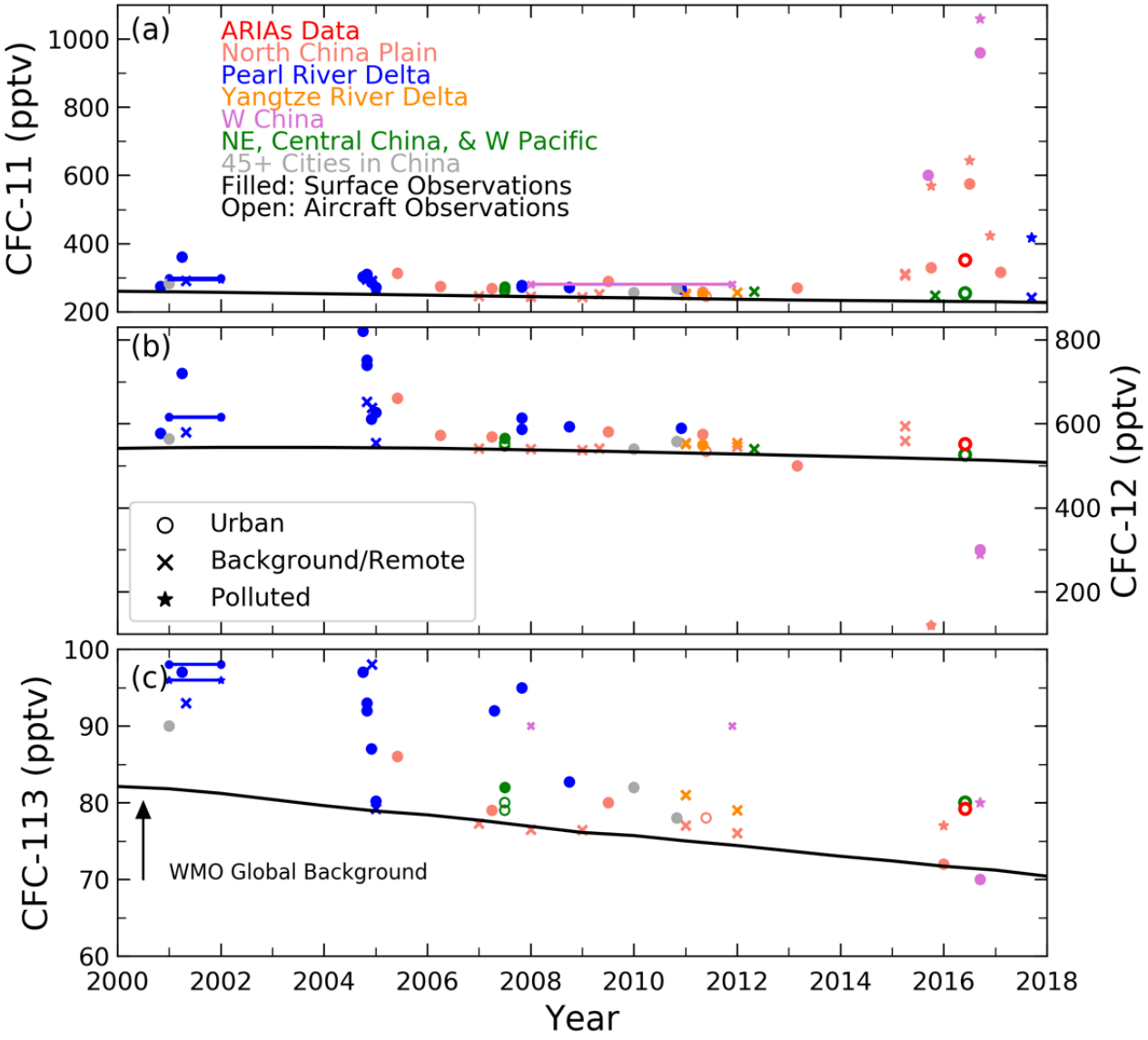

Figure 3.5. Timeseries of average mixing ratios from peer-reviewed journal articles of CFC-11 (a), CFC-12 (b), and CFC-113 (c) since 2000. Studies conducted over several years are shown by lines. The shape indicates if the sample was urban (circle), background/remote (x), or influenced by polluted meteorological conditions (stars). The color denotes the location of the study. Filled shapes denote surface observations while open shapes represent airborne studies. The black line shows the WMO 2018 global background. In 2016, the thick red open circle shows mean mixing ratios of all ARIAs WAS canisters. The thick green open circle shows observations during Chinese outflow presented in Simpson et al. (2020).

River Delta (PRD). The PRD was a significant producer and consumer of CFCs before the global phaseout (Zhang et al., 2014c) and a common study region compared to other more rural areas of China.

After 2015, abundant concentrations of CFC-11, CFC-12, and CFC-113 above the global background were first detected throughout the North China Plain and published in peer-reviewed journals, but were not tied to new production or use. Even in rural, mountain-top locations in southern China, high levels of CFC-11 were observed in October 2017 (Lin et al., 2019), largely due to contributions from less developed regions in southwestern and central China. The highest CFC-11 and CFC-113 mixing ratios were measured in Chengdu in western China in Fall 2016, with an average mixing ratio of 1060 pptv and 80 pptv, respectively, during days when hourly O_3 was > 90 ppbv (Deng et al., 2019). However, northeast and northwest winds were dominant during the time of this study and the authors note their measurements were partly affected by the petrochemical refinery located north of the sampling site.

The Deng et al. (2019) study and another by the same research group in fall 2015 in northwestern Beijing (Li et al., 2016a) observed amounts of CFC-12 substantially below global, tropospheric background levels (300 and 120 pptv). These low mixing ratios are reported in tables within these papers, but the analytical methods or remarks about these anomalous concentrations are not discussed. Therefore, we believe these CFC-12 observations may have large uncertainty or error, but still include these measurements since values of CFC-11 and CFC-113 are more reasonable and provide valuable information about locations of CFCs release in recent years.

The 2016 KORUS-AQ study, concurrent with ARIAs, provides the opportunity to compare aloft CFCs mixing ratios around the same time period over large urban regions. Six flights along the West Sea jetway at low altitude (<500 m) measured outflow from China (Simpson et al., 2020). During these flights, mean CFC-11, CFC-12, and CFC-113 were above global, tropospheric background levels. However, CFC-11 was found to be more elevated in air over Seoul during stagnant meteorological conditions than in air from China. In contrast, concentrations of other long-lived halocarbons (CFC-113, CFC-114, and CCl_4) were higher in air arriving from China.

Reported measured levels of ODSs regulated by the Montreal Protocol are dependent upon the calibration scale and the year in which the samples were collected, as well as seasonal cycles, latitudinal gradients, and long-term trends in the ambient atmosphere.

3.5 Interspecies Correlations during ARIAs

To understand the source characteristics of halocarbons measured during ARIAs, an interspecies correlation matrix of the 16 halocarbons (N=27) is presented in Figure 3.6. Due to the limited number of WAS canisters collected during ARIAs, the distribution of some compounds is neither obviously normal nor lognormal. One outlier for CFC-11, CFC-114, CH_2Cl_2, and $C_3H_6Cl_2$ and two outliers for HCFC-22 were removed and displayed in Figure 3.7 because these points represent extreme concentrations of ODSs. The presence of outliers is indicative of ongoing emission of ODSs in the immediate area of measurements during ARIAs. By removing these outliers, we present results on underlying ODSs relationships not associated with extremely high concentrations of ODSs. The emergence of strong correlations of CFCs

with other chemicals emitted from anthropogenic activity such as CH_2Cl_2 and HCFC-22 is shown in Figure 3.8 and provides further evidence for continued emissions of many ODSs and CFCs. In the following section, we use correlations of halocarbons with feedstock compounds to investigate the possibility of new, unreported production of CFCs.

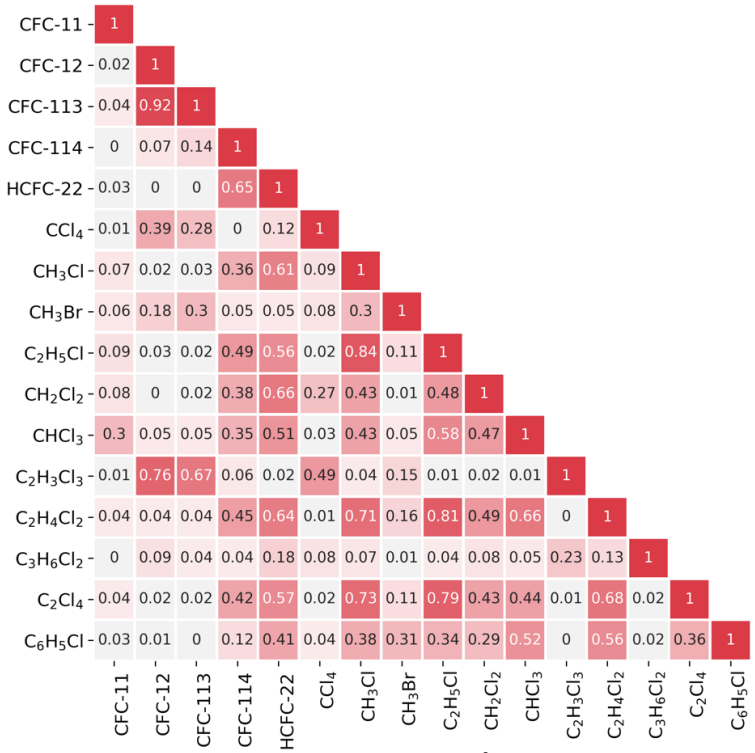

Figure 3.6. Interspecies correlation matrix (r^2) for the 16 halocarbons quantified in all 27 WAS canisters during ARIAs. The strength of the correlation is shown by the color of the box with the value printed inside. Correlations with r^2>0.52 are denoted in white text.

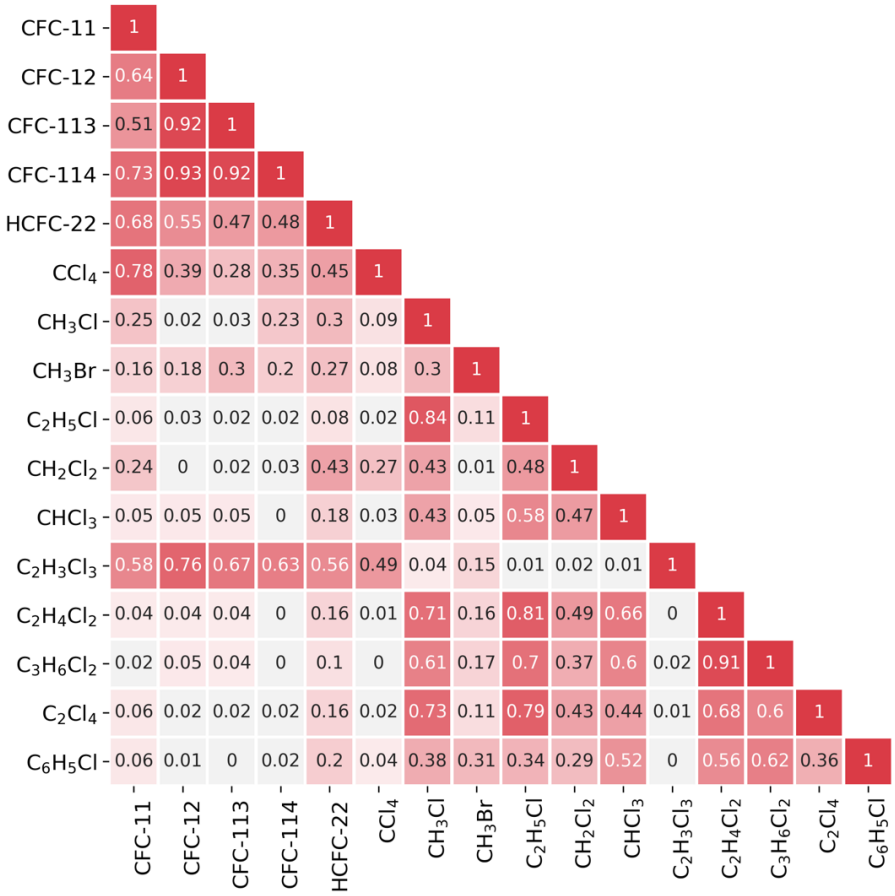

Figure 3.7. Interspecies correlation matrix (r^2) for the 16 halocarbons (N=25-27) quantified during ARIAs. The strength of the correlation is shown by the color of the box with the value printed inside. Correlations with r^2>0.52 are denoted in white text. Outliers for CFC-11, CFC-114, HCFC-22, CH_2Cl_2, and $C_3H_6Cl_2$ were removed.

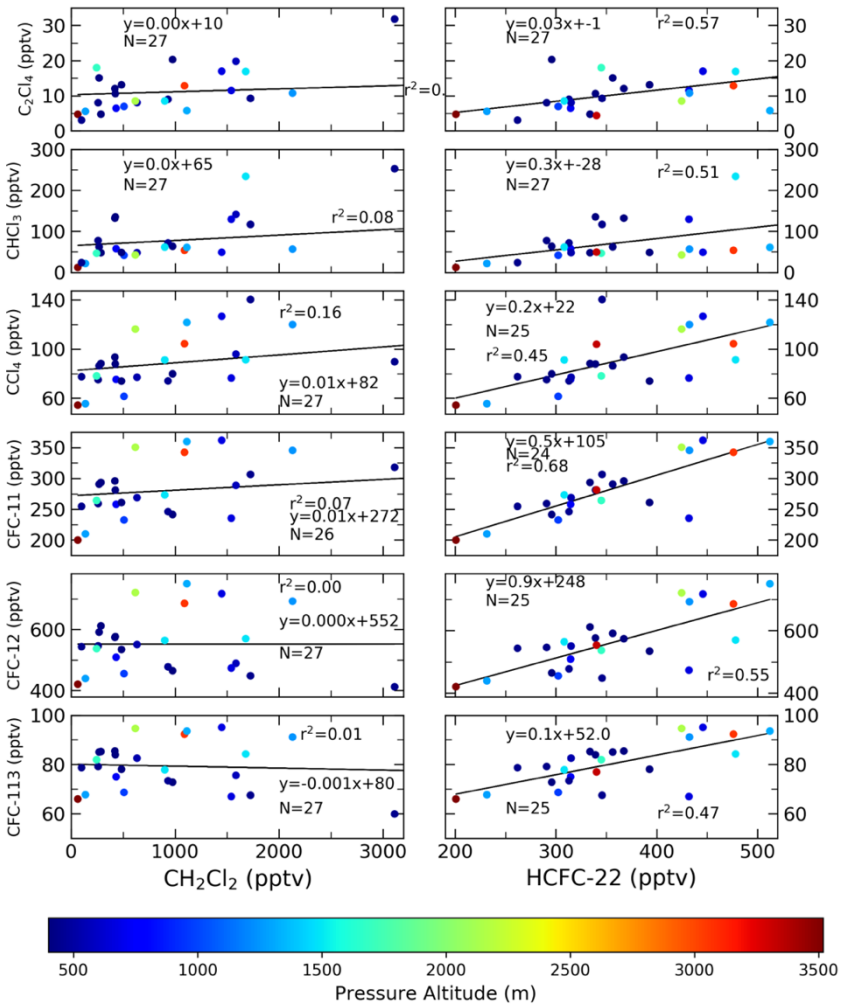

Figure 3.8. Correlations among halocarbons during ARIAs colored by sampling pressure altitude (m). The linear regression slope and Pearson correlation coefficient (r^2) are based upon the number of samples (N) denoted in each subplot. Outliers of halocarbons were excluded as noted in the main text.

If we assume the number of whole air canisters represents the total number of discrete sampled airmasses (degrees of freedom), we estimate a significant correlation (r^2) with 99% confidence to vary between 0.24-0.26 (with variations due to the removal of outliers of CFC-11, CFC-114, CH_2Cl_2, $C_2H_4Cl_2$, and HCFC-22). However, a more rigorous assessment may designate the degrees of freedom is better represented as the number of flights (N=11). In this case, a correlation (r^2) with 99% confidence is 0.54. In the following section, we denote correlations around the more relaxed threshold of

0.24-0.26 (depending on the species) as weak, whereas anything above the more rigorous limit of 0.54 is strong.

Moderate correlations of CH_2Cl_2 with C_2Cl_4 (r^2=0.43) and $CHCl_3$ (r^2=0.47) suggest these halocarbons were emitted from similar sources such as industrial solvent use or experienced a similar loss behavior due to their similar lifetimes. In contrast to a surface study in the PRD from August 2001-December 2002 that found a moderate correlation of CH_2Cl_2 with CCl_4 (r^2=0.45) attributed to solvent use (Guo et al., 2009), the weak positive correlation between CH_2Cl_2 with CCl_4 (r^2=0.27) suggests that enhanced concentrations measured for CCl_4 were not of solvent origin for ARIAs samples.

Chloromethane plants typically produce higher chlorinated methanes, like $CHCl_3$, which is manufactured for use as a feedstock gas for HCFC-22. We find moderate correlations of $CHCl_3$ with CH_3Cl (r^2=0.43) and HCFC-22 (r^2=0.51), suggesting production of HCFC-22 through this pathway. HCFC-22, an urban tracer, also correlates with a number of other markers for vehicle exhaust, such as toluene (r^2=0.63), m/p-xylene (r^2=0.63), octane (r^2=0.80) and isopentane (r^2=0.63), indicating colocation of petrochemical and vehicular emissions or leakage of HCFC-22 from vehicular air conditioning systems. The strong correlation between HCFC-22 and CFC-11 (r^2=0.68) did not have a strong spatial or altitudinal dependence, suggesting widespread release of these compounds across eastern China.

In our study, the weak positive correlation between CH_3Cl and HCFC-22 (r^2=0.30) suggests different anthropogenic sources. Guo et al. (2009) estimated 40% of the CH_3Cl in the greater PRD was of industrial origin and 48% originated from

biomass/biofuel burning. We find weak correlations of CH_3Cl with biomass burning markers like CH_3Br (r^2=0.30) and stronger correlations with CH_2Cl_2 (r^2=0.43), suggesting a minor contribution of biomass burning and a larger proportion of solvent sources to enhanced mixing ratios of CH_3Cl observed during ARIAs.

As discussed earlier, one sample containing 2163 pptv of CFC-11 is likely due to industrial applications such as SPF in the immediate vicinity and no correlation appears with other halocarbons, such as CFC-12 and CFC-113. When this maximum value is excluded, a strong, positive correlation between CFC-11 and CFC-12 appears (r^2=0.64) (Figure 3.9). In this case, the median CFC-11/CFC-12 ratio is 0.49. Moreover, CCl_4, often used as a feedstock for CFC production, correlates moderately with CFCs (r^2~0.30-0.50), except CFC-11. The high correlation between CCl_4 and

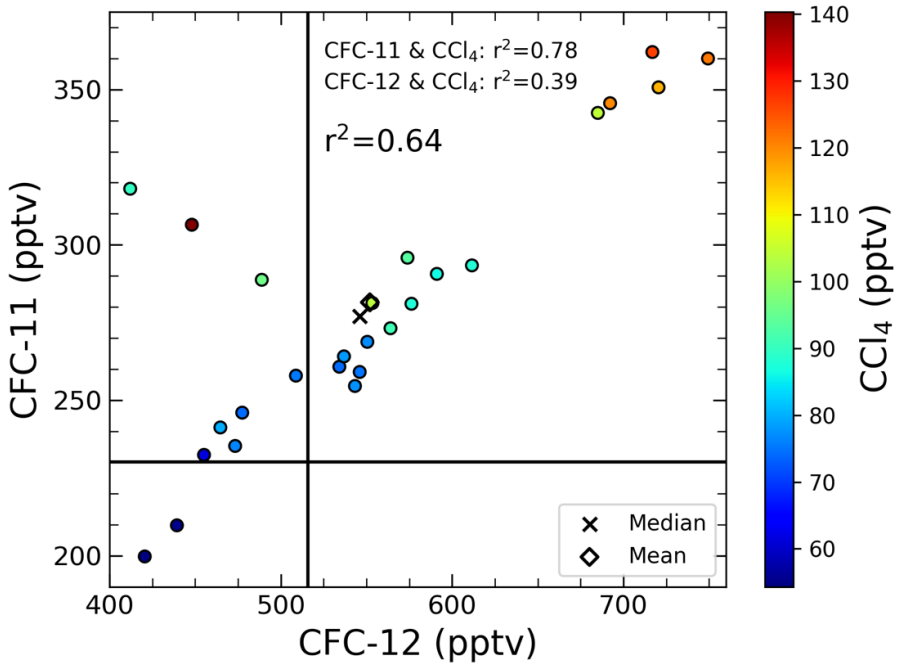

Figure 3.9. Scatter plot of mixing ratios of CFC-11 (pptv) and CFC-12 (pptv) colored by the CCl4 mixing ratio (pptv) excluding the 2163 pptv CFC-11 sample. The horizontal and vertical lines on the plot show the 2016 global abundance values of CFC-11 and CFC-12 from the 2018 WMO Ozone Assessment. The x shows the median values of CFC-11 and CFC-12, while the diamond denotes mean amounts.

CFC-11 (r^2=0.78) suggests widespread release due to the production, rather than consumption of refrigerants throughout ARIAs (Figure 3.10). A few lower values of CFC-12 reduce the correlation with CCl_4 (r^2=0.39, Figure 3.10).

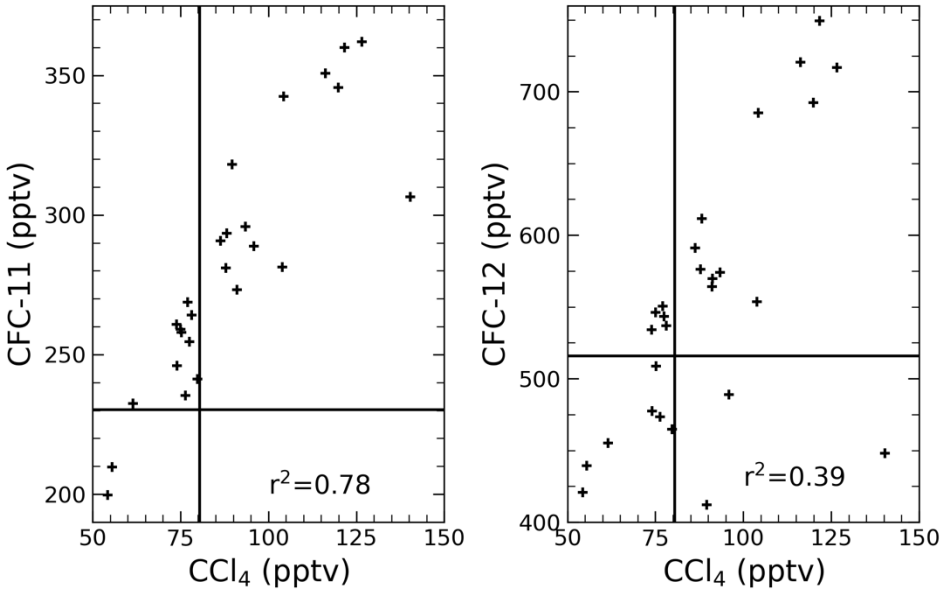

Figure 3.10. Scatter plot of CCl_4 and CFC-11 excluding the 2163 pptv sample and CCl_4 and CFC-12 (all samples). Units are pptv. The horizontal and vertical black lines denote the 2016 global, tropospheric atmospheric abundance from the 2018 WMO Ozone Assessment.

We find no statistically significant correlations of CCl_4 with CH_3Cl and C_2Cl_4, two historical methods for producing CCl_4. Tetrachloroethylene is associated with dry cleaning, textile operations, and metal degreasing activities, as well as used as a feedstock to produce CFC-113 and CFC-114. We find strong correlations between $C_2H_4Cl_2$ and C_2Cl_4 (r^2=0.68), one widely used method for C_2Cl_4 production, as well as between $C_3H_6Cl_2$ (r^2=0.91), an intermediate in the production process. No correlation between C_2Cl_4 is found with CFC-113 or CFC-114. We explore how relationships between ODSs and feedstocks change when considering WAS samples with similar air mass origins in section 3.6.

The very strong correlations between CFC-12, CFC-113, and CFC-114 (r^2>0.92) are indicative of similar sources or use patterns. These three ODSs correlate more strongly with a different feedstock, $C_2H_3Cl_3$ (r^2~0.60-0.80), often used to manufacture HCFC-141b and HCFC-142b, than CCl_4 (r^2~0.30-0.50). In the greater PRD region, where significant enhancements of most halocarbons were found in 2000 (Chan and Chu, 2007), correlations between CFC-12 and CFC-113 were lower, around 0.59 in the early 2000s (Guo et al., 2009) and 0.3-0.70 in 2007 (Zhang et al., 2010b). Similarly, lower correlations between CFCs and $C_2H_3Cl_3$ (r^2 ~0.10-0.50) were observed in Gosan, South Korea from November 2007-December 2008 when flow was from mainland China (Li et al., 2011). The very high correlations of CFC-12, CFC-113, CFC-114, and $C_2H_3Cl_3$ found in our aloft observations combined with large variations in mixing ratios may be suggestive of alternative CFC production pathways or colocation of emission sources.

3.6 Potential Emission Source Regions

To gain insight into the different source regions of ODSs emissions during ARIAs, we first examine interspecies correlations for three typical meteorological clusters during the sampling period (Figure 3.11). The first cluster originated from the northwest near Inner Mongolia (IM), an autonomous region of northern China (Cluster IM, 41% of trajectories, N=289) and passed through parts of Shanxi and Hebei. The second cluster originated in southwest Shanxi (SAX) (Cluster SAX, 20% of trajectories, N=139) and traveled to the northeast before arriving in the ARIAs flight domain. The third cluster emerged from southern Shandong (SD) and passed northwest towards Hebei (Cluster SD, 39% of trajectories, N=274).

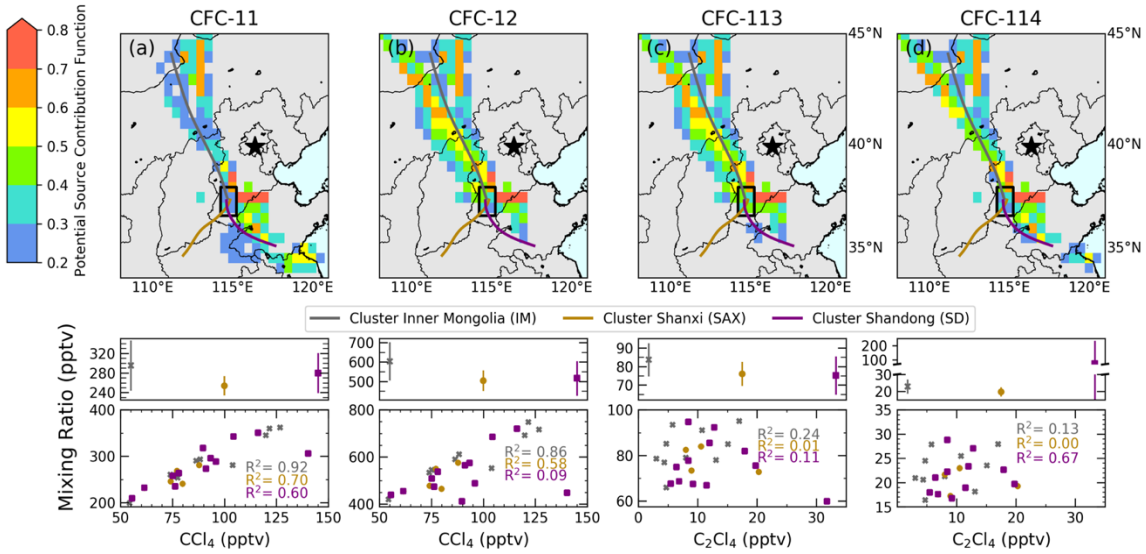

Figure 3.11. Maps showing meteorological clusters (colored lines) and the potential source contribution function (PSCF, colored grid cells) for CFC-11 (a) and CFC-12 (b), CFC-113 (c), and CFC-114 during the ARIAs campaign in Spring 2016. Below each map is the mean and standard deviation mixing ratio (pptv) for each cluster and correlation with feedstock CCl_4 or C_2Cl_4 in the same color as shown on the map. Three meteorological setups dominated during ARIAs: Flow from Inner Mongolia, shown by a grey line on map and grey cross on the bottom mixing ratio plots (N=289), flow from Shanxi Province denoted by the golden line on the map and golden circles on the mixing ratio plots (N=139), and flow from Shandong Province indicated by the purple line on the map and purple squares on the mixing ratio plots (N=274). The black box shows the same latitude and longitude boundaries as the cyan box in Figure 1 and the star denotes the location of Beijing. The color scale indicates the PSCF values. Regions with high PSCF values have large potential source contributions to the receptor site. The 75th percentiles (306, 591, 85, and 25 pptv for CFC-11, CFC-12, CFC-113, and CFC-114 respectively) were used as the criteria values for computing PSCF. An outlier of CFC-114 associated with flow from Shandong is responsible for the large standard deviation. Map data created in MeteoInfo 1.4.7. These results provide no evidence of new manufacturing of CFC-113, but demonstrate new CFC-114 production in Shandong, of CFC-12 in Shandong and Inner Mongolia, and of CFC-11 throughout eastern China including locally in Hebei.

Cluster IM shows the largest mean mixing ratios of CFC-11 (295 ± 49 pptv), CFC-12 (604 ± 94 pptv), CFC-113 (84 ± 9 pptv), and CCl_4 (94 ± 22 pptv). Previous reports have suggested unlicensed factories based in Inner Mongolia have provided chemical facilities in eastern China with CFC-11 (Environmental Investigation Agency, 2018). Our observations of elevated mixing ratios of CFC-11, CFC-12, and the feedstock CCl_4 for the IM cluster along with very strong correlations of these CFCs

with CCl_4 (r^2 = 0.92 and 0.86 for CFC-11 and CFC-12, respectively) suggests production of these ODS through CCl_4 fluorination in Inner Mongolia. No correlation of C_2Cl_4 and CFC-113 or CFC-114 suggests release of CFC-113 and CFC-114 from banks from IM. The strong correlation of CFC-113 and CFC-114 with CCl_4 (r^2=0.77 and r^2=0.76) from Inner Mongolia suggests colocation of CFC-11 and CFC-12 production with release of CFC-113 and CFC-114.

Cluster SAX describes parcels coming from the southwest from Shanxi and is associated with the lowest mean mixing ratios of the ODSs studied (254 ± 18 pptv for CFC-11, 505 ± 49 pptv for CFC-12, 77 ± 9 pptv for CCl_4, and 20 ± 2 pptv for CFC-114). Moderate correlations of CFC-11 and CFC-12 with CCl_4 (r^2=0.70 and 0.58 respectively) suggest release from new production. Similar to Cluster IM, no correlation of either CFC-113 or CFC-114 is found with C_2Cl_4, but strong correlations with CCl_4 (R^2=0.63 and R^2=0.61) suggest colocation of CFCs sources. Additionally, we find a stronger correlation between CFC-11 and HCFC-22 from Cluster IM (r^2=0.85, N=289) and Cluster SAX (r^2=0.77, N=139) than considering all data. These strong correlations may be indicative of additional colocation of CFCs sources.

Cluster SD exhibits the largest mean mixing ratios of CFC-114 (73 ± 157 pptv), driven in part due to one sample containing 543 pptv CFC-114. Strong correlations between CFC-11 with CCl_4 (r^2=0.60) suggest release from new production. Weak correlations of CFC-12 with CCl_4 (r^2=0.09) and CFC-11 (r^2=0.30) suggest no new production of CFC-12 for airmasses in this cluster. The moderate correlation of CFC-114 with C_2Cl_4 (r^2=0.67) and no correlation with CCl_4 suggests new production of CFC-114 that is not collocated with emissions of CCl_4. The lack of correlation of CFC-

113 with C_2Cl_4 and CCl_4, but strong correlations with CFC-12 (r^2=0.92) and $C_2H_3Cl_3$ (r^2=0.86), suggests colocation of emission sources or an alternative CFC production pathway. Mean mixing ratios of CFC-113 from Cluster SD and Cluster SAX are approximately the same (~77 pptv), but this analysis identifies different sources based on origin of the airmass.

Next, we apply another trajectory-based approach called PSCF for further source region identification associated with high concentrations of CFCs. The dominant source regions of CFC-11 (Figure 3.11) include Hebei, Shandong to the southeast, and Inner Mongolia to the northwest. While the clustering technique indicates that air parcels coming from Shanxi influenced the ARIAs campaign, there are no high PSCF values from that location because the WAS canisters associated with those trajectories contained concentrations of CFC-11 lower than the criterion value. Therefore, air parcels with the highest CFC-11 mixing ratios observed during ARIAs came from less developed regions near Inner Mongolia in addition to Hebei and Shandong.

The results of this work expand upon earlier studies locating the origin of CFC-11 emissions. Rigby et al. (2019) used chemical transport model simulations joined with CFC-11 observations in Gosan, South Korea and Hateruma, Japan to identify Shandong and Hebei Provinces as partly responsible for the global rise in CFC-11 emissions. Lin et al. (2019) observed high levels of CFC-11 in Nanjing, China in October 2017 were from less developed regions in southwestern and central China, with a minor fraction emerging from the PRD metropolitan region. Results from our

study extend the potential sources regions of CFC-11 in China to include Inner Mongolia, a region these studies were not sensitive to.

The PSCF spatial distribution of CFC-12 and CFC-113 (Figure 3.12) and CFC-114 (Figure 3.13) is similar to CFC-11, but shows high PSCF values along northern Shanxi Province and less of a contribution from Shandong. Several other ODS show a PSCF spatial distribution similar to CFC-11, such as HCFC-22 and CCl_4 (Figure 3.13).

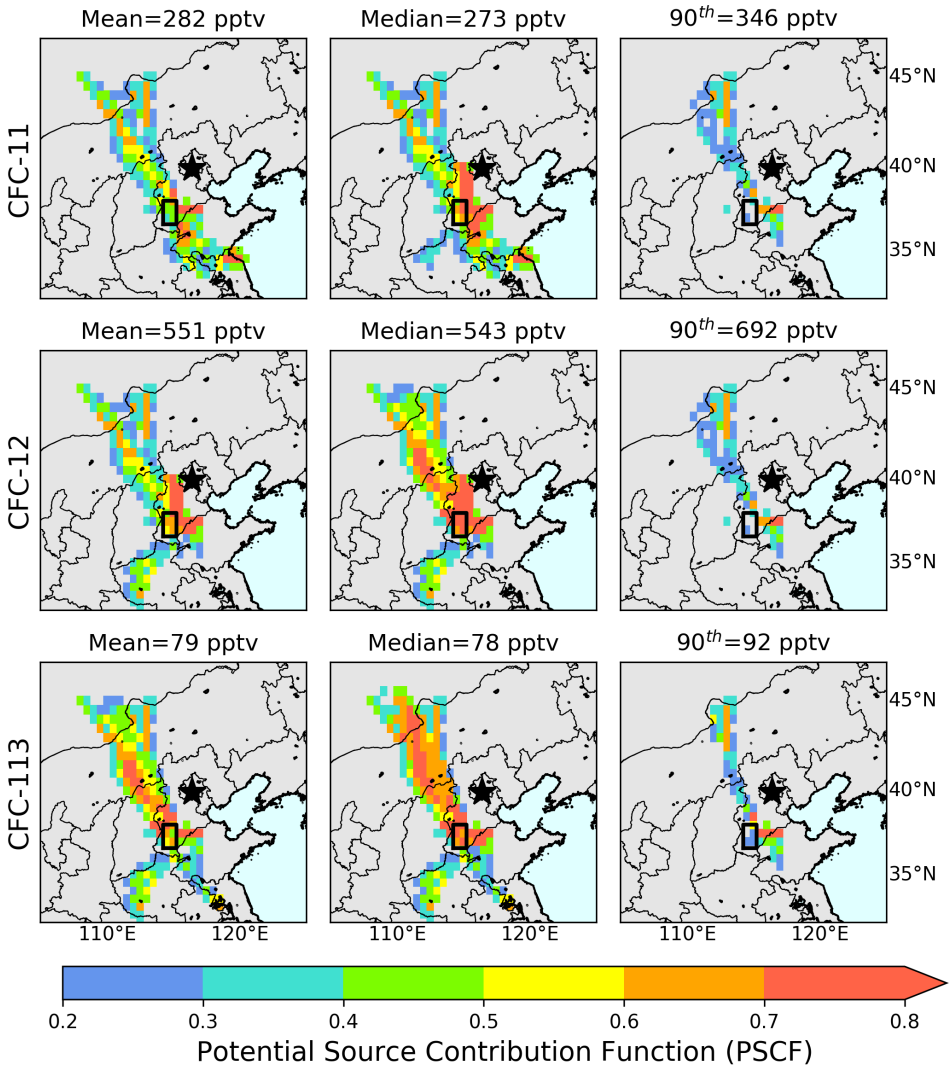

Figure 3.12. Maps showing the effect of different criterion values (mean, median, and 90th percentiles) on the PSCF for CFC-11 (top row), CFC-12 (middle row), and CFC-113 (bottom row). The black box in each panel denotes the ARIAs study location and the star shows the location of Beijing.

All of these ODSs could be coproduced, like CFC-12, or collocated with other petrochemical facilities.

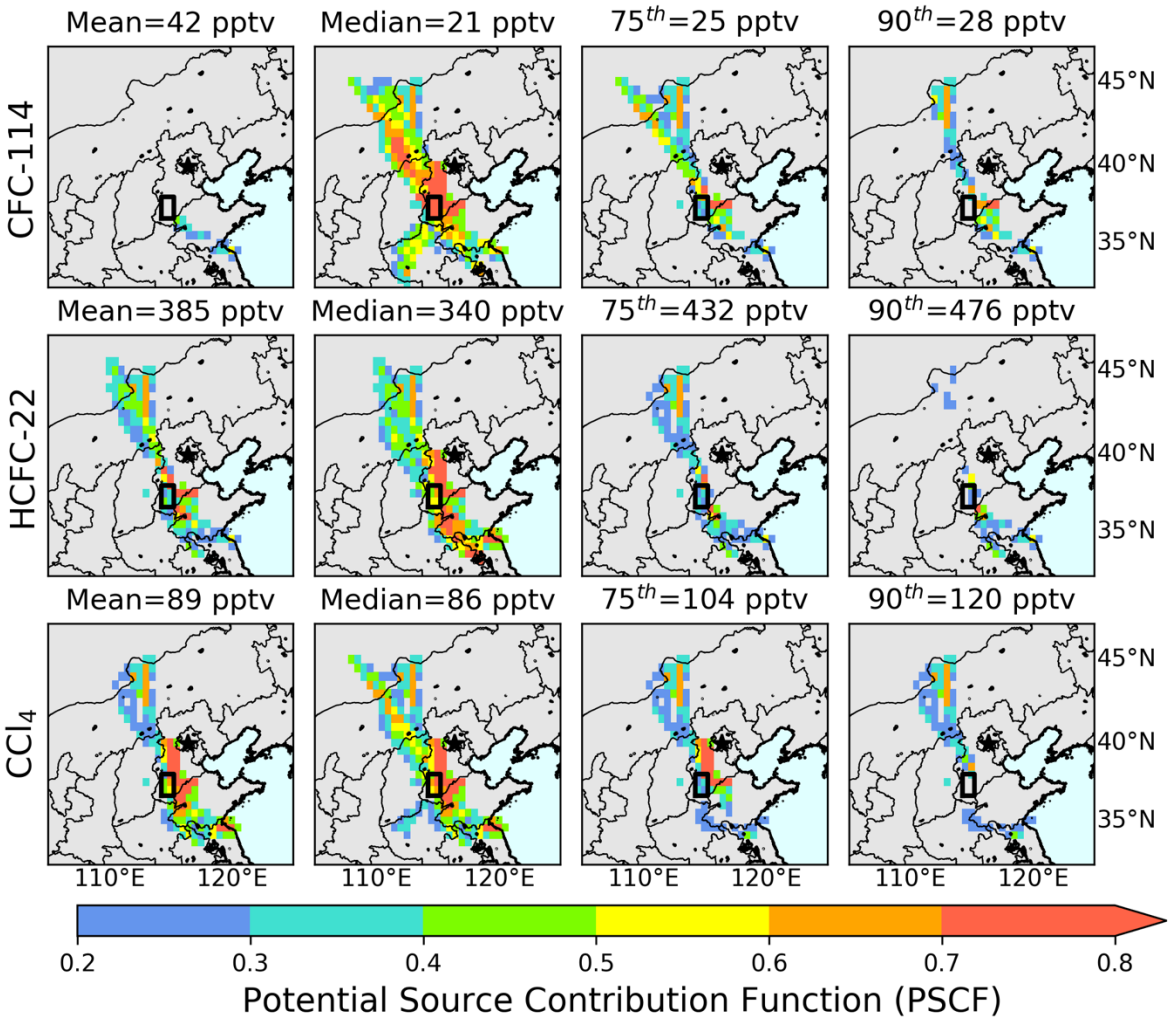

Figure 3.13. Maps showing the effect of different criterion values (mean, median, 75th, and 90th percentiles) on the potential source contribution function (PSCF) for CFC-114 (top row), HCFC-22 (middle row), and CCl_4 (bottom row). The black box in each panel denotes the ARIAs study location and the star shows the location of Beijing.

3.7 Conclusions

In this study, we evaluate mixing ratios of 16 halocarbons collected in 27 whole air samples onboard a research aircraft over Hebei Province, China in May and June 2016. The frequently-measured elevated mixing ratios of CFCs and feedstock

compounds CCl_4 and C_2Cl_4 indicate continued release of these compounds throughout the study region. We find large enhancements for median values of HCFC-22 (47%), CFC-114 (47%), CFC-11 (22%), CFC-113 (10%), and CFC-12 (6%) above 2016 global, tropospheric background levels. We use correlations of CFCs and feedstock compounds to understand potential locations for new production. When correlations of CFCs and feedstocks CCl_4 and C_2Cl_4 are broken up into three typical meteorological conditions, we find evidence for CFC-11 production across eastern China, while new production of CFC-12 only from Inner Mongolia and Shanxi Province. We identify no evidence of manufacture of new CFC-113 during our study, but results indicate new CFC-114 production in Shandong.

The results of this work extend two recent studies evaluating emissions of CFCs. Rigby et al. (2019) identified Shandong and Hebei as the origin of elevated CFC-11 to Gosan, South Korea and Hateruma, Japan, but trajectories did not cover regions north and west of Hebei. They did not conclude that emissions were tied to new production and found no indication of increased CFC-12 emissions. Our flights directly over the source region suggest new manufacture of CFC-11 and we show the spatial distribution of CFCs emissions to include Inner Mongolia. Lickley et al. (2020) concluded banks account for most of the current estimated CFC-11 (excluding the increased emissions after 2012) and CFC-12 emissions, but raised concerns about CFC-113 sources. In contrast, we find emissions of CFC-12 as a result of new production in Inner Mongolia and Shanxi, as well as the likely release of CFC-113 from banks.

The discovery of substantial release and probable new production of CFC-11, CFC-12, and CFC-114 and continued release of CFC-113 from banks may have

implications for the Montreal Protocol and the subsequent recovery of the ozone layer (Dhomse et al., 2019). More detailed research, including measurements of other species (such as HCFC-141b and HCFC-142b), are required to confirm exact locations of CFCs emissions worldwide, including areas that did not influence our study, such as Beijing. Additional airborne measurements over urban regions may help clarify sources of CFCs and pinpoint exact locations of high emissions requiring control. Renewed efforts to control and remove emission sources of CFCs, including banks, around the world could help decrease concentrations of ODSs and speed the recovery of the ozone layer.

Chapter 4 The Effect of Meteorology on Springtime Air Quality and Transport in the North China Plain

4.1 Introduction

Severe air pollution is a major public health concern in heavily populated and industrialized cities in China. Despite national regulations to improve air quality, air pollution levels throughout the NCP still persist above WMO and CAAQS regularly during favorable meteorology (Karplus et al., 2018; Shao et al., 2009). The highest amounts of surface O_3 typically occur under stagnant meteorological conditions that trap local precursor emissions and suppress the influence of distant emission sources (Fiore et al., 2002). The substantial amounts of pollution in China visible by satellite measurements (Li et al., 2017a; Richter et al., 2005) can be transported with the prevailing westerlies over East Asia and affect air quality in downwind regions.

The rapid vertical transport of pollutants from the PBL into the FT allows for dispersal that increases atmospheric lifetimes and range of influence (Cooper et al., 2006; Dickerson et al., 2007). Some pollutants in the PBL, such as NO_2 and SO_2, as well as the aerosols they can form, are removed by dry deposition and thus are short-lived. If lofted into the FT, SO_2 can more rapidly convert to sulfate aerosols, impacting atmospheric radiative balance and cloud properties (Dickerson et al., 2007). While the formation of O_3 is most efficient over metropolitan regions where primary precursors are released (Chen et al., 2013), photochemical production can continue as the plume travels downwind until NO_x concentrations fall to ~10-30 pptv (Crawford et al., 1997).

Air pollution transport from Asia typically peaks in early to mid-spring (Liu et al., 2003), traveling distances from several hundreds of meters up to thousands of

kilometers (Chung, 1985). Utilizing Spring 2001 airborne measurements, Kondo et al. (2004) reports net O_3 production occurs in the marine PBL over the western Pacific due to relatively high NO levels combined with strong westerly advection. The influence of Asian continental outflow has been estimated to raise daytime surface O_3 concentrations by ~10 ppbv at Fukue Island, Japan in Spring 2009 (Kanaya et al., 2016) and degrade air quality as far as the West Coast of North America (Bertschi and Jaffe, 2005; Jaffe et al., 2003; Jaffe and Zhang, 2017; Price et al., 2004). Ground-based March 2005 measurements of $\Delta O_3/\Delta CO$ ratios from eight surface stations in Northeast Asia increased with age of the polluted airmasses during eastward transport events due to en route photochemical production of O_3 (Tanimoto et al., 2008). These studies have concluded emissions from East Asia are an important source region of O_3 precursors from numerous downwind regions in spring.

The dominant pathway promoting the outflow of Asian pollution in early spring is due to lifting of a warm and moist airmass ahead of a cold front (Jacob et al., 2003), termed the warm conveyor belt (WCB) (Cooper et al., 2004; Hess, 2005). The rising tropospheric air in the WCB may subsequently mix with stratospheric air (Pan et al., 2010). Frontal boundaries and dry convection may also facilitate lifting pollution from the PBL into the FT (Bey et al., 2001; Liu et al., 2003; Oshima et al., 2004). Most polluted airmasses are trapped in the PBL over Asia before expulsion behind cold fronts in spring and transported to the NE Pacific (Liang et al., 2004). The processes allowing for pollution displacement can have a significant impact on the vertical structure of trace gases and aerosols, impacting the extent of downwind transport and chemical transformation.

Two field measurement campaigns in East Asia in Spring 2016 were performed to better understand how synoptic conditions affect the vertical distribution and transport of trace gases and aerosols. The U.S. National Science Foundation-sponsored ARIAs joint experiment in partnership with Peking University, Beijing Normal University, and the Hebei provincial weather service collected airborne measurements over Hebei Province in the NCP. Concurrently, the U.S. NASA in cooperation with the Korean National Institute of Environmental Research (NIER) conducted an intensive measurement campaign involving multiple aircraft, ground sites, and ships over the Korean Peninsula and surrounding waters. Significant long range transport of pollution and dust during these field experiments was constrained to a few short events, implying the majority of pollutants sampled during KORUS-AQ originated from local sources (Peterson et al., 2019).

Previous research has focused on characterizing the composition and sources of air pollutants over the NCP (Li et al., 2015a; Quan et al., 2011; Zhao et al., 2013). However, the ARIAs campaign provides the unique opportunity to examine the mesoscale meteorology present over East Asia previously described by Peterson et al. (2019) and the resulting chemical composition observed over the source region. This chapter provides a brief overview of each pollution regime by employing ARIAs airborne and surface measurements in China. The period of persistent high pressure (May 17-22) is chosen as a case study and discussed in more detail since surface and aloft measurements indicate this period coincided with the highest amount of O_3 pollution. Backward trajectories are combined with the Community Multiscale Air Quality (CMAQ) model output to provide insight into local and regional contributions

to surface air quality. Additional perspective of NO_2 from OMI furnishes a discussion of locations that may have contributed to poor air quality during this multi-day exceedance event.

4.2 Methods

4.2.1 Airborne and Surface Measurements

From May 8-June 11, 2016, 11 research flights were conducted over the southern part of Hebei Province (Figure 4.1). The Y-12 research aircraft payload included a suite of meteorological, trace gas, and aerosol optical property instrumentation, previously described in Chapters 1 and 2. The Y-12 aircraft sampled ~300 to ~3500 m pressure altitude over a highly urban region at four spiral locations (Shijiazhuang, Xingtai, Julu, and Quzhou) and also between these megacities in rural Hebei.

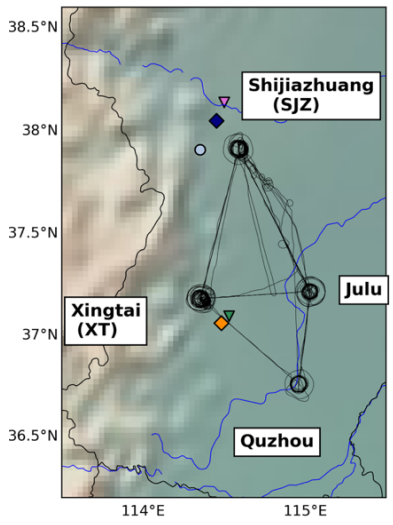

Figure 4.1. Map of ARIAs Y-12 flight tracks (black lines) in southern Hebei Province during May-June 2016. The colored markers denote the locations of five surface sites from the CMEE network that will be discussed in more detail in this chapter. Triangles denote suburban sites, diamonds indicate urban sites, and a circle shows the rural site.

Hourly, ground-based monitoring data for O_3, NO_2, SO_2, $PM_{2.5}$, and CO for May-June 2016 were downloaded from https://quotsoft.net/air/, which archived the data from the China Ministry of Ecology and Environment (CMEE) monitoring network. The automated CMEE network included ~1450 monitoring sites in 2016. This study focuses on five CMEE sites located near two of the most sampled spiral locations during ARIAs, which are considered to be representative of regional source signatures (Figure 4.1). The sites are categorized by urban, suburban, and rural locations by investigating the surroundings on Google Earth. Three sites in the capitol and main economic center of Hebei in Shijiazhuang (SJZ) are used: an urban spot in the main city center, a suburban station north of city center but south of the Hutuo River, and a rural location in Fenglong Mountain, a historical and cultural area, south of the main city. The remaining two sites are located 125 km south of Shijiazhuang in urban and suburban Xingtai (XT), a megacity nestled in the Taihang Mountains with a population over 7 million.

Different measurement techniques and analyzers from various commercial companies are used throughout the CMEE network, so a brief summary is provided here. In most cases, SO_2 was measured by ultraviolet fluorescence (TEI, Model 43i from Thermo Fisher Scientific Inc., USA or EC9850 from Ecotech Pty Ltd., Australia) and O_3 measurements were obtained using UV-spectrophotometry (TEI model 49i from Thermo Fisher Scientific Inc., USA, or EC9810 from Ecotech Pty Ltd., Australia) (Zhao et al., 2016). Measurements of NO_2 were achieved by chemiluminescence (TEI Model 42i from Thermo Fisher Scientific Inc., USA, or EC9841 from Ecotech Pty Ltd., Australia), a technique that suffers from substantial interferences with alkenes (Alam

et al., 2020) and other NO_y compounds. Due to these interferences, chemiluminescence methods actually obtain measurements closer to NO_y than NO_x (Dickerson et al., 2019). Carbon monoxide was measured with non-dispersive infrared absorption and the gas filter correlation infrared absorption methods (API Model 300 from Teledyne Advanced Pollution Instrumentation, USA, or TEI, Model 48i from Thermo Fisher Scientific Inc., USA, or EC9830 from Ecotech Pty Ltd., Australia), while the micro oscillating balance method (TEOM from Rupprecht & Patashnick Co., Inc., USA) and the β absorption method (BAM 1020 from Met One Instrument Inc., USA or Tianhong Co., China or Xianhe Co., China) were used to measure $PM_{2.5}$ and PM_{10}. The data released by CMEE can be used to evaluate the spatial and temporal evolution of air pollution, but are only considered reference values for health advice and cannot be directly used for compliance evaluation of air quality rankings (Zhao et al., 2016).

4.2.2 Community Multiscale Air Quality Model Set-up

The CMAQ model configurations used in this study were coordinated by Dr. Hao He and will be described in more detail by (He et al., in prep). The Community Multiscale Air Quality (CMAQ) model version 5.2 (Environmental Protection Agency, 2017) with the Carbon Bond 6 (CB6r3) gaseous chemistry scheme and the Aero 6 aerosol scheme (Appel et al., 2013) is used to simulate air quality during the ARIAs campaign. The CB6r3 chemical mechanism (Yarwood et al., 2010) includes improved chemistry for organic and peroxyacyl nitrates (PAN) to better simulate SOA and tropospheric O_3 in the United States. Meteorology is simulated using the WRF model version 3.8.1 driven by the European Center for Medium-Range Weather Forecasts (ECMWF) ERA-Interim products (dsb627.0, https://rda.ucar.edu/datasets/dsb627.0)

(Dee et al., 2011). Two nested domains (Figure 4.2) with 35 vertical layers from the surface to 50 hPa (~20 layers in the lowest 2 km) are applied in the simulation, where the inner region (d02 in Figure 4.2) covers Hebei Province and several surrounding provinces with a grid resolution of 12 km. The outer region includes Eastern Asia at a resolution of 36 km. May and June are chosen as the simulation period, with the two weeks in April as spin-up. The default concentration profiles built into CMAQ are used as chemical initial and boundary conditions for the coarse domain and results for the nested domain were derived from the larger domain.

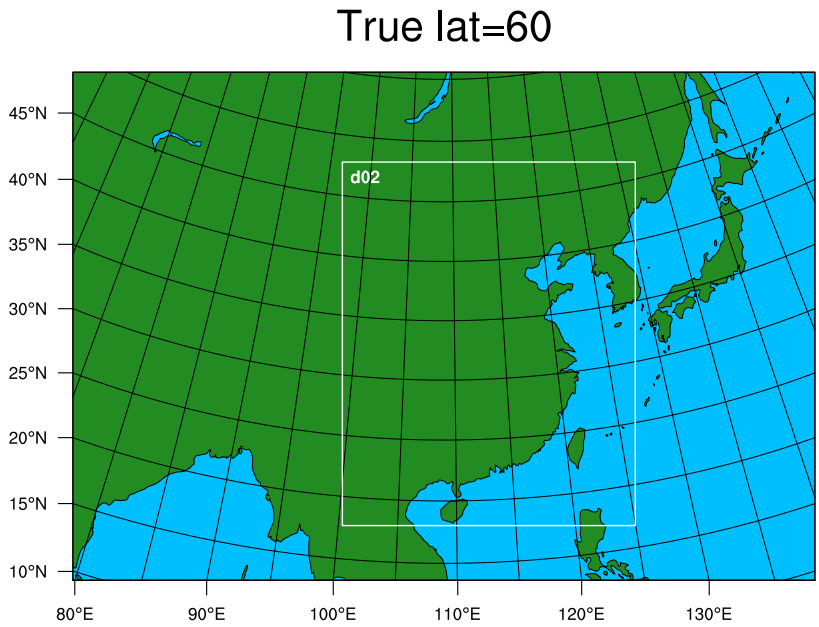

Figure 4.2. Nested 36/12 km domain over East Asia. Courtesy of Dr. Hao He.

Anthropogenic emissions from the Emissions Database for Global Atmospheric Research Version 4.2 (EDGAR v4.2, 0.1°×0.1° resolution) are used for the year 2010, an approach widely used by the chemical transport modeling community (European Commission: Joint Research Centre (JRC), 2011). The EDGAR v4.2 inventory includes emissions from energy, industry, residential, and transport sectors. Following

the approach from He et al. (2012), stack height specification for power plants in the energy sector were placed at 200 m above the surface as an approximation for average stack height and plume rise. The EPA Sparse Matrix Operator Kernel Emissions (SMOKE) modeling system Version 4.5 (The Institute for the Environment-The University of North Carolina at Chapel Hill, 2017) is used to project EDGAR emissions to the modeling domain. The United States Geological Survey (USGS) 24 category land use dataset merged with the inline Biogenic Emission Inventory System (BEIS) version 3 (Environmental Protection Agency, 2017) emission factors table generate the input files necessary for CMAQ inline biogenic emission modeling. The baseline model performance driven by the 2010 EDGAR emissions is compared to aircraft measurements in Table 4.1 and is discussed in more detail below. By comparing to aircraft data, this baseline run captures the basic spatial and temporal variations of O_3 and its precursors, but significantly underestimates their concentrations.

Table 4.1. Statistics of the baseline and adjusted CMAQ performance compared with ARIAs aircraft measurements over the NCP. Courtesy of Dr. Hao He.

	Run	Mean Diff (ppbv)	Slope	STD (ppbv)	Corr. R	NMB (%)	NME (%)	RMSE (ppbv)	Mean Ratio
O_3	Baseline	–21.35	0.56	13.25	0.37	–25.14	25.86	25.10	0.75
	Adjusted	–15.18	0.81	14.83	0.33	–17.87	20.33	21.18	0.82
CO	Baseline	–183.56	0.21	165.92	0.23	–60.26	60.26	246.98	0.40
	Adjusted	–10.445	0.52	175.48	0.21	–34.29	45.03	203.6	0.66
NO_2	Baseline	–1.72	0.31	3.09	0.58	–593.91	64.59	3.52	0.40

	Adjusted	–1.47	0.38	3.01	0.59	–51.23	61.62	3.33	0.49
NO	Baseline	–0.25	0.99	0.47	0.68	–32.23	45.4	0.53	0.68
	Adjusted	–0.16	1.13	0.52	0.67	–20.31	45.46	0.54	0.80

To achieve better model performance, EDGAR emissions over East Asia are adjusted based on ratios of OMI and MOPITT satellite column retrievals. The OMI Level 2 swatch information was used to sample the NO_2 vertical profiles simulated by CMAQ. Next, the CMAQ NO_2 column was calculated using the OMI averaging kernel (AK). The OMI and CMAQ NO_2 column contents were averaged to create daily 0.25º × 0.25º Level 3 products following the method developed by Canty et al. (2015). A similar approach was used to obtain CMAQ HCHO Level 3 products using the OMI HCHO retrievals (see details in Ring et al. (2018)). The tropospheric CO concentrations at ~900 hPa in CMAQ were averaged to 1.0º × 1.0 º daily products using the MOPITT CO AK (MOPITT Science Team, 2013). The daily gridded satellite and CMAQ products were averaged throughout May and June 2016 for comparison.

The difference between OMI and CMAQ columns of NO_2, HCHO, and CO is shown in Figure 4.3 (analysis by He et al. (in prep)). The analysis indicates CMAQ underpredicts the OMI NO_2 column (mean ratio=0.81; e.g., CMAQ predicts 81% of the OMI NO_2 column) in the aircraft campaign region, but in urban regions like Beijing, CMAQ substantially overestimates column NO_2 by up to 30%. The differences

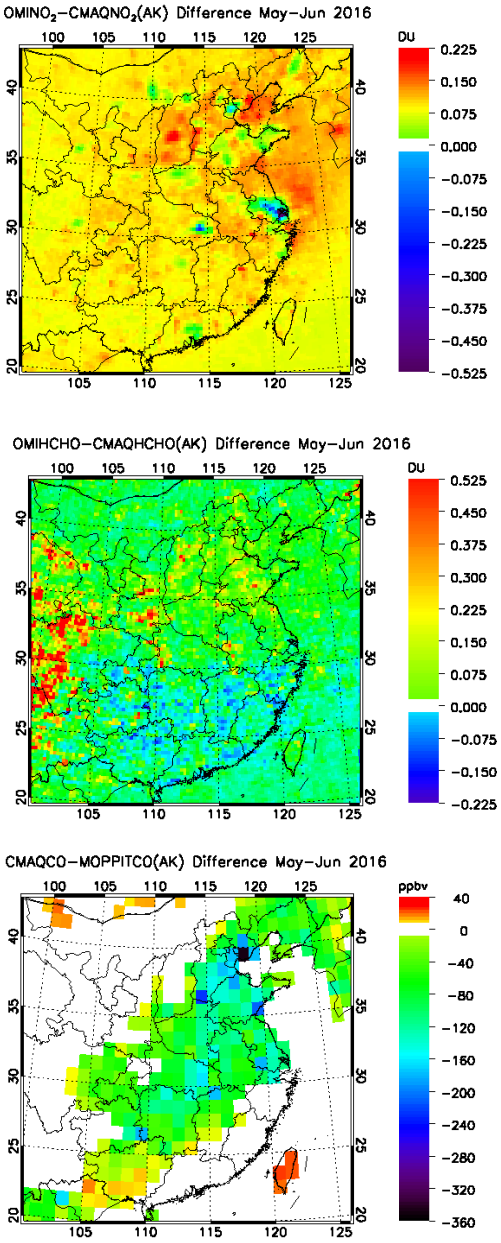

Figure 4.3. Difference between OMI and CMAQ of NO_2 (left, Unit=DU), HCHO (middle, Unit=DU), and CO (right, Unit=ppbv). Figure courtesy of Dr. Hao He.

between measured and modeled NO_2 in these regions represent changes in NO_x emissions due to recent air pollution regulations and is consistent to conclusions from independent studies using OMI products (Krotkov et al., 2016). Similar to NO_2, CMAQ simulates high column contents of HCHO over the NCP in spring and underestimates HCHO in the ARIAs sampling area by <20%. Column HCHO in south China where biogenic VOCs dominate is underestimated in the model compared to OMI. The MOPITT CO retrievals also show high near-surface CO concentrations over eastern China, but only predicts 42% of the CO over the ARIAs aircraft region.

The comparison of satellite measurements with CMAQ output suggests that both NO_x and VOCs emissions during ARIAs need to be adjusted to accurately simulate tropospheric O_3. The model/satellite ratios of NO_x, HCHO, and CO in East Asia are used to adjust the anthropogenic 2010 EDGAR emissions simulation (referred to as the "baseline" simulation in Table 4.1). The "adjusted" run using the model/satellite ratios moderately improves simulations of O_3, with the root mean square error (RSME) decreasing from 25.10 ppbv in the baseline case to 21.18 ppbv in the modified simulation. The O_3 mean ratio of CMAQ simulations to aircraft observations increases from 0.75 in the baseline case to 0.82 in the adjusted simulation. The model performance of CO also improves, with the RMSE decreasing from 246.98 ppbv to 203.60 ppbv and the mean ratio increasing from 0.40 to 0.66 from the baseline to the adjusted simulation. The satellite adjustment has a small impact on nitrogen compounds of NO_2, NO, and NO_y, possibly due to VOC-sensitive chemistry over the NCP.

4.2.3 Lagrangian particle trajectory model

The Lagrangian particle dispersion model, HYSPLIT version 4.0 (Stein et al., 2015), is employed to evaluate the spatiotemporal patterns of airmass transport. Meteorology from the WRF model version 3.8.1 with a 36 km domain is used in the back-trajectory calculations, the same meteorology used to drive CMAQ. Seventy-two hour back trajectories arriving at 500 m AGL are computed for every hour throughout May 2016 for the five selected CMEE surface stations in Section 4.2.1. Points along the trajectory path are removed from this analysis if WRF indicates any amount of precipitation. Trajectories are split into a morning (0:00-3:00 UTC) and afternoon (7:00-10:00 UTC) analysis each day to study the diurnal changes of transport.

4.2.4 OMI Tropospheric Column NO_2

OMI Level 3, Version 3 NO_2 (OMNO2d, available: https://disc.gsfc.nasa.gov/datasets/OMNO2d_003/summary) data is used to identify tropospheric pollution plumes during ARIAs. Onboard the NASA Aura satellite and operational since 2005, OMI is a UV/visible solar backscatter spectrometer in a polar sun-synchronous orbit with a local equator crossing time of 13:45 in the ascending node (Lamsal et al., 2010; Levelt et al., 2006). The total column amount of NO_2 is measured in a 2600 km swath divided into 60 unequal area pixels, with a nadir pixel size of 13 km × 24 km. OMI achieves daily global coverage over 14-15 orbits.

The OMI measures the radiance reaching the instrument's detector. OMI measurements include a spectral region of 264-504 nm with a spectral resolution between 0.42 and 0.63 nm that is used to provide products for a number of trace gases. The NO_2 retrieval uses the modified Differential Optical Absorption Spectroscopy

(DOAS) spectral analysis to derive the NO_2 slant column densities (SCD) (Krotkov et al., 2016). After subtracting the stratospheric contribution, the SCDs are converted to tropospheric vertical column densities (VCD) by applying an air mass factor (AMF). The AMFs are derived from optical atmospheric and surface properties and calculated with a priori NO_2 monthly mean vertical profile shapes from the Global Modeling Initiative (GMI) model (Bucsela et al., 2013). A partial blockage in the detector's field of view has limited the number of valid measurements by blocking consistent rows (called the row anomaly) since June 2007 (see http://projects.knmi.nl/omi/research/product/rowanomaly-background.php). The Level 3 NO_2 data are provided for near clear sky conditions (NO_2 retrievals where cloud radiance fraction is less than 30%).

4.3 Overview of General Meteorology and Observed Pollution

During late Spring 2016, the position and intensity of the polar jet stream was highly variable over the Asian continent, affecting the transport of dust, wildfire smoke, and pollution (Peterson et al., 2019). While most of the precipitation falls during the summer months in the NCP, several frontal systems bringing rainfall traversed the study domain during ARIAs. The prevailing meteorology during ARIAs was predominantly high-pressure conditions, bringing weak surface winds and suppressed vertical mixing. These synoptic features resulted in several pollution regimes at the surface and aloft during ARIAs. Maximum daily eight-hour average O_3 (MDA8) concentrations at the five selected CMEE sites (Figure 4.4) indicate many days above the 75 ppbv CAAQS during ARIAs. Surface and airborne observations (Figure 4.5) also point to a wide distribution of pollutant concentrations that depended upon meteorological conditions. Next, we discuss surface and aloft pollution signatures observed over the Chinese source region and place these in the context of the four

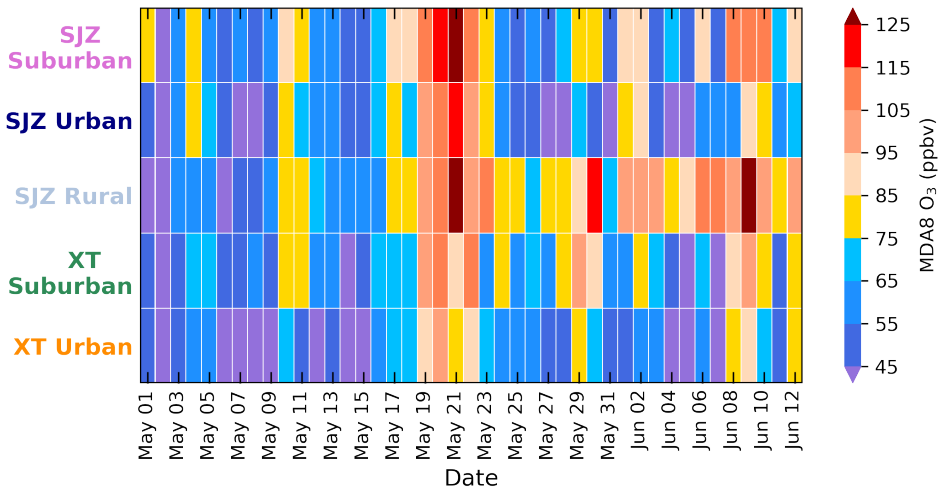

Figure 4.4. Timeseries of maximum daily eight-hour average (MDA8) O_3 mixing ratios in ppbv at the five selected CMEE sites throughout the ARIAs campaign. The marker colors on Figure 27 correspond to the text label colors shown here.

synoptic set-ups classified by Peterson et al. (2019), that affected East Asia in Spring 2016.

4.3.1 Dynamic Meteorology (May 1-16, 3 RFs)

A relatively strong polar jet stream was frequently positioned north of the study region, along the border between China and Mongolia during early May 2016 (Peterson et al., 2019). The strength and position of the polar jet stream combined with flow over the Taihang Mountains allowed for upper-level disturbances to induce vertical motion in a region known for low-level cyclogenesis during spring (Chen et al., 1991). Several

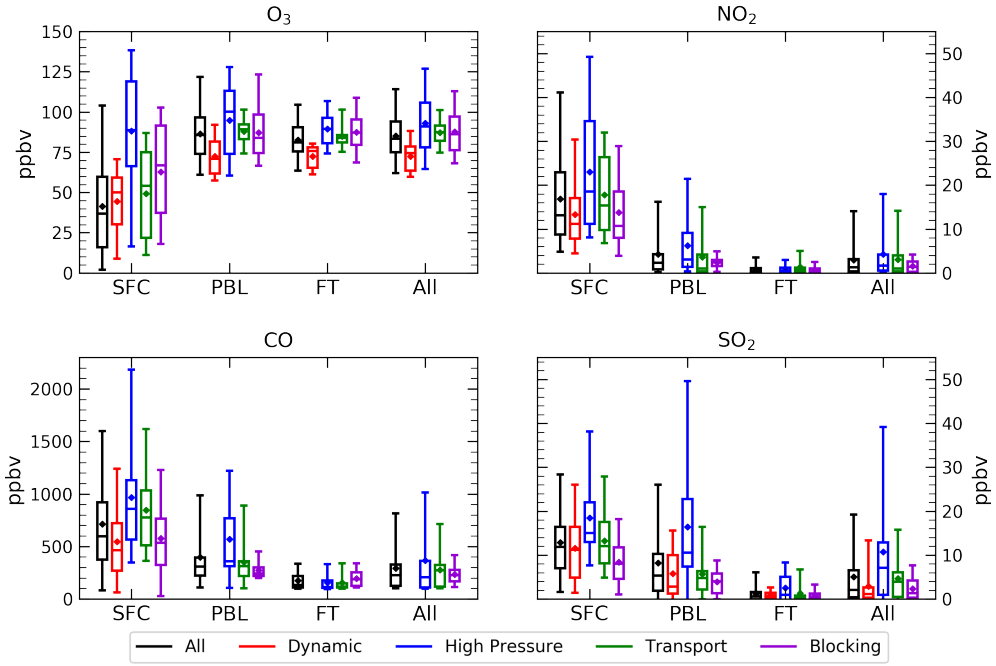

Figure 4.5. Distributions of O_3, NO_2, CO, and SO_2 from surface and airborne measurements during ARIAs. The five CMEE surface site hourly distribution (SFC) only includes days a research flight occurred and the general time period of flights (8:00-19:00 LST). One-second Y-12 measurements are separated into planetary boundary layer (PBL), free troposphere (FT), and all Y-12 observations (All) based on water vapor and potential temperature profiles for each flight. The different colors denote the prevailing synoptic conditions that affected ARIAs observations, with all observations from ARIAs shown in black. No measurements of NO_2 and CO are available for the first several ARIAs flights due to power constraints and a converter issue. The whiskers extend to the 5th and 95th percentiles and the box denotes the 25th and 75th percentiles. The horizontal line is the median and the diamond shows the mean.

mid-latitude cyclones developed over this region and brought frontal boundaries to the NCP from the west, resulting in rapid cycles between cloudy and clear conditions. The ARIAs observations were influenced by the frequent switch of meteorological conditions. Cooler temperatures during early May 2016 compared to the rest of the ARIAs period may have impacted release of BVOCs (Pusede et al., 2014) and anthropogenic VOCs from tailpipe (George et al., 2015) and evaporative emissions (Rubin et al., 2006). Mean Y-12 mixing ratios of O_3 and SO_2 during this period were ~10 and ~7 ppbv lower, respectively, than the ARIAs campaign mean of 11 RFs in May and June 2016 (Figure 4.5). The dynamic meteorology period was the longest synoptic setup condition during ARIAs, but the five proximate CMEE sites infrequently (only 2-3 days) observed MDA8 O_3 above the CAAQS of 75 ppbv (Figure 4.4). In fact, for several days the MDA8 O_3 concentrations were below 40 ppbv at the urban sites.

4.3.2 Persistent High Pressure (May 17-22, 3 RFs)

Stagnant conditions during this period resulted in weak synoptic flow, reduced winds speeds, and increased surface temperatures that enhanced the production of O_3 and led to numerous violations of the CAAQS. Stagnant high pressure systems typically allow for little lofting of pollutants above the boundary layer, instead trapping pollutants near the surface, where these compounds undergo photolysis and other chemical reactions (Dickerson et al., 2007). On May 17 and 18, half the CMEE sites, including both sites in XT, measured below but close to the MDA8 O_3 standard (Figure 4.4). Throughout the rest of the high pressure episode, MDA8 O_3 values from these sites were 25-55 ppbv higher than the CAAQS standard. Elevated concentrations of O_3,

NO_2, CO, and SO_2 persisted throughout and above the PBL during this period (Figure 4.5). The persistent high pressure episode will be discussed in more detail as a case study in Section 4.4.

4.3.3 Transport (May 25-31, 2 RFs)

During this time period, the weaker polar jet stream over central Asia and progression of the low-level monsoon boundary to the north resulted in relatively weaker and sluggish frontal passages (Peterson et al., 2019). Reduced vertical motion favored low-level westerly transport from East Asia across the Yellow Sea to Korea, which experienced the unhealthiest surface air quality during this period (Peterson et al., 2019). The intensified polar jet stream over the Pacific Ocean at the end of ARIAs (May 25-June 10) is associated with the temperature gradient induced by the northward migration of the East Asian Monsoon (Sampe and Xie, 2010). In China, the low-level boundary between warm and moist monsoonal air and cooler and drier mid-latitude air is referred to as “Meiyu”. The strengthening of the springtime southwesterly wind, upward tropospheric motion, and convergence of low-level water vapor over south east China results in the beginning of the local rainy season and gradually marches farther north throughout the springtime (Zhao et al., 2007). The monsoon boundary is identified by a quasi-stationary band of convective clouds and thunderstorms, usually reaching the NCP by late spring.

A morning and afternoon flight on May 28 documented source region characteristics before eastward travel. In the morning (3:02-3:30 UTC, 11:02-11:30 LST), a temperature inversion was observed over XT (Figure 4.6), with high RH and aerosol scattering in the lowest 1500 m. Mixing ratios of O_3 below 1500 m ranged from 70-90 ppbv and above 1500 m were ~90 ppbv. By the afternoon spiral (9:15-9:42 UTC), the temperature inversion ~1000 m sustained hazardous pollution levels of O_3 (95-100 ppbv) near the surface. Surface MDA8 O_3 concentrations at the five CMEE sites during this period showed several exceedances but were not the highest

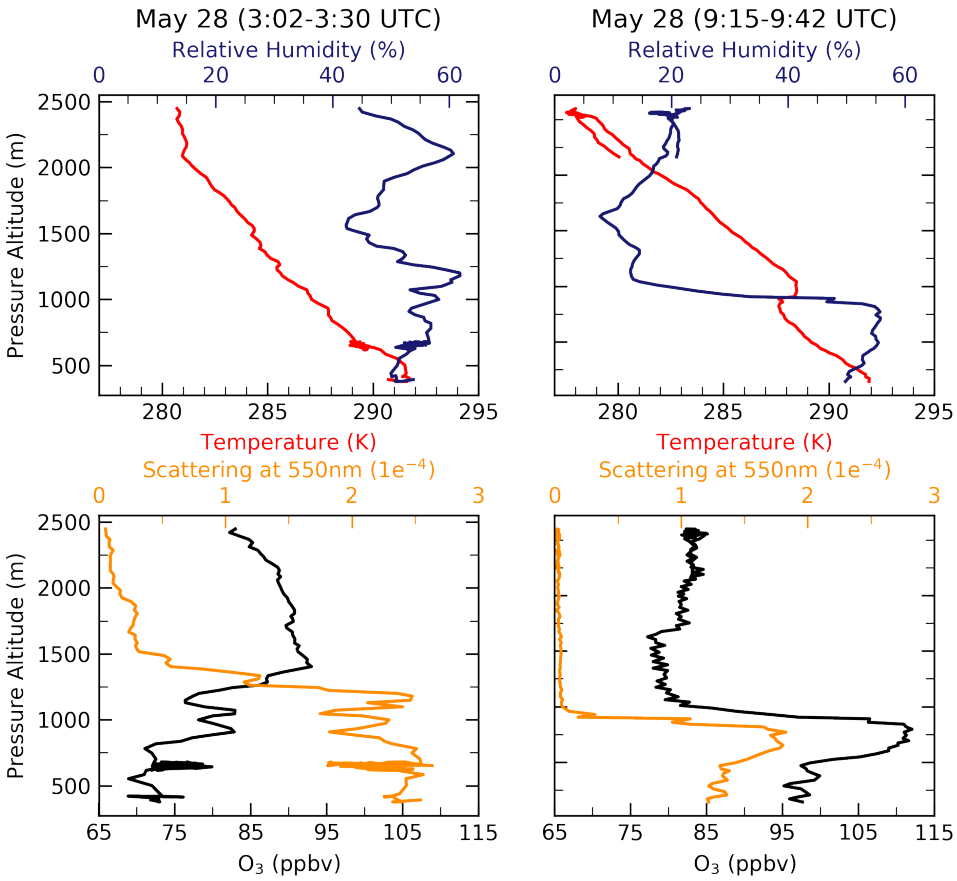

Figure 4.6. Vertical profiles during morning and afternoon spirals over Xingtai. Temperature (red) and relative humidity (blue) are shown on top and ozone mixing ratios (black) and aerosol scattering at 550 nm (orange) are plotted on the bottom. The morning spiral is shown on the left and the afternoon spiral is shown on the right.

concentrations observed in May (Figure 4.4). The high aerosol scattering during the morning flight may have sufficiently reduced the UV radiation flux, resulting in a decrease in the O_3 production efficiency (Wang et al., 2014b). Measurements from the Y-12 indicate large variations of mixing ratios of CO, NO_2, and SO_2 in the PBL, likely due to sampling of local pollution sources (Figure 4.5).

While infrequent, this period had numerous impacts on Spring 2016 South Korean air quality previously quantified. Using GEOS-Chem, Choi et al. (2019) estimated Chinese source contributions accounted for almost 68% of surface $PM_{2.5}$ concentrations in South Korea. From flights over the Yellow Sea during Asian continental outflow, Tang et al. (2019) estimated 29-51% of CAM-Chem tagged CO simulations originated from middle East Asia, which included Hebei Province. High aloft levels of $ClNO_2$ in the morning were attributed from vertical or horizontal transport of air masses from the west (Jeong et al., 2019) and enhanced NO_3^- and SO_4^{2-} concentrations during biomass burning periods were associated with the regional transport of air masses from polluted regions of eastern China (Park et al., 2018).

4.3.4 Blocking (June 1-11, 3 RFs)

At the end of the ARIAs measurement period, a high-pressure ridge over central Mongolia north of a low-pressure area in central China, characteristic of a Rex Block, influenced East Asia. Rex Blocks bring dry conditions near the high pressure system and stormy conditions around the low pressure system, remaining stationary until either pressure system changes intensity. This period hindered any significant changes in meteorology for over a week, resulting in stagnant conditions and minimal pollution transport. Surface observations of MDA8 O_3 indicate a large range of values both below

and above the CAAQS levels (Figure 4.4), driven by increased cloud cover towards the end of this period (Peterson et al., 2019). The stagnant conditions allowed for elevated SO_2 and NO_2 in the FT (Figure 4.5).

4.4 Case Study: Persistent High Pressure Episode

4.4.1 Synoptic Set-Up and Measurements

Stagnant conditions developed on May 17 in the wake of the final frontal system (Peterson et al., 2019). Figure 4.7 shows 850 hPa maps and wind speeds from the NCEP Climate Forecast System version 2 (CFSv2, available at: https://rda.ucar.edu/datasets/ds094.0/) (Saha et al., 2014) from May 15-May 22 at 00Z (approximately 08:00 LST). On May 15, an upper-level trough positioned itself over eastern mainland China, producing strong northerly winds in the region. A strong low-level jet was present over the Yellow Sea and North Korea, which has been found to be a dominant player in the export of pollutants from urban areas with light synoptic wind (Chen et al., 2018). By May 16, the NCP was behind the trough and weak northwesterly winds prevailed, allowing the accumulation of pollutants. The anticyclone formed over the region on May 17 and persisted for several days, slowly moving eastward. The anticyclonic system brought large-scale subsidence, allowing for weak upper-level wind speeds and increased surface temperatures favoring the

formation of O_3. The system was disrupted by May 22 when a series of weak cold fronts traversed the study region.

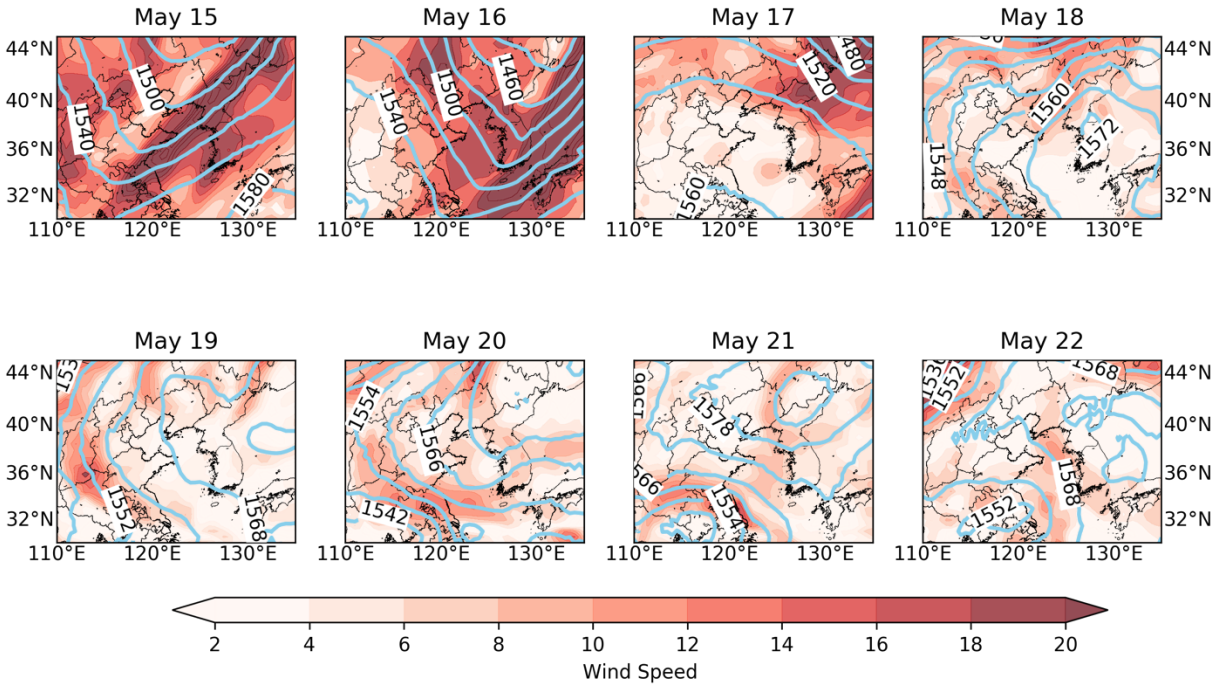

Figure 4.7. Maps of 850 hPa heights (blue contours) and 850 hPa wind speeds (m/s, colored) from 00Z (approximately 08:00 LST) May 15-May 22, 2016 from the NCEP CFSv2 reanalysis.

Vertical profiles from May 17 (RF4), May 19 (RF5), and May 21 (RF6) can provide insight into the evolution of the concentration of pollutants in the PBL and FT throughout the persistent high pressure episode. Figure 4.8 shows vertical profiles of potential temperature (theta), relative humidity (RH), O_3, NO_2, the aerosol scattering coefficient (b_{sp}) at 550 nm, and CO in 250 m bins from the three flights during this period. Since the RFs sampled at different times each day, these profiles are also influenced by diurnal cycles of chemistry and emissions.

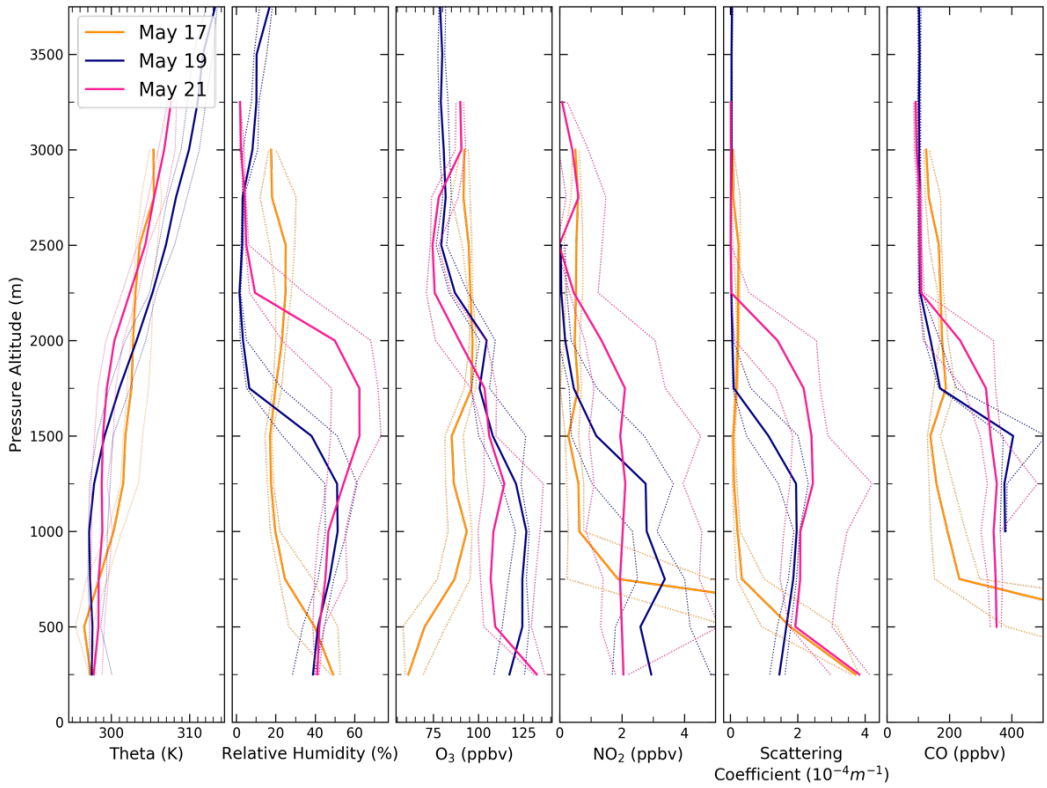

Figure 4.8. Vertical profiles of 1-second potential temperature (theta), relative humidity (RH), O_3 mixing ratio, NO_2 mixing ratio up to 5 ppbv, the scattering coefficient at 550 nm, and the CO mixing ratio up to 450 ppbv from three flights during the high pressure episode during ARIAs. The dashed lines indicate the 10^{th} and 90^{th} percentiles, while the solid line represents the median. High amounts of NO_2 ~23 ppbv and CO ~968 ppbv measured during the morning flight on May 17 indicate local emissions and not shown here to demonstrate differences in the aloft profiles among the three flights.

The morning flight on May 17 (1:21-3:13 UTC or 9:21-11:13 LST) observed relatively unstable and dry conditions (RH <50%) with high amounts of NO_2 (median=20 ppbv), b_{sp} (median=4×10^{-4} m^{-1}), and CO (median=968 ppbv) in the lowest 500 m. The O_3 concentrations recorded a minimum near the surface of ~60 ppbv and increasing concentrations up to ~100 ppbv at 1000 m, with high levels measured throughout the FT. Contrary to the O_3 vertical profile, b_{sp} peaked near the surface and decreased aloft.

Two days later during May 19 (7:42-9:09 UTC or 15:42-15:54 LST), the PBL became slightly more moist and median levels of O_3, NO_2, CO, and b_{sp} were elevated throughout the boundary layer. Due to air traffic control restrictions, the Y-12 aircraft solely flew spirals over Shijiazhuang, providing temporal and altitudinal evolution observations of O_3 over one of the most polluted cities in China. Ozone concentrations in the FT were lower than measurements from May 17, but even above 3000 m, the median mixing ratios were ~80 ppbv.

Profiles from May 21 (3:57-6:41 UTC or 11:57-14:41 LST) measured increasing RH near the surface (~40%) to ~2000 m (~60%). Median O_3 concentrations and scattering near the surface were slightly larger than the earlier RFs, whereas median NO_2 levels (~2 ppbv) were the lowest observed during this episode. High median NO_2, CO, and b_{sp} levels were observed below 1500 m mimicked the RH profile. Above 2500 m, median concentrations of O_3 and NO_2 and scattering were comparable to the earlier RFs. Analysis of atmospheric composition from May 17 to 22 indicates sufficient concentrations of NO_2 and CO throughout the profiles to produce O_3 during this episode.

Since CO is a tracer for long range transport of pollution due to its long lifetime and also a precursor of O_3, correlations between O_3 and CO are useful indicators for O_3 production efficiency and export. The correlation between O_3 and CO on May 17 is moderately negative ($R = -0.62$, all 10-second average data). Previous studies have attributed negative correlations to stratospheric influence (Parrish et al., 1998b), chemical production of CO (Mao and Talbot, 2004), or photochemical O_3 destruction (Real et al., 2008). Conversely, correlations between O_3 and CO on May 19 and 21 are

strongly positive (R=0.88 and 0.91, respectively, both 10-second average data), demonstrative of photochemical O_3 production (Tsutsumi and Matsueda, 2000).

Next, we use the $\Delta O_3/\Delta CO$ ratio to diagnostically evaluate photochemical production of O_3 in pollution episodes. The relative enhancement of O_3 to CO (the $\Delta O_3/\Delta CO$ ratio, unitless) and the relative humidity profile for the three RFs during the high pressure episode are shown in Figure 4.9. The Δ values represent the difference from the mean ARIAs Y-12 concentration for each flight between 2500 and 3500 m for May 17 (CO=139.9 ppbv, O_3=91.5 ppbv) and between 3000 and 3500 m for May 19 (CO=103.3 ppbv, O_3=80.8 ppbv) and May 21 (CO=91.6 ppbv, O_3=89.5 ppbv). Throughout the PBL, the $\Delta O_3/\Delta CO$ ratio is approximately between –0.1 and +0.1 during the three flights. Lower $\Delta O_3/\Delta CO$ ratios (<0.10) are characteristic of mineral dust or transport in the boundary layer, whereas ratios between 0.2-0.5 are distinctive of transport of industrial and/or biomass burning (Price et al., 2004). The lower ratios

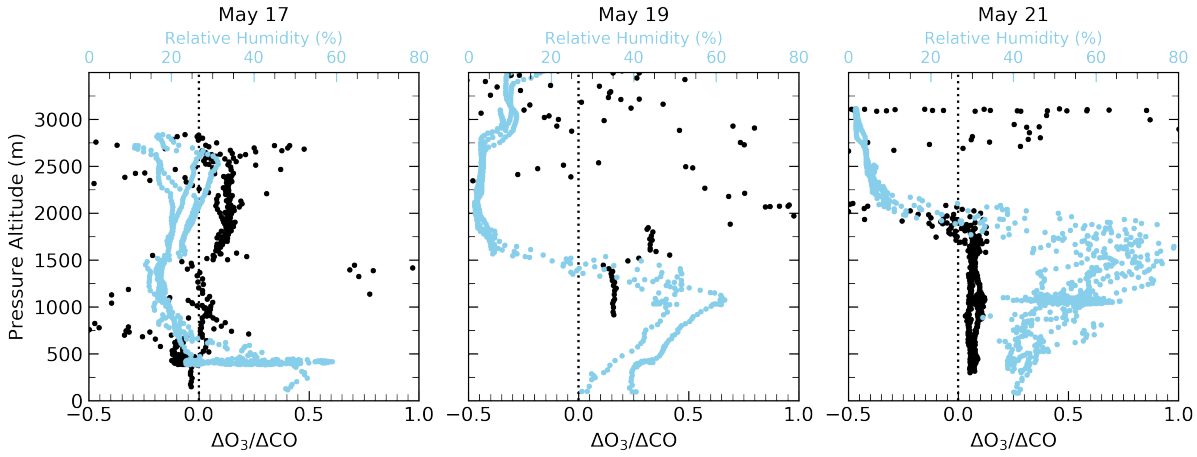

Figure 4.9. Vertical profiles of 10-second average $\Delta O_3/\Delta CO$ (black) between –0.5 and 1.0 and relative humidity (blue) for RFs on May 17 (left), May 19 (middle), and May 21 (right). The dotted black line shows where $\Delta O_3/\Delta CO$ is 0.

observed during ARIAs in the PBL likely resulted from the shorter lifetime of O_3 at lower altitudes.

Once above the PBL, the $\Delta O_3/\Delta CO$ ratio shows a large variation between positive and negative values. Observations from the Photochemical Ozone Budget of the Northeast Pacific (PHOBEA) experiments and other airborne observations in the North Pacific from 1997-2002 found a smaller range of $\Delta O_3/\Delta CO$ ratios of –0.06 to 1.52 (Price et al., 2004), although these studies collected measurements far from source regions. The large variation of the $\Delta O_3/\Delta CO$ ratios above the PBL during these flights are likely a result of local emissions combined with transport of polluted air masses. Ratios greater than 0.5 in the FT have been attributed to mixing of long range transport plumes with O_3-rich upper tropospheric air (Price et al., 2004). The $\Delta O_3/\Delta CO$ ratios in the FT on May 19 and 21 show substantial variation. Combined with low RH on May 19 and 21 (<10%) and concurrent mixing ratios of CO ~100 ppbv, these $\Delta O_3/\Delta CO$ ratios may be indicative of stratospheric influence.

To further examine the role of stratospheric influence during the high pressure episode, water vapor imagery from the Japan Meteorological Agency's Himawari-8 geostationary satellite is presented. Himawari-8 is equipped with a visible infrared radiometer with 16 bands called the Advanced Himawari Imager (AHI), which collects high temporal (2.5 minutes over Japan and 10 minutes over full viewing domain which covers East Asia) and spatial (0.5-2 km) resolution observations (Bessho et al., 2016). Three water vapor bands (#8-10 at 6.2, 6.9, and 7.3 μm) are sensitive to middle-to-upper tropospheric humidity. Water vapor imagery from the three bands was

downloaded from the University of Wisconsin—Madison's Space Science and Engineering Center (SSEC) MCFETCH portal (https://mcfetch.ssec.wisc.edu/).

Figure 4.10 shows water vapor imagery from Band 9 (Bands 8 and 10 showed comparable features) over East Asia on May 17, 19, and 21 at times when the Y-12 aircraft sampling altitudes were ~ 3 km. On May 17 at 2:30 UTC, the satellite imagery shows a dark grey color (indicating less water vapor or drier conditions) over the ARIAs flight domain. To the west of the flight domain, the imagery shows encroaching whiter colors (denoting more water vapor). By May 19 at 8:00 UTC, the majority of the NCP was influenced by moist conditions throughout the upper troposphere (not shown). This water vapor imagery suggests that the May 19 flight was not largely influenced by the stratosphere. Alternatively, the May 21 RF at 4:30 UTC shows a large region protruding south of drier conditions, also visible at Bands 8 and 10 (not shown). These drier conditions on May 21 combined with large $\Delta O_3/\Delta CO$ ratios suggests a possible contribution of O_3-rich, dry stratospheric air. Overall, these results largely suggest continuing photochemical production of O_3 and demonstrate a local influence of emissions, with a small impact of stratospheric air on May 21.

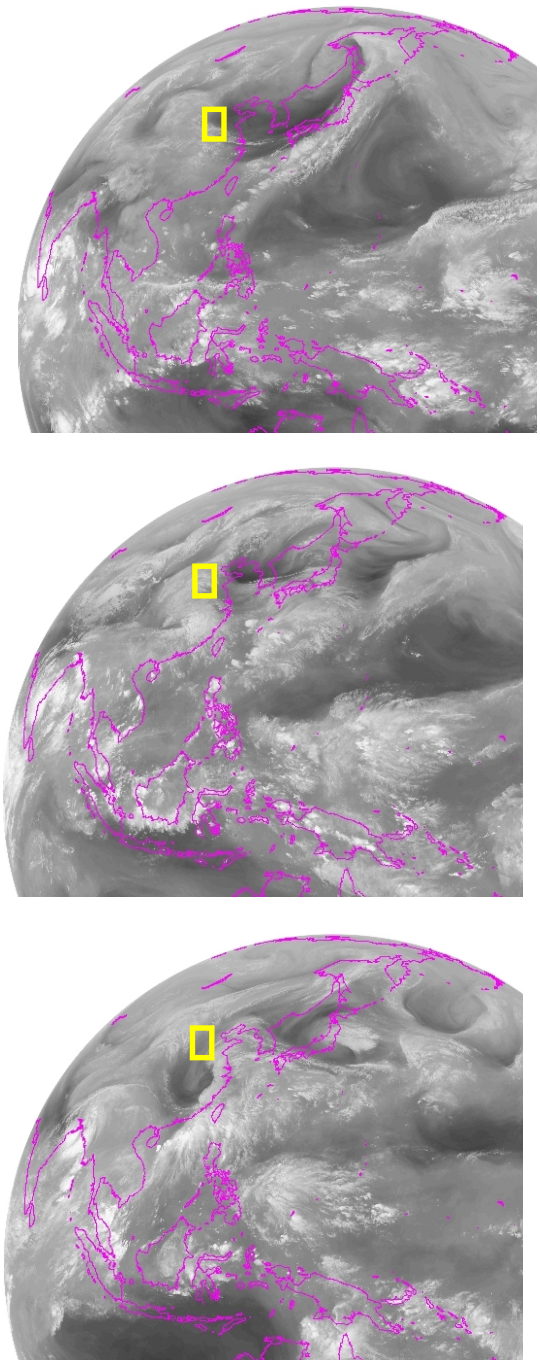

Figure 4.10. Himawari water vapor imagery from Band 9 (6.9 µm) over East Asia retrieved by UW-Madison SSEC MCFETCH. The left image shows 2:30 UTC on May 17, the middle is 8:00 UTC on May 19, and the right image is 4:30 UTC on May 21. The yellow box denotes the approximate location of Y-12 sampling. The greyscale denotes the brightness temperature with cooler temperatures (more water vapor) shown in whiter colors and warmer temperatures (less water vapor) denoted by darker colors.

4.4.2 Measured and Modeled O_3, NO_2, and CO

In this section, 1-minute average Y-12 measurements of O_3, NO_2, and CO are compared to CMAQ simulations with adjusted emissions using OMI and MOPITT (see Section 4.2.2) to evaluate model performance during this widespread O_3 pollution event. The hourly surface observations at the suburbans sites in SJZ and XT are also comapred to CMAQ output.

Figure 4.11 shows measured O_3 concentrations along each RF plotted over modeled O_3. To create the curtain of modeled O_3, the closest surface CMAQ grid cell is located spatially and temporally to the Y-12 aircraft observations. The concentrations are extracted from all the grid layers above the located grid cell. The extracted concentration is plotted as a function of time and height for comparison to ARIAs

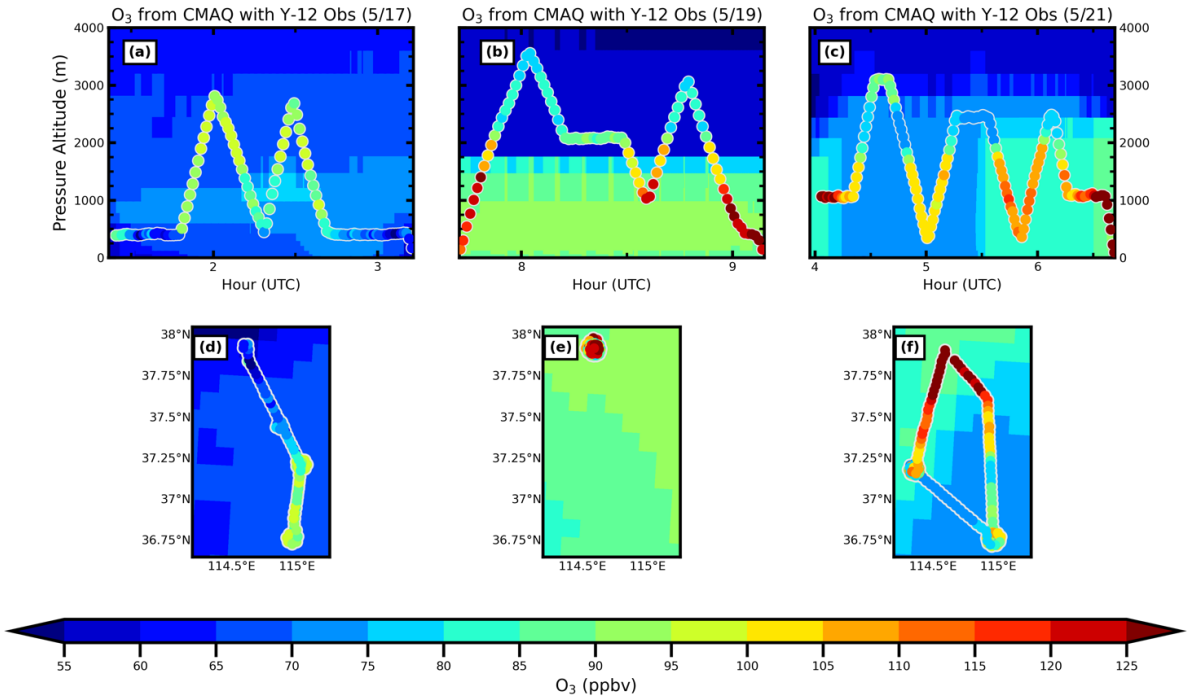

Figure 4.11. Top: Timeseries of 1-minute average O_3 mixing ratios sampled from the Y-12 aircraft plotted over curtains of modeled O_3 concentrations from the closest CMAQ grid point for (a) May 17 (RF4), (b) May 19 (RF5), and (c) May 21 (RF6). Bottom: Maps of 1-minute average O_3 mixing ratios plotted over average 1 km CMAQ O_3 at 2:00 UTC (d), 8:00 UTC (e), and 5:00 UTC (f). All units: ppbv.

measurements. This model extraction method provides a means to sample CMAQ output in a similar manner to how the aircraft observed the real atmosphere. Figure 4.11 (d, e, f) shows the average of the first 1 km (approximately 10 model layers) of O_3 from CMAQ at hours 2:00 (10:00), hour 8:00 (16:00), and hour 5:00 (13:00) UTC (LST).

In general the model significantly underestimates measured O_3. On May 17 (Figure 4.11a), the model and data show better good agreement below 500 m at the beginning and end of the flight than at higher altitudes in the middle of the flight. For the vertical ascent at 1:45 UTC over Julu (Figure 4.11d), the model and data indicate differences of about 20 ppbv. As the aircraft descended and flew south to Quzhou, the model and data indicate better agreement. The model resolves a small packet of high O_3 on May 17 corresponding to measured aircraft values between 2:15 and 2:30 UTC from 1000 to 1500 m as the aircraft spiraled upward around Quzhou. However, the model fails to reproduce observed concentrations of O_3 below 1000 m and above 1500 m.

For May 19 (Figure 4.11b), worse agreement between measured and modeled O_3 is found below 1500 m compared to May 17. The Y-12 measurements indicate O_3 concentrations as high as 120 ppbv below 1500 m, while the model indicates only ~90 ppbv. Above the PBL at 8:00 UTC, the model underestimates O_3 mixing ratios by ~20 ppbv. During a flat transect between 8:15 and 8:30 UTC, the Y-12 observed ~90 ppbv O_3, while the model indicates <60 ppbv. CMAQ does predict elevated O_3 concentrations upwards of ~ 90 ppbv near the surface with some vertical gradient.

However, the overall magnitude of these surface O_3 levels is between ~10-20 ppbv lower than actually observed.

Comparison of modeled and measured O_3 from May 21(Figure 4.11c) show results similar to that found for May 19, however the differences between the observations and simulations are even greater (see 4:00 and 6:30 UTC). One-minute average Y-12 mixing ratios at the beginning and end of the flight were ~130 ppbv. The model does predict an O_3 plume at both times, but the overall magnitude of O_3 is underestimated by ~40-45 ppbv. As the aircraft ascended and flew south toward Quzhou at 4:30 UTC (Figure 4.11f), there is good agreement between the model and data from 2000 to 2750 m of ~ 70 ppbv O_3. Above 3000 m, the model again underpredicts O_3 concentrations by 25-30 ppbv. The spiral near Quzhou (~5:00 UTC) observed ~100 ppbv O_3 in the lowest 2000 m, whereas the model indicates ~70 ppbv. The model accurately predicts higher O_3 levels during sampling near Xingtai, but the magnitude compared to Y-12 measurements is underestimated by 25-30 ppbv.

Correlations of the measured and modeled O_3 for each RF are shown in Figure 4.12. All three panels indicate a moderate correlation of the measurements with its corresponding closest CMAQ grid points and vertical levels for all three RFs. However, the model generally underestimates O_3 concentrations compared to 1-minute average Y-12 O_3, as indicated by the normalized mean bias (NMB) and ratios less than 1. Similar to the baseline CMAQ run by He et al. (2019) finding a 25% error in 10-minute. average concentrations from all research flights, O_3 concentrations from May 17, 19 and 22 using updated emissions are underestimated by 22-31%. In order for modeled and measured O_3 to have good agreement, CMAQ must produce the correct magnitude

of O_3 in the appropriate grid cell. Based on Figure 4.11, we see that CMAQ generally produced elevated concentrations of O_3 in the right locations, but substantially underestimated its magnitude, helping to explain the moderate correlations in Figure 4.12.

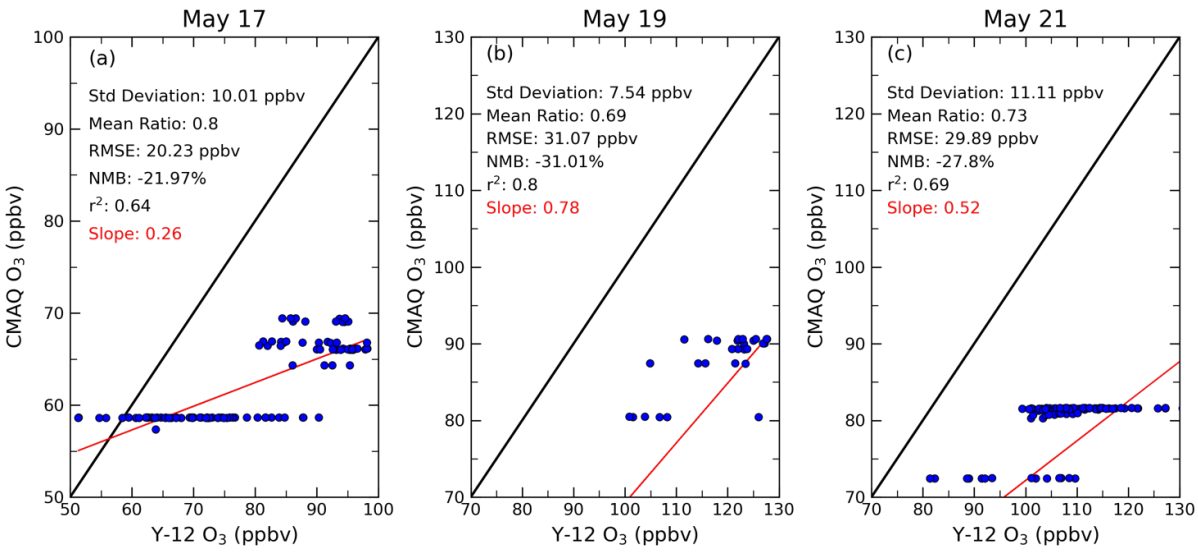

Figure 4.12. Scatterplots comparing 1-minute average O_3 from the Y-12 aircraft and modeled CMAQ from the closest grid point and model layer for (a) May 17 (RF4), (b) May 19 (RF5), and (c) May 21 (RF6). The standard deviation, mean ratio (CMAQ O_3/Y-12 O_3), root mean square error (RMSE), normalized mean bias (NMB), linear fit, and r^2 are calculated for each flight.

Comparisons of measured and modeled NO_2 after OMI and MOPITT adjustments were made are also performed. In order to accurately model O_3 production, appropriate representation of NO_2 in the CMAQ model framework is required. Figure 4.13 panels a, b, and c show 1-minute average NO_2 along the Y-12 flight path over a curtain of modeled NO_2 from CMAQ from the closest grid point. Near surface modeled NO_2 are generally low compared to the Y-12 measured values, especially on May 17 at 1:30 UTC (Figure 4.13a) when NO_2 concentrations reached ~40 ppbv. Above 2000 m, measured and modeled NO_2 shows good agreement. Comparison of Figures 4.11a

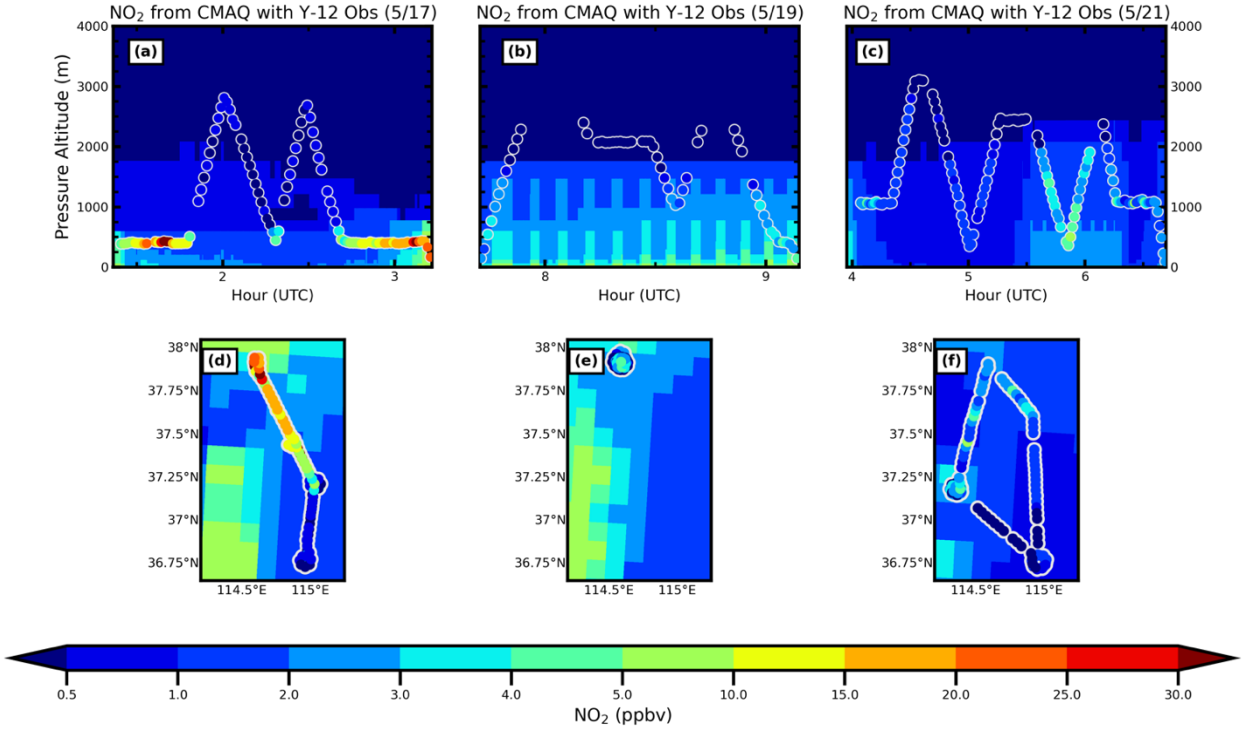

Figure 4.13. Top: Timeseries of 1-minute average NO_2 mixing ratios sampled from the Y-12 aircraft plotted over curtains of modeled NO_2 concentrations from the closest CMAQ grid point for (a) May 17 (RF4), (b) May 19 (RF5), and (c) May 21 (RF6). Bottom: Maps of 1-minute average NO_2 mixing ratios plotted over average 1 km CMAQ NO_2 at 2:00 UTC (d), 8:00 UTC (e), and 5:00 UTC (f). All units: ppbv.

and 4.13a show low O_3 concentrations collocated with high NO_2 around 1:30 UTC (9:30 LST) during May 17. The presence of high NO_2 with low O_3 during the morning may indicate titration of NO_x or VOC-sensitivity within the CMAQ model framework. The corresponding measurements of O_3 generally agree with the model, whereas the observations of NO_2 do not. Therefore, model adjustments to NO_2 are needed to rectify the model and data discrepancy.

For May 19, the model generally predicts the NO_2 concentration gradient while flying spirals over Shijiazhuang (Figure 4.13b). At the beginning and end of the flight (~7:30 and ~9:15 UTC), the corresponding measurement of NO_2 agrees well with the model prediction of ~3-4 ppbv below 750 m. Furthermore, the model is able to

reproduce NO_2 concentrations during the rapid descent at 8:30 UTC from <0.5 ppbv above 2000 m to 2-3 ppbv at 1000 m. The corresponding measurements of O_3 in these regions do not agree with the model (Figure 4.11b). Similar to May 19, the model generally reproduces the correct NO_2 concentrations where it could not predict O_3 mixing ratios on May 21, except ~6:00 UTC. The Y-12 observed ~7 ppbv NO_2 below 500 m on May 21, but the model only simulates a small plume with the incorrect magnitude.

Figure 4.14 shows correlations of measured and modeled NO_2 during the high pressure episode. The correlations of NO_2 vary greatly based on the RF, although in general the model underestimates NO_2, especially at higher concentrations. May 17 (Figure 4.14a) shows the biggest underestimation of NO_2 due to the high concentrations observed near the surface that the model was unable to reproduce. In some cases on May 19 (Figure 4.14b) and May 21 (Figure 4.14c), the model slightly overestimates

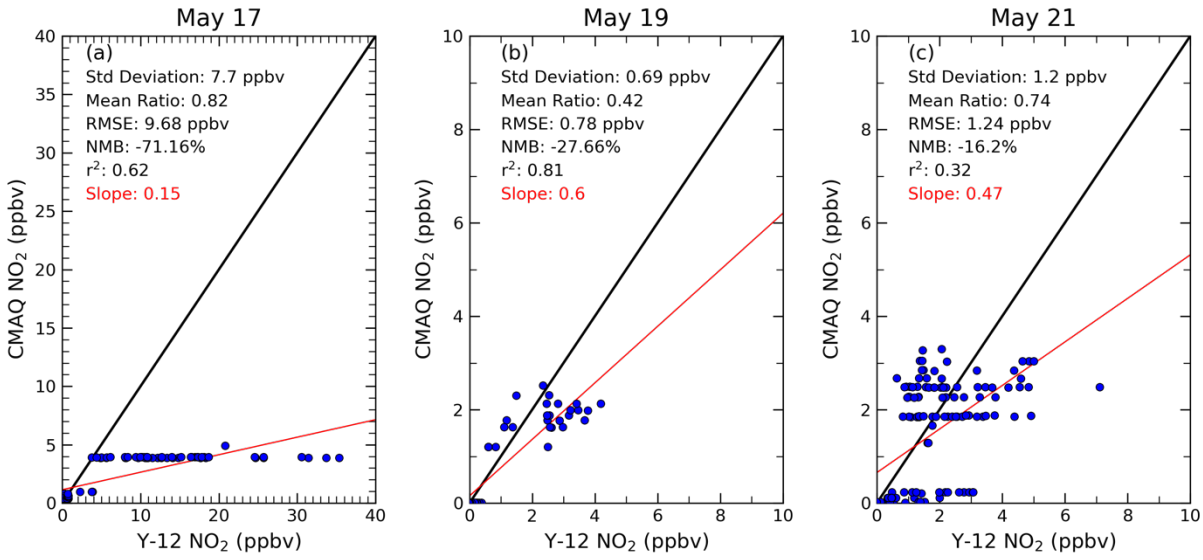

Figure 4.14. Scatterplots comparing 1-minute average NO_2 from the Y-12 aircraft and modeled CMAQ from the closest grid point and model layer for (a) May 17 (RF4), (b) May 19 (RF5), and (c) May 21 (RF6). The standard deviation, mean ratio (CMAQ NO_2/Y-12 NO_2), root mean square error (RMSE), normalized mean bias (NMB), linear fit, and r^2 are calculated for each flight.

NO_2 mixing ratios, particularly below 2000 m. These results showcase an improvement in simulating NO_2 compared to the baseline case (He et al., 2019).

The comparison of measured and modeled CO is presented in Figure 4.15. Panels a, b, and c show the 1-minute average Y-12 observations overlaid on the model curtain output from the closest CMAQ grid cell. Similar to NO_2 (Figure 4.13), the model produces lower CO concentrations below the PBL, especially on May 17 and 21 when enhanced NO_2 levels were also observed.

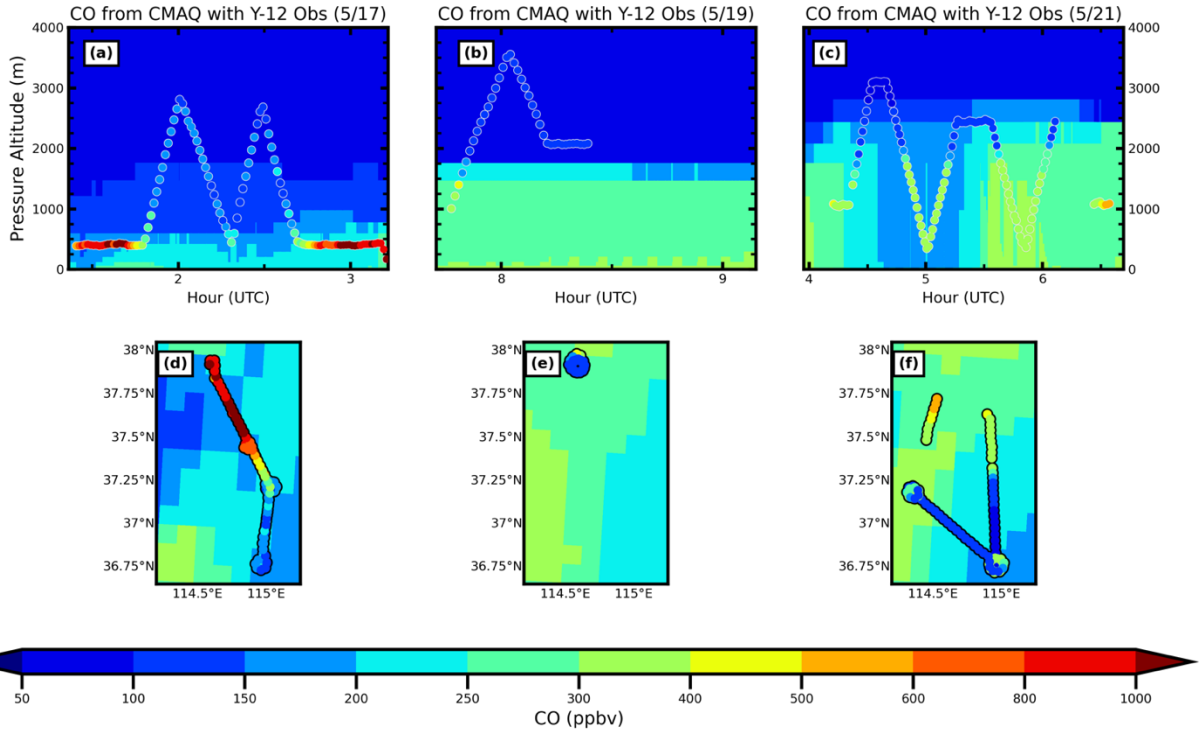

Figure 4.15. Top: Timeseries of 1-minute average CO mixing ratios sampled from the Y-12 aircraft plotted over curtains of modeled CO concentrations from the closest CMAQ grid point for (a) May 17 (RF4), (b) May 19 (RF5), and (c) May 21 (RF6). Bottom: Maps of 1-minute average CO mixing ratios plotted over average 1 km CMAQ CO at 2:00 UTC (d), 8:00 UTC (e), and 5:00 UTC (f). All units: ppbv.

Figure 4.16 shows scatterplots comparing measured and modeled CO for the respective RFs. The Y-12 aircraft observed much larger CO values than are produced in CMAQ, especially on May 17 shown in panel a. May 21 (panel c) shows the best agreement but is still consistently low compared to observations. The underestimation near the surface could indicate CO emissions are too low in the model.

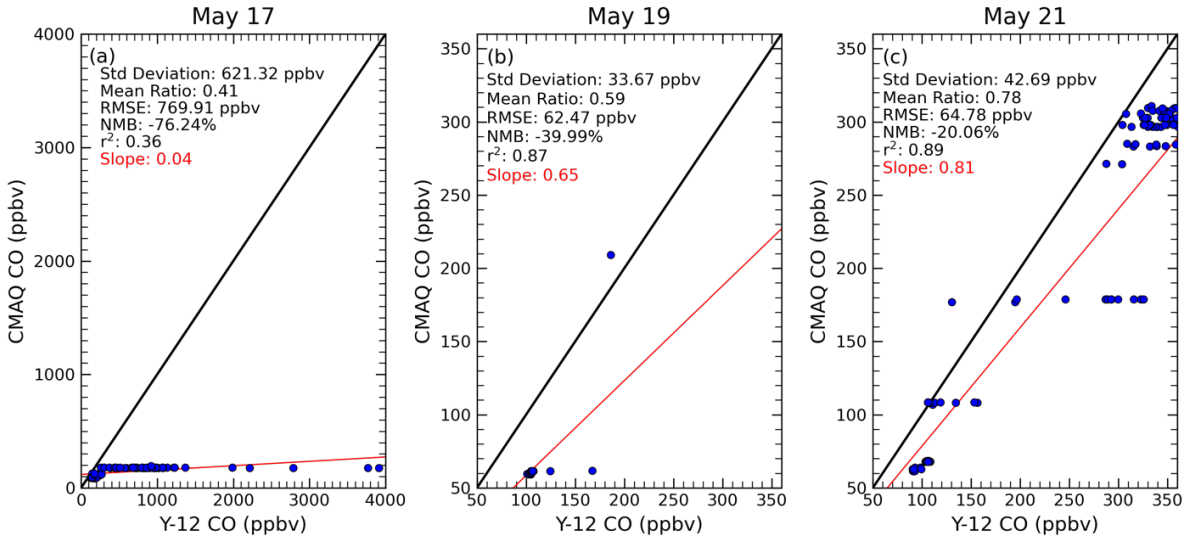

Figure 4.16. Scatterplots comparing 1-minute average CO from the Y-12 aircraft and modeled CMAQ from the closest grid point and model layer for (a) May 17 (RF4), (b) May 19 (RF5), and (c) May 21 (RF6). The standard deviation, mean ratio (CMAQ CO/Y-12 CO), root mean square error (RMSE), normalized mean bias (NMB), linear fit, and r^2 are calculated for each flight.

Next, hourly surface timeseries of O_3, NO_2, and CO at the suburban SJZ and XT sites are compared to CMAQ output in Figure 4.17. The diurnal profiles from the CMEE network (solid line) and the nearest CMAQ grid cell (dotted line) are shown from May 17-May 22. Since the urban SJZ site did not record hourly O_3 data, only the suburban sites are presented. In general, the other CMEE sites showed comparable diurnal patterns during this time period but the model often underestimates concentrations of O_3 precursors.

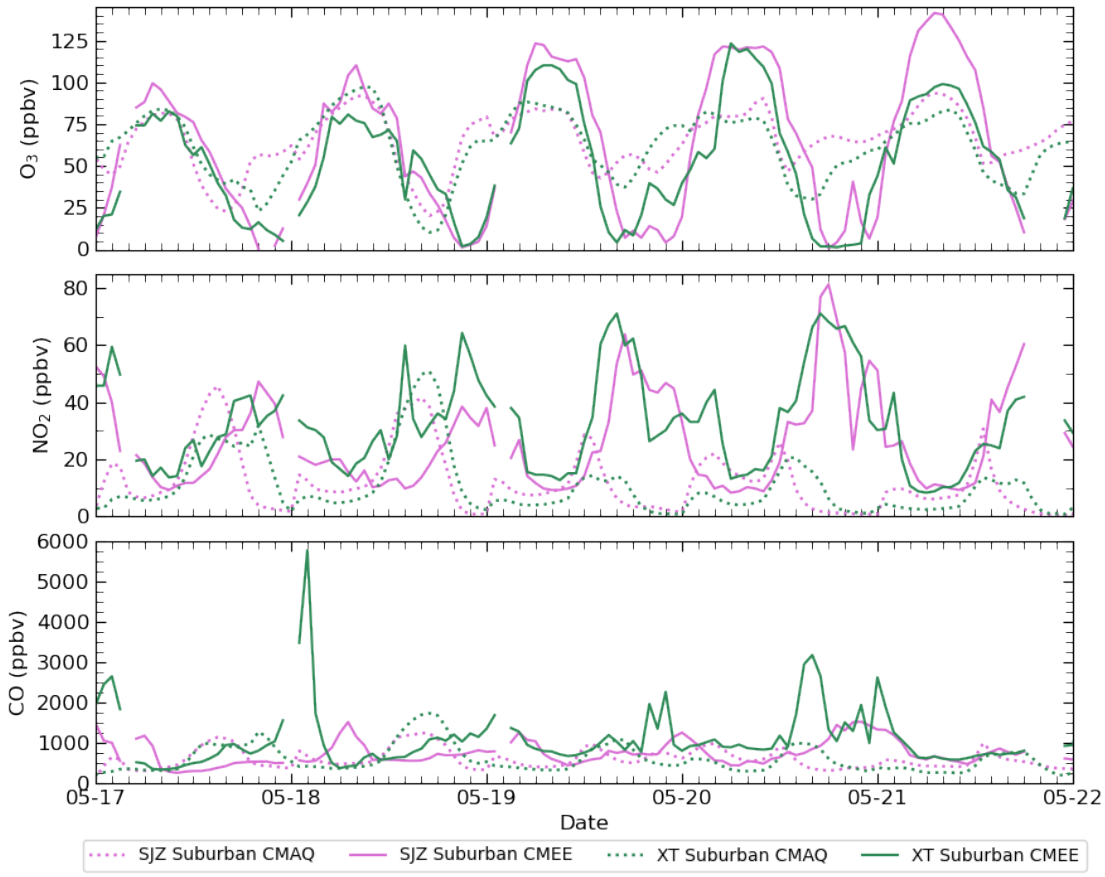

Figure 4.17. Timeseries of O_3 (top), NO_2 (middle), and CO (bottom) at the SJZ suburban site. The solid line shows the hourly average concentrations reported by CMEE and the dotted line indicates the CMAQ simulation from the nearest grid cell. All units are ppbv.

Measured concentrations of O_3 showed minimums in the morning and at night, with peaks in the early afternoon. Concentration were generally higher in SJZ than XT, particularly in the afternoon. The simulated O_3 concentration generally reproduces the correct temporal evolution, but overpredicts morning mixing ratios by 50-75 ppbv while underestimating the afternoon peaks by 25-50 ppbv, due most likely to underestimated precursor concentrations. The measured O_3 peaks in SJZ generally increased by ~10 ppbv per day, with May 22 measuring nearly 145 ppbv between 14:00

and 16:00 LST. The highest O_3 concentrations were measured on May 20 ~125 ppbv between 14:00 and 16:00 LST. CMAQ does not capture an increasing trend in the highest O_3 levels.

Concentrations of NO_2 peak in the morning and evening hours corresponding to traffic and PBL depth. Similar to O_3, concentrations were usually higher in SJZ than XT. On May 21, measurements showed substantially high levels of NO_2 at both sites in the early hours of ~80 ppbv. While the modeled magnitude of some peaks on May 18 and 19 are close to the observations, the model often underpredicts concentrations at the end of the episode.

Unlike O_3 and NO_2, the observed concentrations of CO were usually higher in XT than SJZ, possibly reflective of the winter wheat residue straw burning in this area in May. In SJZ, concentrations of CO generally peaked mid-morning between 1000 and 2000 ppbv, whereas one peak reached much larger concentrations up to 6000 pbv in XT. Simulated CO concentrations often miss the correct magnitude of peaks.

Scatterplots comparing measured and modeled O_3, NO_2, and CO at the SJZ suburban site and the XT suburban site from May 17-22 are shown in Figures 4.18 and 4.19, respectively. Among the three variables, there is poor agreement between the measurements and model. The model overpredicts some low O_3 concentrations, while underpredicts the high O_3 concentrations at both sites. Similarly, the model underpredicts high concentrations of NO_2, especially at the XT site, and some low NO_2 concentrations are overpredicted. However, since the CMEE sites utilize chemiluminescence measurements of NO_2 which experience interferences from NO_y and alkenes (Alam et al., 2020), measured NO_2 could be overestimated (Dickerson et

al., 2019). CMAQ reproduces some high concentrations of CO, but at the wrong time. Both sites observed much larger CO values than are produced in CMAQ, indicating CO surface emissions are too low in the model. Overall, emissions used in CMAQ need improvements in order to be reliably modeled

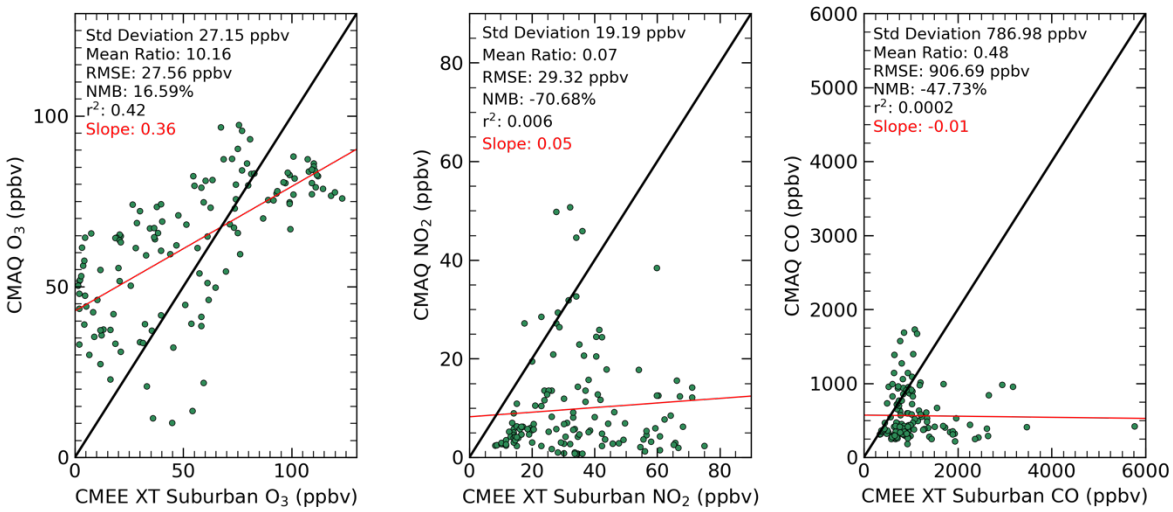

Figure 4.18. Scatterplots comparing measured concentrations of O_3 (left), NO_2 (middle), and CO (right) to modeled CMAQ levels from the closest grid point from the XT suburban site. The points include hourly data and simulations for May 17-22. The standard deviation, mean ratio (CMAQ/CMEE), RMSE, NMB, linear fit, and r^2 are calculated for each compound.

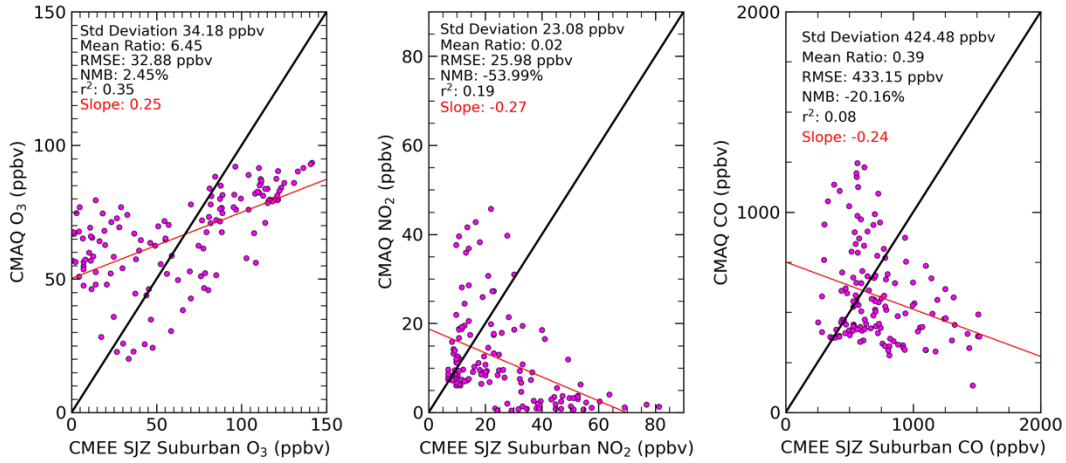

Figure 4.19. Scatterplots comparing measured concentrations of O_3 (left), NO_2 (middle), and CO (right) to modeled CMAQ levels from the closest grid point from the SJZ suburban site. The points include hourly data and simulations for May 17-22. The standard deviation, mean ratio (CMAQ/CMEE), RMSE, NMB, linear fit, and r^2 are calculated for each compound.

A comparison of observed and simulated aloft and surface concentrations of NO_2 during the high pressure episode is shown in Figure 4.20. The mean measured vertical profiles of NO_2 are comparable to the model with adjusted emissions using OMI. The largest discrepancies between the model and data are seen in the lowest 500 m, particularly during the morning flight on May 17. Simulated concentrations of NO_2 at the XT and SJZ suburban sites on May 17 are similarly too low compared to the measurements, although these observations were acquired with chemiluminescence, which can lead to overestimates in NO_2. The modeled and observed relative humidity (RH) profiles provide insight into the PBL height that may be useful for differentiating

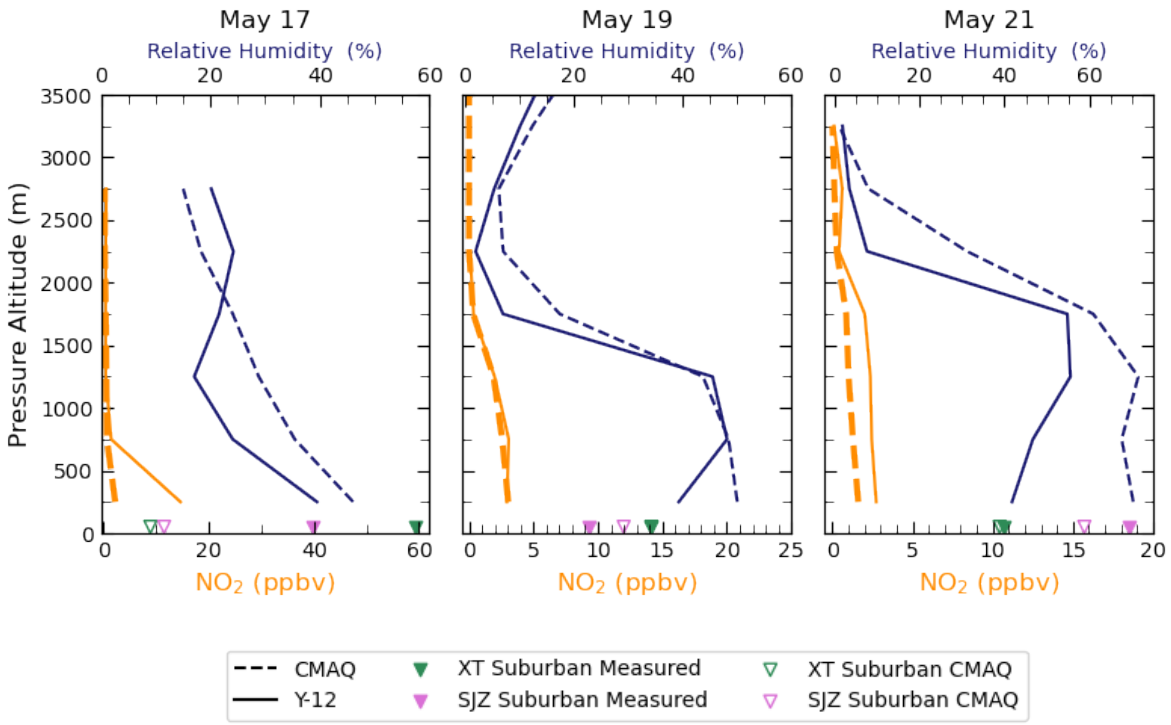

Figure 4.20. Mean vertical profiles in 500 m bins of NO_2 (orange) and relative humidity (blue). The dashed line shows the modeled profiles, while the solid line denotes the Y-12 measurements. The observed (closed triangles) and simulated (open triangles) surface NO_2 concentrations are shown at the XT (green) and SJZ (magenta) suburban sites in the same colors as shown in earlier figures.

errors due to dilution from errors from chemical transport (Castellanos et al., 2011). In the lowest 1500 m, the model overpredicts RH on May 17 and 21. While the general modeled profile of RH is correct on May 19 and 21, the simulated RH profile on May 17 fails to reproduce the observations. The surface measurements of NO_2 and vertical profiles of RH during the afternoon May 19 and 21 RFs show better agreement with the model. The underestimation of near surface NO_2 by the model suggests additional emission improvements integrating measurements with better surface sensitivity or improved diurnal information (such as PBL height) are needed.

4.4.3 Trajectory Analysis

In order to investigate concentrations and trajectories of air masses simultaneously, a cluster analysis of morning back trajectories is conducted for the suburban site in SJZ. This site is selected because it experienced some of the highest MDA8 levels during the campaign (Figure 4.4). However, HYSPLIT backward trajectories for each site indicate comparable travel paths. Trajectories for the entire month of May 2016 ending 500 m AGL above the location of the site between 0:00-3:00 UTC are used in this analysis and merged with the corresponding hourly CMEE measurements. In contrast to the cluster analysis presented in Chapter 3, trajectories are grouped using the Euclidean distance method in TrajStat, given by Equation 8:

$$d_{12} = \sqrt{\sum_{i=1}^{n}((X_1(i) - X_2(i))^2 + (Y_1(i) - Y_2(i))^2} \quad (8)$$

where X_1 (Y_1) and X_2 (Y_2) indicate the longitude and latitude coordinates of backward trajectories 1 and 2, respectively. The main advantage of the Euclidean distance method is the incorporation of distance and directions of the trajectories into the clustering

result, which is ideal for this study of short-lived compounds in the troposphere. An eight-cluster solution is adopted in this analysis.

Figure 4.21 shows a map with eight different colored lines indicating the eight-cluster solution. In the same color as the cluster, concentrations statistics measured at the CMEE site and simulated by CMAQ are shown on the right for CO, NO_2, O_3, and SO_2. The cluster with the highest measured mean concentrations of O_3, NO_2, and CO (Cluster 7, N=21) includes most days during the high pressure episode. Similar to the model-measurement comparison in Section 4.4.2, the modeled average levels of CO and NO_2 are underestimated compared to observations in Cluster 7, whereas the model overestimates concentrations of O_3. Average levels of SO_2 agree well between the model and measurements. Cluster 3 (N=31) indicates approximately the same mixing ratios of measured CO and NO_2 as Cluster 7. The dates in Cluster 3 are mostly towards the end of the month during the transport period (May 25-31), as well as two trajectories during the high pressure episode. Similar to Cluster 7, the model underestimates CO and NO_2 concentrations, overestimates O_3 levels, but agrees better with SO_2 mixing ratios in this cluster. Clusters 2 (N=7) and 5 (N=5) traverse through nearby provinces before sampling, but generally do not exhibit substantially elevated concentrations of NO_2 or SO_2. An exception is for high SO_2 during Cluster 5, likely indicative of coal combustion sources. Cluster 5 indicates the largest measurement-model disagreement for SO_2, while Clusters 1 and 3 show the largest discrepancy for O_3, NO_2, and CO. Clusters 4 (N=13) and 6 (N=10) travel similar paths, but the observed concentrations during these time periods were substantially different. For instance, a large variability in measured concentrations of CO, NO_2, and SO_2 are found during Cluster 4, while

Cluster 6 indicates some of the lowest measurements of NO_2 and SO_2. Since a known disadvantage of the Euclidean distance method is the different classification of two identical backward trajectories except for their speeds, it is possible that trajectories in Cluster 6 traveled faster away from pollution sources than those in Cluster 4. Despite these shortcomings, Cluster 4 and 6 show the best agreement between measured and modeled O_3.

To provide a direct link between polluted air masses from sources and receptor measured by the suburban SJZ site during the high pressure episode, we combine backward HYSPLIT trajectories with CMAQ output. This analysis is split to study the impact of transport in the morning (0:00-3:00 UTC or 8:00-11:00 LST) and afternoon (7:00-10:00 UTC or 15:00-18:00 LST) in Figures 4.22 and 4.23. After locating the closest CMAQ grid cell in time and space for each hour, trajectories between 0:00-3:00

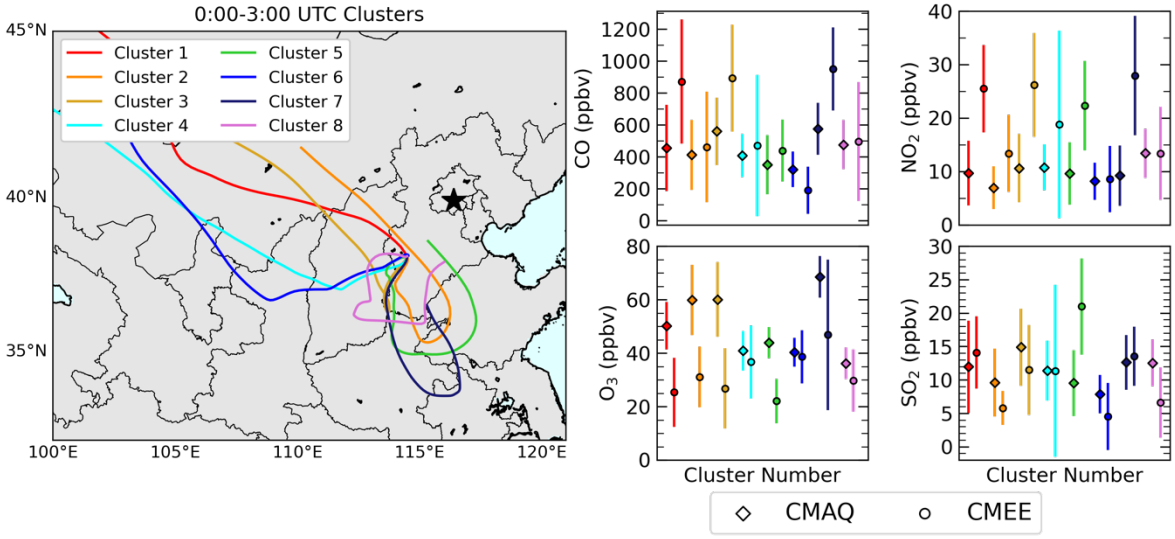

Figure 4.21. Backward trajectory clustering results for hours 0:00-3:00 UTC in May 2016 at the suburban SJZ sites. The map shows the paths of the 8 clusters in different colors. On the right, mean and ± standard deviation concentrations are shown for CO, NO_2, O_3, and SO_2 from CMAQ simulations (diamonds) and the CMEE measurements (circles). The color of the trajectory on the map corresponds to the same colored line on the right. The star indicates the location of Beijing. All units are ppbv.

and 7:00-10:00 UTC are grouped based on the number of hours before sampling. Next, mean and standard deviation values are calculated for a number of variables. The CMEE sampling time is indicated when the hour back approaches 0. As discussed in Section 4.2.2, concentrations of O_3, NO_2, and CO are often underestimated in CMAQ compared to observations, particularly near the surface. Therefore, the discussion that follows focuses on how concentrations qualitatively change in the model and not on overall magnitude.

Seventy-two hour HYSPLIT backward trajectories initialized between 0:00-3:00 UTC from May 17-22 at the SJZ suburban site (Figure 4.22) show dynamic transport pathways during this multi-day high pressure case study. During high

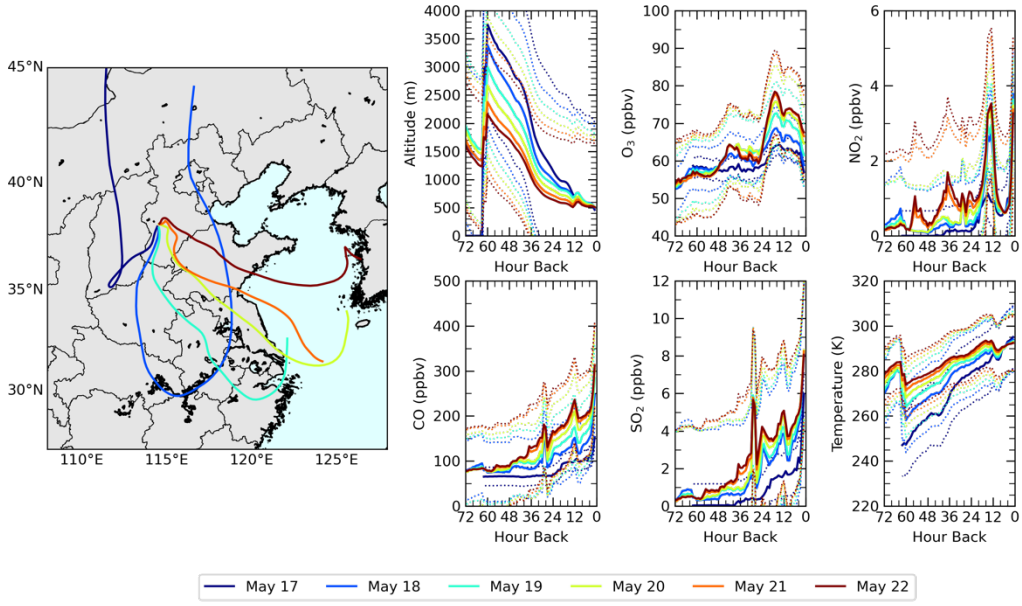

Figure 4.22. HYSPLIT backward trajectories between 0:00-3:00 UTC (8:00-11:00 LST) combined with CMAQ model output. The colors indicate the day in which the trajectories were initialized with the suburban SJZ site as the receptor. Left: Map showing the paths of 72-hour HYSPLIT backward trajectories for six days (different colors) during the high pressure episode. Right: Hourly timeseries of altitude, concentrations of O_3, NO_2, CO, and SO_2, and temperature for six days (different colors) during the high pressure event. The number of hours back indicates the number of hours before sampling, with zero showing the measurement time. The average is shown in the solid line and the ± standard deviation is shown by the dotted lines.

pressure events, entrainment of FT air into the PBL during the morning can increase the mixing depth and pollution levels (Huang et al., 2010; Parrish et al., 2010). On May 17, a polar continental airmass (cP) traversed through Inner Mongolia and Shanxi Province to the west bringing cold and dry conditions to the NCP before sampling. Flow on May 18 indicated another cP airmass traveled through Inner Mongolia, but passed farther east and proceeded over Beijing and several heavily polluted coastal provinces (Shandong, Jiangsu) before recirculating and flowing northward. By May 19, anticyclonic flow allowed a moist and warm maritime tropical (mT) airmass to pass over the Yellow Sea and traverse through several provinces (Zhegiiang, Anhui, and Henan) to the south before traveling northward to ground locations in Hebei. A comparable pattern of an mT airmass traveling through industrialized coastal provinces before sampling is indicated for May 20, 21, and 22, with a gradual stronger westward component than southward. Trajectories on May 20-22 72 hours before sampling illustrate flow near the Korean Peninsula. These morning trajectories indicate general subsidence before sampling in the NCP on all days, with the mean altitude decreasing with time.

Between 48 and 72 hours before sampling, simulated mean concentrations of O_3, NO_2, CO, and SO_2 are generally comparable in the morning among the six different days. At the end of the period (May 21 and 22), the larger fluctuations in concentrations (denoted by spread of the standard deviation) suggest these air masses are more polluted between 48-72 hours before sampling than at the beginning of the episode (May 17 and 18). It is likely that these higher concentrations are a result of the lower altitudes and warmer temperatures than found on other days. These conditions would

allow for passage closer to ground-based emission sources and favor O_3 production due to faster reaction rates and higher release of biogenic VOCs (Sillman and Samson, 1995). In addition, the location of the May 21 and 22 trajectories 48-72 hours before sampling are over the Yellow Sea, potentially promoting O_3 formation. Based on ship and ground observations from multiple field campaigns, Goldberg et al. (2014) posited that daytime O_3 concentrations were elevated over the Chesapeake Bay due to shallower boundary layers, higher photolysis rates, less boundary layer venting, and a slower deposition velocity. The same mechanisms may be at play over the Yellow Sea on May 21 and 22 which supported the buildup of O_3. Simulated mean concentrations of O_3 along the trajectories for all days are relatively constant ~60 ppbv between 48-72 hours back in time, slightly higher than estimates of background O_3 concentrations using GEOS-Chem of 40-50 ppbv (Ni et al., 2018; Wang et al., 2011). Background O_3 levels can consist of production from natural precursor sources, contributions from the stratosphere, and include long-range transport from non-domestic anthropogenic emissions (Huang et al., 2010).

Modeled concentrations of O_3, NO_2, CO, and SO_2 increase for all days ~36 hours before sampling when all trajectories are over Hebei or nearby provinces. May 21 and 22 express the largest concentration in magnitude whereas May 17 shows the smallest enhancement. Concentrations of O_3 spike on May 21 and 22 while levels of CO and NO_2 also peak, suggesting a combination of en route production and transport. Several peaks of NO_2, CO, and SO_2 on May 21 and 22 are suggestive of sampling of polluted air masses. While mixing ratios of NO_2, CO, and SO_2 are all simulated to increase upon sampling time (when hour back is 0), levels of O_3 are projected to

decrease. The dip in O_3 concentrations before sampling suggest loss from dry deposition or reaction with NO to produce NO_2 (which spiked at the same time).

The 72-hour HYSPLIT backward trajectories initialized between 7:00-10:00 UTC from May 17-22 at the SJZ suburban site (Figure 4.23) are comparable to the morning trajectories. The main difference is the May 18 trajectory did not travel as far as the morning trajectories. Additionally, the mT air masses on May 19-22 originate farther in the Yellow Sea within the time frame. The trajectories all indicate subsidence from May 17-22 and the earlier trajectories (May 17 and 18) similarly had a higher starting altitude than the later trajectories (May 21 and 22).

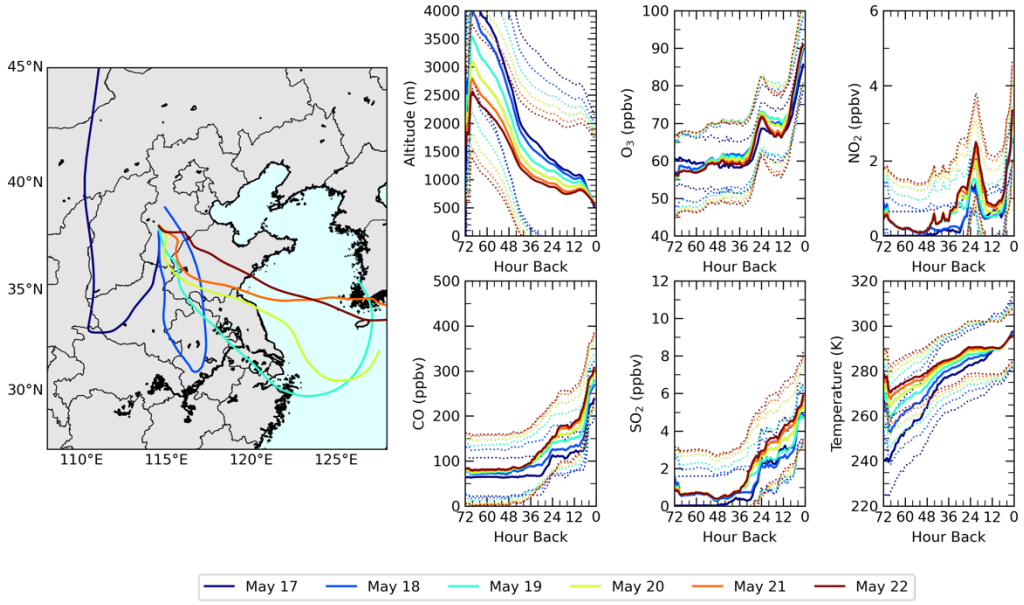

Figure 4.23. HYSPLIT backward trajectories between 7:00-10:00 UTC (15:00-18:00 LST) combined with CMAQ model output. The colors indicate the day in which the trajectories were initialized with the suburban SJZ site as the receptor. Left: Map showing the paths of 72-hour HYSPLIT backward trajectories for six days (different colors) during the high pressure episode. Right: Hourly timeseries of altitude, concentrations of O_3, NO_2, CO, and SO_2, and temperature for six days (different colors) during the high pressure event. The number of hours back indicates the number of hours before sampling, with zero showing the measurement time. The average is shown in the solid line and the ± standard deviation is shown by the dotted lines.

Similar to Figure 4.21, concentrations of NO_2, CO, and SO_2 in the afternoon trajectories are low 36-72 hours before sampling. Unlike the morning trajectories, O_3 levels in the afternoon trajectories between 36-72 hours before sampling are higher on May 17 and 18 than May 21 and 22 by ~5 ppbv. Between 36-72 hours before sampling, the higher O_3 levels on May 17 are accompanied by lower temperatures than simulated on May 22. Mixing ratios of O_3, NO_2, CO, and SO_2 increased ~36 hours before sampling. Unlike the morning, the afternoon mean concentrations of O_3 between 12-36 hours before sampling are lower on May 22 than May 17. By the sampling time, O_3 levels are comparable for all days except May 17 and levels of NO_2, CO, and SO_2 are all relatively comparable.

The important role local emissions play on air quality in Hebei presented here appear to be consistent with more sophisticated modeling studies. Li et al. (2016) demonstrated the role of local sources on surface transport of O_3, CO, and SO_2 between the NCP and the purlieus of Beijing due to changes in the prevailing wind direction. On days with simulated MDA8 O_3 >100 ppbv, the GEOS-Chem model predicts domestic anthropogenic sources account for 41% of the surface O_3 concentrations from May-August in the NCP (Lu et al., 2019). Previous ground-based observations at an urban site in Shijiazhuang from April to August 2018 found air masses transported from short-distances (<50 km) have the largest contributions to measured VOCs (Guan et al., 2020). While $PM_{2.5}$ was not available in this study, Chang et al. (2019) found 32-53% of the annually averaged $PM_{2.5}$ concentrations in 13 cities in the BTH region were due to local sources using the Integrated Source Apportionment Model (ISAM)

tool in CMAQ. This study also found emissions from Shandong and Henan Provinces had the largest contributions to $PM_{2.5}$ levels (8.4% and 4.5%, respectively).

4.4.4 OMI Tropospheric NO_2

Space-based measurements of tropospheric column NO_2 are widely used to study temporal and spatial patterns (e.g. Lin et al., 2015) and long-term trends (e.g. Krotkov et al., 2016) as well as infer NO_x sources (e.g. Lin, 2012) and top-down emissions (e.g. Liu et al., 2018) over China. In this section, we use OMI measurements to qualitatively identify locations that may have impacted the NCP during the high pressure episode (Figure 4.24). Data from OMI are contaminated by clouds and affected by the row anomaly, so only a limited snapshot can be shown.

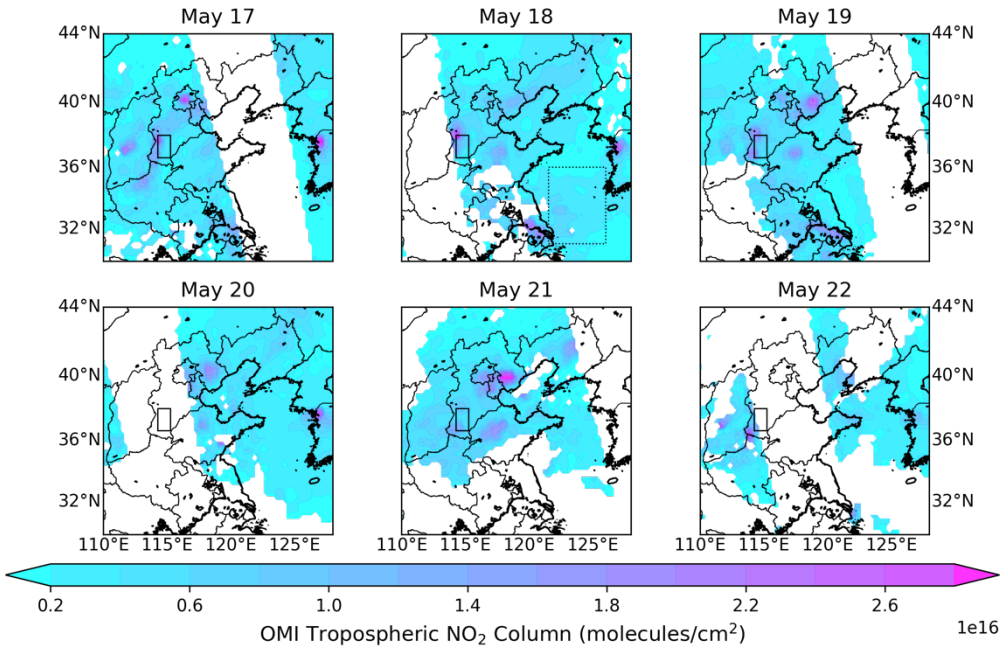

Figure 4.24. Maps of tropospheric column NO_2 from OMI during the high pressure episode. The black box indicates the region of ARIAs flights and the dotted box on May 18 denotes the NO_2 plume over the Yellow Sea. While clouds and outages often obscured the OMI retrievals, high column contents are observed over the BTH region and the Yellow Sea.

Evident from Figure 4.24 are hotspots of tropospheric NO_2 over the NCP, particularly in the BTH region, as well as the YRD. Measurements of high tropospheric NO_2 columns over Seoul, South Korea are observed. Based on DISCOVER-AQ and KORUS-AQ measurements, OMI NO_2 values are found to be about a factor of 2 lower compared to aircraft observations in highly polluted environments due to inaccurate retrieval assumptions but mostly related to OMI's large footprint (Choi et al., 2020).

The OMI retrieval on May 18 reveals an NO_2 plume to the southwest of South Korea over the Yellow Sea. Based on 850 mbar heights from Figure 4.7 and previous analysis by Peterson et al. (2019), winds over this region were weak and flowing to the north. HYSPLIT forward trajectories from the KORUS-AQ flight over the Yellow Sea on May 18 show airmass travel to the north and northwest, but missed the ARIAs flight domain. Measurements from the KORUS-AQ shipboard Pandora Spectrometer Instrument found variability of total column NO_2 over the ocean was mostly affected by local anthropogenic emissions and highly dynamic air mass transport pathways (Tzortziou et al., 2018). Unlike the high-frequency ship remote-sensing sensors, Tzortziou et al. (2018) discovered the OMI was not able to detect small-scale, short-term changes in NO_2 over coastal waters.

High tropospheric columns of NO_2 are also seen on multiple days in northwestern Shandong Province over the heavily industrialized and capital city, Jinan. While trajectories are not shown during the OMI overpass time, morning and afternoon trajectories from the suburban SJZ site (Figures 4.22 and 4.23) both pass over Shandong Province on May 20-22. In addition, vertical profiles and $\Delta O_3/\Delta CO$ (Figures 4.8 and 4.9) demonstrate a transport contribution on May 21, possibly from Shandong.

4.5 Summary and Conclusions

In this chapter, we analyze airborne measurements from ARIAs and surface observations from the CMEE network in Hebei Province of the NCP from May-June, 2016. We discuss these observations in relation to four meteorological setups affecting the ARIAs and concurrent KORUS-AQ field campaigns described by Peterson et al. (2019). The results from a multiday persistent high pressure episode are discussed in more detail due to the incessant levels of pollution observed during this period. Airborne measurements are compared to CMAQ simulations with updated emissions using OMI and MOPITT satellite retrievals over East Asia. The CMAQ simulations are merged with HYSPLIT backward trajectories for five CMEE surface sites in the NCP to understand the evolution of pollutants (O_3, CO, NO_2, SO_2) before sampling. Finally, OMI measurements of tropospheric NO_2 are shown throughout this high pressure episode to assess locations possibly contributing to the large pollution loading during the high pressure episode.

High amounts of O_3 and its precursors were ubiquitous in May and June 2016 over the NCP during a variety of synoptic conditions. While the aim of ARIAs was to characterize the source region, transboundary pollution events to the Korean Peninsula were uncommon in Spring 2016. The highest surface and aloft O_3 mixing ratios were observed during a multi-day persistent high pressure episode from May 17-22 due to favorable atmospheric conditions. Computed $\Delta O_3/\Delta CO$ ratios from the ARIAs airborne data indicates high efficiency of O_3 production and suggests airmass transport throughout and above the PBL on May 19 and 21. Dry upper tropospheric conditions as seen from the Himawari satellite combined with observations of low mixing ratios

of CO and high amounts of O_3 in the FT on May 21 suggests a small stratospheric contribution to ARIAs measurements. CMAQ results are compared during the high pressure episode to measured Y-12 and surface concentrations. Overall, concentrations of O_3, NO_2, and CO are severely underestimated by CMAQ compared to the observations. The model generally reproduces locations and time periods of elevated levels, but misses the full magnitude of the measured concentrations. The preliminary analysis presented here illustrates additional improvements in the emission inventory are needed, especially near the surface, to rectify measurement and model discrepancies.

We investigate concentrations along trajectories to delve into the influence of local and regional sources on air quality during the high pressure episode. HYSPLIT backward trajectories demonstrate several days are influenced by a warm and moist maritime tropical airmass originating near the Korean Peninsula, traversing over several industrialized provinces before sampling in Hebei. When these trajectories are combined with the CMAQ output, concentrations of O_3, CO, NO_2, and SO_2 generally increase within the last 24 hours before sampling, suggesting local transport from nearby provinces. The spatial and temporal distributions of NO_2 in east Asia show high levels in the Beijing-Tianjin-Hebei and Yangtze River Delta regions during the high pressure episode. The HYSPLIT backward trajectories on May 20-22 pass near Jinan, the capital of Shandong Province, another region with high tropospheric columns of NO_2. Since the highest spatial resolution of OMI (13 km × 24 km) is too coarse to identify fine spatial features of NO_2 abundance, better resolution (7 km × 3.5 km) satellite measurements from the TROPospheric Monitoring Instrument

(TROPOMI) and the Geostationary Environment Monitoring Spectrometer (GEMS) may help improve assessing NO_2 hotspots at a fine scale for future study. Analysis of the ARIAs measurements reveals that a key to understanding springtime pollution in the NCP is the intricacies between emission sources and meteorology.

Chapter 5: Concluding Remarks

5.1 Summary of Results

In this dissertation, I illustrate a few aspects of the air pollution problem in the NCP by analyzing a U.S.-China collaborative project called ARIAs. Airborne measurements of trace gases (O_3, CO, NO_2, NO, SO_2, and VOCs) and aerosol optical properties (scattering and absorption) were collected over Hebei Province in May and June 2016. This intensive airborne data set acquired inland measurements over one of the most polluted regions in the world while a collaborative NASA-NIER Korean air quality study (KORUS-AQ) obtained observations downwind over the Korean Peninsula. We obtained *in situ* profiles over the Chinese source region to facilitate Lagrangian experiments on the formation and modification of aerosols and trace gases. The work presented in this thesis provides the following contributions to understanding air quality during ARIAs by answering the questions presented in Section 1.4:

1) How is aloft O_3 photochemistry affected by NO_x and VOCs in Hebei Province and which VOCs are most influential in the production of O_3? What characteristic pollution source signatures are present and how do they compare to previous studies in China and to other areas where pollution controls measures have been successfully implemented?

Analysis of ARIAs observations shows high but variable pollutant loadings throughout the PBL (O_3: 45-145 ppbv, CO: 80-6054 ppbv, NO_x: 0-53 ppbv). Total observed mixing ratios of VOCs range from 4 to 23 ppbv in the PBL, mostly dominated by alkanes and dependent upon collection altitude. While the most abundant species measured during ARIAs such as ethane, propane, and acetylene are comparable to

previous surface studies, mixing ratios aloft in the PBL are generally lower and originate from diverse sources due to unique emission source characteristics found throughout China. Sources of VOCs at flight altitudes include vehicular emissions, fuel and solvent evaporation, and biomass burning.

My analyses confirm that VOC reactivity and emission amount should be considered collectively when formulating control strategies for O_3. I find m/p-xylene, ethylene, propylene, and i-pentane play significant roles in the aloft production of O_3 in Hebei Province. Box model simulations estimate a peak rate of mean O_3 production of ~7 ppbv/hour in the PBL below 500 m, albeit pollution frequently extended into the FT where NO_2 mixing ratios ~400 pptv leads to net production rates of O_3 up to ~3 ppbv/hour. These production rates are sufficient to continue to produce O_3 downwind. My study agrees with previous ground-based research that identifed the most reactive VOCs in the NCP and found NO_x-sensitivity for O_3 production throughout the PBL over Hebei, while more VOC-sensitivity at low altitudes near urban centers. My research shows controlling both NO_x and VOCs is necessary, but stricter VOCs controls in certain VOC-sensitive areas may provide additional benefits.

The observed ratios between different pollutants are used to characterize regional combustion source signatures. The ARIAs measurement-derived CO/CO_2 ratio (3.1%) is indicative of low-efficiency fuel combustion, and together with large amounts of SO_2 suggests a residential coal burning source. Even though our aloft measurements cover only a small area in the NCP, our observed CO/CO_2 ratio is consistent with Chinese-sourced inflow obtained from airborne observations during KORUS-AQ (1-4% CO/CO_2) (Halliday et al., 2019). Occasionally higher CO/CO_2

ratios (~10%) with less SO_2 are observed, reflective of biomass burning sources (Andreae and Merlet, 2001). Low CO/CO_2 and SO_2/CO_2 ratios indicate combustion sources using a sulfur scrubber or burning low sulfur fuel from high combustion efficiency power plants. Compared to observations in the mid-2000s in Beijing, the ARIAs CO/CO_2 ratio is 0.1-2.7% lower, demonstrative of some success in regional pollution control strategies. By contrast, the ARIAs CO/CO_2 ratio is higher than satellite-derived ratios over megacities across the globe where extensive pollution control measures have been implemented. The work of Chapter 2, summarized above, was published in November 2020 in *Atmospheric Chemistry and Physics* (Benish et al., 2020a).

2) Do atmospheric abundances of CFCs observed over a suspected source region agree with global and Northern Hemisphere background levels? How do different meteorological conditions affect the levels and sources of measured CFCs?

I find high amounts of CFCs well above the 2016 global, tropospheric background that are reflective of local release. Median enhancements above background levels for CFC-11, CFC-12, CFC-113, and CFC-114 are 22%, 6%, 10%, and 47%, respectively. Correlations of CFCs with substances used in their manufacture are selected to investigate the possibility of new, unreported production. The correlation of CFC-11 with the feedstock CCl_4 (r^2=0.78) and the closely related, co-produced CFC-12 (r^2=0.64) suggests widespread release due to new production of these compounds, in violation of the Montreal Protocol. One whole air sample contained an

unusually large amount of CFC-11 (2163 pptv), likely due to sampling of industrial applications such as spray polyurethane foam in the immediate vicinity.

An analysis combining backward trajectories with measurements of CFCs and materials commonly used as feedstock provides new insight into potential source regions of CFCs production. I discovered new production of CFC-11 throughout eastern China, while new production of CFC-12 is only identified when flow is from Inner Mongolia and Shanxi Province. I find no evidence for new production of CFC-113, but strong correlations of CFC-114 with the feedstock C_2Cl_4 suggests new production of CFC-114 from Shandong Province. My analysis of CFCs over a suspected CFC-11 source region is the first to show new production of CFC-12 from regions to which previous modeling studies (Rigby et al., 2019) were insensitive. The findings of this study confirm high levels of ODSs over Hebei due to new production and continued use, in conflict with the international Montreal Protocol. This research, presented in Chapter 3, is currently under review at the *Journal of Geophysical Research: Atmospheres* (Benish et al., 2020b).

3) How do meteorological conditions affect the vertical distribution and transport of trace gases over the NCP? Do atmospheric models agree with observations?

In Chapter 4, four meteorological periods affecting East Asia in May and June 2016 as identified by Peterson et al. (2019) are discussed in context of pollution composition during ARIAs. During the first dynamic meteorology period (May 1-15), several frontal boundaries passed through the NCP, resulting in rapid changes between

cloudy and clear conditions. Due to the frequent shift of conditions, mean airborne ratios of O_3 and SO_2 were 15-20 ppbv and 7-10 ppbv, respectively, below the ARIAs campaign mean. Similarly, the five surface sites in the region observed some of the lowest MDA8 O_3 levels, sometimes even below 40 ppbv. A persistent high pressure episode (May 17-22) trapped pollutants near the surface, throughout the PBL, and even extended into the FT. The anticyclonic system brought large-scale subsidence, allowing for weak upper-level wind speeds and increased surface temperatures favoring the formation of O_3. Surface MDA8 O_3 values were 25-55 ppbv higher than the Chinese Ambient Air Quality standard. The transport period (May 25-31) allowed for low-level westerly transport from East Asia across the Yellow Sea to the Korean Peninsula, which observed the unhealthiest air during this period. Vertical profiles over Xingtai in the morning indicate a temperature inversion capped pollutants near the surface, allowing near-surface O_3 levels to rise from ~75 ppbv in the morning to ~100 ppbv by the afternoon. Surface MDA8 O_3 recorded several exceedances during this period, but were not the highest concentrations observed in Spring. The high aerosol scattering present in the morning may have sufficiently reduced UV radiation to decrease the O_3 production efficiency. At the end of the ARIAs measurement period, a high-pressure blocking pattern (June 1-11) hindered any changes in meteorology for over a week. Surface observations of MDA8 O_3 documented a large range of observations below and above air quality standards, driven by increased cloud cover towards the end of this period.

Due to the frequent MDA8 O_3 exceedances experienced during the high pressure episode, this period is chosen as a case study to delve into the impacts from

meteorology and photochemistry. High ratios and correlations of $\Delta O_3/\Delta CO$ from May 19 and 21 in the PBL are indicative of transport of a polluted airmass. We evaluate model performance during this high pressure event. Overall, the model produces an O_3 exceedance event, but misses the full magnitude of the afternoon measured O_3 concentrations. Underestimations of precursors (NO_x and CO) in the emission inventory, especially near the surface, and limitations due to model resolution may be to blame for this discrepancy. Modeled concentrations of O_3, CO, NO_2, and SO_2 increase 24 hours before sampling when the airmass is traveling over nearby provinces, suggesting a local contribution to poor air quality in the NCP during this high pressure event. These same provinces often show high tropospheric column contents of NO_2 from OMI, showcasing the regional nature of the air pollution problem in China. My assessment of meteorology and resulting air quality will be submitted for publication to the journal *Atmospheric Environment.*

5.2 Recommendations and Future Work

Although the body of this work makes considerable progress towards answering the key science questions defined in Section 1.4, certain items would benefit from continued investigation. For example, Chapter 2 demonstrates that the top 10 VOCs in terms of O_3 production only constitute one-third of the total volume mixing ratio of measured VOCs. I posit that targeting the most reactive VOCs from particular sources will have the greatest benefit in controlling O_3, but current Chinese regulations on VOCs emissions aim for a nationwide 10% reduction without considering reactivity or chemical speciation. Future airborne measurements of VOCs over various polluted

megacities and different seasons could significantly expand the community's understanding of the role VOCs for producing O_3 in a country with rapidly changing emissions. Such measurements may also provide insight into the evolution of O_3 sensitivity and efficiency as emissions decrease. Speciated measurements of VOCs in the PBL including oxygenates and consumer products would allow scientists to identify compounds important to O_3 production (based on the MIR scales) that have the potential to be transported downwind. An interesting additional finding is that although isoprene has been shown to play a key role in the formation of O_3 during the summer months by others (e.g. Li et al., 2015), I find isoprene is not the dominant VOC in the region during our spring time study. Quantifying the vertical profile and temporal evolution of isoprene could help estimate the biogenic VOC contribution to O_3 as well as refine biogenic emission inventories.

Further investigation is also recommended to quantify the origin of ODSs emissions and their repercussions on the recovery of the O_3 layer. Additional airborne observations of CFCs during other seasons with different dominant meteorological conditions may improve the understanding of the ODSs spatial distributions and sources in China. For instance, a recent study using a Bayesian probabilistic model concludes the banks of CFC-11 and CFC-12 are likely to be substantially larger than suggested by recent scientific assessments, in part due to underreporting of production (Lickley et al., 2020). As shown in Chapter 3, the high amounts of CFC-11 and CFC-12 measured during ARIAs are attributed to new production in certain areas of East Asia. In addition to more measurements, an improved understanding of emissions from banks of CFC-11 and CFC-12 is warranted, using updated emission rates from foam

use and quantifying the timing of emissions from banks by region to further understand the geographic dependence. Lastly, the scientific community must assess where and how potential unreported production of other ODSs still allowed under the Montreal Protocol may occur. For instance, some compounds, like CFC-113 and CCl_4, can continue to be used as feedstock for production of other chemicals. Identifying when the cost of producing the replacement compound is more than price of the banned substance will help ensure the continued compliance of the Montreal Protocol. Nonetheless, atmospheric emission during manufacturing should be monitored and controlled. Moreover, CFC-113 emissions are much larger than expected (Lickley et al., 2020), raising questions about feedstock leakage or the potential for unreported non-feedstock production and use. Accurately identifying the origin (i.e., new production or release from banks) of these emissions is critical in informing the Parties to the Montreal Protocol and protecting the O_3 layer.

With only 11 research flights (RFs), Chapter 4 exposes a persistent underestimation in simulated precursor and O_3 concentrations that remains to be resolved. The ARIAs RFs provided a rare opportunity to measure the vertical distribution of pollutants over Hebei Province during the peak season of transport. However, this study covers only a few locations over a short period of time. Emission inventories used in chemical transport models for China are often compiled for longer time periods and not readily updated to reflect the rapidly changing emission composition in China. For example, global inventories have been found to underestimate CO emissions despite increased consumption of fossil fuels due to swift technological changes implementing emission control measures (Zheng et al. 2018).

Furthermore, a challenge comparing modeling results to airborne observations near emission sources is to improve the spatial, temporal, and vertical resolution of both models and emission inventories. In order to document the rapidly changing emission characteristics in China and properly constrain chemical transport models, extensive future observations near emission source regions are fundamental.

In summary, research in this dissertation provides a snapshot of understanding Hebei Province air pollution and its large-scale impacts during ARIAs. Future efforts integrating additional *in situ* observations, satellite retrievals, and model simulations will be crucial to effectively mitigate air pollution in China, a problem with regional roots but global effects.

Bibliography

Abelson, A. and Stieb, D. M.: Health effects of outdoor air pollution, Am. J. Respir. Crit. Care Med., 153(2), 477–498, doi:10.1164/ajrccm.153.2.8564086, 2011.

Acevedo-Whitehouse, K. and Duffus, A. L. J.: Effects of environmental change on wildlife health, Philos. Trans. R. Soc. B Biol. Sci., 364(1534), 3429–3438, doi:10.1098/rstb.2009.0128, 2009.

Air Resources Laboratory: HYSPLIT Basic Tutorial Contents, [online] Available from: https://www.ready.noaa.gov/documents/Tutorial/html/traj_ensem.html (Accessed 4 May 2020), n.d.

Al-Saadi, J., Carmichael, G., Crawford, J., Emmons, L., Kim, S., Song, C. K., Chang, L. S., Lee, G., Kim, J. and Park, R.: NASA Contributions to KORUS-AQ: An International Cooperative Air Quality Field Study in Korea., 2015.

Alam, M., Crilley, L., Lee, J., Kramer, L., Pfrang, C., Vázquez-Moreno, M., Muñoz, A., Ródenas, M. and Bloss, W.: Interference from alkenes in chemiluminescent NOx measurements, Atmos. Meas. Tech. Discuss., 13(x), 5977–5991, doi:10.5194/amt-2020-164, 2020.

An, J., Wang, J., Zhang, Y. and Zhu, B.: Source Apportionment of Volatile Organic Compounds in an Urban Environment at the Yangtze River Delta, China, Arch. Environ. Contam. Toxicol., 72(3), 335–348, doi:10.1007/s00244-017-0371-3, 2017.

An, X., Zhou, L., Yao, B., Xu, L. and Ma, L.: Analysis on source features of halogenated gases at Shangdianzi regional atmospheric background station, Atmos. Environ., 57, 91–100, doi:10.1016/j.atmosenv.2012.04.042, 2012.

An, Z., Huang, R. J., Zhang, R., Tie, X., Li, G., Cao, J., Zhou, W., Shi, Z., Han, Y., Gu, Z. and Ji, Y.: Severe haze in northern China: A synergy of anthropogenic emissions and atmospheric processes, Proc. Natl. Acad. Sci. U. S. A., 116(18), 8657–8666, doi:10.1073/pnas.1900125116, 2019.

Anderson, J. G., Brune, W. H. and Proffitt, M. H.: Ozone destruction by chlorine radicals within the Antarctic vortex: the spatial and temporal evolution of ClO-O_3 anticorrelation based on in situ ER-2 data, J. Geophys. Res., 94(D9), doi:10.1029/jd094id09p11465, 1989.

Andreae, M. O. and Merlet, P.: Emission of trace gases and aerosols from biomass burning, Global Biogeochem. Cycles, 15(4), 955–966, doi:10.1029/2000GB001382, 2001.

Ankley, G. T., Diamond, S. A., Tietge, J. E., Holcombe, G. W., Jensen, K. M., DeFoe, D. L. and Peterson, R.: Assessment of the risk of solar ultraviolet radiation to amphibians. I. Dose-dependent induction of hindlimb malformations in the northern leopard frog (Rana pipiens), Environ. Sci. Technol., 36(13), 2853–2858, doi:10.1021/es011195t, 2002.

Apel, E. C., Emmons, L. K., Karl, T., Flocke, F., Hills, A. J., Madronich, S., Lee-Taylor, J., Fried, A., Weibring, P., Walega, J., Richter, D., Tie, X., Mauldin, L., Campos, T., Weinheimer, A., Knapp, D., Sive, B., Kleinman, L., Springston, S., Zaveri, R., Ortega, J., Voss, P., Blake, D., Baker, A., Warneke, C., Welsh-Bon, D., de Gouw, J., Zheng, J., Zhang, R., Rudolph, J., Junkermann, W. and Riemer, D. D.: Chemical evolution of volatile organic compounds in the outflow of the Mexico City Metropolitan area, Atmos. Chem. Phys., 10(5), 2353–2375, doi:10.5194/acp-10-2353-2010, 2010.

Appel, K. W., Pouliot, G. A., Simon, H., Sarwar, G., Pye, H. O. T., Napelenok, S. L., Akhtar,

F. and Roselle, S. J.: Evaluation of dust and trace metal estimates from the Community Multiscale Air Quality (CMAQ) model version 5.0, Geosci. Model Dev., 6(4), 883–899, doi:10.5194/gmd-6-883-2013, 2013.

Atkinson, R. and Arey, J.: Atmospheric Degradation of Volatile Organic Compounds, Chem. Rev., 103(3), 4605–4638, doi:10.1021/cr0206420, 2003.

Avnery, S., Mauzerall, D. L., Liu, J. and Horowitz, L. W.: Global crop yield reductions due to surface ozone exposure: 2. Year 2030 potential crop production losses and economic damage under two scenarios of O_3 pollution, Atmos. Environ., 45(13), 2297–2309, doi:10.1016/j.atmosenv.2011.01.002, 2011.

Baker, A. K., Beyersdorf, A. J., Doezema, L. A., Katzenstein, A., Meinardi, S., Simpson, I. J., Blake, D. R. and Sherwood Rowland, F.: Measurements of nonmethane hydrocarbons in 28 United States cities, Atmos. Environ., 42(1), 170–182, doi:10.1016/j.atmosenv.2007.09.007, 2008.

Barletta, B., Meinardi, S., Rowland, F. S., Chan, C. Y., Wang, X., Zou, S., Lo, Y. C. and Blake, D. R.: Volatile organic compounds in 43 Chinese cities, Atmos. Environ., 39(32), 5979–5990, doi:10.1016/j.atmosenv.2005.06.029, 2005.

Barletta, B., Meinardi, S., Simpson, I. J., Rowland, F. S., Chan, C., Wang, X., Zou, S., Yin, L. and Blake, D. R.: Ambient halocarbon mixing ratios in 45 Chinese cities, Atmos. Environ., 40, 7706–7719, doi:10.1016/j.atmosenv.2006.08.039, 2006.

Bell, M. L., Peng, R. D. and Dominici, F.: The Exposure – Response Curve for Ozone and Risk of Mortality and the Adequacy of Current Ozone Regulations, Environ. Health Perspect., 114(4), 532–536, doi:10.1289/ehp.8816, 2006.

Benedick, R. E.: Ozone Diplomacy : New Directions in Safeguarding the Planet, Harrvard University Press., 1991.

Benish, S. E., Salawitch, R. J., He, H., Ren, X. and Dickerson, R. R.: Airborne Observations over Hebei Province, China Confirm Production and Use of CFCs, J. Geophys. Res. Atmos., Under Review, 2020a.

Benish, S. E., He, H., Ren, X., Roberts, S. J., Salawitch, R. ., Li, Z., Wang, Y., Zhang, F., Shao, M., Lu, S. and Dickerson, R. R.: Measurement Report: Aircraft Observations of Ozone, Nitrogen Oxides, and Volatile Organic Compounds over Hebei Province, China, Atmos. Chem. Phys., 20(2), 14523–1454, doi:https://doi.org/10.5194/acp-2020-194, 2020b.

Bertschi, I. T. and Jaffe, D. A.: Long-range transport of ozone, carbon monoxide, and aerosols to the NE Pacific troposphere during the summer of 2003: Observations of smoke plumes from Asian boreal fires, J. Geophys. Res. D Atmos., 110(5), 1–14, doi:10.1029/2004JD005135, 2005.

Bessho, K., Date, K., Hayashi, M., Ikeda, A., Imai, T., Inoue, H., Kumagai, Y., Miyakawa, T., Murata, H., Ohno, T., Okuyama, A., Oyama, R., Sasaki, Y., Shimazu, Y., Shimoji, K., Sumida, Y., Suzuki, M., Taniguchi, H., Tsuchiyama, H., Uesawa, D., Yokota, H. and Yoshida, R.: An introduction to Himawari-8/9 — Japan's new-generation geostationary meteorological satellites, J. Meteorol. Soc. Japan, 94(2), 151–183, doi:10.2151/jmsj.2016-009, 2016.

Bey, I., Jacob, D. J., Logan, J. A. and Yantosca, R. M.: Asian chemical outflow to the Pacific in spring: Origins, pathways, and budgets, J. Geophys. Res. Atmos., 106(D19), 23097–23113, doi:10.1029/2001JD000806, 2001.

Beyer, S.: Environmental Law and Policy in the People's Republic of China., 2006.

Blake, D. R., Smith, T. W., Chen, T.-Y., Whipple, W. J. and Rowland, F. S.: Effects of biomass burning on summertime nonmethane hydrocarbon concentrations in the Canadian wetlands, J. Geophys. Res., 99(D1), 1699, doi:10.1029/93jd02598, 1994.

Blake, N. J., Blake, D. R., Simpson, I. J., Meinardi, S., Swanson, A. L., Lopez, J. P., Katzenstein, A. S., Barletta, B., Shirai, T., Atlas, E., Sachse, G., Avery, M., Vay, S., Fuelberg, H. E., Kiley, C. M., Kita, K. and Rowland, F. S.: NMHCs and halocarbons in Asian continental outflow during the Transport and Chemical Evolution over the Pacific (TRACE-P) Field Campaign : Comparison With PEM-West B, J. Geophys. Res., 108, 1–24, doi:10.1029/2002JD003367, 2003.

Blaustein, A. R., Kiesecker, J. M., Chivers, D. P. and Anthony, R. G.: Ambient UV-B radiation causes deformities in amphibian embryos, Proc. Natl. Acad. Sci. U. S. A., 94(25), 13735–13737, doi:10.1073/pnas.94.25.13735, 1997.

British Petroleum Company: Statistical Review of World Energy 2017, London, UK. [online] Available from: http://oilproduction.net/files/especial-BP/bp-statistical-review-of-world-energy-2017-full-report.pdf, 2017.

Brocco, D., Fratarcangeli, R., Lepore, L., Petricca, M. and Ventrone, I.: Determination of aromatic hydrocarbons in urban air of Rome, Atmos. Environ., 31(4), 557–566, doi:10.1016/S1352-2310(96)00226-9, 1997.

Buckley, C. and Fountain, H.: In a High-Stakes Environmental Whodunit, Many Clues Point to China, New York Times, 24th June [online] Available from: https://www.nytimes.com/2018/06/24/world/asia/china-ozone-cfc.html, 2018.

Bucsela, E. J., Krotkov, N. A., Celarier, E. A., Lamsal, L. N., Swartz, W. H., Bhartia, P. K., Boersma, K. F., Veefkind, J. P., Gleason, J. F. and Pickering, K. E.: A new stratospheric and tropospheric NO_2 retrieval algorithm for nadir-viewing satellite instruments: Applications to OMI, Atmos. Meas. Tech., 6(10), 2607–2626, doi:10.5194/amt-6-2607-2013, 2013.

Cai, C. J., Geng, F. H., Tie, X. X., Yu, Q., Peng, L. and Zhou, G. Q.: Characteristics of ambient volatile organic compounds (VOCs) measured in Shanghai, China, Sensors, 10(8), 7843–7862, doi:10.3390/s100807843, 2010.

Canty, T. P., Hembeck, L., Vinciguerra, T. P., Anderson, D. C., Goldberg, D. L., Carpenter, S. F., Allen, D. J., Loughner, C. P., Salawitch, R. J. and Dickerson, R. R.: Ozone and NOx chemistry in the eastern US: Evaluation of CMAQ/CB05 with satellite (OMI) data, Atmos. Chem. Phys., 15(19), 10965–10982, doi:10.5194/acp-15-10965-2015, 2015.

Cao, G., Zhang, X., Gong, S. and Zheng, F.: Investigation on emission factors of particulate matter and gaseous pollutants from crop residue burning, J. Environ. Sci., 20(1), 50–55, doi:10.1016/S1001-0742(08)60007-8, 2008.

Cao, X., Zevitas, C. D., Spengler, J. D., Coull, B., McNeely, E., Jones, B., Loo, S. M., MacNaughton, P. and Allen, J. G.: The on-board carbon dioxide concentrations and ventilation performance in passenger cabins of US domestic flights, Indoor Built Environ., 28(6), 761–771, doi:10.1177/1420326X18793997, 2019.

Cao, Z., Sheng, L., Liu, Q., Yao, X. and Wang, W.: Interannual increase of regional haze-fog in North China Plain in summer by intensified easterly winds and orographic forcing, Atmos. Environ., 122, 154–162, doi:10.1016/j.atmosenv.2015.09.042, 2015.

Di Carlo, P., Brune, W. H., Martinez, M., Harder, H., Lesher, R., Ren, X., Thornberry, T., Carroll, M. A., Young, V., Shepson, P. B., Riemer, D., Apel, E. and Campbell, C.:

Missing OH Reactivity in a Forest: Evidence for Unknown Reactive Biogenic VOCs, Science (80-.)., 304(5671), 722–725, doi:10.1126/science.1094392, 2004.
Carter, C. A.: China's Agriculture: Achievements and Challenges., 2011.
Carter, C. A., Cui, X., Ding, A., Ghanem, D., Jiang, F., Yi, F. and Zhong, F.: Stage-specific, Nonlinear Surface Ozone Damage to Rice Production in China, Sci. Rep., 7(44224), doi:10.1038/srep44224, 2017.
Carter, W. P. .: Updated Maximum Incremental Reactivity Scale and Hydrocarbon Bin Reactivities for Regulatory Applications, Riverside, CA. [online] Available from: https://ww3.arb.ca.gov/regact/2009/mir2009/mir10.pdf, 2010.
Carter, W. P. L.: Development of Ozone Reactivity Scales for Volatile Organic Compounds, J. Air Waste Manage. Assoc., 44(7), 881–899, doi:10.1080/1073161X.1994.10467290, 1994.
Castellanos, P., Marufu, L. T., Doddridge, B. G., Taubman, B. F., Schwab, J. J., Hains, J. C., Ehrman, S. H. and Dickerson, R. R.: Ozone, oxides of nitrogen, and carbon monoxide during pollution events over the eastern United States: An evaluation of emissions and vertical mixing, J. Geophys. Res. Atmos., 116(16), 1–16, doi:10.1029/2010JD014540, 2011.
Central Committee of the Communist Party of China: The 13th Five-Year Plan for Economic and Social Development of the People's Republic of China, Beijing, China., 2016.
Chan, C. Y., Tang, J. H., Li, Y. S. and Chan, L. Y.: Mixing ratios and sources of halocarbons in urban , semi-urban and rural sites of the Pearl River Delta, South China, Atmos. Environ., 40, 7331–7345, doi:10.1016/j.atmosenv.2006.06.041, 2006a.
Chan, L. Y. and Chu, K. W.: Halocarbons in the atmosphere of the industrial-related Pearl River Delta region of China, J. Geophys. Res. Atmos., 112(August 2006), 1–10, doi:10.1029/2006JD007097, 2007.
Chan, L. Y., Chu, K. W., Zou, S. C., Chan, C. Y., Wang, X. M., Barletta, B., Blake, D. R., Guo, H. and Tsai, W. Y.: Characteristics of nonmethane hydrocarbons (NMHCs) in industrial, industrial-urban, and industrial-suburban atmospheres of the Pearl River Delta (PRD) region of south China, J. Geophys. Res. Atmos., 111(11), 1–9, doi:10.1029/2005JD006481, 2006b.
Chang, C., Lai, C., Wang, C., Liu, Y., Shao, M., Zhang, Y. and Wang, J.: Variability of ozone depleting substances as an indication of emissions in the Pearl River Delta, China, Atmos. Environ., 42(2008), 6973–6981, doi:10.1016/j.atmosenv.2008.04.051, 2008.
Chang, X., Wang, S., Zhao, B., Xing, J., Liu, X., Wei, L., Song, Y., Wu, W., Cai, S., Zheng, H., Ding, D. and Zheng, M.: Contributions of inter-city and regional transport to $PM_{2.5}$ concentrations in the Beijing-Tianjin-Hebei region and its implications on regional joint air pollution control, Sci. Total Environ., 660, 1191–1200, doi:10.1016/j.scitotenv.2018.12.474, 2019.
Chen, B. and Kan, Æ. H.: Air pollution and population health: a global challenge, , (2), 94–101, doi:10.1007/s12199-007-0018-5, 2008.
Chen, J., Li, C., Ristovski, Z., Milic, A., Gu, Y., Islam, M. S., Wang, S., Hao, J., Zhang, H., He, C., Guo, H., Fu, H., Miljevic, B., Morawska, L., Thai, P., LAM, Y. F., Pereira, G., Ding, A., Huang, X. and Dumka, U. C.: A review of biomass burning: Emissions and impacts on air quality, health and climate in China, Sci. Total Environ., 579, 1000–1034, doi:10.1016/j.scitotenv.2016.11.025, 2017.

Chen, P., Quan, J., Zhang, Q., Tie, X., Gao, Y., Li, X. and Huang, M.: Measurements of vertical and horizontal distributions of ozone over Beijing from 2007 to 2010, Atmos. Environ., 74, 37–44, doi:10.1016/j.atmosenv.2013.03.026, 2013.
Chen, S.-J., Kuo, Y.-H., Zhang, P.-Z. and Bai, Q.-F.: Synoptic Climatology of Cyclogenesis over East Asia, 1958-1987, Mon. Weather Rev., 119(6), 1407–1418, doi:10.1175/1520-0493(1991)119<1407:scocoe>2.0.co;2, 1991.
Chen, Y., An, J., Sun, Y., Wang, X., Qu, Y., Zhang, J., Wang, Z. and Duan, J.: Nocturnal Low-levelWinds and Their Impacts on Particulate Matter over the Beijing Area, Adv. Atmos. Sci., 35(12), 1455–1468, doi:10.1007/s00376-018-8022-9, 2018.
Cheng, H. R., Guo, H., Saunders, S. M., Lam, S. H. M., Jiang, F., Wang, X. M., Simpson, I. J., Blake, D. R., Louie, P. K. K. and Wang, T. J.: Assessing photochemical ozone formation in the Pearl River Delta with a photochemical trajectory model, Atmos. Environ., 44(34), 4199–4208, doi:10.1016/j.atmosenv.2010.07.019, 2010.
Cheng, M.-D. and Lin, C.: Receptor modeling for smoke of 1998 biomass burning in Central America, J. Geophys. Res., 106(D19), 2001.
Cheng, X., Zhao, T., Gong, S., Xu, X., Han, Y., Yin, Y., Tang, L., He, H. and He, J.: Implications of East Asian summer and winter monsoons for interannual aerosol variations over central-eastern China, Atmos. Environ., 129, 218–228, doi:10.1016/j.atmosenv.2016.01.037, 2016.
Cheng, Y., Wang, Y., Zhang, Y., Chen, G., Crawford, J. H., Kleb, M. M., Diskin, G. S. and Weinheimer, A. J.: Large biogenic contribution to boundary layer O_3-CO regression slope in summer, Geophys. Res. Lett., 44(13), 7061–7068, doi:10.1002/2017GL074405, 2017.
Choi, J., Park, R. J., Lee, H., Lee, S., Jo, D. S., Jeong, J. I., Henze, D. K., Woo, J., Ban, S., Lee, M., Lim, C., Park, M., Shin, H. J., Cho, S., Peterson, D. and Song, C.: Impacts of local vs . trans-boundary emissions from different sectors on $PM_{2.5}$ exposure in South Korea during the KORUS-AQ campaign, Atmos. Environ., 203, 196–205, doi:10.1016/j.atmosenv.2019.02.008, 2019.
Choi, S., Lamsal, L. N., Follette-Cook, M., Joiner, J., Krotkov, N. A., Swartz, W. H., Pickering, K. E., Loughner, C. P., Appel, W., Pfister, G., Saide, P. E., Cohen, R. C., Weinheimer, A. J. and Herman, J. R.: Assessment of NO_2 observations during DISCOVER-AQ and KORUS-AQ field campaigns, Atmos. Meas. Tech., 13(5), 2523–2546, doi:10.5194/amt-13-2523-2020, 2020.
Chung, Y. S.: Air Pollution Detection by Satellites: The Transport and Deposition of Air Pollutants over Oceans, Atmos. Environ., 20(4), 1985.
Conner, T. L., Lonneman, W. A. and Seila, R. L.: Transportation-related volatile hydrocarbon source profiles measured in Atlanta, J. Air Waste Manag. Assoc., 45(5), 383–394, doi:10.1080/10473289.1995.10467370, 1995.
Cooper, O. R., Forster, C., Parrish, D., Trainer, M., Dunlea, E., Ryerson, Y., Hüber, G., Fehsenfeld, F., Nicks, D., Holloway, J., de Gouw, J., Warneke, C., Roberts, J. M., Flocke, F. and Moody, J.: A case study transpacific warm conveyor belt transport: Influence of merging airstreams on trace gas import to North America, J. Geophys. Res. D Atmos., 109(23), 1–17, doi:10.1029/2003JD003624, 2004.
Cooper, O. R., Stohl, A., Trainer, M., Thompson, A. M., Witte, J. C., Oltmans, S. J., Morris, G., Pickering, K. E., Crawford, J. H., Chen, G., Cohen, R. C., Bertram, T. H., Wooldridge, P., Perring, A., Brune, W. H., Merrill, J., Moody, J. L., Tarasick, D.,

Nedelec, P., Forbes, G., Newchurch, M. J., Schmidlin, F. J., Johnson, B. J., Turquety, S., Baughcum, S. L., Ren, X., Fehsenfeld, F. J., Meagher, J. F., Spichtinger, N., Brown, C. C., McKeen, S. A., McDermid, I. S. and Leblanc, T.: Large upper tropospheric ozone enhancements above midlatitude North America during summer: In situ evidence from the IONS and MOZAIC ozone measurement network, J. Geophys. Res. Atmos., 111(24), 1–19, doi:10.1029/2006JD007306, 2006.

Crawford, J., Davis, D., Chen, G., Bradshaw, J., Sandholm, S., Kondo, Y., Liu, S., Browell, E., Gregory, G., Anderson, B., Sachse, G., Collins, J., Barrick, J., Blake, D., Talbot, R. and Singh, H.: An assessment of ozone photochemistry in the extratropical western North Pacific: Impact of continental outflow during the late winter/early spring, J. Geophys. Res., 102(D23), 28469, doi:10.1029/97JD02600, 1997.

Crutzen, P. J.: Ozone Production Rates in an Oxygen-Hydrogen-Nitrogen Oxide Atmosphere, J. Geophys. Res., 76(30), 7311–7327, 1971.

Crutzen, P. J. and Zimmerman, P. .: The changing photochemistry of the troposphere, Tellus, 43AB, 136–151, 1991.

Cunnold, D. M., Weiss, R. F., Prinn, R. G., Hartley, D., Simmonds, P. G., Fraser, P. J., Miller, B., Alyea, F. N. and Porter, L.: GAGE/AGAGE measurements indicating reductions in global emissions of CCl_3F and CCl_2F_2 in 1992-1994, J. Geophys. Res. Atmos., 102(D1), 1259–1269, doi:10.1029/96JD02973, 1997.

Dee, D. P., Uppala, S. M., Simmons, A. J., Berrisford, P., Poli, P., Kobayashi, S., Andrae, U., Balmaseda, M. A., Balsamo, G., Bauer, P., Bechtold, P., Beljaars, A. C. M., van de Berg, L., Bidlot, J., Bormann, N., Delsol, C., Dragani, R., Fuentes, M., Geer, A. J., Haimberger, L., Healy, S. B., Hersbach, H., Hólm, E. V., Isaksen, L., Kållberg, P., Köhler, M., Matricardi, M., Mcnally, A. P., Monge-Sanz, B. M., Morcrette, J. J., Park, B. K., Peubey, C., de Rosnay, P., Tavolato, C., Thépaut, J. N. and Vitart, F.: The ERA-Interim reanalysis: Configuration and performance of the data assimilation system, Q. J. R. Meteorol. Soc., 137(656), 553–597, doi:10.1002/qj.828, 2011.

Deng, Y., Li, J., Li, Y., Wu, R. and Xie, S.: Characteristics of volatile organic compounds, NO_2, and effects on ozone formation at a site with high ozone level in Chengdu, J. Environ. Sci., 75(2), 334–345, doi:10.1016/j.jes.2018.05.004, 2019.

Department of Defense: Assessment on U.S. Defense Implications of China's Expanding Global Access. [online] Available from: https://media.defense.gov/2019/Jan/14/2002079292/-1/-1/1/EXPANDING-GLOBAL-ACCESS-REPORT-FINAL.PDF, 2018.

Dhomse, S. S., Feng, W., Montzka, S. A., Hossaini, R., Keeble, J., Pyle, J. A., Daniel, J. S. and Chipperfield, M. P.: Delay in recovery of the Antarctic ozone hole from unexpected CFC-11 emissions, Nat. Commun., 10(1), 1–12, doi:10.1038/s41467-019-13717-x, 2019.

Di, Q., Dai, L., Wang, Y., Zanobetti, A., Choirat, C., Schwartz, J. D. and Dominici, F.: Association of Short-term Exposure to Air Pollution With Mortality in Older Adults, J. Am. Med. Assoc., 318(24), 2446, doi:10.1001/jama.2017.17923, 2017.

Dickerson, R. R., Kondragunta, S., Stenchikov, G., Civerolo, K. ., Doddridge, B. G. and Holben, B. N.: The Impact of Aerosols on Solar Ultraviolet Radiation and Photochemical Smog, Science (80-.)., 278(5339), 827–830, doi:10.1126/science.278.5339.827, 1997.

Dickerson, R. R., Li, C., Li, Z., Marufu, L. T., Stehr, J. W., Mcclure, B., Krotkov, N., Chen,

H., Wang, P., Xia, X., Ban, X., Gong, F., Yuan, J. and Yang, J.: Aircraft observations of dust and pollutants over northeast China : Insight into the meteorological mechanisms of transport, J. Geophys. Res., 112, 1–13, doi:10.1029/2007JD008999, 2007.

Dickerson, R. R., Anderson, D. C. and Ren, X.: On the use of data from commercial NOx analyzers for air pollution studies, Atmos. Environ., 214(June), 116873, doi:10.1016/j.atmosenv.2019.116873, 2019.

Ding, A., Huang, X. and Fu, C.: Air Pollution and Weather Interaction in East Asia, Oxford Res. Encylopedia Environ. Sci., 1, 1–26, doi:10.1093/acrefore/9780199389414.013.536, 2017.

Ding, A. J., Wang, T., Thouret, V., Cammas, J.-P. and Nédélec, P.: Tropospheric ozone climatology over Beijing: analysis of aircraft data from the MOZAIC program, Atmos. Chem. Phys., 8(1), 1–13, doi:10.5194/acp-8-1-2008, 2008.

Draxler, R. and Hess, G. D.: Description of HYSPLIT-4 Modeling System. [online] Available from: https://www.arl.noaa.gov/documents/reports/arl-224.pdf, 2014.

Duce, R. A., Unni, C. K., Ray, B. J., Prospero, J. M. and Merrill, J. T.: Long-Range Atmospheric Transport of Soil Dust from Asia to the Tropical North Pacific: Temporal Variability, Science (80-.)., 209, 1522–1525, 1980.

Elkins, J. W., Thompson, T. M., Swanson, T. H., Butler, J. H., Hall, B. D., Cummings, S. O., Fisher, D. A. and Raffo, A. G.: Decrease in the growth rates of atmospheric chlorofluorocarbons 11 and 12, Lett. to Nat., 364(August), 8–11, 1993.

Environmental Investigation Agency: Blowing It: Illegal Production and Use of Banned CFC-11 in China's Foam Blowing Industry, London. [online] Available from: https://eia-global.org/reports/20180709-blowing-it-illegal-production-and-use-of-banned-cfc-11-in-chinas-foam-blowing-industry, 2018.

Environmental Protection Agency: CMAQ (Version 5.2) Scientific Document, Zenodo, , doi:10.5281/zenodo.1167892, 2017.

Environmental Protection Agency - Integrated Risk Information System: Benzene ; CASRN 71-43-2., 2003.

European Commission: Joint Research Centre (JRC): Emission Database for Global Atmospheric Research (EDGAR), release version 4.2, [online] Available from: https://edgar.jrc.ec.europa.eu/ (Accessed 1 October 2020), 2011.

Fahey, D. W., Keim, E. R., Boering, K. A., Brock, C. A., Wilson, J. C., Jonsson, H. H., Anthony, S., Hanisco, T. F., Wennberg, P. O., Miake-Lye, R. C., Salawitch, R. J., Louisnard, N., Woodbridge, E. L., Gao, R. S., Donnelly, S. G., Wamsley, R. C., Del Negro, L. A., Solomon, S., Daube, B. C., Wofsy, S. C., Webster, C. R., May, R. D., Kelly, K. K., Loewenstein, M., Podolske, J. R. and Chan, K. R.: Emission measurements of the concorde supersonic aircraft in the lower stratosphere, Science (80-.)., 270(5233), 70–74, doi:10.1126/science.270.5233.70, 1995.

Fan, H., Zhao, C. and Yang, Y.: A comprehensive analysis of the spatio-temporal variation of urban air pollution in China during 2014–2018, Atmos. Environ., 220, 117066, doi:10.1016/j.atmosenv.2019.117066, 2020.

Fang, X., Wu, J., Xu, J., Huang, D., Shi, Y., Wan, D., Wu, H., Shao, M. and Hu, J.: Ambient mixing ratios of chlorofluorocarbons, hydrochloro fluorocarbons and hydrofluorocarbons in 46 Chinese cities, Atmos. Environ., 54, 387–392, doi:10.1016/j.atmosenv.2012.02.070, 2012.

Fang, X., Saito, T., Park, S., Li, S., Yokouchi, Y. and Prinn, R. G.: Performance of Back-Trajectory Statistical Methods and Inverse Modeling Method in Locating Emission Sources, ACS Earth Sp. Chem., 2, 843–851, doi:10.1021/acsearthspacechem.8b00062, 2018.
Farman, J. C., Gardiner, B. G. and Shanklin, J. D.: Large losses of total ozone in Antarctica, Nature, 315, 207–210, 1985.
Fedkin, N., Li, C., Dickerson, R. R., Canty, T. and Krotkov, N. A.: Linking improvements in sulfur dioxide emissions to decreasing sulfate wet deposition by combining satellite and surface observations with trajectory analysis, Atmos. Environ., doi:S1352231018308197, 2018.
Feng, J., Liao, H.,Gu, Y.: A Comparison of Meteorology-Driven Interannual Variations of Surface Aerosol Concentrations in the Eastern United States , Eastern China , and Europe, SOLA, 12(October), 146–152, doi:10.2151/sola.2016-031, 2016.
Finlayson-Pitts, B. J. and Pitts, J. N.: Chemistry of the Upper and Lower Atmosphere, Academic Press, San Diego, CA., 1999.
Fiore, A. M., Jacob, D. J., Bey, I., Yantosca, R. M., Field, B. D., Fusco, A. C. and Wilkinson, J. G.: Background ozone over the United States in summer: Origin, trend, and contribution to pollution episodes, J. Geophys. Res. Atmos., 107(15), 2002.
Florig, H. K., Sun, G. and Song, G.: Evolution of particulate regulation in China — prospects and challenges of exposure-based control, Chemosphere, 49, 1163–1174, 2002.
Formicki, G., Stawarz, R., Lukač, N., Putała, A. and Kuczkowska, A.: Combined effects of cadmium and ultraviolet radiation on mortality and mineral content in common frog (Rana temporaria) larvae, J. Environ. Sci. Heal. - Part A Toxic/Hazardous Subst. Environ. Eng., 43(10), 1174–1183, doi:10.1080/10934520802171717, 2008.
De Foy, B., Lu, Z. and Streets, D. G.: Satellite NO_2 retrievals suggest China has exceeded its NOx reduction goals from the twelfth Five-Year Plan, Sci. Rep., 6(December 2013), 1–9, doi:10.1038/srep35912, 2016.
Fraser, M. P., Cass, G. R. and Simoneit, B. R. T.: Gas-phase and particle-phase organic compounds emitted from motor vehicle traffic in a Los Angeles roadway tunnel, Environ. Sci. Technol., 32(14), 2051–2060, doi:10.1021/es970916e, 1998.
Gao, J., Zhang, J., Li, H., Li, L., Xu, L., Zhang, Y., Wang, Z., Wang, X., Zhang, W., Chen, Y., Cheng, X., Zhang, H., Peng, L., Chai, F. and Wei, Y.: Comparative study of volatile organic compounds in ambient air using observed mixing ratios and initial mixing ratios taking chemical loss into account – A case study in a typical urban area in Beijing, Sci. Total Environ., 628–629(8), 791–804, doi:10.1016/j.scitotenv.2018.01.175, 2018.
Gao, M., Guttikunda, S. K., Carmichael, G. R., Wang, Y., Liu, Z., Stanier, C. O., Saide, P. E. and Yu, M.: Health impacts and economic losses assessment of the 2013 severe haze event in Beijing area, Sci. Total Environ., 511(January 2013), 553–561, doi:10.1016/j.scitotenv.2015.01.005, 2015.
Gao, N., Hopke, P. K., Reid, N. W., Gao, N., Hopke, P. K. and Reid, N. W.: Possible Sources for Some Trace Elements Found in Airborne Particles and Precipitation in Dorset , Ontario Possible Sources for Some Trace Elements Found in Airborne Particles and Precipitation in Dorset , Ontario, J. Air Waste Manag. Assoc., 46(11), 1035–1047, doi:10.1080/10473289.1996.10467539, 2012.
Garcia, T. S., Romansic, J. M. and Blaustein, A. R.: Survival of three species of anuran

metamorphs exposed to UV-B radiation and the pathogenic fungus Batrachochytrium dendrobatidis, Dis. Aquat. Organ., 72(2), 163–169, doi:10.3354/dao072163, 2006.
Gaubert, B., Emmons, L. K., Raeder, K., Tilmes, S., Miyazaki, K., Jr, A. F. A., Elguindi, N., Granier, C., Tang, W., Barré, J., Worden, M., Buchholz, R. R., Edwards, D. P., Franke, P. and Anderson, J. L.: Correcting model biases of CO in East Asia: impact on oxidant distributions during KORUS-AQ, Atmos. Chem. Phys. Discuss., doi:https://doi.org/10.5194/acp-2020-599, 2020.
Ge, W., Chen, R., Song, W. and Kan, H.: Daily visibility and hospital admission in Shanghai, China, Biomed. Environ. Sci., 24(2), 117–121, doi:10.3967/0895-3988.2011.02.005, 2011.
Geng, F., Zhang, Q., Tie, X., Huang, M., Ma, X. and Deng, Z.: Aircraft measurements of O_3, NO_x, CO, VOCs, and SO_2 in the Yangtze River Delta region, Atmos. Environ., 43(3), 584–593, doi:10.1016/j.atmosenv.2008.10.021, 2009.
George, I. J., Hays, M. D., Herrington, J. S., Preston, W., Snow, R., Faircloth, J., George, B. J., Long, T. and Baldauf, R. W.: Effects of Cold Temperature and Ethanol Content on VOC Emissions from Light-Duty Gasoline Vehicles, Environ. Sci. Technol., 49(21), 13067–13074, doi:10.1021/acs.est.5b04102, 2015.
Gilman, J. B., Lerner, B. M., Kuster, W. C. and De Gouw, J. A.: Source signature of volatile organic compounds from oil and natural gas operations in northeastern Colorado, Environ. Sci. Technol., 47(3), 1297–1305, doi:10.1021/es304119a, 2013.
Goldan, P. D., Parrish, D. D., Kuster, W. C., Trainer, M., McKeen, S. A., Holloway, J., Jobson, B. T., Sueper, D. T. and Fehsenfeld, F. C.: Airborne measurements of isoprene, CO, and anthropogenic hydrocarbons and their implications, J. Geophys. Res. Atmos., 105(D7), 9091–9105, doi:10.1029/1999JD900429, 2000.
Goldberg, D. L., Loughner, C. P., Tzortziou, M., Stehr, J. W., Pickering, K. E., Marufu, L. T. and Dickerson, R. R.: Higher surface ozone concentrations over the Chesapeake Bay than over the adjacent land: Observations and models from the DISCOVER-AQ and CBODAQ campaigns, Atmos. Environ., 84, 9–19, doi:10.1016/j.atmosenv.2013.11.008, 2014.
Gu, Y., Li, Q., Wei, D., Gao, L., Tan, L., Su, G., Liu, G., Liu, W., Li, C. and Wang, Q.: Emission characteristics of 99 NMVOCs in di ff erent seasonal days and the relationship with air quality parameters in Beijing , China, Ecotoxicol. Environ. Saf., 169(September 2018), 797–806, doi:10.1016/j.ecoenv.2018.11.091, 2019.
Guan, D., Su, X., Zhang, Q., Peters, G. P., Liu, Z., Lei, Y. and He, K.: The socioeconomic drivers of China's primary $PM_{2.5}$ emissions, Environ. Res. Lett., 9, doi:10.1088/1748-9326/9/2/024010, 2014.
Guan, Y., Wang, L., Wang, S., Zhang, Y., Xiao, J., Wang, X., Duan, E. and Hou, L.: Temporal variations and source apportionment of volatile organic compounds at an urban site in Shijiazhuang, China, J. Environ. Sci. (China), 97, 25–34, doi:10.1016/j.jes.2020.04.022, 2020.
Guanlin, L., Zhen, H., Guipeng, Y. and Da, Y.: Distribution characteristics and sea-to-air fluxes of volatile halocarbons in the East China Sea in autumn, China Environ. Sci., 37(5), 1724–1734, 2017.
Guo, H., Ding, A. J., Wang, T., Simpson, I. J., Blake, D. R., Barletta, B., Meinardi, S., Rowland, F. S., Saunders, S. M., Fu, T. M., Hung, W. T. and Li, Y. S.: Source origins , modeled profiles , and apportionments of halogenated hydrocarbons in the greater

Pearl River Delta region , southern China, J. Geophys. Res., 114, 1–19, doi:10.1029/2008JD011448, 2009.
Guo, S., Tan, J., Ma, Y., Yang, F., Yu, Y. and Wang, J.: Characteristics of atmospheric non-methane hydrocarbons during high PM10 episodes and normal days in Foshan, China, Atmos. Res., 101(3), 701–710, doi:10.1016/j.atmosres.2011.04.022, 2011.
Guo, S., Hu, M., Zamora, M. L., Peng, J., Shang, D., Zheng, J., Du, Z., Wu, Z., Shao, M., Zeng, L., Molina, M. J. and Zhang, R.: Elucidating severe urban haze formation in China, Proc. Natl. Acad. Sci. U. S. A., 111(49), 17373–17378, doi:10.1073/pnas.1419604111, 2014.
Guttikunda, S. K. and Goel, R.: Health impacts of particulate pollution in a megacity-Delhi, India, Environ. Dev., 6(1), 8–20, doi:10.1016/j.envdev.2012.12.002, 2013.
Haagen-Smit, A. J.: Chemistry and Physiology of Los Angeles Smog, Ind. Eng. Chem., 44(6), 1342–1346, doi:10.1021/ie50510a045, 1952.
Häkkinen, J., Pasanen, S. and Kukkonen, J. V. K.: The effects of solar UV-B radiation on embryonic mortality and development in three boreal anurans (Rana temporaria, Rana arvalis and Bufo bufo), Chemosphere, 44(3), 441–446, doi:10.1016/S0045-6535(00)00295-2, 2001.
Halliday, H. S., Digangi, J. P., Choi, Y., Diskin, G. S., Pusede, S. E. and Rana, M.: Using Short-Term CO/CO_2 Ratios to Assess Air Mass Differences over the Korean Peninsula during KORUS-AQ, J. Geophys. Res. Atmos., 124, 10,951–10,972, doi:10.1029/2018JD029697, 2019.
Han, S., Kondo, Y., Oshima, N., Takegawa, N., Miyazaki, Y., Hu, M., Lin, P., Deng, Z., Zhao, Y., Sugimoto, N. and Wu, Y.: Temporal variations of elemental carbon in Beijing, J. Geophys. Res. Atmos., 114(23), 1–16, doi:10.1029/2009JD012027, 2009.
Han, S., Yao, Q., Tie, X., Zhang, Y., Zhang, M., Li, P. and Cai, Z.: Analysis of surface and vertical measurements of O_3 and its chemical production in the NCP region, China, Atmos. Environ., 241, 117759, doi:10.1016/j.atmosenv.2020.117759, 2020.
Hao, J., He, D., Wu, Y., Fu, L. and He, K.: A study of the emission and concentration distribution of vehicular pollutants in the urban area of Beijing ☪, Atmos. Environ., 34(9712705), 2000.
Hatakeyama, S., Takami, A., Wang, W. and Tang, D.: Aerial observation of air pollutants and aerosols over Bo Hai, China, Atmos. Environ., 39(32), 5893–5898, doi:10.1016/j.atmosenv.2005.06.025, 2005.
He, H., Li, C., Loughner, C. P., Li, Z., Krotkov, N. A., Yang, K., Wang, L., Zheng, Y., Bao, X., Zhao, G. and Dickerson, R. R.: SO2 over central China: Measurements, numerical simulations and the tropospheric sulfur budget, J. Geophys. Res., 117, 1–15, doi:10.1029/2011JD016473, 2012.
He, H., Ren, X., Benish, S. E., Li, Z., Wang, F., Wang, Y., Canty, T. P., Dong, X., Lv, F., Hu, Y., Zhu, T. and Dickerson, R. R.: Evaluation of Anthropogenic Emissions and Ozone Pollution in the North China Plain: Insights from the Air Chemistry Research in Asia (ARIAs) Campaign, Atmos. Chem. Phys. Discuss, 1–45, doi:https://doi.org/10.5194/acp-2019-248, 2019.
He, H., Ren, X., Benish, S. E., Li, Z., Wang, F., Wang, Y., Canty, T. P., Dong, X., Lv, F., Hu, Y., Zhu, T. and Dickerson, R. R.: Ozone Pollution over the North China Plain during the 2016 Air Chemistry Research in Asia (ARIAs) Campaign: Observations and a Modeling Study, J. Geophys. Res. Atmos., n.d.

Helmig, D. and Bottenheim, J.: Volatile organic compounds in the global atmosphere, Eos, Trans. Am. Geophys. Union, 90(52), 1–3, doi:10.1029/2009EO520001, 2009.
Hembeck, L., He, ., Vinciguerra, T. ., Canty, T. P., Dickerson, R. R., Salawitch, R. J. and Loughner, C.: Measured and modelled ozone photochemical production in the Baltimore-Washington airshed, Atmos. Environ. X, 2(July 2018), 100017, doi:10.1016/j.aeaoa.2019.100017, 2019.
Hess, P. G.: A comparison of two paradigms: The relative global roles of moist convective versus nonconvective transport, J. Geophys. Res. D Atmos., 110(20), 1–14, doi:10.1029/2004JD005456, 2005.
Ho, K. F., Lee, S. C., Guo, H. and Tsai, W. Y.: Seasonal and diurnal variations of volatile organic compounds (VOCs) in the atmosphere of Hong Kong, Sci. Total Environ., 322(1–3), 155–166, doi:10.1016/j.scitotenv.2003.10.004, 2004.
Hong, C., Zhang, Q., Zhang, Y., Davis, S. J., Tong, D., Zheng, Y., Liu, Z., Guan, D., He, K. and Schellnhuber, H. J.: Impacts of climate change on future air quality and human health in China, Proc. Natl. Acad. Sci. U. S. A., 116(35), 17193–17200, doi:10.1073/pnas.1812881116, 2019.
Hopke, P. K., Cheng, M., Li, C. and Xie, Y.: Possible sources and preferred pathways for biogenic and non-sea-salt sulfur for the high Arctic, J. Geophys. Res., 100(95), 1995.
Hu, W., Niu, H., Zhang, D., Wu, Z., Chen, C., Wu, Y., Shang, D. and Hu, M.: Insights into a dust event transported through Beijing in spring 2012: Morphology, chemical composition and impact on surface aerosols, Sci. Total Environ., 565, 287–298, doi:10.1016/j.scitotenv.2016.04.175, 2016.
Huang, M., Carmichael, G. R., Adhikary, B., Spak, S. N., Kulkarni, S., Cheng, Y. F., Wei, C., Tang, Y., Parrish, D. D., Oltmans, S. J., D'Allura, A., Kaduwela, A., Cai, C., Weinheimer, A. J., Wong, M., Pierce, R. B., Al-Saadi, J. A., Streets, D. G. and Zhang, Q.: Impacts of transported background ozone on California air quality during the ARCTAS-CARB period-a multi-scale modeling study, Atmos. Chem. Phys., 10(14), 6947–6968, doi:10.5194/acp-10-6947-2010, 2010.
Huang, M., Carmichael, G. R., Crawford, J. H., Wisthaler, A., Zhan, X., Hain, C. R., Lee, P. and Guenther, A. B.: Biogenic isoprene emissions driven by regional weather predictions using different initialization methods: Case studies during the SEAC4RS and DISCOVER-AQ airborne campaigns, Geosci. Model Dev., 10(8), 3085–3104, doi:10.5194/gmd-10-3085-2017, 2017.
Huang, X., Wang, T., Talbot, R., Xie, M., Mao, H., Li, S., Zhuang, B., Yang, X., Fu, C., Zhu, J., Huang, X. and Xu, R.: Temporal characteristics of atmospheric CO_2 in urban Nanjing, China, Atmos. Res., 153, 437–450, doi:10.1016/j.atmosres.2014.09.007, 2015.
Hui, L., Liu, X., Tan, Q., Feng, M., An, J., Qu, Y., Zhang, Y. and Cheng, N.: VOC characteristics, sources and contributions to SOA formation during haze events in Wuhan, Central China, Sci. Total Environ., 650, 2624–2639, doi:10.1016/j.scitotenv.2018.10.029, 2019.
Inomata, Y., Iwasaka, Y., Osada, K., Hayashi, M., Mori, I., Kido, M., Hara, K. and Sakai, T.: Vertical distributions of particles and sulfur gases (volatile sulfur compounds and SO_2) over East Asia: Comparison with two aircraft-borne measurements under the Asian continental outflow in spring and winter, Atmos. Environ., 40(3), 430–444, doi:10.1016/j.atmosenv.2005.09.055, 2006.

Jacob, D.: Introduction to Atmospheric Chemistry, Princeton University Press., 1999.
Jacob, D. J., Crawford, J. H., Kleb, M. M., Connors, V. S., Bendura, R. J., Raper, J. L., Sachse, G. W., Gille, J. C., Emmons, L. and Heald, C. L.: Transport and Chemical Evolution over the Pacific (TRACE-P) aircraft mission: Design, execution, and first results, J. Geophys. Res. Atmos., 108(20), doi:10.1029/2002JD003276, 2003.
Jaffe, D. A. and Zhang, L.: Meteorological anomalies lead to elevated O_3 in the western U.S. in June 2015, Geophys. Res. Lett., 44(4), 1990–1997, doi:10.1002/2016GL072010, 2017.
Jaffe, D. A., Anderson, T., Covert, D., Kotchenruther, R., Trost, B., Danielson, J., Simpson, W., Harris, J., Carmichael, G. and Uno, I.: Transport of Asian Air Pollution to North America, Geophys. Res. Lett., 26(6), 711–714, 1999.
Jaffe, D. A., Price, H., Parrish, D., Goldstein, A. and Harris, J.: Increasing background ozone during spring on the west coast of North America, Geophys. Res. Lett., 30(12), 1–4, doi:10.1029/2003GL017024, 2003.
Jeong, D., Seco, R., Gu, D., Lee, Y., Nault, B. A., Knote, C. J., Mcgee, T., Sullivan, J. T., Jimenez, J. L., Campuzano-Jost, P., Blake, D. R., Sanchez, D., Guenther, A. B., Tanner, D., Gregory Huey, L., Long, R., Anderson, B. E., Hall, S. R., Ullmann, K., Shin, H. J., Herndon, S. C., Lee, Y., Kim, D., Ahn, J. and Kim, S.: Integration of airborne and ground observations of nitryl chloride in the Seoul metropolitan area and the implications on regional oxidation capacity during KORUS-AQ 2016, Atmos. Chem. Phys., 19(19), 12779–12795, doi:10.5194/acp-19-12779-2019, 2019.
Jerrett, M., Burnett, R. T., Pope, C. A., Ito, K., Thurston, G., Krewski, D., Shi, Y., Calle, E. and Thun, M.: Long-Term Ozone Exposure and Mortality, N. Engl. J. Med., 360(11), 1085–1095, doi:10.1056/NEJMoa0803894, 2009.
Jia, C., Mao, X., Huang, T., Liang, X., Wang, Y., Shen, Y., Jiang, W., Wang, H., Bai, Z., Ma, M., Yu, Z., Ma, J. and Gao, H.: Non-methane hydrocarbons (NMHCs) and their contribution to ozone formation potential in a petrochemical industrialized city, Northwest China, Atmos. Res., 169, 225–236, doi:10.1016/j.atmosres.2015.10.006, 2016.
Jobson, B. T., Berkowitz, C. M., Kuster, W. C., Goldan, P. D., Williams, E. J., Fesenfeld, F. C., Apel, E. C., Karl, T., Lonneman, W. A. and Riemer, D.: Hydrocarbon source signatures in Houston, Texas: Influence of the petrochemical industry, J. Geophys. Res. D Atmos., 109(24), 1–26, doi:10.1029/2004JD004887, 2004.
Johnson, D., Utembe, S. R. and Jenkin, M. E.: Simulating the detailed chemical composition of secondary organic aerosol formed on a regional scale during the TORCH 2003 campaign in the southern UK, Atmos. Chem. Phys., 6(2), 419–431, doi:10.5194/acp-6-419-2006, 2006.
Johnston, H.: The Concorde, Oxides of Nitrogen, and Stratospheric Ozone, Search, 3(8), 276–282, 1973.
Kanaya, Y., Tanimoto, H., Yokouchi, Y., Taketani, F., Komazaki, Y., Irie, H., Takashima, H., Pan, X., Nozoe, S. and Inomata, S.: Diagnosis of photochemical ozone production rates and limiting factors in continental outflow air masses reaching Fukue Island, Japan: Ozone-control implications, Aerosol Air Qual. Res., 16(2), 430–441, doi:10.4209/aaqr.2015.04.0220, 2016.
Karplus, V. J., Zhang, S. and Almond, D.: Quantifying coal power plant responses to tighter SO_2 emissions standards in China, PNAS, 115(27), 7004–7009,

doi:10.1073/pnas.1800605115, 2018.
Kelley, P., Dickerson, R. R., Luke, T. and Kok, G. L.: Rate of NO2 photolysis from the surface to 7.6 km altitude in clear-sky and clouds, Geophys. Res. Let., 22(19), 2621–2624, 1995.
Kirchstetter, T. W., Singer, B. C., Harley, R. A., Kendall, G. R. and Ghan, W.: Impact of oxygenated gasoline use on California light-duty vehicle emissions, Environ. Sci. Technol., 30(2), 661–670, doi:10.1021/es950406p, 1996.
Kleinman, L.: A comparative study of ozone production in five U.S. metropolitan areas, J. Geophys. Res., 110(D2), D02301, doi:10.1029/2004JD005096, 2005a.
Kleinman, L.: The dependence of tropospheric ozone production rate on ozone precursors, Atmos. Environ., 39(3), 575–586, doi:10.1016/j.atmosenv.2004.08.047, 2005b.
Klimont, Z., Streets, D. G., Gupta, S., Cofala, J., Lixin, F. and Ichikawa, Y.: Anthropogenic emissions of non-methane volatile organic compounds in China, Atmos. Environ., 36(8), 1309–1322, doi:10.1016/S1352-2310(01)00529-5, 2002.
Kondo, Y., Nakamura, K., Chen, G., Takegawa, N., Koike, M., Miyazaki, Y., Kita, K., Crawford, J., Ko, M., Blake, D. R., Kawakami, S., Shirai, T., Liley, B., Wang, Y. and Ogawa, T.: Photochemistry of ozone over the western Pacific from winter to spring, J. Geophys. Res. D Atmos., 109(23), 1–19, doi:10.1029/2004JD004871, 2004.
Krotkov, N. A., McLinden, C. A., Li, C., Lamsal, L. N., Celarier, E. A., Marchenko, S. V., Swartz, W. H., Bucsela, E. J., Joiner, J., Duncan, B. N., Folkert Boersma, K., Pepijn Veefkind, J., Levelt, P. F., Fioletov, V. E., Dickerson, R. R., He, H., Lu, Z. and Streets, D. G.: Aura OMI observations of regional SO2 and NO2 pollution changes from 2005 to 2015, Atmos. Chem. Phys., 16(7), 4605–4629, doi:10.5194/acp-16-4605-2016, 2016.
Lai, C. H., Chang, C. C., Wang, C. H., Shao, M., Zhang, Y. and Wang, J. L.: Emissions of liquefied petroleum gas (LPG) from motor vehicles, Atmos. Environ., 43(7), 1456–1463, doi:10.1016/j.atmosenv.2008.11.045, 2009.
Lamsal, L. N., Martin, R. V., Van Donkelaar, A., Celarier, E. A., Bucsela, E. J., Boersma, K. F., Dirksen, R., Luo, C. and Wang, Y.: Indirect validation of tropospheric nitrogen dioxide retrieved from the OMI satellite instrument: Insight into the seasonal variation of nitrogen oxides at northern midlatitudes, J. Geophys. Res. Atmos., 115(5), 1–15, doi:10.1029/2009JD013351, 2010.
Lan, Q., Zhang, L., Li, G., Vermeulen, R., Weinberg, R. S., Dosemeci, M., Rappaport, S. M., Shen, M., Alter, B. P., Wu, Y., Kopp, W., Waidyanatha, S., Rabkin, C., Guo, W., Chanock, S., Hayes, R. B., Linet, M., Kim, S., Yin, S., Rothman, N. and Smith, M. T.: Hematotoxicity in Workers Exposed to Low Levels of Benzene, Science (80-.)., 306(5702), 1774–1776, doi:10.1126/science.1102443, 2004.
Landrigan, P. J., Fuller, R., Acosta, N. J. R., Adeyi, O., Arnold, R., Basu, N., Baldé, A. B., Bertollini, R., Bose-O'Reilly, S., Boufford, J. I., Breysse, P. N., Chiles, T., Mahidol, C., Coll-Seck, A. M., Cropper, M. L., Fobil, J., Fuster, V., Greenstone, M., Haines, A., Hanrahan, D., Hunter, D., Khare, M., Krupnick, A., Lanphear, B., Lohani, B., Martin, K., Mathiasen, K. V., McTeer, M. A., Murray, C. J. L., Ndahimananjara, J. D., Perera, F., Potočnik, J., Preker, A. S., Ramesh, J., Rockström, J., Salinas, C., Samson, L. D., Sandilya, K., Sly, P. D., Smith, K. R., Steiner, A., Stewart, R. B., Suk, W. A., van Schayck, O. C. P., Yadama, G. N., Yumkella, K. and Zhong, M.: The Lancet Commission on pollution and health, Lancet, 391, doi:10.1016/S0140-

6736(17)32345-0, 2018.
Lelieveld, J., Evans, J. S., Fnais, M., Giannadaki, D. and Pozzer, A.: The contribution of outdoor air pollution sources to premature mortality on a global scale, Nature, 525(7569), 367–371, doi:10.1038/nature15371, 2015.
Lelieveld, J., Klingmüller, K., Pozzer, A., Burnett, R. T., Haines, A. and Ramanathan, V.: Effects of fossil fuel and total anthropogenic emission removal on public health and climate, PNAS, 116(15), 7192–7197, doi:10.1073/pnas.1819989116, 2019.
Levelt, P. F., Van Den Oord, G. H. J., Dobber, M. R., Mälkki, A., Visser, H., De Vries, J., Stammes, P., Lundell, J. O. V. and Saari, H.: The ozone monitoring instrument, IEEE Trans. Geosci. Remote Sens., 44(5), 1093–1100, doi:10.1109/TGRS.2006.872333, 2006.
Li, B., Sai, S., Ho, H., Gong, S., Ni, J., Li, H., Han, L., Yang, Y. and Qi, Y.: Characterization of VOCs and their related atmospheric processes in a central Chinese city during severe ozone pollution periods, Atmos. Chem. Phys., 617–638, 2019.
Li, C., Krotkov, N. A., Dickerson, R. R., Li, Z., Yang, K. and Chin, M.: Transport and evolution of a pollution plume from northern China: A satellite-based case study, J. Geophys. Res., 115, D00K03, doi:10.1029/2009JD012245, 2010.
Li, C., McLinden, C., Fioletov, V., Krotkov, N., Carn, S., Joiner, J., Streets, D., He, H., Ren, X., Li, Z. and Dickerson, R. R.: India Is Overtaking China as the World's Largest Emitter of Anthropogenic Sulfur Dioxide, Sci. Rep., 7(1), 14304, doi:10.1038/s41598-017-14639-8, 2017a.
Li, G., Wei, W., Shao, X., Nie, L., Wang, H., Yan, X. and Zhang, R.: A comprehensive classification method for VOC emission sources to tackle air pollution based on VOC species reactivity and emission amounts, J. Environ. Sci., 67, 78–88, doi:10.1016/j.jes.2017.08.003, 2018a.
Li, J., Xie, S. D., Zeng, L. M., Li, L. Y., Li, Y. Q. and Wu, R. R.: Characterization of ambient volatile organic compounds and their sources in Beijing, before, during, and after Asia-Pacific Economic Cooperation China 2014, Atmos. Chem. Phys., 15(14), 7945–7959, doi:10.5194/acp-15-7945-2015, 2015a.
Li, J., Wu, R., Li, Y., Hao, Y., Xie, S. and Zeng, L.: Effects of rigorous emission controls on reducing ambient volatile organic compounds in Beijing, China, Sci. Total Environ., 557–558, 531–541, doi:10.1016/j.scitotenv.2016.03.140, 2016a.
Li, J., Zhai, C., Yu, J., Liu, R., Li, Y., Zeng, L. and Xie, S.: Spatiotemporal variations of ambient volatile organic compounds and their sources in Chongqing, a mountainous megacity in China, Sci. Total Environ., 627, 1442–1452, doi:10.1016/j.scitotenv.2018.02.010, 2018b.
Li, L., Xie, S., Zeng, L., Wu, R. and Li, J.: Characteristics of volatile organic compounds and their role in ground-level ozone formation in the Beijing-Tianjin-Hebei region, China, Atmos. Environ., 113, 247–254, doi:10.1016/j.atmosenv.2015.05.021, 2015b.
Li, L., Lei, Y., Pan, D., Yu, C. and Si, C.: Economic evaluation of the air pollution effect on public health in China's 74 cities, Springerplus, 5(1), doi:10.1186/s40064-016-2024-9, 2016b.
Li, L. Y., Chen, Y. and Xie, S. D.: Spatio-temporal variation of biogenic volatile organic compounds emissions in China, Environ. Pollut., 182, 157–168, doi:10.1016/j.envpol.2013.06.042, 2013.
Li, M., Jia, L., Zhang, F., Hu, M., Shi, Y. and Chen, X.: Characteristics of haze weather in

Chongqing, China and its determinants analysis based on automatic monitoring stations, Atmos. Pollut. Res., 7(4), 638–646, doi:10.1016/j.apr.2016.02.012, 2016c.
Li, P., De Marco, A., Feng, Z., Anav, A., Zhou, D. and Paoletti, E.: Nationwide ground-level ozone measurements in China suggest serious risks to forests, Environ. Pollut., 1–11, doi:10.1016/j.envpol.2017.11.002, 2017b.
Li, S., Kim, J., Kim, K., Jens, M., Kim, S., Park, M., Stohl, A., Arnold, T., Harth, C. M., Salameh, P. K. and Weiss, R. F.: Emissions of Halogenated Compounds in East Asia Determined from Measurements at Jeju Island , Korea, Enviromental Sci. Technol., 45, 5668–5675, doi:10.1021/es104124k, 2011.
Li, Y., Ye, C., Liu, J., Zhu, Y., Wang, J., Tan, Z., Lin, W. and Zeng, L.: Observation of regional air pollutant transport between the megacity Beijing and the North China Plain, Atmos. Chem. Phys, 14265–14283, doi:10.5194/acp-16-14265-2016, 2016d.
Li, Z., Xia, X., Cribb, M., Mi, W., Holben, B., Wang, P., Chen, H., Tsay, S. C., Eck, T. F., Zhao, F., Dutton, E. G. and Dickerson, R. R.: Aerosol optical properties and their radiative effects in northern China, J. Geophys. Res. Atmos., 112(22), 1–11, doi:10.1029/2006JD007382, 2007.
Li, Z., Lau, W. K. M., Ramanathan, V., Wu, G., Ding, Y., Manoj, M. G., Liu, J., Qian, Y., Li, J., Zhou, T., Fan, J., Rosenfeld, D., Ming, Y., Wang, Y., Huang, J., Wang, B., Xu, X., Lee, S. S., Cribb, M., Zhang, F., Yang, X., Zhao, C., Takemura, T., Wang, K., Xia, X., Yin, Y., Zhang, H., Guo, J., Zhai, P. M., Sugimoto, N., Babu, S. S. and Brasseur, G. P.: Aerosol and monsoon climate interactions over Asia, Rev. Geophys., 54(4), 866–929, doi:10.1002/2015RG000500, 2016e.
Li, Z., Rosenfeld, D. and Fan, J.: Aerosols and Their Impact on Radiation, Clouds, Precipitation, and Severe Weather Events., 2017c.
Liang, F., Xiao, Q., Huang, K., Yang, X., Liu, F., Li, J., Lu, X., Liu, Y. and Gu, D.: The 17-y spatiotemporal trend of PM2.5 and its mortality burden in China, Pr, 1–8, doi:10.1073/pnas.1919641117, 2020.
Liang, Q., Jaeglé, L., Jaffe, D. A., Weiss-Penzias, P., Heckman, A. and Snow, J. A.: Long-range transport of Asian pollution to the northeast Pacific: Seasonal variations and transport pathways of carbon monoxide, J. Geophys. Res. D Atmos., 109(23), 1–16, doi:10.1029/2003JD004402, 2004.
Liang, X., Chen, X., Zhang, J., Shi, T., Sun, X., Fan, L., Wang, L. and Ye, D.: Reactivity-based industrial volatile organic compounds emission inventory and its implications for ozone control strategies in China, Atmos. Environ., 162(2), 115–126, doi:10.1016/j.atmosenv.2017.04.036, 2017.
Lickley, M., Rigby, M., Solomon, S., Fletcher, S., Velders, G. J. M., Daniel, J., Montzka, S. A., Kuijpers, L. J. M. and Stone, K.: Quantifying contributions of chlorofluorocarbon banks to emissions and impacts on the ozone layer and climate, Nat. Commun., (11), doi:10.1038/s41467-020-15162-7, 2020.
Lin, J., van Donkelaar, A., Xin, J., Che, H. and Wang, Y.: Clear-sky aerosol optical depth over East China estimated from visibility measurements and chemical transport modeling, Atmos. Environ., 95, 258–267, doi:10.1016/j.atmosenv.2014.06.044, 2014.
Lin, J. T.: Satellite constraint for emissions of nitrogen oxides from anthropogenic, lightning and soil sources over East China on a high-resolution grid, Atmos. Chem. Phys., 12(6), 2881–2898, doi:10.5194/acp-12-2881-2012, 2012.
Lin, J. T., Liu, M. Y., Xin, J. Y., Boersma, K. F., Spurr, R., Martin, R. and Zhang, Q.:

Influence of aerosols and surface reflectance on satellite NO_2 retrieval: Seasonal and spatial characteristics and implications for NOx emission constraints, Atmos. Chem. Phys., 15(19), 11217–11241, doi:10.5194/acp-15-11217-2015, 2015.
Lin, Y., Gong, D., Lv, S., Ding, Y., Wu, G. and Wang, H.: Observations of High Levels of Ozone-Depleting CFC-11 at a Remote Mountain-Top Site in Southern China, Environ. Sci. Technol. Lett., doi:10.1021/acs.estlett.9b00022, 2019.
Liu, F., Zhang, Q., Tong, D., Zheng, B., Li, M., Huo, H. and He, K. B.: High-resolution inventory of technologies, activities, and emissions of coal-fired power plants in China from 1990 to 2010, Atmos. Chem. Phys., 15(23), 13299–13317, doi:10.5194/acp-15-13299-2015, 2015.
Liu, F., Beirle, S., Zhang, Q., A, R. J. Van Der, Zheng, B., Tong, D. and He, K.: NO_x emission trends over Chinese cities estimated from OMI observations during 2005 to 2015, Atmos. Chem. Phys., (2), 9261–9275, 2017.
Liu, F., Van Der, R. J. A., Eskes, H., DIng, J. and Mijling, B.: Evaluation of modeling NO_2 concentrations driven by satellite-derived and bottom-up emission inventories using in situ measurements over China, Atmos. Chem. Phys., 18(6), 4171–4186, doi:10.5194/acp-18-4171-2018, 2018.
Liu, H., Jacob, D. J., Bey, I., Yantosca, R. M., Duncan, B. N. and Sachse, G. W.: Transport pathways for Asian pollution outflow over the Pacific: Interannual and seasonal variations, J. Geophys. Res. D Atmos., 108(D20), 8786, doi:10.1029/2002jd003102, 2003.
Liu, J. and Si, W.: Using NDVI and air temperature to monitoring winter-wheat phenology in Xingtai, Hebei, China, in 2011 International Conference on Control, Automation and Systems Engineering, CASE 2011, Singapore., 2011.
Liu, Y., Shao, M., Fu, L., Lu, S., Zeng, L. and Tang, D.: Source profiles of volatile organic compounds (VOCs) measured in China: Part I, Atmos. Environ., 42(25), 6247–6260, doi:10.1016/j.atmosenv.2008.01.070, 2008a.
Liu, Y., Shao, M., Lu, S., Chang, C., Wang, J. and Chen, G.: Volatile Organic Compound (VOC) measurements in the Pearl River Delta (PRD) region, China, Atmos. Chem. Phys, 8, 1531–1545, 2008b.
Liu, Y., Liao, W., Lin, X. and Li, L.: Assessment of Co-benefits of vehicle emission reduction measures for 2015-2020 in the Pearl River Delta region, China, Environ. Pollut., 223(2017), 62–72, doi:10.1016/j.envpol.2016.12.031, 2020.
Long, X., Tie, X., Cao, J., Huang, R., Feng, T., Li, N., Zhao, S., Tian, J., Li, G. and Zhang, Q.: Impact of crop field burning and mountains on heavy haze in the North China Plain: A case study, Atmos. Chem. Phys., 16(15), 9675–9691, doi:10.5194/acp-16-9675-2016, 2016.
Lu, X., Zhang, L., Chen, Y., Zhou, M., Zheng, B., Li, K., Liu, Y., Lin, J., Fu, T. M. and Zhang, Q.: Exploring 2016-2017 surface ozone pollution over China: Source contributions and meteorological influences, Atmos. Chem. Phys., 19(12), 8339–8361, doi:10.5194/acp-19-8339-2019, 2019.
Lunt, M. F., Park, S., Li, S., Henne, S., Manning, A. J., Ganesan, A. L., Simpson, I. J., Blake, D. R., Liang, Q., O'Doherty, S., Harth, C. M., Mühle, J., Salameh, P. K., Weiss, R. F., Krummel, P. B., Fraser, P. J., Prinn, R. G., Reimann, S. and Rigby, M.: Continued Emissions of the Ozone Depleting Substance Carbon Tetrachloride from Eastern Asia, Geophys. Res. Lett., 4, 1–8, doi:10.1029/2018GL079500, 2018.

Ma, M., Gao, Y., Wang, Y., Zhang, S., Ruby Leung, L., Liu, C., Wang, S., Zhao, B., Chang, X., Su, H., Zhang, T., Sheng, L., Yao, X. and Gao, H.: Substantial ozone enhancement over the North China Plain from increased biogenic emissions due to heat waves and land cover in summer 2017, Atmos. Chem. Phys., 19(19), 12195–12207, doi:10.5194/acp-19-12195-2019, 2019.

Mao, H. and Talbot, R.: O3 and CO in New England: Temporal variations and relationships, J. Geophys. Res. D Atmos., 109(21), 1–19, doi:10.1029/2004JD004913, 2004.

Marrot, L. and Meunier, J. R.: Skin DNA photodamage and its biological consequences, J. Am. Acad. Dermatol., 58(5 SUPPL. 2), 139–148, doi:10.1016/j.jaad.2007.12.007, 2008.

Mazzuca, G. M., Ren, X., Loughner, C. P., Estes, M., Crawford, J. H., Pickering, K. E., Weinheimer, A. J. and Dickerson, R. R.: Ozone production and its sensitivity to NOx and VOCs: Results from the DISCOVER-AQ field experiment, Houston 2013, Atmos. Chem. Phys., 16(22), 14463–14474, doi:10.5194/acp-16-14463-2016, 2016.

McElroy, M. B., Salawitch, R. J., Wofsy, S. C. and Logan, J. A.: Reductions of Antarctic ozone due to synergistic interactions of chlorine and bromine, Nature, 321(6072), 759–762, doi:10.1038/321759a0, 1986.

McGaughey, G. R., Desai, N. R., Allen, D. T., Seila, R. L., Lonneman, W. A., Fraser, M. P., Harley, R. A., Pollack, A. K., Ivy, J. M. and Price, J. H.: Analysis of motor vehicle emissions in a Houston tunnel during the Texas Air Quality Study 2000, Atmos. Environ., 38(20), 3363–3372, doi:10.1016/j.atmosenv.2004.03.006, 2004.

Menon, S., Hansen, J. and Nazarenko, L.: Climate Effects of Black Carbon Aerosols in China and India, Science (80-.)., 297(5590), 2250–2254, 2002.

Midgley, T.: From the Periodic Table to Production, Ind. Eng. Chem., 29(2), 241–244, doi:10.1021/ie50326a032, 1937.

Miller, B. R., Weiss, R. F., Salameh, P. K., Tanhua, T., Greally, B. R., Mühle, J. and Simmonds, P. G.: Medusa: A sample preconcentration and GC/MS detector system for in situ measurements of atmospheric trace halocarbons, hydrocarbons, and sulfur compounds, Anal. Chem., 80(5), 1536–1545, doi:10.1021/ac702084k, 2008.

Ministry of Environmental Protection, T. P. R. of C.: 2015 Report of the State of the Environment in China., 2016.

Mo, Z., Shao, M., Lu, S., Qu, H., Zhou, M., Sun, J. and Gou, B.: Process-specific emission characteristics of volatile organic compounds (VOCs) from petrochemical facilities in the Yangtze River Delta, China, Sci. Total Environ., 533, 422–431, doi:10.1016/j.scitotenv.2015.06.089, 2015.

Mo, Z., Shao, M., Wang, W., Liu, Y., Wang, M. and Lu, S.: Evaluation of biogenic isoprene emissions and their contribution to ozone formation by ground-based measurements in Beijing, China, Sci. Total Environ., 627, 1485–1494, doi:10.1016/j.scitotenv.2018.01.336, 2018.

Molina, L. T. and Molina, M. J.: Production of Cl2O2 from the self-reaction of the ClO radical, J. Phys. Chem., 91(2), 433–436, doi:10.1021/j100286a035, 1987.

Molina, M. J. and Rowland, F. S.: Stratospheric sink for chlorofluoromethanes: chlorine atomc-atalysed destruction of ozone, Nature, 249, 810–812, 1974.

Monod, A., Sive, B. C., Avino, P., Chen, T., Blake, D. R. and Sherwood Rowland, F.: Monoaromatic compounds in ambient air of various cities: A focus on correlations between the xylenes and ethylbenzene, Atmos. Environ., 35(1), 135–149,

doi:10.1016/S1352-2310(00)00274-0, 2001.
Montzka, S. A., Reimann, S., Engel, A., Krüger, K., O'Doherty, S., Sturges, W. T., Blake, D., Dorf, M., Fraser, P., Froidevaux, L., Jucks, K., Kreher, K., Kurylo, M. J., Mellouki, A., Miller, J., Nielsen, O.-J., Orkin, V. L., Prinn, R. G., Rhew, R., Santee, M. L., Stohl, A. and Verdonik, D.: Ozone-Depleting Substances (ODSs) and Related Chemicals, Geneva, Switzerland., 2011.
Montzka, S. A., Dutton, G. S., Yu, P., Ray, E., Portmann, R. W., Daniel, J. S., Kuijpers, L., Hall, B. D., Mondeel, D., Siso, C., Nance, J. D., Rigby, M., Manning, A. J., Hu, L., Moore, F., Miller, B. R. and Elkins, J. W.: An unexpected and persistent increase in global emissions of ozone-depleting CFC-11, Nature, 557(7705), 413–417, doi:10.1038/s41586-018-0106-2, 2018.
Moody, J. L. and Galloway, J. N.: Quantifying the relationship between atmospheric transport and the chemical composition of precipitation on Bermuda, Tellus, 40B, 463–479, 1988.
MOPITT Science Team: MOPITT/Tera Level 3 Gridded Daily CO (on a latitude/longitude/pressure grid) derived from Near and Thermal Infrarred Radiances, version 7, 2013.
Moreira Dos Santos, C. Y., De Almeida Azevedo, D. and De Aquino Neto, F. R.: Atmospheric distribution of organic compounds from urban areas near a coal-fired power station, Atmos. Environ., 38(9), 1247–1257, doi:10.1016/j.atmosenv.2003.11.026, 2004.
Morrison, W. M.: China's Economic Rise: History, Trends, Challenges, and Implications for the United States, Washington, D.C., 2018.
Nel, A.: Air Pollution – Related Illness : Effects of Particles, Science (80-.)., 308(5723), 804–806, doi:10.1126/science.1108752, 2005.
Neuman, J. A., Nowak, J. B., Zheng, W., Flocke, F., Ryerson, T. B., Trainer, M., Holloway, J. S., Parrish, D. D., Frost, G. J., Peischl, J., Atlas, E. L., Bahreini, R., Wollny, A. G. and Fehsenfeld, F. C.: Relationship between photochemical ozone production and NO_x oxidation in Houston, Texas, J. Geophys. Res., 114, D00F08, doi:10.1029/2008JD011688, 2009.
Ni, R., Lin, J., Yan, Y., Lin, W. and Chen, H.: Foreign and Domestic Contributions to Springtime Anthropogenic Ozone Pollution over China Severe Ozone Pollution in China, Atmos. Chem. Phys, 18, 11447–11469, 2018.
Oh, H. R., Ho, C. H., Kim, J., Chen, D., Lee, S., Choi, Y. S., Chang, L. S. and Song, C. K.: Long-range transport of air pollutants originating in China: A possible major cause of multi-day high-PM_{10} episodes during cold season in Seoul, Korea, Atmos. Environ., 109, 23–30, doi:10.1016/j.atmosenv.2015.03.005, 2015.
Organization for Economic Cooperation and Development: Energy-Renewable Energy, , doi:10.1787/aac7c3f1-en, 2020.
Oshima, N., Koike, M., Nakamura, H., Kondo, Y., Takegawa, N., Miyazaki, Y., Blake, D. R., Shirai, T., Kita, K., Kawakami, S. and Ogawa, T.: Asian chemical outflow to the Pacific in late spring observed during the PEACE-B aircraft mission, J. Geophys. Res. D Atmos., 109(23), 1–17, doi:10.1029/2004JD004976, 2004.
Osterman, G. B., Salawitch, R. J., Sen, B., Toon, G. C., Stachnik, R. A., Pickett, H. M., Margitan, J. J., Blavier, J. F. and Peterson, D. B.: Implications and loss of ozone, Geophys. Res. Let., 24(9), 1107–1110, 1997.

Pan, L. L., Bowman, K. P., Atlas, E. L., Wofsy, S. C., Zhang, F., Bresch, J. F., Ridley, B. A., Pittman, J. V., Homeyer, C. R., Romashkin, P. and Cooper, W. A.: The stratosphere-troposphere analyses of regional transport 2008 experiment, Bull. Am. Meteorol. Soc., 91(3), 327–342, doi:10.1175/2009BAMS2865.1, 2010.

Park, S., Yu, G. H. and Lee, S.: Optical absorption characteristics of brown carbon aerosols during the KORUS-AQ campaign at an urban site, Atmos. Res., 203(November 2017), 16–27, doi:10.1016/j.atmosres.2017.12.002, 2018.

Parrish, D. D., Trainer, M., Young, V., Goldan, P. D., Kuster, W. C., Jobson, B. T., Fehsenfeld, F. C., Lonneman, W. A., Zika, R. D., Farmer, C. T., Riemer, D. D. and Rodgers, M. O.: Internal consistency tests for evaluation of measurements of anthropogenic hydrocarbons in the troposphere, J. Geophys. Res. Atmos., 103(D17), 22339–22359, doi:10.1029/98JD01364, 1998a.

Parrish, D. D., Trainer, M., Holloway, J. S., Yee, J. E., Warshawsky, M. S., Fehsenfeld, F. C., Forbes, G. L. and Moody, J. L.: Relationships between ozone and carbon monoxide at surface sites in the North Atlantic region, J. Geophys. Res. Atmos., 103(D11), 13357–13376, doi:10.1029/98JD00376, 1998b.

Parrish, D. D., Aikin, K. C., Oltmans, S. J., Johnson, B. J., Ives, M. and Sweeny, C.: Impact of transported background ozone inflow on summertime air quality in a California ozone exceedance area, Atmos. Chem. Phys., 10(20), 10093–10109, doi:10.5194/acp-10-10093-2010, 2010.

Perry, R. and Gee, I. L.: Vehicle emissions in relation to fuel composition, Sci. Total Environ., 169(1–3), 149–156, doi:10.1016/0048-9697(95)04643-F, 1995.

Peterson, D. A., Hyer, E. J., Han, S. O., Crawford, J. H., Park, R. J., Holz, R., Kuehn, R. E., Eloranta, E., Knote, C., Jordan, C. E. and Lefer, B. L.: Meteorology influencing springtime air quality, pollution transport, and visibility in Korea, Elementa, 7(1), 57, doi:10.1525/elementa.395, 2019.

Polissar, A. V. and Hopke, P. K.: Source Regions for Atmospheric Aerosol Measured at Barrow, Alaska, Enviromental Sci. Technol., 35(21), 4214–4226, doi:10.1021/es0107529, 2001.

Polissar, A. V., Hopke, P. K., Paatero, P., Kaufmann, Y. J., Hall, D. K., Bodhaine, B. A., Dutton, E. G. and Harris, J. M.: The aerosol at Barrow, Alaska : long-term trends and source locations, Atmos. Environ., 33(16), 2441–2458, 1999.

Price, H. U., Jaffe, D. A., Cooper, O. R. and Doskey, P. V.: Photochemistry, ozone production, and dilution during long-range transport episodes from Eurasia to the northwest United States, J. Geophys. Res. Atmos., 109(D23S13), 2004.

Pusede, S. E., Gentner, D. R., Wooldridge, P. J., Browne, E. C., Rollins, A. W., Min, K. E., Russell, A. R., Thomas, J., Zhang, L., Brune, W. H., Henry, S. B., Digangi, J. P., Keutsch, F. N., Harrold, S. A., Thornton, J. A., Beaver, M. R., St. Clair, J. M., Wennberg, P. O., Sanders, J., Ren, X., Vandenboer, T. C., Markovic, M. Z., Guha, A., Weber, R., Goldstein, A. H. and Cohen, R. C.: On the temperature dependence of organic reactivity, nitrogen oxides, ozone production, and the impact of emission controls in San Joaquin Valley, California, Atmos. Chem. Phys., 14(7), 3373–3395, doi:10.5194/acp-14-3373-2014, 2014.

Qin, D.: Decline in the concentrations of chlorofluorocarbons (CFC-11 , CFC-12 and CFC-113) in an urban area of Beijing , China, Atmos. Environ., 41, 8424–8430, doi:10.1016/j.atmosenv.2007.07.005, 2007.

Quan, J., Zhang, Q., He, H., Liu, J., Huang, M. and Jin, H.: Analysis of the formation of fog and haze in North China Plain (NCP), Atmos. Chem. Phys., 11(15), 8205–8214, doi:10.5194/acp-11-8205-2011, 2011.

Ran, L., Zhao, C. S., Xu, W. Y., Lu, X. Q., Han, M., Lin, W. L., Yan, P., Xu, X. B., Deng, Z. Z., Ma, N., Liu, P. F., Yu, J., Liang, W. D. and Chen, L. L.: VOC reactivity and its effect on ozone production during the HaChi summer campaign, Atmos. Chem. Phys., 11(10), 4657–4667, doi:10.5194/acp-11-4657-2011, 2011.

Real, E., Law, K. S., Schlager, H., Roiger, A., Huntrieser, H., Methven, J., Cain, M., Holloway, J., Neuman, J. A., Ryerson, T., Flocke, F., De Gouw, J., Atlas, E., Donnelly, S. and Parrish, D.: Lagrangian analysis of low altitude anthropogenic plume processing across the North Atlantic, Atmos. Chem. Phys., 8(24), 7737–7754, doi:10.5194/acp-8-7737-2008, 2008.

Reich, P. B. and Amundson, R. G.: Ambient levels of ozone reduce net photosynthesis in tree and crop species, Science (80-.)., 230(4725), 566–570, doi:10.1126/science.230.4725.566, 1985a.

Reich, P. B. and Amundson, R. G.: Ambient Levels of Ozone Reduce Net Photosynthesis in Tree and Crop Species, Science (80-.)., 230(4725), 566–570, doi:10.1126/science.230.4725.566, 1985b.

Ren, X., Salmon, O. E., Hansford, J. R., Ahn, D., Hall, D., Benish, S. E., Stratton, P. R., He, H., Sahu, S., Grimes, C., Heimburger, A. M. F., Martin, C. R., Cohen, M. D., Stunder, B., Salawitch, R. J., Ehrman, S. H., Shepson, P. B. and Dickerson, R. R.: Methane Emissions from the Baltimore-Washington Area Based on Airborne Observations: Comparison to Emissions Inventories, J. Geophys. Res. Atmos., 123(16), 8869–8882, doi:10.1029/2018JD028851, 2018.

Rhoderick, G. C., Hall, B. D., Harth, C. M., Kim, J. S., Lee, J., Montzka, S. A., Mühle, J., Reimann, S., Vollmer, M. K. and Weiss, R. F.: Comparison of halocarbon measurements in an atmospheric dry whole air sampleInter-comparison of halocarbons in an atmospheric dry whole air sample, Elementa, 3, 1–13, doi:10.12952/journal.elementa.000075, 2015.

Richter, A., Burrows, J. P., Nüß, H., Granier, C. and Niemeier, U.: Increase in tropospheric nitrogen dioxide over China observed from space, Nature, 437(7055), 129–132, doi:10.1038/nature04092, 2005.

Rigby, M., Park, S., Saito, T., Western, L. M., Redington, A. L., Fang, X., Henne, S., Manning, A. J., Prinn, R. G., Ganesan, A. L., Hall, B. D., Harth, C. M., Kim, J., Lee, T., Li, S., Dutton, G. S., Liang, Q., Lunt, M. F., Montzka, S. A., Reimann, S., Tunnicliffe, R. L., Weiss, R. F., Yokouchi, Y. and Young, D.: Increase in CFC-11 emissions from eastern China based on atmospheric observations, Nature, 546–550, doi:10.1038/s41586-019-1193-4, 2019.

Ring, A. M., Canty, T. P., Anderson, D. C., Vinciguerra, T. P., He, H., Goldberg, D. L., Ehrman, S. H., Dickerson, R. R. and Salawitch, R. J.: Evaluating commercial marine emissions and their role in air quality policy using observations and the CMAQ model, Atmos. Environ., 173(June 2017), 96–107, doi:10.1016/j.atmosenv.2017.10.037, 2018.

Rogak, S. N., Pott, U., Dann, T. and Wang, D.: Gaseous Emissions from Vehicles in a Traffic Tunnel in Vancouver, British Columbia, J. Air Waste Manag. Assoc., 48(7), 604–615, doi:10.1080/10473289.1998.10463713, 1998.

Rubin, J. I., Kean, A. J., Harley, R. A., Millet, D. B. and Goldstein, A. H.: Temperature dependence of volatile organic compound evaporative emissions from motor vehicle, J. Geophys. Res. Atmos., 111(3), 1–7, doi:10.1029/2005JD006458, 2006.
Russo, R. S., Zhou, Y., White, M. L., Mao, H., Talbot, R. and Sive, B. C.: Multi-year (2004-2008) record of nonmethane hydrocarbons and halocarbons in New England: Seasonal variations and regional sources, Atmos. Chem. Phys., 10(10), 4909–4929, doi:10.5194/acp-10-4909-2010, 2010.
Sagebiel, J. C., Zielinska, B., Pierson, W. R. and Gertler, A. W.: Real-world emissions and calculated reactivities of organic species from motor vehicles, Atmos. Environ., 30(12), 2287–2296, doi:10.1016/1352-2310(95)00117-4, 1996.
Saha, S., Moorthi, S., Wu, X., Wang, J., Nadiga, S., Tripp, P., Behringer, D., Hou, Y. T., Chuang, H. Y., Iredell, M., Ek, M., Meng, J., Yang, R., Mendez, M. P., Van Den Dool, H., Zhang, Q., Wang, W., Chen, M. and Becker, E.: The NCEP climate forecast system version 2, J. Clim., 27(6), 2185–2208, doi:10.1175/JCLI-D-12-00823.1, 2014.
Sampe, T. and Xie, S. P.: Large-scale dynamics of the meiyu-baiu rainband: Environmental forcing by the westerly jet, J. Clim., 23(1), 113–134, doi:10.1175/2009JCLI3128.1, 2010.
Satish, U., Mendell, M. J., Shekhar, K., Hotchi, T., Sullivan, D., Streufert, S. and Fisk, W. J.: Is CO_2 an indoor pollutant? direct effects of low-to-moderate CO_2 concentrations on human decision-making performance, Environ. Health Perspect., 120(12), 1671–1677, doi:10.1289/ehp.1104789, 2012.
Seinfeld, J. H. and Pandis, S. N.: Atmospheric Chemsitry and Physics, 2nd ed., John Wiley & Sons, Inc., New Jersey., 2006.
Shao, M., Tang, X., Zhang, Y. and Li, W.: City clusters in China: air and surface water pollution, Ecol. Soc. Am., 2006.
Shao, M., Zhang, Y., Zeng, L., Tang, X., Zhang, J., Zhong, L. and Wang, B.: Ground-level ozone in the Pearl River Delta and the roles of VOC and NOx in its production, J. Environ. Manage., 90(1), 512–518, doi:10.1016/j.jenvman.2007.12.008, 2009.
Shao, M., Huang, D., Gu, D., Lu, S., Chang, C. and Wang, J.: Estimate of anthropogenic halocarbon emission based on measured ratio relative to CO in the Pearl River Delta region , China, Atmos. Chem. Phys., 5011–5025, doi:10.5194/acp-11-5011-2011, 2011.
Shaughnessy, R. J., Haverinen-Shaughnessy, U., Nevalainen, A. and Moschandreas, D.: A preliminary study on the association between ventilation rates in classrooms and student performance, Indoor Air, 16(6), 465–468, doi:10.1111/j.1600-0668.2006.00440.x, 2006.
Sherry, D., Mcculloch, A., Liang, Q., Reimann, S. and Newman, P. A.: Current sources of carbon tetrachloride (CCl_4) in our atmosphere, Environ. Res. Lett., 13(024004), 2018.
Si, Y., Wang, H., Cai, K., Chen, L., Zhou, Z. and Li, S.: Long-term (2006–2015) variations and relations of multiple atmospheric pollutants based on multi-remote sensing data over the North China Plain, Environ. Pollut., 255, 113323, doi:10.1016/j.envpol.2019.113323, 2019.
Sillman, S. and Samson, P. J.: Impact of temperature on oxidant photochemistry in urban polluted rural and remote environments, J. Geophys. Res., 100(D6), doi:10.1029/94jd02146, 1995.
Sillman, S., Logan, A. and Wofsy, C.: The Sensitivity of Ozone to Nitrogen Oxides and

Hydrocarbons in Regional Ozone Episodes, J. Geophys. Res., 95, 1837–1851, 1990.
Silva, S. J., Arellano, A. F. and Worden, H. M.: Toward anthropogenic combustion emission constraints from space-based analysis of urban CO_2/CO sensitivity, Geophys. Res. Lett., 40(18), 4971–4976, doi:10.1002/grl.50954, 2013.
Simpson, I. J., Blake, D. R., Blake, N. J., Meinardi, S., Barletta, B., Hughes, S. C., Fleming, L. T., Crawford, J. H., Diskin, G. S., Emmons, L. K., Fried, A., Guo, H., Peterson, D. A., Wisthaler, A., Woo, J.-H., Barré, J., Gaubert, B., Kim, J., Kim, M. J., Kim, Y., Knote, C., Mikoviny, T., Pusede, S. E., Schroeder, J. R., Wang, Y., Wennberg, P. O. and Zeng, L.: Characterization, sources and reactivity of volatile organic compounds (VOCs) in Seoul and surrounding regions during KORUS-AQ, Elem Sci Anth, 8(1), 37, doi:10.1525/elementa.434, 2020.
Sirois, A. and Bottenheim, J. W.: Use of backward trajectories to interpret the 5-year record of PAN and 0_3 ambient air concentrations at Kejimkujik National Park , Nova Scotia, J. Geo, 100, 2867–2881, 1995.
Šitum, M., Buljan, M., Bulat, V., Mihic, L. L., Bolanèa, Z. and Simic, D.: The role of UV radiation in the development of Basal cell carcinoma, Coll. Antropol., 32(SUPPL. 2), 167–170, 2008.
Solomon, S.: The discovery of the Antarctic ozone hole, Nature, 575(7), 46–47, 2019.
Solomon, S., Garcia, R. R., Rowland, S. F. and Wuebbles, D. J.: On the depletion of Antarctic ozone, Lett. to Nat., 5–8 [online] Available from: https://www.nature.com/articles/321755a0, 1986.
Souri, A., Nowlan, C., González Abad, G., Zhu, L., Blake, D., Fried, A., Weinheimer, A., Woo, J.-H., Zhang, Q., Chan Miller, C., Liu, X. and Chance, K.: An Inversion of NO_x and NMVOC Emissions using Satellite Observations during the KORUS-AQ Campaign and Implications for Surface Ozone over East Asia, Atmos. Chem. Phys., 1, 1–39, doi:10.5194/acp-2020-220, 2020.
Stavrakou, T., Müller, J., Bauwens, M., Smedt, I. De, Lerot, C. and Roozendael, M. Van: Substantial Underestimation of Post-Harvest Burning Emissions in the North China Plain Revealed by Multi-Species Space Observations, Nat. Publ. Gr., 6, 32307, doi:10.1038/srep32307, 2016.
Stein, A. F., Draxler, R. R., Rolph, G. D., Stunder, B. J. B., Cohen, M. D. and Ngan, F.: NOAA's HYSPLIT atmospheric transport and dispersion modeling system, Bull. Am. Meteorol. Soc., 96(12), 2059–2077, doi:10.1175/BAMS-D-14-00110.1, 2015.
Stohl, A., Forster, C., Eckhardt, S., Spichtinger, N., Huntrieser, H., Heland, J., Schlager, H., Wilhelm, S., Arnold, F. and Cooper, O.: A backward modeling study of intercontinental pollution transport using aircraft measurements, J. Geophys. Res. Atmos., 108(12), doi:10.1029/2002jd002862, 2003.
Stroud, C. A., Morneau, G., Makar, P. A., Moran, M. D., Gong, W., Pabla, B., Zhang, J., Bouchet, V. S., Fox, D., Venkatesh, S., Wang, D. and Dann, T.: OH-reactivity of volatile organic compounds at urban and rural sites across Canada: Evaluation of air quality model predictions using speciated VOC measurements, Atmos. Environ., 42(33), 7746–7756, doi:10.1016/j.atmosenv.2008.05.054, 2008.
Sun, X., Wan, D., Shi, Y., Zhang, J. and Hu, J.: Concentrations and Trends of CFCs and CCl_4 in the Atmosphere of Beijing, Res. Environ. Sci., 23, 2010.
Tang, G., Wang, Y., Li, X., Ji, D., Hsu, S. and Gao, X.: Spatial-temporal variations in surface ozone in Northern China as observed during 2009-2010 and possible implications for

future air quality control strategies, Atmos. Chem. Phys., 12(5), 2757–2776, doi:10.5194/acp-12-2757-2012, 2012.
Tang, J. H., Chan, L. Y., Chan, C. Y., Li, Y. S., Chang, C. C., Liu, S. C., Wu, D. and Li, Y. D.: Characteristics and diurnal variations of NMHCs at urban, suburban, and rural sites in the Pearl River Delta and a remote site in South China, Atmos. Environ., 41(38), 8620–8632, doi:10.1016/j.atmosenv.2007.07.029, 2007.
Tang, J. H., Chan, L. Y., Chang, C. C., Liu, S. and Li, Y. S.: Characteristics and sources of non-methane hydrocarbons in background atmospheres of eastern, southwestern, and southern China, J. Geophys. Res. Atmos., 114(D3), D03304, doi:10.1029/2008JD010333, 2009.
Tang, W., Arellano, A. F., DiGangi, J. P., Choi, Y., Diskin, G. S., Agustí-Panareda, A., Parrington, M., Massart, S., Gaubert, B., Lee, Y., Kim, D., Jung, J., Hong, J., Hong, J. W., Kanaya, Y., Lee, M., Stauffer, R. M., Thompson, A. M., Flynn, J. H. and Woo, J. H.: Evaluating high-resolution forecasts of atmospheric CO and CO_2 from a global prediction system during KORUS-AQ field campaign, Atmos. Chem. Phys., 18(15), 11007–11030, doi:10.5194/acp-18-11007-2018, 2018.
Tang, W., Emmons, L. K., Jr, A. F. A., Gaubert, B., Knote, C., Tilmes, S., Buchholz, R. R., Gabriele, G. P., Diskin, G. S., Blake, D. R., Blake, N. J., Meinardi, S., Digangi, J. P., Choi, Y., Woo, J. H. and He, C.: Source Contributions to Carbon Monoxide Concentrations During KORUS-AQ Based on CAM-chem Model Applications, J. Geophys. Res. Atmos., 124, 2796–2822, doi:10.1029/2018JD029151, 2019.
Tang, W., Worden, H. M., Deeter, M. N., Edwards, D. P., Emmons, L. K., Martínez-Alonso, S., Gaubert, B., Buchholz, R. R., DIskin, G. S., DIckerson, R. R., Ren, X., He, H. and Kondo, Y.: Assessing Measurements of Pollution in the Troposphere (MOPITT) carbon monoxide retrievals over urban versus non-urban regions, Atmos. Meas. Tech., 13(3), 1337–1356, doi:10.5194/amt-13-1337-2020, 2020.
Tang, Z. and Zhang, K. H.: China's urbanization and socioeconomic impact., 2017.
Tanimoto, H., Sawa, Y., Yonemura, S., Yumimoto, K., Matsueda, H., Uno, I., Hayasaka, T., Mukai, H., Tohjima, Y., Tsuboi, K. and Zhang, L.: Diagnosing recent CO emissions and ozone evolution in East Asia using coordinated surface observations, adjoint inverse modeling, and MOPITT satellite data, Atmos. Chem. Phys., 8(14), 3867–3880, doi:10.5194/acp-8-3867-2008, 2008.
Technology and Economic Assessment Panel: May 2006 Progress Report, Nairobi., 2006.
Technology and Economic Assessment Panel: CFC-11 background information, , 3 [online] Available from: https://ozone.unep.org/system/files/documents/TEAP_CFC-11-background-information_revised.pdf, 2018.
Thach, T. Q., Wong, C. M., Chan, K. P., Chau, Y. K., Chung, Y. N., Ou, C. Q., Yang, L. and Hedley, A. J.: Daily visibility and mortality: Assessment of health benefits from improved visibility in Hong Kong, Environ. Res., 110(6), 617–623, doi:10.1016/j.envres.2010.05.005, 2010.
The Institute for the Environment-The University of North Carolina at Chapel Hill: SMOKE v4.5 User's Manual., 2017.
Tsai, W. Y., Chan, L. Y., Blake, D. R. and Chu, K. W.: Vehicular fuel composition and atmospheric emissions in South China: Hong Kong, Macau, Guangzhou, and Zhuhai, Atmos. Chem. Phys., 3281–3288, 2006.
Tsutsumi, Y. and Matsueda, H.: Relationship of ozone and CO at the summit of Mt. Fuji

(35.35°N, 138.73°E, 3776m above sea level) in summer 1997, Atmos. Environ., 34(4), 553–561, doi:10.1016/S1352-2310(99)00238-1, 2000.
Tzortziou, M., Parker, O., Lamb, B., Herman, J., Lamsal, L., Stauffer, R. and Abuhassan, N.: Atmospheric Trace Gas (NO_2 and O_3) Variability in South Korean Coastal Waters, and Implications for Remote Sensing of Coastal Ocean Color Dynamics, Remote Sens., 10(10), 1587, doi:10.3390/rs10101587, 2018.
UNEP: Rigid and Flexible Foams Technical Options Committee (FTOC) 2018 Assessment Report, Nairobi., 2018.
Velasco, E., Lamb, B., Westberg, H., Allwine, E., Sosa, G. and Jobson, B. T.: Distribution, magnitudes, reactivities, ratios and diurnal patterns of volatile organic compounds in the Valley of Mexico during the MCMA 2002 & 2003 field campaigns, Atmos. Chem. Phys., 329–353, 2007.
Velders, G. J., Andersen, S. O., Daniel, J. S., Fahey, D. W. and McFarland, M.: The importance of the montreal protocol in protecting Earth's hydroclimate, J. Clim., 26(12), 4049–4068, doi:10.1175/JCLI-D-12-00675.1, 2013.
Vodonos, A., Awad, Y. A. and Schwartz, J.: The concentration-response between long-term PM2.5exposure and mortality; A meta-regression approach, Environ. Res., 166(May), 677–689, doi:10.1016/j.envres.2018.06.021, 2018.
Vollmer, M. K., Zhou, L. X., Greally, B. R., Henne, S., Yao, B., Reimann, S., Stordal, F., Cunnold, D. M., Zhang, X. C., Maione, M., Zhang, F., Huang, J. and Simmonds, P. G.: Emissions of ozone-depleting halocarbons from China, Geophys. Res. Let., 36(August), 1–5, doi:10.1029/2009GL038659, 2009.
Vollmer, M. K., Young, D., Trudinger, C. M., Mühle, J., Henne, S., Rigby, M., Park, S., Li, S., Guillevic, M., Mitrevski, B., Harth, C., Miller, B. R., Reimann, S., Yao, B., Steele, L. ., Wyss, S. A., Lunder, C. R. and Arduini, J.: Atmospheric histories and emissions of chlorofluorocarbons CFC-13, CFC-114, and CFC-115, Atmos. Chem. Phys., 18, 979–1002, 2018.
Wallace, J. M. and Hobbs, P. V.: Atmospheric Science: An Introductory Survey, 2nd ed., Elsevier., 2006.
Wan, D., Xu, J., Zhang, J., Tong, X. and Hu, J.: Historical and projected emissions of major halocarbons in China, Atmos. Environ., 43(36), 5822–5829, doi:10.1016/j.atmosenv.2009.07.052, 2009.
Wang, B., Shao, M., Lu, S. H., Yuan, B., Zhao, Y., Wang, M., Zhang, S. Q. and Wu, D.: Variation of ambient non-methane hydrocarbons in Beijing city in summer 2008, Atmos. Chem. Phys, 10, 5911–5923, doi:10.5194/acp-10-5911-2010, 2010a.
Wang, C., Shao, M., Huang, D., Lu, S., Zeng, L. and Hu, M.: Estimating halocarbon emissions using measured ratio relative to tracers in China, Atmos. Environ., 89, 816–826, doi:10.1016/j.atmosenv.2014.03.025, 2014a.
Wang, F., Li, Z., Ren, X., Jiang, Q., He, H., Dickerson, R. R., Dong, X. and Lv, F.: Vertical distributions of aerosol optical properties during the spring 2016 ARIAs airborne campaign in the North China Plain, Atmos. Chem. Phys. Discuss., 18, 8995–9010, doi:10.5194/acp-2017-1021, 2018a.
Wang, G., Cheng, S., Wei, W., Zhou, Y., Yao, S. and Zhang, H.: Characteristics and source apportionment of VOCs in the suburban area of Beijing , China, Atmos. Pollut. Res., 7(4), 711–724, doi:10.1016/j.apr.2016.03.006, 2016.
Wang, J. L., Chang, C. J. and Lin, Y. H.: Concentration Distributions of Anthropogenic

Halocarbons over a Metropolitan Area, Chemosphere, 36(10), 2391–2400, 1998.
Wang, M., Shao, M., Lu, S. H., Yang, Y. D. and Chen, W. T.: Evidence of coal combustion contribution to ambient VOCs during winter in Beijing, Chinese Chem. Lett., 24(9), 829–832, doi:10.1016/j.cclet.2013.05.029, 2013.
Wang, Q., Han, Z., Wang, T. and Zhang, R.: Impacts of biogenic emissions of VOC and NO_x on tropospheric ozone during summertime in eastern China, Sci. Total Environ., 395(1), 41–49, doi:10.1016/j.scitotenv.2008.01.059, 2008a.
Wang, T., Guo, H., Blake, D. R., Kwok, Y. H., Simpson, I. J. and Li, Y. S.: Measurements of trace gases in the inflow of South China Sea background air and outflow of regional pollution at Tai O, Southern China, J. Atmos. Chem., 52(3), 295–317, doi:10.1007/s10874-005-2219-x, 2005.
Wang, W., Ma, J., Hatakeyama, S., Liu, X., Chen, Y., Takami, A., Ren, L. and Geng, C.: Aircraft measurements of vertical ultrafine particles profiles over Northern China coastal areas during dust storms in 2006, Atmos. Environ., 42(22), 5715–5720, doi:10.1016/j.atmosenv.2008.03.042, 2008b.
Wang, W., Li, X., Shao, M., Hu, M., Zeng, L., Wu, Y. and Tan, T.: The impact of aerosols on photolysis frequencies and ozone production in Beijing during the 4-year period 2012 – 2015, Atmos. Chem. Phys., 19(2), 9413–9429, 2019a.
Wang, Y., Munger, J. W., Xu, S., McElroy, M. B., Hao, J., Nielsen, C. P. and Ma, H.: CO_2 and its correlation with CO at a rural site near Beijing: Implications for combustion efficiency in China, Atmos. Chem. Phys., 10(18), 8881–8897, doi:10.5194/acp-10-8881-2010, 2010b.
Wang, Y., Zhang, Y., Hao, J. and Luo, M.: Seasonal and spatial variability of surface ozone over China: Contributions from background and domestic pollution, Atmos. Chem. Phys., 11(7), 3511–3525, doi:10.5194/acp-11-3511-2011, 2011.
Wang, Y., Li, Z., Zhang, Y., Du, W., Zhang, F., Tan, H., Xu, H., Jin, X., Fan, X., Dong, Z., Wang, Q. and Sun, Y.: Characterization of aerosol hygroscopicity, mixing state, and CCN activity at a suburban site in the central North China Plain, Atmos. Chem. Phys. Discuss., 18, 11739–11752, doi:10.5194/acp-2017-1100, 2018b.
Wang, Y., Dörner, S., Donner, S., Böhnke, S., De Smedt, I., Dickerson, R. R., Dong, Z., He, H., Li, Z., Li, Z., Li, D., Liu, D., Ren, X., Theys, N., Wang, Y., Wang, Y., Wang, Z., Xu, H., Xu, J. and Wagner, T.: Vertical profiles of NO2, SO2, HONO, HCHO, CHOCHO and aerosols derived from MAX-DOAS measurements at a rural site in the central western North China Plain and their relation to emission sources and effects of regional transport, Atmos. Chem. Phys, 19(2), 5417–5449, 2019b.
Wang, Y. H., Hu, B., Ji, D. S., Liu, Z. R., Tang, G. Q., Xin, J. Y., Zhang, H. X., Song, T., Wang, L. L., Gao, W. K., Wang, X. K. and Wang, Y. S.: Ozone weekend effects in the Beijing-Tianjin-Hebei metropolitan area, China, Atmos. Chem. Phys., 14(5), 2419–2429, doi:10.5194/acp-14-2419-2014, 2014b.
Wang, Y. Q., Zhang, X. Y. and Draxler, R. R.: TrajStat: GIS-based software that uses various trajectory statistical analysis methods to identify potential sources from long-term air pollution measurement data, Environ. Model. Softw., 24(8), 938–939, doi:10.1016/j.envsoft.2009.01.004, 2009.
Warneke, C., McKeen, S. A., de Gouw, J. A., Goldan, P. D., Kuster, W. C., Holloway, J. S., Williams, E. J., Lerner, B. M., Parrish, D. D., Trainer, M., Fehsenfeld, F. C., Kato, S., Atlas, E. L., Baker, A. and Blake, D. R.: Determination of urban volatile organic

compound emission ratios and comparison with an emissions database, J. Geophys. Res. Atmos., 112(10), D10S47, doi:10.1029/2006JD007930, 2007.
Watson, J. G., Chow, J. C. and Fujita, E. M.: Review of volatile organic compound source apportionment by chemical mass balance, Atmos. Environ., 35(9), 1567–1584, doi:10.1016/S1352-2310(00)00461-1, 2001.
Wei, J., Guo, X., Marinova, D. and Fan, J.: Industrial SO_2 pollution and agricultural losses in China: Evidence from heavy air polluters, J. Clean. Prod., 64(2014), 404–413, doi:10.1016/j.jclepro.2013.10.027, 2014.
Wolfe, G. M., Marvin, M. R., Roberts, S. J., Travis, K. R. and Liao, J.: The framework for 0-D atmospheric modeling (F0AM) v3.1, Geosci. Model Dev., 9(9), 3309–3319, doi:10.5194/gmd-9-3309-2016, 2016.
World Health Organization: Ambient (outdoor) air pollution, [online] Available from: https://www.who.int/en/news-room/fact-sheets/detail/ambient-(outdoor)-air-quality-and-health (Accessed 23 September 2020), 2018.
World Meteorological Organization: SCIENTIFIC ASSESSMENT OF OZONE DEPLETION: 2018, Geneva, Switzerland., 2018.
Wu, H., Chen, H., Wang, Y., Ding, A. and Chen, J.: The changing ambient mixing ratios of long-lived halocarbons under Montreal Protocol in China, J. Clean. Prod., 188, 774–785, doi:10.1016/j.jclepro.2018.03.159, 2018a.
Wu, J., Fang, X., Xu, W., Wan, D., Shi, Y., Su, S., Hu, J. and Zhang, J.: Chlorofluorocarbons, hydrochlorofluorocarbons, and hydroflurocarbons in the atmosphere of four Chinese cities, Atmos. Environ., 75, 83–91, doi:10.1016/j.atmosenv.2013.04.031, 2013.
Wu, J., Fang, X., Martin, J. W., Zhai, Z., Su, S., Hu, X., Han, J., Lu, S., Wang, C., Zhang, J. and Hu, J.: Estimated emissions of chlorofluorocarbons, hydrochlorofluorocarbons, and hydrofluorocarbons based on an interspecies correlation method in the Pearl River Delta region, China, Sci. Total Environ., 471, 829–834, 2014.
Wu, J., Bei, N., Hu, B., Liu, S., Wang, Y., Shen, Z., Li, X., Liu, L., Wang, R., Liu, Z., Cao, J., Tie, X., Molina, L. T. and Li, G.: Aerosol–photolysis interaction reduces particulate matter during wintertime haze events, Proc. Natl. Acad. Sci. U. S. A., 117(18), 9755–9761, doi:10.1073/pnas.1916775117, 2020a.
Wu, K., Yang, X., Chen, D., Gu, S., Lu, Y., Jiang, Q., Wang, K., Ou, Y., Qian, Y., Shao, P. and Lu, S.: Estimation of biogenic VOC emissions and their corresponding impact on ozone and secondary organic aerosol formation in China, Atmos. Res., 231, 104656, doi:10.1016/j.atmosres.2019.104656, 2020b.
Wu, X., Ding, Y., Zhou, S. and Tan, Y.: Temporal characteristic and source analysis of PM2.5 in the most polluted city agglomeration of China, Atmos. Pollut. Res., 9(6), 1221–1230, doi:10.1016/j.apr.2018.05.008, 2018b.
Wu, Y., Zhang, S., Hao, J., Liu, H., Wu, X., Hu, J., Walsh, M. P., Wallington, T. J., Zhang, K. M. and Stevanovic, S.: On-road vehicle emissions and their control in China: A review and outlook, Sci. Total Environ., 574, 332–349, doi:10.1016/j.scitotenv.2016.09.040, 2017.
Xia, L., Zhang, G., Liu, L., Li, B., Zhan, M., Kong, P. and Wang, H.: Atmospheric CO_2 and CO at Jingdezhen station in central China: Understanding the regional transport and combustion efficiency, Atmos. Environ., 222, 117104, doi:10.1016/j.atmosenv.2019.117104, 2020.

Xie, X., Shao, M., Liu, Y., Lu, S., Chang, C. C. and Chen, Z. M.: Estimate of initial isoprene contribution to ozone formation potential in Beijing, China, Atmos. Environ., 42(24), 6000–6010, doi:10.1016/j.atmosenv.2008.03.035, 2008.

Xie, Y., Dai, H., Zhang, Y., Wu, Y., Hanaoka, T. and Masui, T.: Comparison of health and economic impacts of PM2.5 and ozone pollution in China, Environ. Int., 130(March), 104881, doi:10.1016/j.envint.2019.05.075, 2019.

Xue, L., Wang, T., Simpson, I. J., Ding, A., Gao, J., Blake, D. R., Wang, X., Wang, W., Lei, H. and Jin, D.: Vertical distributions of non-methane hydrocarbons and halocarbons in the lower troposphere over northeast China, Atmos. Environ., 45(36), 6501–6509, doi:10.1016/j.atmosenv.2011.08.072, 2011.

Xue, L. K., Wang, T., Gao, J., Ding, a. J., Zhou, X. H., Blake, D. R., Wang, X. F., Saunders, S. M., Fan, S. J., Zuo, H. C., Zhang, Q. Z. and Wang, W. X.: Ozone production in four major cities of China: sensitivity to ozone precursors and heterogeneous processes, Atmos. Chem. Phys. Discuss., 13(10), 27243–27285, doi:10.5194/acpd-13-27243-2013, 2013.

Xue, Y., Ho, S. S. H., Huang, Y., Li, B., Wang, L., Dai, W., Cao, J. and Lee, S.: Source apportionment of VOCs and their impacts on surface ozone in an industry city of Baoji, Northwestern China, Sci. Rep., doi:10.1038/s41598-017-10631-4, 2017.

Yang, F., Wang, Y., Li, H., Yang, M., Li, T., Cao, F., Chen, J. and Wang, Z.: Influence of Cloud/Fog on Atmospheric VOCs in the Free Troposphere: A Case Study at Mount Tai in Eastern China, Aerosol Air Qual. Res., 17, 2401–2412, doi:10.4209/aaqr.2016.12.0536, 2017.

Yang, M., Wang, Y., Chen, J., Li, H. and Li, Y.: Aromatic Hydrocarbons and Halocarbons at a Mountaintop in Southern China, , 478–491, doi:10.4209/aaqr.2015.03.0197, 2016a.

Yang, X., Wang, X., Yang, W., Xu, J., Ren, L., He, Y., Liu, B., Bai, Z., Meng, F. and Hu, M.: Aircraft measurements of SO_2, NO_x, CO, and O_3 over the coastal and offshore area of Yellow Sea of China, Environ. Monit. Assess., 188(9), doi:10.1007/s10661-016-5533-7, 2016b.

Yao, B., Vollmer, M. K., Xia, L., Zhou, L., Simmonds, P. G., Stordal, F., Maione, M., Reimann, S. and Doherty, S. O.: A study of four-year HCFC-22 and HCFC-142b in-situ measurements at the Shangdianzi regional background station in China, Atmos. Environ., 63, 43–49, doi:10.1016/j.atmosenv.2012.09.011, 2012.

Yarwood, G., Whitten, G. Z., Jung, J., Heo, G. and Allen, D. T.: Development, Evaluation and Testing of Version 6 of the Carbon Bond Chemical Mechanism (CB6), Austin, TX. [online] Available from: https://www.tceq.texas.gov/assets/public/implementation/air/am/contracts/reports/pm/5820784005FY1026-20100922-environ-cb6.pdf, 2010.

Yuan, B., Hu, W. W., Shao, M., Wang, M., Chen, W. T., Lu, S. H., Zeng, L. M. and Hu, M.: VOC emissions, evolutions and contributions to SOA formation at a receptor site in eastern China, Atmos. Chem. Phys., 13(17), 8815–8832, doi:10.5194/acp-13-8815-2013, 2013.

Zhang, F., Wang, X. M., Yi, Z. G., Li, L. F., Zhou, L. X., Blake, D. R., Sheng, G. Y. and Fu, J. M.: Recent levels and trends of trace chlorofluorocarbons (CFCs) in the Pearl River Delta region, Earth Environ., 34, 19–24, 2006.

Zhang, F., Zhou, L., Yao, B., Vollmer, M. K., Greally, B. R., Simmonds, P. G., Reimann, S., Stordal, F., Maione, M., Xu, L. and Zhang, X.: Analysis of 3-year observations of

CFC-11, CFC-12 and CFC-113 from a semi-rural site in China, Atmos. Environ., 44(35), 4454–4462, doi:10.1016/j.atmosenv.2010.07.041, 2010a.
Zhang, G., Yao, B., Vollmer, M. K., Montzka, S. A., Mühle, J., Weiss, R. F., Doherty, S. O., Li, Y., Fang, S. and Reimann, S.: Ambient mixing ratios of atmospheric halogenated compounds at five background stations in China, Atmos. Environ., 160, 55–69, doi:10.1016/j.atmosenv.2017.04.017, 2017.
Zhang, J., Sun, Y., Wu, F., Sun, J. and Wang, Y.: The characteristics , seasonal variation and source apportionment of VOCs at Gongga Mountain , China, Atmos. Environ., 88, 297–305, doi:10.1016/j.atmosenv.2013.03.036, 2014a.
Zhang, L., Wang, T., Lv, M. and Zhang, Q.: On the severe haze in Beijing during January 2013: Unraveling the effects of meteorological anomalies with WRF-Chem, Atmos. Environ., 104(January 2013), 11–21, doi:10.1016/j.atmosenv.2015.01.001, 2015a.
Zhang, Q. and Crooks, R.: Toward an Environmentally Sustainable Future: Country Environmental Analysis of the People's Republic of China. [online] Available from: https://www.adb.org/sites/default/files/publication/29943/toward-environmentally-sustainable-future-prc.pdf, 2012.
Zhang, Q., Yuan, B., Shao, M., Wang, X., Lu, S., Lu, K., Wang, M., Chen, L., Chang, C. C. and Liu, S. C.: Variations of ground-level O_3 and its precursors in Beijing in summertime between 2005 and 2011, Atmos. Chem. Phys., 14(12), 6089–6101, doi:10.5194/acp-14-6089-2014, 2014b.
Zhang, Y., Wang, X., Simpson, I. J., Barletta, B., Blake, D. R., Meinardi, S., Louie, P. K. K., Zhao, X., Shao, M., Zhong, L., Wang, B. and Wu, D.: Ambient CFCs and HCFC-22 observed concurrently at 84 sites in the Pearl River Delta region during the 2008-2009 grid studies, J. Geophys. Res. Atmos., 119, 7699–7717, doi:10.1002/2014JD021626.Received, 2014c.
Zhang, Y. L., Guo, H., Wang, X. M., Simpson, I. J., Barletta, B., Blake, D. R., Meinardi, S., Rowland, F. S., Cheng, H. R., Saunders, S. M. and Lam, S. H. M.: Emission patterns and spatiotemporal variations of halocarbons in the Pearl River Delta region , southern China, J. Geophys. Res., 115, 1–16, doi:10.1029/2009JD013726, 2010b.
Zhang, Z., Wang, X., Zhang, Y., Lü, S. and Huang, Z.: Ambient air benzene at background sites in China's most developed coastal regions : Exposure levels , source implications and health risks, Sci. Total Environ., 511, 792–800, doi:10.1016/j.scitotenv.2015.01.003, 2015b.
Zhao, M., Qiao, T., Huang, Z., Zhu, M., Xu, W., Xiu, G., Tao, J. and Lee, S.: Comparison of ionic and carbonaceous compositions of $PM_{2.5}$ in 2009 and 2012 in Shanghai, China, Sci. Total Environ., 536, 695–703, doi:10.1016/j.scitotenv.2015.07.100, 2015.
Zhao, P., Zhang, R., Liu, J., Zhou, X. and He, J.: Onset of southwesterly wind over eastern China and associated atmospheric circulation and rainfall, Clim. Dyn., 28(7–8), 797–811, doi:10.1007/s00382-006-0212-y, 2007.
Zhao, S., Yu, Y., Yin, D., He, J., Liu, N., Qu, J. and Xiao, J.: Annual and diurnal variations of gaseous and particulate pollutants in 31 provincial capital cities based on in situ air quality monitoring data from China National Environmental Monitoring Center, Environ. Int., 86(January 2013), 92–106, doi:10.1016/j.envint.2015.11.003, 2016.
Zhao, S., Feng, T., Tie, X., Long, X., Li, G., Cao, J., Zhou, W. and An, Z.: Impact of climate change on Siberian High and wintertime air pollution in China in past two decades, , doi:10.1002/eft2.281, 2018.

Zhao, X. J., Zhao, P. S., Xu, J., Meng, W., Pu, W. W., Dong, F., He, D. and Shi, Q. F.: Analysis of a winter regional haze event and its formation mechanism in the North China Plain, Atmos. Chem. Phys., 13(11), 5685–5696, doi:10.5194/acp-13-5685-2013, 2013.

Zheng, B., Chevallier, F., Ciais, P., Yin, Y., Deeter, M. N., Worden, H. M., Wang, Y., Zhang, Q. and He, K.: Rapid decline in carbon monoxide emissions and export from East Asia between years 2005 and 2016, Environ. Res. Lett., 13(4), doi:10.1088/1748-9326/aab2b3, 2018.

Zheng, J., Shao, M., Che, W., Zhang, L., Zhong, L., Zhang, Y. and Streets, D.: Speciated VOC Emission Inventory and Spatial Patterns of Ozone Formation Potential in the Pearl River Delta , China, Enviromental Sci. Technol., 43(22), 8580–8586, 2009.

Zong, R., Yang, X., Wen, L., Xu, C., Zhu, Y., Chen, T., Yao, L., Wang, L., Zhang, J., Yang, L., Wang, X., Shao, M., Zhu, T., Xue, L. and Wang, W.: Strong ozone production at a rural site in the North China Plain: Mixed effects of urban plumes and biogenic emissions, J. Environ. Sci., 71, 261–270, doi:10.1016/j.jes.2018.05.003, 2018.

Zou, Y., Deng, X. J., Zhu, D., Gong, D. C., Wang, H., Li, F., Tan, H. B., Deng, T., Mai, B. R., Liu, X. T. and Wang, B. G.: Characteristics of 1 year of observational data of VOCs, NO_x and O_3 at a suburban site in Guangzhou , China, Atmos. Chem. Phys., 15, 6625–6636, doi:10.5194/acp-15-6625-2015, 2015.